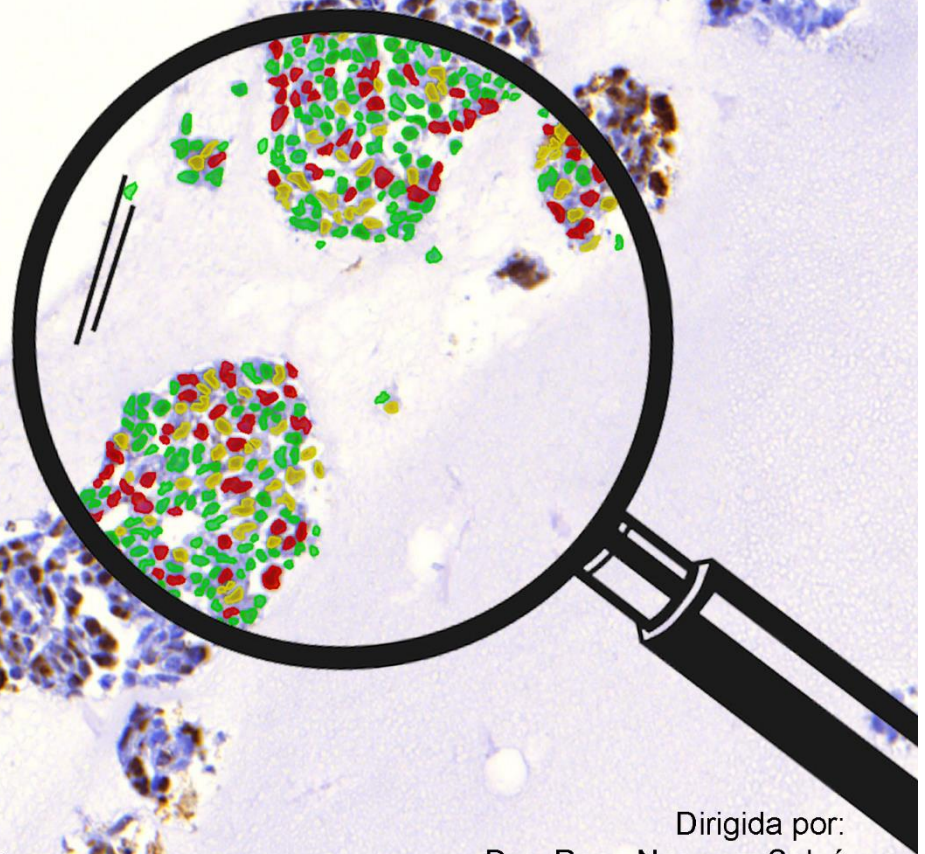


Understanding mechanical transmission signals
in neuroblastoma using 3D in vitro models
for biological and preclinical studies

Transmisión de señales mecánicas
en células indiferenciadas neuroblásticas.
Estudios biológicos y preclínicos en modelos in vitro 3D.

Ezequiel Monferrer Garzarán
Programa de Doctorado en Medicina
Diciembre 2022



VNIVERSITAT
ID VALÈNCIA [Logo]

Facultat de Medicina i Odontologia

Dirigida por:
Dra. Rosa Noguera Salvá

"I am never content until I have constructed a mechanical model of the subject I am studying. If I succeed in making one, I understand. Otherwise, I do not."

Lord Kelvin



VNIVERSITATIS VALÈNCIA

Departament de Patologia, Facultat de Medicina i Odontologia

**UNDERSTANDING MECHANICAL TRANSMISSION SIGNALS
IN NEUROBLASTOMA USING 3D *IN VITRO* MODELS
FOR BIOLOGICAL AND PRECLINICAL STUDIES**

TRANSMISIÓN DE SEÑALES MECÁNICAS
EN CÉLULAS INDIFERENCIADAS NEUROBLÁSTICAS.
ESTUDIOS BIOLÓGICOS Y PRECLÍNICOS EN MODELOS *IN VITRO* 3D

Ezequiel Monferrer Garzarán

Doctoral thesis

Programa de Doctorado: 3139 Medicina: Tumores sólidos pediátricos

Thesis director: Dra. Rosa Noguera Salvá

Valencia, Noviembre 2022

Doña Rosa Noguera Salvá, doctora en Medicina y catedrática de la Facultad de Medicina y Odontología de la Universidad de Valencia,

CERTIFICAN:

Que **Ezequiel Monferrer Garzarán**, graduado en Biotecnología por la Universidad Autónoma de Barcelona, ha realizado, bajo mi dirección, el trabajo titulado:

*Transmisión de señales mecánicas en células indiferenciadas neuroblásticas.
Estudios biológicos y preclínicos en modelos in vitro 3D*

El cual consideramos satisfactorio y apto para ser presentado y defendido como Tesis Doctoral en el Departamento de Patología de la Universidad de Valencia.

Y para que así conste, expedimos este certificado en Valencia, a 30 de Noviembre de 2022.

NOGUERA SALVA,
MARIA ROSA
(AUTENTICACIÓN)

Firmado digitalmente por NOGUERA SALVA, MARÍA ROSA (AUTENTICACIÓN)
Nombre de reconocimiento (DN): c=ES,
serialNumber=19884196Y,
sn=NOGUERA, givenName=MARIA ROSA, cn=NOGUERA SALVA, MARIA ROSA (AUTENTICACIÓN)
Fecha: 2022.11.30 13:57:52 +01'00'

Fdo.: Prof^a. Rosa Noguera Salvá
Prof^a. Catedrática de Histología

Agradecimientos:

Parece obvio pensar que las cosas se empiezan por el principio, ¿quién lo dudaría? Pues en ciencia, los resúmenes que aparecen al principio, y hasta las introducciones, son lo último que se escribe. En las tesis ocurre lo mismo, aquí estoy, redactando una de las primeras páginas como broche final, pero voy a permitirme la licencia de empezar, al menos los agradecimientos, por el principio.

A mis padres, que probablemente sin saberlo, hace ahora aproximadamente 29 años y 3 meses, iniciaron un efecto mariposa que, entre llantos, alegrías, aventuras, recuerdos y toneladas de amor, ha dado pie a la realización de esta tesis doctoral. Por su apoyo incondicional, por su paciencia, por su cariño, porque me lo han dado todo. A mi padre, por los trenes de energía positiva, por los buenos días, por las esperas entre llamada y llamada, por el truco del almendruco, por la filosofía de vida. A mi madre, por las veces que la he necesitado, y por todas las que se ha ofrecido, por su ayuda “sutil”, por su admirable predisposición a compartir, debatir y contrastar opiniones, y por demostrarme que se puede llegar lejos si actúas con pasión. Sé que lo digo poco, así que lo pongo por escrito, OS QUIERO, y me siento afortunado de teneros como padres.

A mi familia, a los que están y a los que no, por el amor, la confianza y el apoyo que siempre me habéis dado, aunque fuese en la distancia.

A mis amigos, pacientes, locos, atemporales, siempre dispuestos, que te hacen sentir querido y bienvenido allá donde estés. Ya sea para charlar, desahogarse, salir, bailar, jugar, patinar, saltar o viajar, siempre estáis ahí.

A mis compañeros de laboratorio, desde 2017 a 2022, que han compartido parte del proceso de este trabajo, me han visto perder el poco pelo que tenía y que me han hecho crecer como persona y como investigador. Gracias a Víctor Zuñiga, Maite Blanquer, Ana Berbegall, Esther Gamero, Aitor Carretero y Federico Lucantoni, por haber participado en este viaje. Especial mención a compañeras como Irene Tadeo, por iniciarme en el análisis de imagen; Susana Martín, cuyo trabajo originó la línea de investigación con hidrogeles; Sabina Sanegre, por su energía, familiaridad y conocimiento; y a Rebeca Burgos, por ser guía y referencia en el laboratorio.

También al séquito multitudinario actual del laboratorio, y a los compañeros que puedo considerar familiares directos de este trabajo, que han estado día tras día engordando conmigo en el laboratorio, ofreciendo consejo, apoyo, ánimo y consuelo; que han hecho del laboratorio mi segunda casa. Amparo López, amante del queso, el buceo y los buenos viajes, por tanto, por todo. A Sofía Granados, aventurera y alma libre, por tu calor humano, tu empatía, tus consejos. A Isaac Vieco, alcahuete, hacker, bailarín talentoso y cocinero exquisito, te debo iniciativas, miles de clusters rodeados a mano, kebabs redactando artículos, scripts en QuPath y gráficos de R entre otras cosas, sin las que esta tesis no sería lo mismo. Por si fuera poco, eres también un hombro amigo y formido en el que apoyarse cuando uno lo necesita.

A Esther Álvarez, Cristina Mongort y Elisa Alonso del servicio de Anatomía Patológica del Hospital Clínico de Valencia, por sus consejos, su amabilidad y su implicación.

A Andrea García, por enseñarme lo que sé de bioimpresión y compresión mecánica en mi visita al IBEC.

A Manuel Salmerón, por acogerme con soberbia hospitalidad en su laboratorio en el CeMi de Glasgow. A Oana Dobre, Aleixandre Rodrigo y Mariana Azevedo, por su dedicación, por haberme hecho sentir parte del grupo, y por haberme enseñado tanto en tan poco tiempo durante mi estancia.

A Rosa Noguera, mi directora de tesis, por tu dedicación, tu pasión, tu experiencia, tu confianza, tus enseñanzas y las oportunidades que me has brindado para crecer personal y profesionalmente.

Quisiera acabar, siendo coherente conmigo mismo, por el final. A mis tres chicas, Nora, por esos abrazos entusiastas día tras día, y por enseñarme que las prisas y los agobios no son buena compañía; Kyla, por mantenerme en forma con tus escapadas, y por dar a mis ideas un buen lavado de cara; Irene, a ti, porque llegaste en la recta final, aguantando lo más duro del camino hasta día de hoy, y, sin embargo, me llenaste de risas, paz, comprensión, ánimo y cariño. Por soportarme, por tu apoyo incondicional, por tu ayuda, por estar, por aportarme tanto, por lo que eres, por cómo eres, por cómo me haces ser, por darme el mejor cierre posible para estos agradecimientos. **GRÀCIES**

Trabajo financiado por la Asociación Fundación Española contra el Cáncer, JAP-AECC (2018/150), CIBERONC (CB16/12/00484), Instituto Carlos III (PI17/01558 y PI20/01107) y Asociación NEN/Nico contra el cáncer infantil.

INDEX

Figures index	1
Tables index	2
Summary	3
Resumen	9
Abbreviations	17
Compendium of articles that support this thesis	18
<i>Article I: A three-dimensional bioprinted model to evaluate the effect of stiffness on neuroblastoma cell cluster dynamics and behavior</i>	<i>19</i>
<i>Article II: Digital Image Analysis Applied to Tumor Cell Proliferation, Aggressiveness, and Migration-Related Protein Synthesis in Neuroblastoma 3D Models</i>	<i>37</i>
<i>Article III: Vitronectin-based hydrogels recapitulate neuroblastoma growth conditions</i>	<i>57</i>
Additional scientific production that complements this thesis	75
<i>Articles as a coauthor</i>	<i>75</i>
<i>Communications in scientific meetings</i>	<i>75</i>
I. INTRODUCTION / STATE OF THE ART	79
1. Biotensegrity and mechanotransduction in euplastic and neoplastic human tissues	81
2. Cancer cell plasticity and adaptability	84
3. Precision diagnostics and therapeutics in oncology	87
4. Translational studies in neuroblastoma (NB)	92
II. METHODOLOGY	97
1. Experiment guideline	99
2. Cell cultures	99
3. <i>In vitro</i> 3D platforms	100
4. Ethics approval and consent to participate	100
5. Digital image analysis	101
6. Statistics	102
7. Thesis illustrations	102

III. HYPOTHESIS, AIMS AND JUSTIFICATION OF THE THESIS BY ARTICLE

COMPENDIUM	103
1. Hypothesis	105
2. Aims	105
3. Justification of the article compendium	106
IV. RESULTS AND DISCUSSION	109
1. Contribution of three-dimension (3D) scaffolding to NB biotensegrity mimicry	111
1.1. <u>Technical features influencing 3D model designing</u>	111
1.1.1 <i>Architecture regarding fabrication procedure</i>	111
1.1.2 <i>Digital pathology as a unifying approach to sample analysis</i>	114
1.1.3 <i>Manufacturing cost demands model mimicry-technical balance and purpose fitness</i>	116
1.2. <u>Improvement of translational research focusing on extracellular matrix 117(ECM) pathophysiological relevance</u>	117
1.2.1 <i>Mechanical properties of the hydrogels: Stiffness and degradability</i> ...119	
1.2.2 <i>Scaffolding functionalization with gelatin and vitronectin (VN)</i>	122
1.2.3 <i>Hydrogel cell hosting capacity</i>	124
2. Biomarkers unraveling the mechanotransduction impact in the models	125
2.1. <u>KANK1 and DOCK8 proteins as intracellular biotensegrity modulators</u>	126
2.2. <u>VN as a potential therapeutic target involved in cell-ECM crosstalk</u>	128
3. Cell plasticity promotes dynamic adaptation in response to biotensegral stimuli	133
3.1. <u>Cell growth dynamics</u>	133
3.2. <u>Differentiation and metabolism dynamics</u>	136
4. Model contribution to precision diagnostic and therapy	145
4.1. <u>Current translational upgrades</u>	145
4.2. <u>Potential translational upgrades</u>	146
V. CONCLUSIONS / CONCLUSIONES	149
REFERENCES	157
APPENDIX	195

Figures index

Figure 1. Representation of the interacting tumor microenvironment elements involved in biotensegrity mechanotransduction signaling.	83
Figure 2. Interplay between tumor adaptation processes.....	86
Figure 3. Standard digital image analysis pipeline followed with the main four softwares used in this doctoral thesis.....	89
Figure 4. Workflow from obtention to analysis of human NB biopsies and NB experimental models used in this thesis.	112
Figure 5. Components used in this thesis for 3D <i>in vitro</i> NB model fabrication, classified according to tissue engineering triad.....	117
Figure 6. Minimum to maximum stiffness range of the hydrogels herein developed at initial and final mechanical determination timepoints (days), compared with human NB stiffness.....	120
Figure 7. SK-N-BE(2) morphology depending on the VN-enriched substrate.....	124
Figure 8. Biotensegral pathways related to cytoskeletal signal mechanotransduction and reorganization involving KANK1 and DOCK8 proteins.	127
Figure 9. VN synthesis in NB cell lines, human NB biopsies, and VN-KO PDX NB samples.	
Figure 10. VN synthesis in GelMA/AlgMA and PEG hydrogels.....	129
Figure 11. VN synthesis evolution in SK-N-BE(2) plus SW10 and SH-SY5Y plus SW10 GelMA/AlgMA hydrogels.....	131
Figure 12. Mechanotherapeutic approach for NB designed in our laboratory using cilengitide and etoposide.	132
Figure 13. Caspase-3 expression in PEG hydrogels.....	135
Figure 14. NB cell molecular pathways related to differentiation, glucose metabolism and TME reshape.	137
Figure 15. Expression of stem cell markers in monolayer cell cultures.....	138
Figure 16. OCT4 and SOX2 expression variation in SK-N-BE(2) GelMA/AlgMA hydrogels due to culture time and SW10 incorporation.	139
Figure 17. Box plot of PTBP1, PTBP2 and PSD-95 expression in GelMA/AlgMA hydrogels revealing NB maturation dynamics.	141
Figure 18. Box plot of PTBP1, PKM2 and MCT1 expression in GelMA/AlgMA hydrogels revealing NB glucose metabolism dynamics.	143

Tables index

Table 1. Distinctive features of human NB biopsies and NB experimental models used in this thesis associated with sample origin.	113
Table 2. Distinctive sample features according to processing and analysis of human NB biopsies and NB experimental models used in this thesis.	115
Table 3. Comparison between the pathophysiological relevance of NB and that of the experimental models used in this thesis.	118
Table 4. Parameters defining the variability of the hydrogel mechanical properties.	121

Summary

Life is widely supported by the self-balancing principle of biotensegrity, which is based in the functional equilibrium between tensional and compressive physical forces in those biological structures built with discontinuous struts supporting compression, connected by a continuous network of flexible tension elements. It allows mechanical transmission signals occurring at all detectable scales, from DNA structures up to organ system functional organization, which in turn triggers mechanical and biochemical responses. Obeying the biotensegral self-balancing principle, cells are equipped with an internal biopolymeric structure, the cytoskeleton, which hard-wires cell membrane, nucleus, and organelles. However, in an extensive way, the intertwined biotensegral signaling pathways within the whole tissue ecosystem, cell-cell and cell-surrounding dialogue, are responsible for coordinated cytoskeletal reorganizations that determine cell behavior and redefine the whole tissue structure, both in homeostasis and in tissue disorders such as cancer. In this regard, cancer diseases display their own aberrant biotensegral systems driving tumorigenesis and illness evolution, which are related to malignant and non-malignant cells crosstalk within the tumor microenvironment; the extracellular matrix composition, the ability to resist deformation, and the topology of the extracellular matrix elements, as well as the innervation presence.

All these parameters rearrange conforming different dynamic tumor signaling scenarios to which malignant cells rapidly adapt due to their plasticity, thus promoting cancer progression, metastasis, and drug resistance. A variety of signal rewiring, epigenetic, and genetic mechanisms are among the major driving forces of cancer cell adaptability. Therefore, tumor cells can undergo morphological and molecular adaptations affecting cell physics, which may involve pleomorphism and cell adhesion loss, but also deeper dedifferentiation and transdifferentiation processes such as reversible epithelial-mesenchymal transition determining cell fate. Remarkably, biotensegral communication between cells and the tumor ecosystem bridges the individual cell adaptations leading to tumor collective adaptability. Indeed, tumor cell cooperation not only triggers transient spatial rearrangement for collective migration of mobile and non-mobile cells as an entity, but also promotes tumor microenvironment remodeling by both reshaping the extracellular matrix and shaping the inflammatory

response. Alternatively, biotensegral signaling within tumor microenvironment promotes tumor genetic heterogeneity, further regulating carcinogenesis, malignancy, and therapeutic resistance. Likewise, metabolic reprogramming has been defined as the ability of cancer cells to redirect their bioenergetic pathways to meet the increased energy demand derived from its proliferation and growth activities, and it has become one of the 10 hallmarks of cancer.

Despite the recent incorporation of biotensegrity paradigm to oncology translational research, it has already provided new insights related to the cell-microenvironment crosstalk determining tumor dynamism and aggressiveness. These findings are intrinsically linked with the rise of digital pathology and artificial intelligence, which have upgraded traditional histological evaluations to be able to depict the complex biotensegral pathways occurring within the tumor ecosystem. In this sense, cumulative advances in digital pathology tools such as digital image analysis have refined complex classification and prediction making processes that have revolutionized precision medicine. However, the extremely complex interplay between elements defining tumor biotensegrity mechanisms, as well as the issues to obtain enough tumor samples from some cancers, shift oncology research towards cancer model designing. Therefore, traditional cancer models such as *in vivo* murine models and *in vitro* monolayer cell cultures emerged as alternatives to respectively obtain large number of highly mimetic or simplified tumor samples. Albeit their usefulness, animal tumors exhibit similar complexity to the patient samples, and monolayer cell cultures are unable to recapitulate spatial biotensegral conditions, so tissue engineering advances have been applied to develop *in vitro* three-dimensional adjustable platforms to recreate tumor biotensegrity in a controllable and accurate way.

Following the expertise of our lab, this thesis initiates a research line by applying digital image analysis approaches in neuroblastoma *in vitro* three-dimensional models to evaluate the biotensegral effect of tumor microenvironment in neuroblastoma aggressiveness. Neuroblastoma is the most common solid extracranial tumor in pediatric age, and it is characterized by a wide spectrum of clinical behaviors. Despite pre-treatment risk classification improves patient survival, the high-risk subgroup still presents a particularly high mortality rate, thus highlighting the need to identify and

validate new diagnostic biomarkers, preclinical models, and alternative therapeutic approaches. In this way, our group have pinpointed some extracellular matrix morphological patterns together with specific vessel structural features to be related to neuroblastoma stiffness and poor prognosis. Particularly, our recent studies highlight vitronectin as a key glycoprotein participating in cell-extracellular matrix biotensegrity-mediated neuroblastoma aggressiveness and suggested it as a potential therapeutic target. Interestingly, biotensegral relevant *in vitro* three-dimensional models have been already developed for neuroblastoma. However, they have been mostly used for traditional drug testing studies. Investigating cell-extracellular matrix biotensegrity implications in neuroblastoma malignancy and the potential of their dialogue as a complementary therapeutic target is the main focus of this thesis.

According to the presented results, we state that biotensegral forces mediate intratumor cell-cell and cell-environment communication processes, which in turn drive the tumor phenotypic and genotypic adaptations promoting neuroblastoma aggressiveness and drug response. Subsequently, we hypothesize that three-dimensional *in vitro* models with modulable biotensegral conditions may trigger tumor cell growth, plasticity, and migration similar to *in vivo*, and that digital image analysis approaches performed on these models will unravel specific biotensegral pathways that confer cancer aggressiveness. Consequently, the models herein presented potentially constitute excellent tools for preclinical tests for mechanotherapeutic approaches.

The general purpose of this research is to transfer the knowledge of the group on neuroblastoma extracellular matrix architecture to pathophysiology relevant *in vitro* neuroblastoma hydrogel modeling, thus depicting the mechanical cues involved in neuroblasts malignancy that can be therapeutically targeted.

The specific objectives in three-dimensional *in vitro* gelatin/alginate hydrogels are: a) bioprinting three-dimensional gelatin plus alginate biocompatible scaffolds for neuroblastoma cell culture; b) determining the mechanical properties of the bioprinted hydrogels; c) comparing cell behavioral adaptations of two different aggressive neuroblastoma cell lines, SK-N-BE(2) and SH-SY5Y, when monocultured or co-cultured with stromal Schwann cells, in different hydrogel stiffness conditions and culture time points; and d) quantifying hydrogel degradation, cell cluster dynamics, migration-related

protein synthesis, differentiation and metabolism dynamics by digital image analysis to define neuroblastoma cell behavior.

The specific objectives in three-dimensional *in vitro* polyethylene glycol hydrogels are: a) fabricating three-dimensional polyethylene glycol biocompatible scaffolds that incorporate vitronectin to recapitulate high-risk neuroblastoma growth conditions; b) ensuring pathophysiological stiffness, functional vitronectin crosslinking and cell viability to validate the usefulness of the model; c) characterizing cell cluster growth and vitronectin synthesis adaptations related to hydrogel stiffness, time of culture and the presence of crosslinked incorporated vitronectin; and d) evaluating vitronectin potential as a secreted biomarker and therapeutic target in high-risk neuroblastoma.

The present doctoral thesis research is presented as a compendium of three scientific publications with complementary work shared at scientific conferences. Additional uncommunicated relevant data is herein provided to further increase the knowledge of the mechanical transmission signals that occur within the 3D tumor microenvironment and drive neuroblastoma cell behavior, highlighting the potential of the *in vitro* models as drug-testing platforms. The articles making up this compendium are:

- I. A three-dimensional bioprinted model to evaluate the effect of stiffness on neuroblastoma cell cluster dynamics and behavior. Monferrer E*, Martín-Vañó S*, Carretero A*, García-Lizarribar A, Burgos-Panadero R, Navarro S, Samitier J, Noguera R. Sci Rep. 2020 Apr 14;10(1):6370.

This article emphasizes the need of three-dimensional conditions for cell culture and the role of the extracellular matrix stiffness when recapitulating the mechanical cues that trigger cell adaptation response over time, such as changes in proliferation and mRNA metabolism activity. The findings reveal that hydrogels based on methacrylate gelatin plus methacrylate alginate allow generating three-dimensional cell culture models with biotensegral properties similar to both *in vivo* neuroblastoma murine models and human neuroblastoma biopsies. Also, alginate composition defines stiffness and scaffold porosity, which are further modified over time by cell culture activity. Results also confirm that stiffness regulates cell cluster growth dynamics, since stiff conditions present lower cluster density and occupancy. In contrast, in cell cultures up to 4 weeks, stiff conditions favor cell malignancy by increasing proliferation as well as

both undifferentiation and metabolic pathways controlled by PTBP1 expression. Albeit stiffness also promotes both Bax apoptosis and Bcl2 antiapoptosis markers, Bcl2 predominance ensure cell survival within the hydrogels. What is more, high mitosis-karyorrhexis index typical of SK-N-BE(2) neuroblastoma cell line is maintained in the generated hydrogels, thus confirming cancer cell aggressiveness.

- II. Digital Image Analysis Applied to Tumor Cell Proliferation, Aggressiveness, and Migration-Related Protein Synthesis in Neuroblastoma 3D Models. **Monferrer E***, Sanegre S*, Martín-Vañó S, García-Lizarribar A, Burgos-Panadero R, López-Carrasco A, Navarro S, Samitier J, Noguera R. *Int J Mol Sci.* 2020 Nov 17;21(22):8676.

This study complements Article I results by evaluating migration-related protein synthesis. We evidence distinctive behavior of aggressive neuroblastoma cell lines depending on their genetic characteristics (*MYCN* amplification or *ALK* mutation), as well as the influence of stromal cells on cancer cells behavior, thus pinpointing the complexity of neuroblastoma. Results on long-term neuroblastoma cell cultures within the hydrogels reveal SK-N-BE(2) cells (*MYCN* amplified) being more proliferative than SH-SY5Y (*ALK* mutated), as well as proliferative indexes decrease in long term cultures. Besides, stiffness affected SH-SY5Y cell proliferation differently from that of SK-N-BE(2). Regarding VN synthesis, both neuroblastoma cell lines firstly express high amounts of this glycoprotein, but their expression drops as time goes by. Despite almost no DOCK8 expression (a protein mainly involved in the cytoskeleton reorganization of immune cells) is found in hydrogels with both neuroblastoma cell lines until very long culture times, KANK1 protein levels (which mediate initial mechanotransduction at focal adhesions) remain stable regardless time, hydrogel stiffness, or neuroblastoma cell genetic background. Critically, Schwann cell incorporation has synergistic but variable effects with microenvironment stiffness, thus affecting cell behavior depending on their genetic background. Particularly, Schwann cells mainly reduce model proliferation indexes and vitronectin synthesis, albeit they seem to boost vitronectin expression in long time cultures. Moreover, Schwann cells greatly promote DOCK8 expression within the hydrogels, especially in SH-SY5Y cultures, but they do not influence KANK1 expression patterns. Therefore, Schwann incorporation radically changes overall model behavior, which evinces the need of designing relevant coculture modeling.

- III. Vitronectin-based hydrogels recapitulate neuroblastoma growth conditions. **Monferrer E***, Dobre O*, Trujillo S, González Oliva MA, Trubert-Paneli A, Acevedo-León D, Noguera R, Salmerón-Sánchez M. *Front. Cell Dev. Biol.* 2022 Oct 11;10:988699.

The goal of this research is to reproduce part of the high-risk neuroblastoma extracellular matrix by incorporating full-length vitronectin as the only bioactive molecule within polyethylene glycol hydrogels and seek to characterize the impact of this specific microenvironment on neuroblastoma cells. Findings from this study confirm that vitronectin can be PEGylated without losing their functionality and being subsequently incorporated into polyethylene glycol structures during hydrogel formation. Also, nanoindentation assessment ensures that polyethylene glycol proportion allows fine regulating model stiffness within the neuroblastoma pathophysiological range, and that vitronectin does not alter initial stiffness conditions. Nevertheless, SK-N-BE(2) cell cultures within the generated platforms and subsequently nanoindentation analysis indicates that vitronectin promote model degradation. Remarkably, live/dead assay corroborates that the designed hydrogels support cell survival and cell cluster formation and growth. Interestingly, stiff environments do not affect cell growth rate at day 7 but are more restrictive to cell cluster allocation. Besides, the obtained results prove that SK-N-BE(2) cells synthesize vitronectin even when it is already present in the environment they grow, and indeed, it can be detected in cell culture media, thus suggesting vitronectin as a potential soluble biomarker for NB.

Overall, the studies carried out in this thesis combine physics, biology, bioengineering and chemistry to achieve accurate pathophysiological relevance in three-dimensional *in vitro* neuroblastoma models, and benefits from image analysis techniques to better understand the biotensegral mechanisms underpinning neuroblastoma aggressiveness. We conclude that tumor behavior changes driven by biotensegrity mechanotransduction evolve differently regarding the system characteristics, thus being extremely complex and hard to predict. Accordingly, basic cancer models recreating biotensegral aspects need to be developed before generating fully pathophysiological platforms, since the former will provide accurate knowledge of specific biotensegrity mechanisms regulating tumor behavior that could be therapeutically targeted in preclinical studies performed on these platforms.

Resumen

La vida se sustenta en gran medida en el principio de autoequilibrio de la biotensegridad, que se basa en el balance funcional de las fuerzas físicas de tensión y compresión de las estructuras biológicas. Los sistemas biológicos están contruidos con soportes discontinuos que soportan la compresión, conectados por una red continua de elementos de tensión flexibles. Este equilibrio permite que las señales mecánicas se transmitan a todas las escalas detectables, desde las estructuras de ADN hasta los sistemas complejos de órganos, lo que a su vez desencadena respuestas mecánicas y bioquímicas. Las células, obedeciendo al principio de autoequilibrio biotensegral, están equipadas con una estructura polimérica interna, el citoesqueleto, que conecta la membrana celular, el núcleo y los orgánulos. Sin embargo, las vías de señalización biotensegral entrelazadas dentro del ecosistema tisular, diálogo célula-célula y célula-entorno, son en gran medida responsables de las reorganizaciones citoesqueléticas coordinadas que determinan el comportamiento celular, y redefinen la estructura del tejido, tanto en homeostasis como en trastornos tisulares como el cáncer. En este sentido, los distintos cánceres muestran sus propios sistemas biotensegrales aberrantes que impulsan la carcinogénesis y definen la evolución de la enfermedad. Dichos sistemas están relacionados con el diálogo entre células malignas y no malignas dentro del microambiente tumoral, la composición, la capacidad de resistir la deformación y topología de los elementos de la matriz extracelular, así como la presencia de inervación.

Estos parámetros se reorganizan conformando diferentes escenarios dinámicos de señalización tumoral a los que las células malignas se adaptan rápidamente debido a su plasticidad, lo cual promueve su progresión, metástasis y resistencias a medicamentos. Entre las principales fuerzas impulsoras de la adaptabilidad de las células cancerosas se encuentran gran variedad de mecanismos genéticos, epigenéticos y de reorganización de señales. Así, las células tumorales pueden sufrir adaptaciones morfológicas y moleculares que afectan la física celular, lo que puede implicar pleomorfismo y pérdida de adhesión celular, pero también procesos más profundos de desdiferenciación y transdiferenciación, como la transición epitelial-mesenquimatosa reversible, que determinan el destino celular. De forma importante, la comunicación biotensegral entre las células y el ecosistema tumoral coordina las adaptaciones celulares individuales para

favorecer la adaptabilidad colectiva del tumor. De hecho, la cooperación de células tumorales no solo desencadena una reorganización espacial transitoria para la migración colectiva de células móviles y no móviles como una entidad, sino que también promueve la remodelación del microambiente tumoral al reconstruir la matriz extracelular y determinar la respuesta inflamatoria. Alternativamente, la señalización biotensegral dentro del microambiente tumoral promueve la heterogeneidad genética del tumor, regulando aún más la carcinogénesis, la malignidad y la resistencia terapéutica. Así mismo, la reprogramación metabólica, definida como la capacidad de las células cancerosas para redirigir sus rutas bioenergéticas para satisfacer la mayor demanda de energía derivada de sus actividades de proliferación y crecimiento, y se ha convertido en una de las 10 particularidades del cáncer.

A pesar de la reciente incorporación del paradigma de la biotensegridad a la investigación traslacional oncológica, ya ha proporcionado nuevos conocimientos relacionados con la intercomunicación célula-microambiente, clave en el dinamismo y la agresividad tumoral. Estos hallazgos están intrínsecamente relacionados con el auge de la patología digital y la inteligencia artificial, que han mejorado las evaluaciones histológicas tradicionales pudiendo así dilucidar las complejas vías biotensegrales que ocurren dentro del ecosistema tumoral. En este sentido, los avances acumulados en las herramientas de patología digital, como el análisis de imagen digital, han perfeccionado procesos de clasificación y elaboración de predicciones clínicas que han revolucionado la medicina de precisión. Sin embargo, tanto la intrincada interacción de los elementos de la biotensegridad tumoral como los problemas para obtener suficientes muestras tumorales de algunos tipos de cáncer, redirigen la investigación oncológica hacia el diseño de modelos experimentales de cáncer. Así, las aproximaciones tradicionales como los modelos murinos *in vivo* y los cultivos celulares en monocapa *in vitro* han permitido obtener gran número de muestras tumorales, que respectivamente, se caracterizan por su elevado mimetismo y su simplicidad. A pesar de su utilidad, los tumores animales exhiben una complejidad similar a las muestras de pacientes, y los cultivos celulares en monocapa no pueden recrear las condiciones biotensegrales espaciales, por lo que se han aprovechado los avances en ingeniería tisular para

desarrollar plataformas ajustables tridimensionales *in vitro* que permitan reproducir la biotensegridad tumoral de forma sencilla, controlable y precisa.

Siguiendo la experiencia de nuestro laboratorio, esta tesis abre una línea de investigación mediante la aplicación del análisis de imagen digital en modelos tridimensionales *in vitro* de neuroblastoma, para evaluar el efecto biotensegral del microambiente tumoral en la agresividad de dicho cáncer. El neuroblastoma es el tumor sólido extracraneal más común en la edad pediátrica y se caracteriza por presentar un amplio espectro de comportamientos clínicos. A pesar de que la clasificación de riesgo pretratamiento mejora la supervivencia del paciente, el subgrupo de alto riesgo aún presenta una tasa de mortalidad particularmente alta, siendo por tanto necesario identificar y validar nuevos biomarcadores de diagnóstico, así como adicionales modelos preclínicos y enfoques terapéuticos alternativos. De esta forma, nuestro grupo ha identificado algunos patrones morfológicos de la matriz extracelular junto con características estructurales vasculares específicas que se relacionan con la rigidez y el mal pronóstico del neuroblastoma. En particular, nuestros estudios recientes destacan la participación clave de la glicoproteína vitronectina en la agresividad del neuroblastoma mediada por la biotensegridad célula-matriz extracelular, por lo que se sugirió como potencial diana terapéutica. Cabe destacar que han sido desarrollados modelos de neuroblastoma en plataformas tridimensionales *in vitro* y que recrean determinados aspectos de la biotensegridad tumoral. Sin embargo, se han utilizado principalmente para testar efectos de quimioterapias tradicionales. Investigar las implicaciones de la biotensegridad célula-matriz extracelular en la malignidad del neuroblastoma y el potencial del diálogo entre ambas como diana terapéutica complementaria es el enfoque principal de esta tesis.

Con los datos expuestos, destacamos que las fuerzas biotensegrales median procesos de comunicación intratumoral célula-célula y célula-ambiente, que a su vez impulsan las adaptaciones fenotípicas y genotípicas del tumor, promotoras de la agresividad y la respuesta farmacológica del neuroblastoma. Por ello, hipotetizamos que los modelos *in vitro* tridimensionales, con condiciones biotensegrales modulables, pueden desencadenar el crecimiento, la plasticidad y la migración de células tumorales de forma similar a como ocurre *in vivo*, y que el análisis de imagen digital realizado en estos

modelos desentrañará algunas vías biotensegrales específicas responsables de la agresividad del cáncer. En consecuencia, los modelos aquí presentados constituyen potencialmente excelentes herramientas para realizar ensayos mecanoterapéuticos preclínicos.

El propósito general de esta investigación es transferir el conocimiento del grupo sobre la arquitectura de la matriz extracelular del neuroblastoma a su modelado *in vitro* en hidrogeles con relevancia fisiopatológica, representando así las señales mecánicas que intervienen en la malignidad de los neuroblastos y que pueden ser dianas terapéuticas.

Los objetivos específicos en hidrogeles de gelatina/alginateo tridimensionales *in vitro* son: a) bioimpresión de andamios tridimensionales biocompatibles de gelatina y alginato para cultivo de células de neuroblastoma; b) determinar las propiedades mecánicas de los hidrogeles bioimpresos; c) comparar las adaptaciones del comportamiento celular de dos líneas celulares de neuroblastoma agresivas diferentes, SK-N-BE(2) y SH-SY5Y, cuando se cultivan en monocultivo o cocultivo con células estromales de Schwann, en diferentes condiciones de rigidez del hidrogel y tiempo de cultivo; y d) cuantificar la degradación del hidrogel, la dinámica de los grupos celulares, la síntesis de proteínas relacionadas con la migración, la diferenciación y la dinámica del metabolismo mediante análisis de imagen digital para definir el comportamiento de los neuroblastos.

Los objetivos específicos en hidrogeles de polietilenglicol *in vitro* tridimensionales son: a) fabricar andamios biocompatibles de polietilenglicol tridimensionales que incorporen vitronectina para recapitular las condiciones de crecimiento de neuroblastoma de alto riesgo; b) asegurar la rigidez fisiopatológica, el entrecruzamiento funcional de vitronectina y la viabilidad celular para validar la utilidad del modelo; c) caracterizar el crecimiento de grupos celulares y sus adaptaciones respecto la síntesis de vitronectina relacionadas con la rigidez del hidrogel, el tiempo de cultivo y la presencia de vitronectina entrecruzada añadida; y d) evaluar el potencial de vitronectina como biomarcador secretado y diana terapéutica en neuroblastoma de alto riesgo.

La presente investigación de tesis doctoral se presenta como un compendio de tres publicaciones científicas junto con trabajo complementario presentado en congresos científicos. Se proporcionan datos relevantes adicionales no comunicados para complementar el conocimiento de las señales de transmisión mecánica, que se producen dentro del microambiente tumoral e impulsan el comportamiento de las células neuroblásticas, lo que destaca el potencial de los modelos *in vitro* como plataformas de prueba de fármacos. Los artículos que componen este compendio son:

- I. A three-dimensional bioprinted model to evaluate the effect of stiffness on neuroblastoma cell cluster dynamics and behavior. Monferrer E*, Martín-Vañó S*, Carretero A*, García-Lizarribar A, Burgos-Panadero R, Navarro S, Samitier J, Noguera R. Sci Rep. 2020 Apr 14;10(1):6370.

Este artículo enfatiza la necesidad de la tridimensionalidad en los cultivos celulares y la importancia de la rigidez de la matriz extracelular para recapitular las señales mecánicas que desencadenan la respuesta de adaptación celular con el tiempo, así como los cambios en la proliferación y la actividad del metabolismo del ARNm asociados a dicha adaptación. Los hallazgos revelan que los hidrogeles a base de gelatina metacrilada con alginato metacrilado permiten generar modelos tridimensionales para el cultivo celular, con propiedades biotensegrales similares tanto a las de los modelos murinos de neuroblastoma como a las de las biopsias humanas de neuroblastoma. Además, la composición del alginato define la rigidez y la porosidad del andamiaje, que se modifican con el tiempo por la actividad del cultivo celular. Los resultados también confirman que la rigidez regula la dinámica de crecimiento de las agrupaciones celulares, siendo menor la densidad y ocupación de estas agrupaciones en entornos más rígidos. Por otro lado, en los cultivos celulares de hasta 4 semanas realizados, las condiciones rígidas favorecen la malignidad celular al aumentar tanto la proliferación como la indiferenciación y las vías metabólicas controladas por la expresión de PTBP1. Aunque la rigidez también promueve tanto la expresión de Bax como marcador de apoptosis, como de Bcl2 como marcador de antiapoptosis, el predominio de Bcl2 asegura la supervivencia celular dentro de los hidrogeles. Además, el alto índice de mitosis-cariorrexis típico de la línea celular SK-N-BE(2) se mantiene en los hidrogeles generados, lo que corrobora la agresividad de las células cancerosas cultivadas.

- II. Digital Image Analysis Applied to Tumor Cell Proliferation, Aggressiveness, and Migration-Related Protein Synthesis in Neuroblastoma 3D Models. **Monferrer E***, Sanegre S*, Martín-Vañó S, García-Lizarribar A, Burgos-Panadero R, López-Carrasco A, Navarro S, Samitier J, Noguera R. *Int J Mol Sci.* 2020 Nov 17;21(22):8676.

Este estudio complementa los resultados previos al evaluar la síntesis de proteínas relacionadas con la migración. Evidenciamos el comportamiento distintivo de las líneas celulares de neuroblastoma agresivo según sus características genéticas (amplificación de *MYCN* o mutación de *ALK*), así como la influencia de las células del estroma en el comportamiento de las células cancerosas. Los resultados de los cultivos celulares de neuroblastoma a largo plazo en los hidrogeles revelan que las células SK-N-BE(2) (con *MYCN* amplificado) son más proliferativas que las SH-SY5Y (con mutación de *ALK*), del mismo modo que revelan una disminución de la proliferación en largos tiempos de cultivo. Además, la rigidez afecta la proliferación de células SH-SY5Y de manera diferente a las SK-N-BE(2). En cuanto a la síntesis de VN, ambas líneas celulares expresan inicialmente cantidades elevadas de esta glicoproteína, pero su expresión disminuye con el paso del tiempo. A pesar de que casi no se encuentra expresión de DOCK8, proteína implicada en reorganización de citoesqueleto principalmente de células relacionadas con la respuesta inmune, en hidrogeles con cultivos neuroblásticos puros hasta tiempos de cultivo muy largos, los niveles proteicos de KANK1, que media inicialmente la mecanotransducción en las adhesiones focales, se mantienen estables independientemente del tiempo, la rigidez del hidrogel o las características genéticas de las líneas celulares. Críticamente, la incorporación de células de Schwann tiene efectos sinérgicos pero variables con la rigidez del microambiente, lo que afecta el comportamiento celular dependiendo del sistema. En particular, las células de Schwann suelen reducir los índices de proliferación del modelo y la síntesis de vitronectina, aunque esta última parece incrementarse en cultivos suficientemente prolongados. Además, las células de Schwann promueven en gran medida la expresión de DOCK8 dentro de los hidrogeles, especialmente en cultivos de SH-SY5Y, pero no influyen en los patrones de expresión de KANK1. Por lo tanto, la incorporación de Schwann cambia radicalmente el comportamiento general del modelo, lo que evidencia la necesidad de diseñar modelos de cocultivo precisos.

- III. Vitronectin-based hydrogels recapitulate neuroblastoma growth conditions. **Monferrer E***, Dobre O*, Trujillo S, González Oliva MA, Trubert-Paneli A, Acevedo-León D, Noguera R, Salmerón-Sánchez M. *Front. Cell Dev. Biol.* 2022 Oct 11;10:988699.

El objetivo de esta investigación es reproducir parte de la matriz extracelular de neuroblastoma de alto riesgo incorporando vitronectina de longitud completa como única molécula bioactiva dentro de los hidrogeles de polietilenglicol, y caracterizar el impacto específico de este microambiente en las células de neuroblastoma. Los hallazgos de este estudio confirman que la vitronectina se puede pegar sin perder su funcionalidad y luego incorporarse a las estructuras de polietilenglicol durante la formación de los hidrogeles. Además, la nanoindentación asegura que la proporción de polietilenglicol permite una regulación precisa de la rigidez del modelo dentro del rango fisiopatológico del neuroblastoma, así como que la vitronectina no altera las condiciones iniciales de rigidez. Sin embargo, la nanoindentación realizada en los cultivos de células SK-N-BE(2) dentro de las plataformas generadas indican que la vitronectina favorece la degradación del modelo. De forma importante, el ensayo de viabilidad celular corrobora que los hidrogeles diseñados respaldan la supervivencia celular, así como la formación y el crecimiento de agrupaciones celulares. Curiosamente, los entornos rígidos no afectan el ritmo de crecimiento celular a los 7 días, pero son más restrictivos en cuanto a la anidación de agrupaciones celulares. Además, los resultados obtenidos prueban que las células SK-N-BE(2) sintetizan vitronectina incluso cuando ya está presente en el entorno en el que crecen, y que de hecho, puede detectarse en los medios de cultivo celular, lo que sugiere la vitronectina como potencial biomarcador soluble en NB.

En general, los estudios llevados a cabo en esta tesis combinan física, biología, bioingeniería y química para lograr una relevancia fisiopatológica precisa en modelos tridimensionales de neuroblastoma *in vitro*, y se benefician de las técnicas de análisis de imagen digital para comprender mejor los mecanismos biotensegrales que sustentan la agresividad del neuroblastoma. Concluimos que los cambios de comportamiento del tumor, impulsados por la mecanotransducción de señales biotensegrales célula-matriz extracelular, evolucionan de manera diferente dependiendo de las características del sistema, por lo que son extremadamente complejos y difíciles de predecir *in vivo*. En consecuencia, es necesario desarrollar mayor número de modelos básicos de cáncer que

recreen aspectos biotensegrales sencillos antes de generar plataformas fisiopatológicas complejas, ya que solo los primeros proporcionarán un conocimiento preciso de los mecanismos biotensegrales específicos que regulan el comportamiento tumoral, y que podrían ser dianas terapéuticas en estudios preclínicos realizados en estas plataformas.

Abbreviations

3-BrPA: 3-bromopyruvate	INRG: International Neuroblastoma Risk Group
3D: three-dimension	KO: knockout
AI: artificial intelligence	MCS: multicellular spheroids
AlgMA: alginate methacrylate	MCT: monocarboxylate transporter
CC: cytochemical	MET: mesenchymal-epithelial transition
ECM: extracellular matrix	MKI: mitosis-karyorrhexis index
EMT: epithelial-mesenchymal transition	MSC: mesenchymal stromal cell
F: fluorescence	MTOC: microtubule organizing center
FA: focal adhesion	NB: neuroblastoma
FFPE: formalin-fixed paraffin-embedded	PDX: patient-derived xenograft
FISH: fluorescent <i>in situ</i> hybridization	PEG: polyethylene glycol
GAGs: glycosaminoglycans	PEG-MAL: polyethylene glycol-maleimide
GelMA: gelatin methacrylate	SH-PEG-SH: dithiol-polyethylene glycol
GEMM: genetically engineered murine model	SNPa: single nucleotide polymorphism array
HC: histochemical	TME: tumor microenvironment
HE: hematoxylin-eosin	VN: Vitronectin
HR: high-risk	VPM: peptide containing Val-Pro-Met amino acid sequence
ICC: immunocytochemical	
IF: immunofluorescence	
IHC: immunohistochemical	

Compendium of articles that support this thesis

This thesis is based on three publications as a compendium in which the candidate is the first author or first co-author. Full text of the publications is shown below.

- I. A three-dimensional bioprinted model to evaluate the effect of stiffness on neuroblastoma cell cluster dynamics and behavior. **Monferrer E***, Martín-Vañó S*, Carretero A*, García-Lizarribar A, Burgos-Panadero R, Navarro S, Samitier J, Noguera R. *Sci Rep.* 2020 Apr 14;10(1):6370.

- II. Digital Image Analysis Applied to Tumor Cell Proliferation, Aggressiveness, and Migration-Related Protein Synthesis in Neuroblastoma 3D Models. **Monferrer E***, Sanegre S*, Martín-Vañó S, García-Lizarribar A, Burgos-Panadero R, López-Carrasco A, Navarro S, Samitier J, Noguera R. *Int J Mol Sci.* 2020 Nov 17;21(22):8676.

- III. Vitronectin-based hydrogels recapitulate neuroblastoma growth conditions. **Monferrer E***, Dobre O*, Trujillo S, González Oliva MA, Trubert-Paneli A, Acevedo-León D, Noguera R, Salmerón-Sánchez M. *Front. Cell Dev. Biol.* 2022 Oct 11;10:988699.

The asterisk (*) indicates equal contribution.

Article I: A three-dimensional bioprinted model to evaluate the effect of stiffness on neuroblastoma cell cluster dynamics and behavior.

Monferrer E*, Martín-Vañó S*, Carretero A*, García-Lizarribar A, Burgos-Panadero R, Navarro S, Samitier J, Noguera R.

*Equal contribution

Sci Rep. 2020. Apr 14; 10(1):6370. doi: 10.1038/s41598-020-62986-w.

NATURE RESEARCH, EISSN: 2045-2322

Impact factor 2020: 4.380

5-year impact factor 2020: 5.134

Multidisciplinary sciences: Q1

Cites: 2



ARTICLE I

OPEN

A three-dimensional bioprinted model to evaluate the effect of stiffness on neuroblastoma cell cluster dynamics and behavior

Ezequiel Monferrer^{1,2,6}, Susana Martín-Vañó^{1,2,6}, Aitor Carretero^{1,6}, Andrea García-Lizarribar^{3,5}, Rebeca Burgos-Panadero^{1,2}, Samuel Navarro^{1,2}, Josep Samitier^{3,4,5*} & Rosa Noguera^{1,2*}

Three-dimensional (3D) bioprinted culture systems allow to accurately control microenvironment components and analyze their effects at cellular and tissue levels. The main objective of this study was to identify, quantify and localize the effects of physical-chemical communication signals between tumor cells and the surrounding biomaterial stiffness over time, defining how aggressiveness increases in SK-N-BE(2) neuroblastoma (NB) cell line. Biomimetic hydrogels with SK-N-BE(2) cells, methacrylated gelatin and increasing concentrations of methacrylated alginate (AlgMA 0%, 1% and 2%) were used. Young's modulus was used to define the stiffness of bioprinted hydrogels and NB tumors. Stained sections of paraffin-embedded hydrogels were digitally quantified. Human NB and 1% AlgMA hydrogels presented similar Young's modulus mean, and orthotopic NB mice tumors were equally similar to 0% and 1% AlgMA hydrogels. Porosity increased over time; cell cluster density decreased over time and with stiffness, and cell cluster occupancy generally increased with time and decreased with stiffness. In addition, cell proliferation, mRNA metabolism and antiapoptotic activity advanced over time and with stiffness. Together, this rheological, optical and digital data show the potential of the 3D *in vitro* cell model described herein to infer how intercellular space stiffness patterns drive the clinical behavior associated with NB patients.

The extracellular matrix (ECM) is a three-dimensional (3D) network that forms part of all body tissues. It can be defined as a biophysical filter that provides protection, nutrition and cell innervation, and is involved in immune response, angiogenesis, fibrosis and tissue regeneration. It is also a transport medium for mechanical forces to the basal membrane through integrins that support the tissue tensegrity system, activating cellular genetic and epigenetic mechanisms¹. ECM alterations result in loss of functions such as cell denervation², loss of regeneration and wound-healing capacity³, loss of the substrate that provides a correct immune response to infectious⁴, tumoral⁵ and toxic agents⁶ and alteration of mechanical transmission (mechanotransduction changes)⁷. 2D cell culture has been one of the most commonly used *in vitro* models for biomedical research, due to its ease of use and low cost; however, it is less effective in reflecting the effect of the ECM and potential cellular microenvironment interactions, being unable to capture the interaction between 3D architecture of cells and ECM⁸. 3D cell culture has been used to show that ECM rigidity may enhance cell motility by modifying their morphological properties to an aggressive phenotype^{9–11}. Furthermore, 3D cell culture has already been used to study the impact of the ECM on cancers such as breast cancer¹², sarcoma¹³ and pancreatic cancer¹⁴. From this approach, tumors can be studied as functional tissues, connected to and dependent on the microenvironment. Regarding model fabrication, 3D bioprinting technology has certain advantages over casted 3D gels, with the first technology permitting direct cell incorporation and homogeneous cell distribution in the model, preparation at room temperature and design of precisely defined mesh structures to facilitate nutrient flow to the cells¹⁵. Thus 3D bioprinting technology can contribute towards standardizing medical devices¹⁶. These 3D microenvironments mimicking human tumors

¹Pathology Department, Medical School, University of Valencia-INCLIVA, Valencia, Spain. ²CIBERONC, Madrid, Spain. ³Institute for Bioengineering of Catalonia, Barcelona Institute of Science and Technology (IBEC-BIST), Barcelona, Spain. ⁴CIBER-BBN, Madrid, Spain. ⁵Department of Electronics and Biomedical Engineering, University of Barcelona, Barcelona, Spain. ⁶These authors contributed equally: Ezequiel Monferrer, Susana Martín-Vañó and Aitor Carretero. *email: jsamitier@ibecbarcelona.eu; rnoguera@uv.es

can be analyzed using several parameters such as Young's modulus, a parameter that characterizes the behavior of elastic material, used to define the stiffness of bioprinted hydrogels and human tumors^{17,18} and tumor cell proliferation biomarkers, that can be easily studied by immunohistochemical (IHC) analysis of the Ki67 marker^{19–22}, as well as via the following: (i) polypyrimidine tract binding protein 1 (PTBP1) staining, which is associated with pre-mRNAs in the nucleus and influences pre-mRNA processing and some aspects of mRNA metabolism and transport^{23–26}. High PTBP1 expression has been associated with aggressive behavior in several types of cancer, especially breast cancer, glioma and ovarian tumors^{27,28}; (ii) the mitosis-karyorrhexis index (MKI), defined as the cellular density sum of mitotic and karyorrhectic cells in a tumor. A high MKI is an indicator of poor prognosis in cancers such as neuroblastoma (NB)^{29–31}; and finally, (iii) Bax and Bcl2 markers, used to characterize cellular signals of apoptosis and antiapoptosis activity, respectively^{32–35}.

NB is among the most common solid cancers in childhood, with a wide variety of presentations and highly variable prognosis, depending largely on anatomical location in the sympathetic nervous system where the primary tumor develops, and metastatic status³⁶. Malignant neuroblastic cells are highly sensitive to the biomechanical properties of their microenvironment^{9,37} and this was verified in our studies, where we observed that the composition of the ECM can define an ultra-high-risk subset within the high-risk group of neuroblastoma patients (HR-NB)³⁸, and that a stiff ECM can be generated and associated with aggressive neuroblastic tumors^{39–41}. Paradoxically, the ECM is not taken into account in standard cancer management practice today, despite evidence pointing to a key role for the ECM during tumor progression and therapy resistance⁴². The use of 3D cell culture with different hydrogel stiffness could help us characterize the effects of ECM stiffness on malignant neuroblastic cell behavior, as well as providing a way to simulate and better understand the biomechanical properties found in HR-NB tumor tissues. In this study we used morphometric digital analysis to evaluate the different effects of ECM stiffness on NB cells over time, using a 3D scaffold-based *in vitro* cell culture platform, demonstrating its value in molecular mechanotherapy evaluation.

Methods

2D and 3D culture of SK-N-BE(2) cells. SK-N-BE(2) cells were acquired from American Type Culture Collection (ATCC, Manassas, VA, USA) and expanded in a growth medium based on Iscove's Modified Dulbecco's Medium (IMDM, Gibco, Thermofisher), supplemented with 10% fetal bovine serum (Thermofisher), 1% Insulin-Transferrin-Selenium G Supplement (Thermofisher), Plasmocin (0.2%) treatment ant-mpt (1/10) (InvivoGen) and 1% penicillin/streptomycin (Thermofisher) at 37 °C and 5% CO₂ atmosphere. 2D cell cultures were grown in 8-well Cell Culture Slides (SPL Life Sciences) until they reached confluence before immunocytochemistry (ICC) analysis.

To create the bioinks, cells were cultured and trypsinized. The resulting pellet was resuspended with the pre-polymer solution at 37 °C to a 2.5×10^6 cell density. The bioink was loaded in a bioprinting syringe and gelified at –20 °C for 3 minutes before printing.

Synthesis of hydrogels. Methacrylated gelatin (GelMA), a photocrosslinkable hydrogel derived from natural gelatin, emulates the ECM for various cells types in combination with non-biodegradable materials such as alginate. We used the synthesis process as previously described⁴³. Briefly, Gelatin (Sigma-Aldrich, USA) was modified to a 40% degree of methacrylation. First the Gelatin was dissolved in PBS 10 mM at a concentration of 10% (w/v), and mixed drop by drop with methacrylic anhydride (Sigma-Aldrich, USA)⁴⁴. One hour later, the reaction was stopped by adding an excess of PBS 10 mM and was dialysed against Milli Q water with 6–8 kDa MWCO membranes (Spectra/por, Spectrumlabs, USA). Sodium alginate (Sigma-Aldrich) was methacrylated (AlgMA) at a maximum degree of methacrylation as previously described⁴⁵. The methacrylation reaction was performed by mixing a solution of 1% (w/v) of the polymer in 50 mM MES buffer at pH 6.5 with 20 mM EDC, 10 mM N-hydroxysuccinimide and 10 mM 2 aminoethylmethacrylate (Sigma-Aldrich). The reaction was stopped after 24 h with the addition of acetone (Panreac, Spain) and filtered using a vacuum flask. The precipitate was dissolved in PBS 10 mM and dialysed against Milli Q water with 3.5 kDa MWCO membranes (Thermofisher, USA). Finally, the solutions of methacrylated polymers were lyophilized and stored at –20 °C. The polymer precursors (GelMA and AlgMA) were mixed at different concentrations and diluted in growth medium containing the photoinitiator, lithium Phenyl (2,4,6 trimethylbenzoyl) phosphinate (LAP) (TCI EUROPE N.V., Belgium), in a concentration of 0.05% w/v⁴³.

These prepolymer solutions were placed at 65 °C for 1 h to obtain homogeneous solutions. Prepolymer solutions were prepared to obtain final concentrations of 5% w/v GelMA and 0%, 1% and 2% w/v AlgMA according to the desired initial stiffness level (the higher the alginate percentage, the stiffer the hydrogel). Prepolymer compositions were mixed with cells to generate the gelified bioinks. All hydrogels were fabricated using a 3D bioprinter (3DDiscovery BioSafety, regenHU, Switzerland; 365 nm, 3 W cm⁻²) polymerized with UV light source as previously reported⁴³. Briefly, cell-laden gelified bioinks were printed applying an air pressure extrusion system, using a 150 μm nozzle. The bioprinter generated 0.4 mm spaced bioink rows to make 5 × 5 mm layers. Successive layers were photocrosslinked by 5 s exposure to UV light at 3 W cm⁻² and printed perpendicularly to generate a 1 mm-high 5-layer network. Next, hydrogels were immersed in growth media to remove unreacted reagents, and then cultured for 2 and 4 weeks before analysis.

Scanning electron microscope. The matrix pore of the three hydrogels was studied with scanning electron microscope (SEM) images. 5% GelMA with 0%, 1% and 2% AlgMA hydrogels were bioprinted as explained previously and incubated in PBS1X for 24 h until they reached the equilibrium swelling state. Hydrogels were dehydrated using a series of ethanol gradient with distilled water: 30%, 50%, 70%, 90%, 96% and 100% for 10 minutes. The critical dry point (K850, Quorum technologies, UK) was obtained by replacing the ethanol by liquid CO₂. The CO₂ was slowly evaporated under 85.06 atm pressure and 35 °C to completely dry the hydrogels. Next,

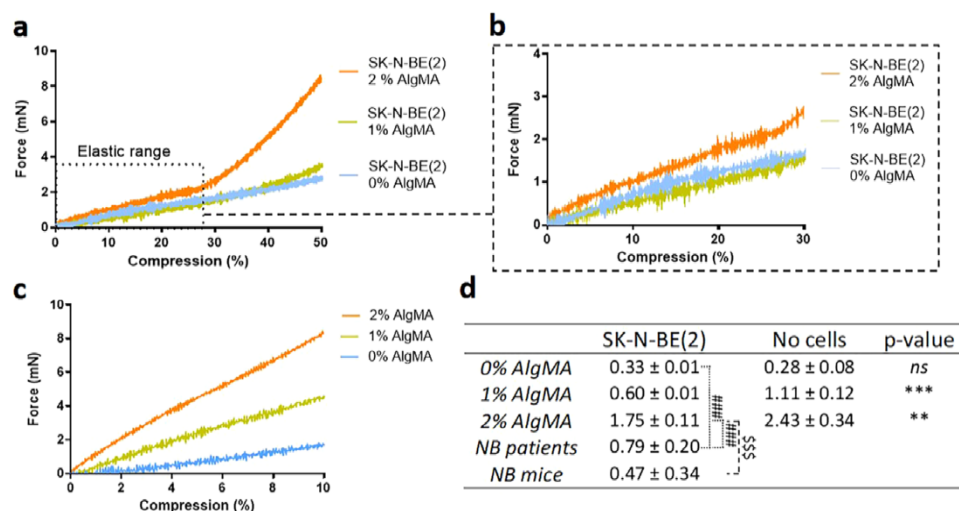


Figure 1. (a–c) Strain-stress curves obtained by testXpert after the compressive test. (a) Representation of the average curves of the 3 hydrogel types: 0%, 1% and 2% AlgMA with SK-N-BE(2). Young's Modulus was obtained from the linear range of the elastic region. (b) Zoom view of the linear range of the elastic region of SK-N-BE(2) laden hydrogels. (c) Zoom view of the linear range of the elastic region in hydrogels without cells. (d) Characterization of the mechanical properties (Young's modulus) of the composite hydrogels, cohort of HR-NB and orthotopic NB mice tumors. Comparative Young's modulus of 5% gelatin methacrylated with 0%, 1% and 2% methacrylated alginate in absence and presence of incubated SK-N-BE(2) cells. Measurements of each hydrogel were performed in quintuplicate. Values are plotted as mean and standard deviation. Statistical analysis using *t-student* test: ^{ns}*p*-value > 0.05, ^{**}*p*-value < 0.01, ^{***}*p*-value < 0.001, comparing SK-N-BE(2) and no cell-hydrogels, ^{###}*p*-value < 0.001, comparing NB patients vs SK-N-BE(2) hydrogels and ^{\$\$\$}*p*-value < 0.001, comparing orthotopic NB mice tumors vs SK-N-BE(2) hydrogels.

hydrogels were gold-spattered and images were taken with ultrahigh resolution SEM (Nova NanoSEM 230, FEI Company, The Netherlands). Pore size distribution was analyzed after processing the images with ImageJ open software.

Mechanical compression assays. Mechanical properties of hydrogels were determined by uniaxial compression assays using a Zwick Z0.5 TN instrument (Zwick-Roell, Germany) with a 5 N load cell, as previously described⁴³. Hydrogels were bioprinted as explained above and incubated at 37 °C to reach the equilibrium swelling state before measurement. The hydrogels were compressed up to 50% of deformation, with a 0.1 mN preload force and 20%/min strain rate. As there were no significant variations between samples measured at 37 °C (Supplementary Fig. 1a), all measurements were performed at room temperature submerged in a medium drop. Young's modulus was calculated from the slope of the elastic region of stress-strain curves⁴⁶ using the testXpert software (Zwick-Roell) (Fig. 1a–c). Measurements of each hydrogel were performed in quintuplicate. Compressive modulus was obtained from four different material groups: i) hydrogels 5% GelMA with 0% AlgMA, 1% AlgMA and 2% AlgMA in absence of cells incubated for 48 hours and ii) with SK-N-BE(2) cells incubated for 24 days, iii) 6 HR-NB human tumors and iv) 6 orthotopic SK-N-BE(2) and SH-SY5Y cells from xenograft-derived tumors. Both HR-NB cohort and orthotopic NB mice tumors were used as comparison groups; 3 out of 6 tumors in each group showed *MYCN* amplification (MNA)⁴⁷. The statistical analysis was performed using *t-student* test.

Paraffin embedding, histochemical analysis and optical microscopy quantification. Hydrogels were collected and placed in Tissue-Tek Paraform biopsy cassettes (Sakura Finetek, USA), fixed in 4% formaldehyde and automatically embedded in paraffin (Leica EG1150H; Leica Microsystems; Wetzlar, Germany). Paraffin-embedded samples were cut into 3 μm sections. Hematoxylin-eosin staining (HE) was performed for morphology and MKI studies. MKI was determined by an expert pathologist in accordance with the Shimada classification⁴⁸: low MKI (<100 MK cells/5000 cells or <2%); intermediate MKI (100–200 MK cells/5000 cells or 2–4%), or high MKI (>200 MK cells/5000 cells or >4%). Automated IHC and ICC stains (Autostainer Link 48; Dako, Glostrup, Denmark) using anti-Ki67 (prediluted), anti-PTBP1 (dil. 1/400), anti-Bax (dil. 1/50) and anti-Bcl2 (prediluted) antibodies, all from Dako (Agilent Technologies, USA), were quantified by optical microscopy. For IHC and ICC markers, cells stained in blue indicated negative cells while brown staining was considered a positive result. Samples were examined and interpreted using the following criteria: - Negative (<1% positive cells); + Low positive (1–20% positive cells); ++ Intermediate positive (20–50% positive cells); +++ High positive (>50% positive cells).

Image analysis. HE, Ki67 and PTBP1 stained sections were digitalized with the whole-slide Panoramic MIDI scanner (3DHISTECH Ltd., Budapest, Hungary) at 20x magnification. Detected artefacts and folded and/or broken regions were considered uninformative and were excluded. HistoQuant module was applied in HE-stained sections to obtain the solid area of hydrogels, defining solid area as the regions of the sample with

cellular clusters and/or biopolymers. The number of cellular clusters, their respective areas and total hydrogel area for each condition were obtained by segmentation with Panoramic Viewer (PV) software (3DHISTECH) (Supplementary Fig. 2). Cell nucleus size and shape were also obtained with the HistoQuant module of the PV software. Ki67 and PTBP1 were also determined using PV software, and their expression-related parameters (number of positive cells) were analyzed automatically applying the NuclearQuant module.

Data treatment. All data from the 3D models was analyzed by comparing i) different timeframes with the same stiffness and ii) different stiffness within each culturing timeframe. 3D data was also compared with the 2D data. In order to define bioprinted hydrogel characteristics and cell behavior, three informative parameters were established: (i) hydrogel porosity, (ii) cell cluster density and (iii) cell cluster occupancy. All these variables were calculated from HE-stained samples. We defined hydrogel porosity as the amount of holes in the hydrogel and was calculated as hollow area/total area percentage, the hollow area representing the total hydrogel area minus hydrogel solid area. Cell clusters were grouped by size and cell number into small ($<400 \mu\text{m}^2$; <10 cells), medium ($400\text{--}2,000 \mu\text{m}^2$; $10\text{--}50$ cells) or large ($>2,000 \mu\text{m}^2$; >50 cells) and cell cluster parameters were calculated for each group. Cell cluster density is a quantitative way to indicate cell cluster presence, calculated as the number of cell clusters/hydrogel solid area (mm^2). Moreover, percentages of different cell cluster sizes were calculated for each stiffness condition under study as an additional variable of cell cluster presence. Cell cluster occupancy quantifies the hydrogel solid area occupied by cell clusters and was calculated as the percentage of cluster area/hydrogel solid area (mm^2) for each condition. Regarding Ki67 and PTBP1 expression-related analysis, positive cell percentages were compared for each condition under study. We calculated the overall percentage of Ki67 and PTBP1 positive cells in each sample and their percentages in each cellular cluster size group. Furthermore, H-score was automatically calculated with Panoramic Viewer in Ki67 and PTBP1 stained samples according to the percentage of positive cells and their staining intensity. This H-score has a value within the range 0–300, where 0 equals the minimum positivity value and staining intensity and 300 the maximum.

A schematic diagram of the complete methodology used for this study is shown in Supplementary Fig. 3.

Results

Characterization of bioprinted hydrogels. *Mechanical properties.* For hydrogels printed in the absence of cells and with 48 h culture, Young's modulus was 0.28 ± 0.08 kPa for 0% AlgMA, 1.11 ± 0.12 kPa for 1% AlgMA and 2.43 ± 0.34 kPa for 2% AlgMA. After 24 days of cell incubation, results were 0.33 ± 0.01 kPa for 0% AlgMA, 0.60 ± 0.005 kPa for 1% AlgMA and 1.75 ± 0.11 kPa for 2% AlgMA. Differences in elastic modulus between composite hydrogels with and without cells were statistically significant ($p < 0.05$) in 1% AlgMA and 2% AlgMA (Fig. 1). We obtained a Young's modulus mean of 0.79 ± 0.20 kPa for HR-NB tumors, in a range between 0.58 to 1.1 kPa. Comparing these results with those obtained in bioprinted hydrogels, we observed that the mean of Young's modulus in human NB was similar to that of the bioprinted hydrogels composed of 1% of AlgMA (Fig. 1). Regarding NB mice tumors, we obtained a Young's modulus mean of 0.47 ± 0.34 kPa in a range between 0.06 to 1.05 kPa, similar to the one of bioprinted hydrogels composed of 0% and 1% of AlgMA (Fig. 1). Therefore, we found that cell presence in the bioink decreased Young's modulus and allowed 0% AlgMA and 1% AlgMA hydrogels to better imitate the mechanical properties of human HR-NB tumors and mice tumors. Supplementary Fig. 1b shows a bar chart of the mechanical properties.

Matrix pore. The fiber mesh of the 5% GelMA with 0%, 1% and 2% AlgMA biomaterials were studied using SEM images. The polymer fibers presented an interconnected mesh with a wide pore size range, so we studied the distribution of the pore area data instead of the average pore size of each composite. All the samples contained pores from the smallest to the largest areas and all showed right-skewed data distribution (Fig. 2a). However, in 0% AlgMA the sample median was higher (Fig. 2b), meaning that the data was biased towards higher area values. 1% AlgMA also showed a higher median than 2% AlgMA, but the difference was less notable. The interquartile range of 1% AlgMA and 2% AlgMA was narrower than 0% AlgMA, suggesting that most data was condensed in the small area values. Hence, the frequency of large pores decreased when the alginate concentration was increased. This was also observed in the SEM images, where 0% AlgMA showed higher number of large pores (Fig. 2c).

Porosity. Differences in porosity observed by optical microscopy were confirmed and quantified by image analysis. The results showed that porosity increased with time, from $14.9\% \pm 4.0$, $4.1\% \pm 2.1$ and $1.9\% \pm 0.5$ at 2 weeks to $23.8\% \pm 5.3$, $20.3\% \pm 4.7$ and $12.6\% \pm 5.0$ at 4 weeks, ordered from low to high initial stiffness condition (Fig. 3b–b4). This indicates that over the same timeframe, as alginate in the initial hydrogel composition increased, the hydrogel became more compact and therefore less porous. Differences in porosity between stiffness conditions were more evident at 2 weeks, which was closer to the time when the hydrogels were created and they had therefore undergone fewer changes. Highest porosity was achieved after 4 weeks, with similar porosities ($22.0\% \pm 3.3$) at 0% and 1% AlgMA (Fig. 3b–b4). The results also showed that 0% AlgMA was the stiffness condition with least variation in porosity over time (8.9% increase) and 1% and 2% AlgMA had 16.2% and 10.7% increase respectively (Fig. 3b–b4). Supplementary Fig. 4d shows bar charts of porosity.

Cluster dynamics over time and by hydrogel stiffness. *Cluster density pattern.* We observed with optical microscopy that in 0% AlgMA hydrogel clusters were small, irregular and occupied a large surface of the model. In contrast, 1% and 2% AlgMA hydrogels showed large, round and compact clusters occupying a smaller surface of the model (Fig. 3a).

These parameters were validated and mathematically quantified by digital analysis. Comparing timeframes within the same stiffness showed that hydrogels with 0% AlgMA represented the highest percentage of small

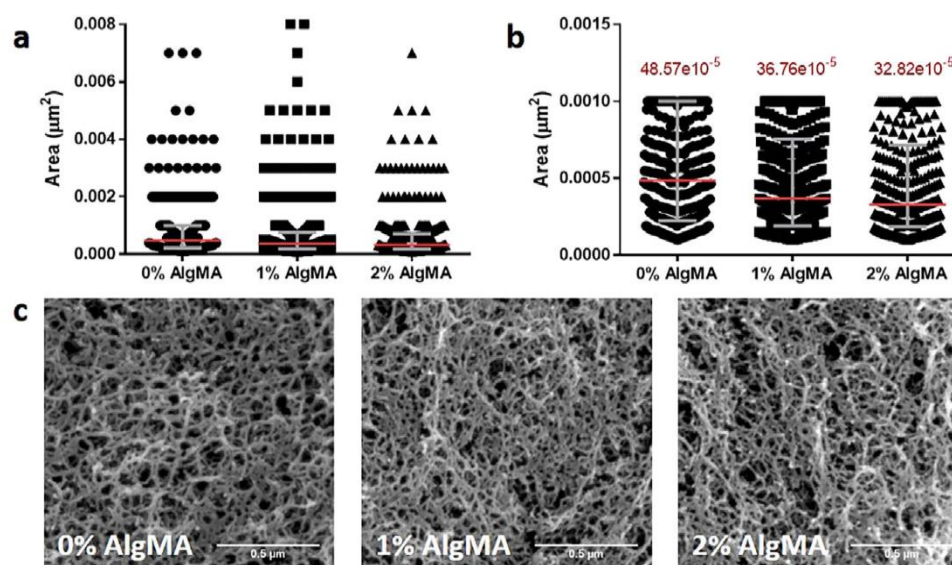


Figure 2. (a) Pore area dot plot of 0%, 1% and 2% AlgMA hydrogels and (b) zoom in of the interquartile region. The interquartile region is shown in grey and the median in red. (c) SEM images of the three hydrogel combinations.

clusters ($53.2\% \pm 2.4$ and $65.4\% \pm 12.8$) and the smallest percentage of large clusters ($14.0\% \pm 2.0$ and $13.6\% \pm 6.3$), at both 2 and 4 weeks culturing, respectively (Fig. 3b-b1). When considering cluster density variation in 0% AlgMA, we observed a high variability on the total number of clusters over time (from 295.5 ± 29.3 to 327.1 ± 123.2 clusters/ mm^2) and a decrease in medium and large cluster sizes (from 97.4 ± 11.7 to 55.4 ± 8.6 and 41.2 ± 7.1 to 31.1 ± 3.3 clusters/ mm^2) (Fig. 3b-b2). At 1% AlgMA, all cluster size percentages ($33.3\% \pm 13.5$) (Fig. 3b-b1) but also total and size-related cluster density (104.1 ± 31.4 and 34.7 ± 15.8 clusters/ mm^2 , respectively) were maintained over the culturing period, with minimal variation within the same size over time (i.e.: 24.8 ± 8.9 – 26.8 ± 8.0 clusters/ mm^2 in large clusters) except medium sized clusters, displaying the highest variations (22.3% and 25.5 clusters/ mm^2 variation over time) (Fig. 3b-b2). Finally, at 2% AlgMA large cluster percentages increased noticeably over time compared to medium and small ($17.9\% \pm 0.9$ to $40.3\% \pm 3.9$) (Fig. 3b-b1). We also observed that total cluster density decreased over the timeframe (98.7 ± 7.4 to 62.7 ± 11.0 clusters/ mm^2), driven by a decrease in small and medium clusters (from 35.3 ± 1.8 to 19.4 ± 2.8 and 45.6 ± 5.6 to 18.0 ± 5.4 clusters/ mm^2 , respectively) and increased in large ones (from 17.8 ± 1.9 to 25.3 ± 5.1 clusters/ mm^2) (Fig. 3b-b2).

Comparing different stiffness at the same time point showed that at 2 weeks, larger clusters were a minority in all stiffness conditions ($14.0\% \pm 2.0$ in 0% AlgMA, $20.8\% \pm 4.8$ in 1% AlgMA and $17.9\% \pm 0.9$ in 2% AlgMA) (Fig. 3b-b1). Furthermore, we observed that the stiffer the hydrogel, the lower the density in all clusters (i.e.: 156.9 ± 16.0 – 39.7 ± 3.7 – 35.3 ± 1.8 clusters/ mm^2 in small clusters) (Fig. 3b-b2). At 4 weeks, each cluster size group behaved differently as stiffness increased: while the proportion of small clusters was reduced ($65.4\% \pm 12.8$ – $50.6\% \pm 7.9$ – $32.1\% \pm 5.3$), the medium clusters remained constant ($21.0\% \pm 6.5$ – $21.0\% \pm 5.6$ – $27.6\% \pm 3.2$) and large clusters increased ($13.6\% \pm 6.3$ – $28.4\% \pm 4.1$ – $40.3\% \pm 3.9$) (Fig. 3b-b1). Furthermore, at 4 weeks cluster density also decreased with stiffness. However, it remained more stable as the clusters increased in size (240.6 ± 117.4 – 46.5 ± 10.6 – 19.4 ± 2.8 clusters/ mm^2 in small clusters, 55.4 ± 8.6 – 22.4 ± 10.3 – 18.0 ± 5.4 clusters/ mm^2 in medium clusters and 31.1 ± 3.1 – 26.8 ± 8.0 – 25.3 ± 5.1 clusters/ mm^2 in large ones) (Fig. 3b-b2). Supplementary Fig. 4a,b shows bar charts of cluster density pattern.

Percentage occupancy. Firstly, we studied the effect of time on cluster occupancy within the same stiffness. At 0% and 1% AlgMA it was observed that large clusters had the highest occupancy at all-time points ($20.0\% \pm 4.7$ and $10.3\% \pm 4.4$ at 2 weeks and $21.5\% \pm 3.1$ and $17.6\% \pm 5.2$ at 4 weeks) (Fig. 3b-b3). In the case of 2% AlgMA hydrogels, medium and large clusters occupied a similar area at 2 weeks ($5.6\% \pm 1.2$ and $5.2\% \pm 1.9$ respectively), slightly dominated by medium clusters, but the area increased at 4 weeks, dominated by large clusters ($19.2\% \pm 1.7$) (Fig. 3b-b3). Additionally, we could observe that time (2 vs 4 weeks) did not affect the total occupancy in 0% AlgMA ($31.6\% \pm 5.7$ vs $29.3\% \pm 2.6$) and 1% AlgMA ($16.0\% \pm 5.0$ vs $20.6\% \pm 6.5$), but a positive one in 2% AlgMA ($12.1\% \pm 1.5$ vs $21.4\% \pm 2.3$).

We also studied the percentage of occupancy and the effect of stiffness within the same culturing period. At 2 weeks we found that generally the stiffer the hydrogel was, the lower percentage of space it occupied (i.e.: $20.0\% \pm 4.7$ – $10.3\% \pm 4.4$ – $5.2\% \pm 1.9$ in large clusters) (Fig. 3b-b3). At 4 weeks slightly lower occupancy was observed in the 1% and 2% AlgMA hydrogels, although in general the percentages were similar (i.e.: $21.5\% \pm 3.1$ – $17.6\% \pm 5.2$ – $19.2\% \pm 1.7$ in large clusters, with increasing stiffness) (Fig. 3b-b3). Supplementary Fig. 4c shows bar charts of percentage occupancy.

Clustered cell behavior across timeframes and by hydrogel stiffness. *Cell nucleus characterization.* Changes in nucleus size and shape were evaluated by digitally quantifying their area and shape factor, revealing

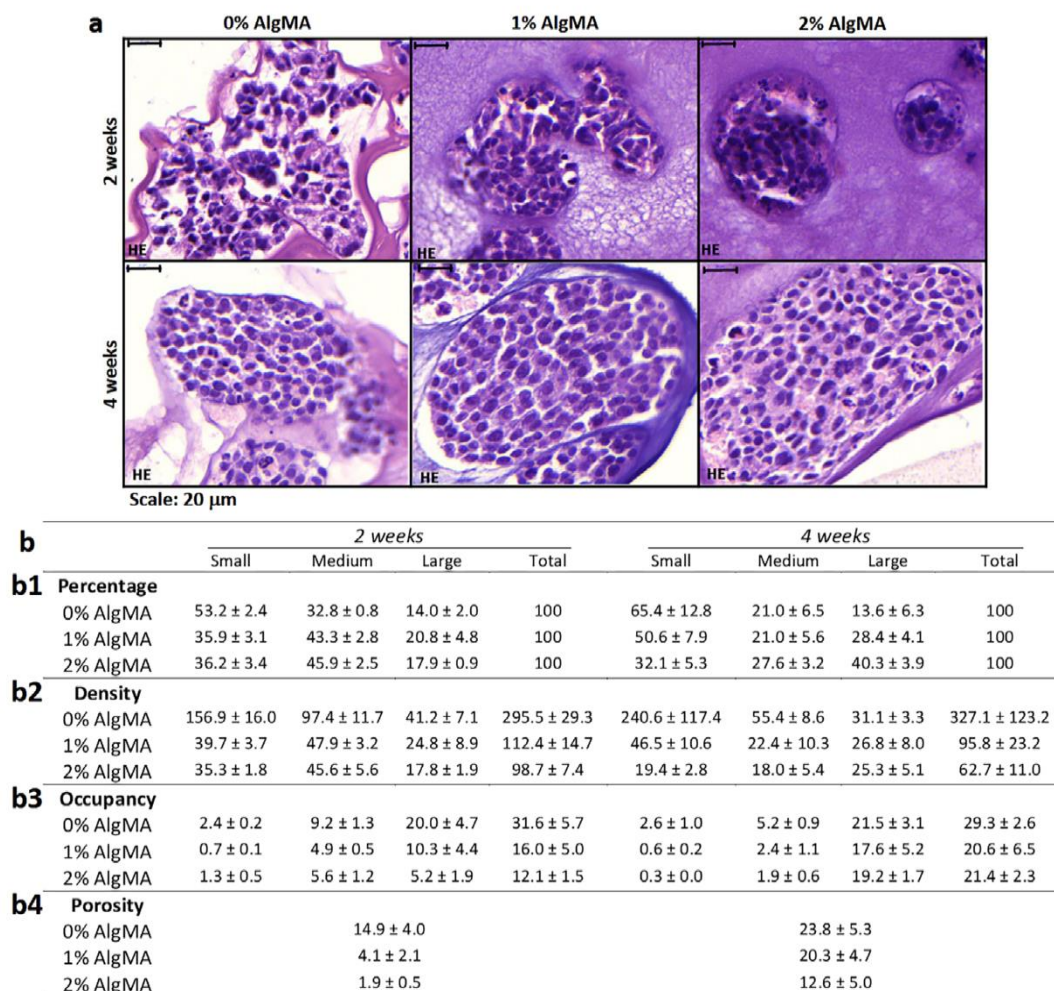


Figure 3. Characterization of bioprinted hydrogels. **(a)** Hydrogels hematoxylin-eosin stains (80×) studying the morphology of the models. **(b)** Percentage of clusters (**b1**), cluster density (**b2**), percentage of occupancy (**b3**) for each cluster size (small: <400; medium: 400–2,000; large: >2,000 μm^2) and (**b4**) porosity of bioprinted hydrogels. Values are plotted as mean and standard error of the mean.

minimal variations in either parameter when compared with time and stiffness. Nucleus areas in 0% AlgMA hydrogels varied from $14.04 \pm 11.20 \mu\text{m}^2$ to $13.61 \pm 11.20 \mu\text{m}^2$, in 1% AlgMA from $17.96 \pm 49.62 \mu\text{m}^2$ to $15.92 \pm 18.26 \mu\text{m}^2$ and in 2% AlgMA from $13.02 \pm 8.45 \mu\text{m}^2$ to $14.88 \pm 48.35 \mu\text{m}^2$ at 2 and 4 weeks respectively. The shape factor increase indicated that nuclei tended to become more irregular with time and stiffness, but changes were minimal. We found that shape factor in 0% AlgMA hydrogels varied from 0.50 ± 0.20 to 0.63 ± 0.21 , in 1% AlgMA from 0.55 ± 0.21 to 0.61 ± 0.23 and in 2% AlgMA from 0.62 ± 0.20 to 0.71 ± 0.19 when comparing values at 2 and 4 weeks respectively.

Cell proliferation (Ki67). 2D cell cultures presented a high proliferation rate (80% positive cells). When cells cultured in hydrogels were analyzed, in all the stiffness considered Ki67 positive cells increased over time by optical microscopy, with a predominantly peripheral cluster distribution. Digital analysis verified and quantified the increase in positive cells and H-score when culturing times and stiffness increased. From 2 to 4 weeks, positive cell percentages increased threefold at 0% AlgMA (from 25.5% to 73.8%; H-score from 47.98 to 200.27), approximately twofold at 1% AlgMA (from 36.9% to 59.8%; H-score from 77.85 to 163.98) and twofold at 2% AlgMA (from 44.5% to 90.7%; H-score from 89.31 to 253.95) (Fig. 4a). The percentage of Ki67 positive and negative cells was also studied across different cluster sizes. No direct effect of the cluster area on percentages of positive and negative cells was observed in any of the conditions studied (Supplementary Fig. 5a).

Polypyrimidine tract binding protein 1 (PTBPI). As previously described for Ki67, SK-N-BE(2) cells presented a high mRNA metabolism (90% positive cells) in 2D culture. Furthermore, there was a significant increase in positive hydrogel cultured cells from 2 to 4 weeks culturing in all stiffness conditions (from $15.2 \pm 6.3\%$ to $97.2 \pm 0.7\%$). At 2 weeks, the increase in stiffness also increased the number of positive cells significantly, from 10.3% in 0% AlgMA to 22.3% in 2% AlgMA, increasing the H-score from 15.71 to 37.68 as well. However, at 4

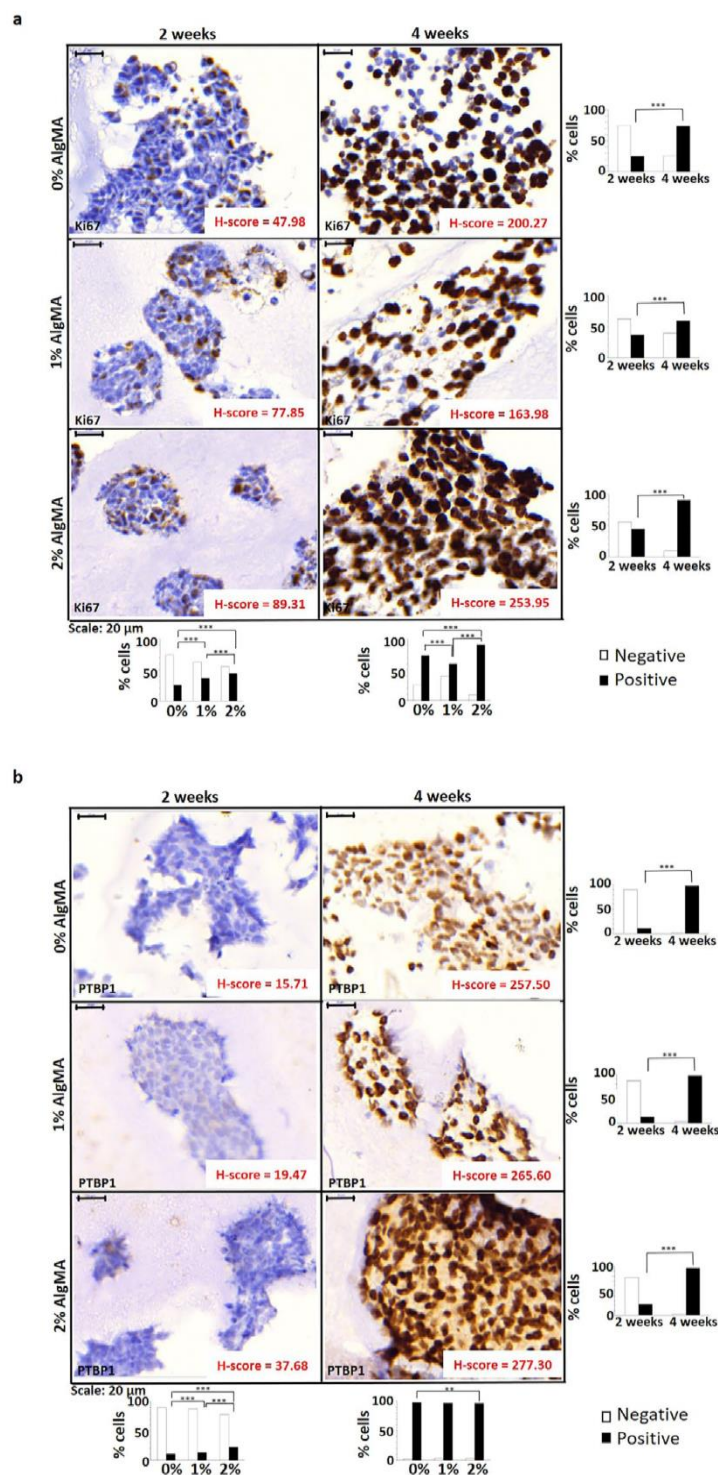


Figure 4. Study of cell proliferation. Immunohistochemistry images (80 \times), percentage of negative and positive cells and H-score for (a) Ki67 and (b) PTBP1. Results expressed as percentage of cells represent total number of cells. White bars: negative cells; Black bars: positive cells. Statistical analysis using χ^2 test: ** p -value < 0.01, *** p -value < 0.001.

weeks the percentage of positive cells were similar in all stiffness conditions ($97.2 \pm 0.7\%$), with minimal increase in the H-score related with high stiffness (from 257.50 to 277.30) (Fig. 4b). In addition, different cluster sizes did not affect the percentage of stained cells in the 0% AlgMA hydrogels either at 2 or at 4 weeks. By contrast, at 2 weeks the hydrogels with 1% and 2% AlgMA evinced a significant decrease in positive cells as the size of the clusters increased (33.8%-21.3%-3.3% and 48.2%-39.6%-9.1%, respectively); this behavior was not maintained at 4 weeks (Supplementary Fig. 5b).

Hydrogel conditions	% Karyorrhexis Cells	% Mitosis Cells	% MK Cells	MKI Classification
0% 2 w	19.6	2.4	22	H
1% 2 w	45	2.6	47.6	H
2% 2 w	28.2	0.6	28.8	H
0% 4 w	20	1.6	21.6	H
1% 4 w	12.8	0.2	13	H
2% 4 w	47.4	1.2	48.6	H

Table 1. MKI results for bioprinted hydrogels. Percentage MK cells > 4% represents high MKI. w: weeks; H: high. w: weeks; H: high.

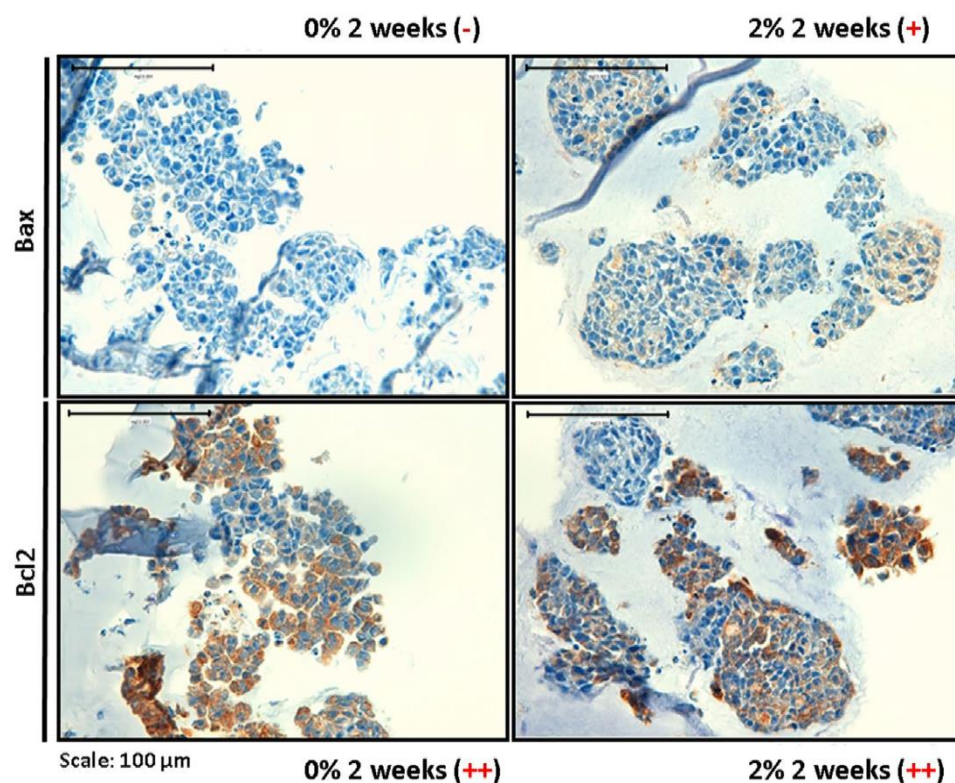


Figure 5. Study of apoptosis and antiapoptosis. Immunohistochemistry images (40 \times) of Bax and Bcl2 markers. Optical microscopy analysis: – Negative (<1% positive cells); + Low positive (1–20% positive cells); ++ Intermediate positive (20–50% positive cells).

Mitosis-Karyorrhexis index. A high MKI score was determined by optical microscopy (MK cells > 4%) and showed that the prevalence of cells in karyorrhexis was much higher than the number of mitotic cells in 2D culture (24% vs 2%) and in all hydrogel samples ($28.8 \pm 14.3\%$ vs $1.4 \pm 0.9\%$), with the highest MKI in 2% AlgMA at 4 weeks of culture (48.6% MK cells). Results are shown in Table 1.

Apoptosis and antiapoptosis markers. 2D cell cultures presented high Bcl2 expression (95% of positive cells) and intermediated Bax expression (40% of positive cells). Optical microscopy in hydrogel samples also revealed a greater number of antiapoptosis markers (Bcl2) than apoptosis markers (Bax), increasing with stiffness (Fig. 5). Nevertheless, the amount of positive cells in 3D culture was much lower than in 2D culture, while Bcl2 positive cells remained between 20% and 50%, 100% of Bax negative cells were present in 0% AlgMA and Bax positive cells varied between 1% and 20% in 2% AlgMA.

Discussion

The detailed mechanisms by which a physical stimulus is converted into a biochemical response in cancer are not well understood, consequently, molecular events occurring in the tumor microenvironment during pathogenesis and tumor progression, such as cell-cell/ECM interactions or fluid shear forces, are a current focus of research⁴⁹. Standard *in vivo* and *in vitro* models are traditionally used to elucidate the mechanisms involved in pathobiology and evaluate chemotherapeutics. However, the individual contribution of interconnected physical and biochemical parameters cannot easily be assessed in *in vivo* models⁵⁰ and they also fail to predict the clinical

efficacy of new drug candidates. The challenge in treating HR-NB is gaining insight into structural, molecular and microenvironmental changes that can be applied to halt tumor metastasis and resistance to multiple chemotherapeutic drugs. 3D scaffold-based NB cell models have only recently been used in studies^{51,52} yet provide valuable platforms for analyzing the biological signs underlying disease progression. In the present study we successfully characterized SK-N-BE(2) neuroblastic cell behavior in 3D culture, using bioprinted hydrogels composed from GelMA and different percentages of AlgMA to represent various ECM initial stiffness conditions. SK-N-BE(2) cells present MNA, a well-known marker of aggressiveness in NB. SK-N-BE(2) cells maintained MNA in our 3D culture conditions, and therefore this cell line is suitable to study ECM mechanical properties in relation to the MNA NB tumor microenvironment in a patient cohort. Furthermore, as the cultured cells can be removed from the scaffolds by trypsin-mediated hydrogel degradation, the bioprinted 3D models presented herein permit varied study with isolated cell clusters.

This study confirms the capacity of GelMA and different percentages of AlgMA scaffolds to support NB cell line growth, as previously described in the collagen-based scaffolds used by Curtin *et al.* and Duarte Campos *et al.* in their respective studies^{51,52}. The stiffness properties of the printed hydrogels without bioinks, determined by Young's modulus as previously described, increased in line with AlgMA concentrations⁴³, and no significant differences were found comparing the Young's modulus values of each stiffness at 37 °C or at room temperature, which confirms that all measurements carried out in human tumors, mice tumors and hydrogels are comparable at room temperature. However, the Young's modulus decrease in composite hydrogels bioprinted and incubated with SK-N-BE(2) for 24 days with 1% and 2% AlgMA indicates an increased elasticity in these hydrogels⁵³. Among other factors, this could be linked to cell-mediated hydrogel degradation as cells grow, releasing matrix metalloproteinases (MMP)⁵⁴, but also to cell proliferation and migration through the hydrogel, and the softer consistency of the tumor cells compared to the ECM^{55,56}. Furthermore, elasticity is increased in tumors derived from NB cells inoculated orthotopically into mice, highlighting the differences between human tumors and animal tissues. Murine tumor models can simulate certain physiopathological conditions but do not completely resemble human disease, owing to differences in tumor microenvironment, ECM composition and high cell density⁵⁷. Despite that, the similarities found between the elastic properties of 1% AlgMA hydrogels and those present in HR-NB and xenograft NB models prove an advantage for prospective 3D bioprinted models. Moreover, since the fabricated composite hydrogels show viscoelastic behavior in the range of the stiffness described in neurons, normal epithelial colonies and adipocytes (from 0.1 to 1 kPa)⁵⁸ and have adjustable stiffness properties, they provide promising insights for future design of fine-tuning mimetic NB 3D models. As expected, porosity in the bioprinted hydrogels decreased alongside increased alginate concentration, as hydrogels became stiffer and more compact⁴³. Although final porosity varied only minimally between stiffness conditions, it increased particularly with culturing time in the stiffest bioprinted hydrogels. Porosity could be generated by cell activity, driving hydrogel degradation with MMP⁵⁴ or generating gaps by cluster detachment. Moreover, porosity could be a consequence of the sample preanalytical processing (fixation, paraffin embedding and sectioning). However, further studies are needed to confirm whether MMPs are responsible for the strong porosity observed and to pinpoint the causes of highest susceptibility in the stiffest hydrogels.

In accordance with current knowledge of biology and cell cultures, we expected that cell cluster density and occupancy would increase over time in our 3D models, due to cell migration and proliferation⁵². Moreover, given that ECM with high stiffness has been associated with aggressiveness in NB³⁸, we predicted cell cluster density and occupancy would increase with stiffness. We found growth in cell cluster occupancy, but density tended to decrease over time, meaning that cluster generation processes like cell migration and cluster division were under-represented compared to cell cluster growth, death and detachment processes. Additionally, contrary to expectation, we observed that cell cluster density and occupancy were reduced with increasing stiffness^{1,7}. Compared to the permissive characteristics of the low stiffness hydrogels, high stiffness equals a restrictive ECM, which apparently hinders initial cell migration and growth. In restricted environments cell migration is affected not only by matrix stiffness but also by initial matrix pore size, as compared to the cell nucleus size⁵⁹, and by pore shape⁶⁰. Despite this, we report very small pore size in our models, almost without change between different stiffness levels, which could inhibit cell spreading¹⁵. In fact, cell nucleus morphology changes were also minimal, suggesting that in our models, cell migration would not be driven by nucleus deformation related to matrix pore size, although these pores could facilitate matrix tunneling by cell MMP activity^{54,61}. Nevertheless, temporal cell growth increase in the stiffest hydrogels equilibrates the occupancy values between the different modelled conditions. Observed growth capacity can be explained by cell adaptation, but also by a loss of stiffness to a more permissive state, related to cell-mediated hydrogel degradation. Persistent reduction in small cluster density in the highest stiffness levels at 4 weeks suggests that malignant neuroblasts would be preparing genetic and epigenetic pathways to promote cell migration.

One explanatory cellular behavior pattern could be permissive cell growth at lowest stiffness with later cell death in unadapted cells, with highest stiffness conversely only allowing cell proliferation in cells capable of adapting. Alternatively, cellular loss at lowest stiffness could also be explained by cellular detachment, as these hydrogels are less compact scaffolds. Initial culture times and lowest stiffness conditions are the most variable ones, suggesting that cells have an initial adaptive process while they are proliferating, migrating and dying until reaching a stable condition. Another observation is that as the most physiologically similar bioprinted hydrogel, 1% AlgMA condition shows lower cluster density variation and reaches final density values quickly.

We also noted greater cell proliferation as stiffness and culture time increased, regardless of the size of clusters analyzed, which as expected indicates that no cell contact inhibition of proliferation mechanisms are related to the stiffness of the scaffolding⁶². In fact, we observed that a similar increase of cells in the proliferative phase and with high mRNA processing index occurs at 4 weeks culture, nearly reaching the expression values found in 2D cell cultures. The high MKI values obtained are consistent with the characteristic SK-N-BE(2) aggressiveness found in malignant NB²⁹⁻³¹, and also demonstrate that this cell line could be adequately replicated in a high stiffness ECM

proliferative tumor model. The higher increase found in the antiapoptosis marker (Bcl2), cell proliferation and mRNA processing index, compared with those found in the apoptosis marker (Bax) and the individual increases in stiffness, confirm that the cells adapt more efficiently with the highest stiffness. Interestingly, Bcl2 and Bax expression patterns in 3D structures replicated human tumor behavior more accurately than 2D cultured cells, in which both biomarkers were overexpressed.

Having characterized the cellular dynamics of SK-N-BE(2) cell line according to time and stiffness in a 3D *in vitro* NB model, we successfully generated long-term 3D culture platforms for an aggressive NB cell line and established preliminary mechanical conditions physiologically similar to NB tumors in the 3D model. We conclude that increased stiffness hinders initial cell proliferation and loses part of its impact over time by cell-mediated hydrogel degradation and cell growth recovery. Including Schwann cells and other components of the cellular matrix like immune cells and vessels in the bioinks could improve the physiopathological preliminary 3D *in vitro* model of aggressive NB, adding ECM components to better mimic tumor mechanotransduction. All these systems will enhance the use of 3D models in biomedicine, providing useful insights for tailoring biomimetic systems to each physiological and/or tumor tissue, and can be used to advance preclinical research.

Data availability

The datasets generated and/or analyzed during the current study are available from the corresponding author on reasonable request.

Received: 4 July 2019; Accepted: 19 March 2020;

Published online: 14 April 2020

References

- Noguera, R., Nieto, O. A., Tadeo, I., Farinas, F. & Alvaro, T. Extracellular matrix, biotensegrity and tumor microenvironment. An update and overview. *Histol. Histopathol.* **27**, 693–705, <https://doi.org/10.14670/HH-27.693> (2012).
- Estofolete, C. F. *et al.* Effects of myenteric denervation on extracellular matrix fibers and mast cell distribution in normal stomach and gastric lesions. *Cancer Cell. Int.* **10**, 18, <https://doi.org/10.1186/1475-2867-10-18> (2010).
- Lu, P., Takai, K., Weaver, V. M. & Werb, Z. Extracellular matrix degradation and remodeling in development and disease. *Cold Spring Harb. Perspect. Biol.* **3**, <https://doi.org/10.1101/cshperspect.a005058> (2011).
- Tomlin, H. & Piccinini, A. M. A complex interplay between the extracellular matrix and the innate immune response to microbial pathogens. *Immunology.* **155**, 186–201, <https://doi.org/10.1111/imm.12972> (2018).
- Walker, C., Mojares, E. & Del Rio Hernandez, A. Role of Extracellular Matrix in Development and Cancer Progression. *Int. J. Mol. Sci.* **19**, <https://doi.org/10.3390/ijms19103028> (2018).
- Jinka, R., Kapoor, R., Sistla, P. G., Raj, T. A. & Pande, G. Alterations in Cell-Extracellular Matrix Interactions during Progression of Cancers. *Int. J. Cell Biol.* **2012**, 219196, <https://doi.org/10.1155/2012/219196> (2012).
- Tadeo, I., Berbegall, A. P., Escudero, L. M., Alvaro, T. & Noguera, R. Biotensegrity of the extracellular matrix: physiology, dynamic mechanical balance, and implications in oncology and mechanotherapy. *Front. Oncol.* **4**, 39, <https://doi.org/10.3389/fonc.2014.00039> (2014).
- Doyle, A. D. & Yamada, K. M. Mechanosensing via cell-matrix adhesions in 3D microenvironments. *Exp. Cell Res.* **343**, 60–66, <https://doi.org/10.1016/j.yexcr.2015.10.033> (2016).
- Denys, H. *et al.* The extracellular matrix regulates cancer progression and therapy response: implications for prognosis and treatment. *Curr. Pharm. Des.* **15**, 1373–1384 (2009).
- Lejeune, M. & Alvaro, T. Clinicobiological, prognostic and therapeutic implications of the tumor microenvironment in follicular lymphoma. *Haematologica.* **94**, 16–21, <https://doi.org/10.3324/haematol.2008.001255> (2009).
- Kenny, P. A. & Bissell, M. J. Tumor reversion: correction of malignant behavior by microenvironmental cues. *Int. J. Cancer.* **107**, 688–695, <https://doi.org/10.1002/ijc.11491> (2003).
- Imamura, Y. *et al.* Comparison of 2D- and 3D-culture models as drug-testing platforms in breast cancer. *Oncol. Rep.* **33**, 1837–1843, <https://doi.org/10.3892/or.2015.3767> (2015).
- Gao, S., Shen, J., Hornicek, F. & Duan, Z. Three-dimensional (3D) culture in sarcoma research and the clinical significance. *Biofabrication.* **9**, 032003, <https://doi.org/10.1088/1758-5090/aa7fdb> (2017).
- Kuen, J., Darowski, D., Kluge, T. & Majety, M. Pancreatic cancer cell/fibroblast co-culture induces M2 like macrophages that influence therapeutic response in a 3D model. *Plos One.* **12**, e0182039, <https://doi.org/10.1371/journal.pone.0182039> (2017).
- Fan, C. & Wang, D. A. Macroporous Hydrogel Scaffolds for Three-Dimensional Cell Culture and Tissue Engineering. *Tissue Eng. Part B Rev.* **23**, 451–461, <https://doi.org/10.1089/ten.TEB.2016.0465> (2017).
- Huang, Y., Zhang, X. F., Gao, G., Yonezawa, T. & Cui, X. 3D bioprinting and the current applications in tissue engineering. *Biotechnol. J.* **12**, <https://doi.org/10.1002/biot.201600734> (2017).
- Cavo, M. *et al.* Microenvironment complexity and matrix stiffness regulate breast cancer cell activity in a 3D *in vitro* model. *Sci. Rep.* **6**, 35367, <https://doi.org/10.1038/srep35367> (2016).
- Vedadghavami, A. *et al.* Manufacturing of hydrogel biomaterials with controlled mechanical properties for tissue engineering applications. *Acta Biomater.* **62**, 42–63, <https://doi.org/10.1016/j.actbio.2017.07.028> (2017).
- Gerdes, J. *et al.* Cell cycle analysis of a cell proliferation-associated human nuclear antigen defined by the monoclonal antibody Ki-67. *J. Immunol.* **133**, 1710–1715 (1984).
- Scott, R. J. *et al.* A comparison of immunohistochemical markers of cell proliferation with experimentally determined growth fraction. *J. Pathol.* **165**, 173–178, <https://doi.org/10.1002/path.1711650213> (1991).
- McCormick, D., Chong, H., Hobbs, C., Datta, C. & Hall, P. A. Detection of the Ki-67 antigen in fixed and wax-embedded sections with the monoclonal antibody MIB1. *Histopathology.* **22**, 355–360 (1993).
- Li, L. T., Jiang, G., Chen, Q. & Zheng, J. N. Ki67 is a promising molecular target in the diagnosis of cancer (review). *Mol. Med. Rep.* **11**, 1566–1572, <https://doi.org/10.3892/mmr.2014.2914> (2015).
- Kamath, R. V., Leary, D. J. & Huang, S. Nucleocytoplasmic shuttling of polypyrimidine tract-binding protein is uncoupled from RNA export. *Mol. Biol. Cell.* **12**, 3808–3820, <https://doi.org/10.1091/mbc.12.12.3808> (2001).
- Castelo-Branco, P. *et al.* Polypyrimidine tract binding protein modulates efficiency of polyadenylation. *Mol. Cell. Biol.* **24**, 4174–4183 (2004).
- Lou, H., Helfman, D. M., Gagel, R. F. & Berget, S. M. Polypyrimidine tract-binding protein positively regulates inclusion of an alternative 3'-terminal exon. *Mol. Cell. Biol.* **19**, 78–85 (1999).
- Valcarcel, J. & Gebauer, F. Post-transcriptional regulation: the dawn of PTB. *Curr. Biol.* **7**, R705–708 (1997).
- Cheung, H. C. *et al.* Splicing factors PTBP1 and PTBP2 promote proliferation and migration of glioma cell lines. *Brain.* **132**, 2277–2288, <https://doi.org/10.1093/brain/awp153> (2009).

28. He, X. *et al.* Knockdown of polypyrimidine tract-binding protein suppresses ovarian tumor cell growth and invasiveness *in vitro*. *Oncogene*. **26**, 4961–4968, <https://doi.org/10.1038/sj.onc.1210307> (2007).
29. Gestblom, C., Hoehner, J. C. & Pahlman, S. Proliferation and apoptosis in neuroblastoma: subdividing the mitosis-karyorrhexis index. *Eur. J. Cancer*. **31A**, 458–463 (1995).
30. Atikankul, T. *et al.* MIB-1 Index as a Surrogate for Mitosis-Karyorrhexis Index in Neuroblastoma. *Am. J. Surg. Pathol.* **39**, 1054–1060, <https://doi.org/10.1097/PAS.0000000000000478> (2015).
31. Joshi, V. V., Chatten, J., Sather, H. N. & Shimada, H. Evaluation of the Shimada classification in advanced neuroblastoma with a special reference to the mitosis-karyorrhexis index: a report from the Childrens Cancer Study Group. *Mod. Pathol.* **4**, 139–147 (1991).
32. Portt, L., Norman, G., Clapp, C., Greenwood, M. & Greenwood, M. T. Anti-apoptosis and cell survival: a review. *Biochim. Biophys. Acta*. **1813**, 238–259, <https://doi.org/10.1016/j.bbamcr.2010.10.010> (2011).
33. Elmore, S. Apoptosis: a review of programmed cell death. *Toxicol. Pathol.* **35**, 495–516, <https://doi.org/10.1080/01926230701320337> (2007).
34. Antignani, A. & Youle, R. J. How do Bax and Bak lead to permeabilization of the outer mitochondrial membrane? *Curr. Opin. Cell Biol.* **18**, 685–689, <https://doi.org/10.1016/j.ceb.2006.10.004> (2006).
35. Hata, A. N., Engelman, J. A. & Faber, A. C. The BCL2 Family: Key Mediators of the Apoptotic Response to Targeted Anticancer Therapeutics. *Cancer Discov.* **5**, 475–487, <https://doi.org/10.1158/2159-8290.CD-15-0011> (2015).
36. Wilt, D. & Vats, T. S. Neuroblastoma in children. A retrospective review and update on treatment. *J. Kans. Med. Soc.* **84**(386–388), 396 (1983).
37. Marastoni, S., Ligresti, G., Lorenzon, E., Colombatti, A. & Mongiat, M. Extracellular matrix: a matter of life and death. *Connect. Tissue Res.* **49**, 203–206, <https://doi.org/10.1080/03008200802143190> (2008).
38. Tadeo, I. *et al.* Extracellular matrix composition defines an ultra-high-risk group of neuroblastoma within the high-risk patient cohort. *Br. J. Cancer*. **115**, 480–489, <https://doi.org/10.1038/bjc.2016.210> (2016).
39. Tadeo, I., Berbegall, A. P., Navarro, S., Castel, V. & Noguera, R. A stiff extracellular matrix is associated with malignancy in peripheral neuroblastic tumors. *Pediatr. Blood Cancer.* **64**, <https://doi.org/10.1002/pbc.26449> (2017).
40. Tadeo, I. *et al.* Lymph microvascularization as a prognostic indicator in neuroblastoma. *Oncotarget.* **9**, 26157–26170, <https://doi.org/10.18632/oncotarget.25457> (2018).
41. Tadeo, I. *et al.* 1p36 deletion results in a decrease in glycosaminoglycans which is associated with aggressiveness in neuroblastic tumors. *Histol. Histopathol.* **33**, 487–495, <https://doi.org/10.14670/HH-11-947> (2018).
42. Giraldo, N. A. *et al.* The clinical role of the TME in solid cancer. *Br. J. Cancer.* **120**, 45–53, <https://doi.org/10.1038/s41416-018-0327-z> (2019).
43. Garcia-Lizarribar, A. *et al.* Composite Biomaterials as Long-Lasting Scaffolds for 3D Bioprinting of Highly Aligned Muscle Tissue. *Macromol. Biosci.* **18**, e1800167, <https://doi.org/10.1002/mabi.201800167> (2018).
44. Visser, J. *et al.* Reinforcement of hydrogels using three-dimensionally printed microfibrils. *Nat. Commun.* **6**, 6933, <https://doi.org/10.1038/ncomms7933> (2015).
45. Kloxin, A. M., Benton, J. A. & Anseth, K. S. *In situ* elasticity modulation with dynamic substrates to direct cell phenotype. *Biomaterials.* **31**, 1–8, <https://doi.org/10.1016/j.biomaterials.2009.09.025> (2010).
46. McKee, C. T., Last, J. A., Russell, P. & Murphy, C. J. Indentation versus tensile measurements of Young's modulus for soft biological tissues. *Tissue Eng. Part B Rev.* **17**, 155–164, <https://doi.org/10.1089/ten.TEB.2010.0520> (2011).
47. Brodeur, G. M., Seeger, R. C., Schwab, M., Varmus, H. E. & Bishop, J. M. Amplification of N-myc in untreated human neuroblastomas correlates with advanced disease stage. *Science.* **224**, 1121–1124 (1984).
48. Shimada, H. *et al.* Histopathologic prognostic factors in neuroblastic tumors: definition of subtypes of ganglioneuroblastoma and an age-linked classification of neuroblastomas. *J. Natl. Cancer Inst.* **73**, 405–416 (1984).
49. Caballero, D., Blackburn, S. M., de Pablo, M., Samitier, J. & Albertazzi, L. Tumour-vessel-on-a-chip models for drug delivery. *Lab Chip.* **17**, 3760–3771, <https://doi.org/10.1039/c7lc00574a> (2017).
50. Caballero, D. & Samitier, J. Topological Control of Extracellular Matrix Growth: A Native-Like Model for Cell Morphodynamics. *Studies. ACS Appl. Mater. Interfaces.* **9**, 4159–4170, <https://doi.org/10.1021/acsami.6b13063> (2017).
51. Curtin, C. *et al.* A physiologically relevant 3D collagen-based scaffold-neuroblastoma cell system exhibits chemosensitivity similar to orthotopic xenograft models. *Acta Biomater.* **70**, 84–97, <https://doi.org/10.1016/j.actbio.2018.02.004> (2018).
52. Duarte, D. F. *et al.* Exploring Cancer Cell Behavior *In Vitro* in Three-Dimensional Multicellular Bioprintable Collagen-Based Hydrogels. *Cancers.* **11**, 180, <https://doi.org/10.3390/cancers11020180> (2019).
53. Joyce, M. H. *et al.* Phenotypic Basis for Matrix Stiffness-Dependent Chemoresistance of Breast Cancer Cells to Doxorubicin. *Front. Oncol.* **8**, 337, <https://doi.org/10.3389/fonc.2018.00337> (2018).
54. Wu, Y., Puperi, D. S., Grande-Allen, K. J. & West, J. L. Ascorbic acid promotes extracellular matrix deposition while preserving valve interstitial cell quiescence within 3D hydrogel scaffolds. *J. Tissue Eng. Regen. Med.* **11**, 1963–1973, <https://doi.org/10.1002/term.2093> (2017).
55. Tsou, Y. H., Khoneisser, J., Huang, P. C. & Xu, X. Hydrogel as a bioactive material to regulate stem cell fate. *Bioact. Mater.* **1**, 39–55, <https://doi.org/10.1016/j.bioactmat.2016.05.001> (2016).
56. Lin, H. H. *et al.* Mechanical phenotype of cancer cells: cell softening and loss of stiffness sensing. *Oncotarget.* **6**, 20946–20958, <https://doi.org/10.18632/oncotarget.4173> (2015).
57. Pickup, M. W., Mouw, J. K. & Weaver, V. M. The extracellular matrix modulates the hallmarks of cancer. *EMBO Rep.* **15**, 1243–1253, <https://doi.org/10.15252/embr.201439246> (2014).
58. Liu, J., Zheng, H., Poh, P. S., Machens, H. G. & Schilling, A. F. Hydrogels for Engineering of Perfusable Vascular Networks. *Int. J. Mol. Sci.* **16**, 15997–16016, <https://doi.org/10.3390/ijms160715997> (2015).
59. Wolf, K. *et al.* Physical limits of cell migration: control by ECM space and nuclear deformation and tuning by proteolysis and traction force. *J. Cell Biol.* **201**, 1069–1084, <https://doi.org/10.1083/jcb.201210152> (2013).
60. Green, B. J. *et al.* Pore Shape Defines Paths of Metastatic Cell Migration. *Nano Lett.* **18**, 2140–2147, <https://doi.org/10.1021/acs.nanolett.8b00431> (2018).
61. Al-Abboodi, A. *et al.* *In situ* generation of tunable porosity gradients in hydrogel-based scaffolds for microfluidic cell culture. *Adv. Healthc. Mater.* **3**, 1655–1670, <https://doi.org/10.1002/adhm.201400072> (2014).
62. McClatchey, A. I. & Yap, A. S. Contact inhibition (of proliferation) redux. *Curr. Opin. Cell Biol.* **24**, 685–694, <https://doi.org/10.1016/j.ceb.2012.06.009> (2012).

Acknowledgements

The authors thank Elisa Alonso, Miriam Funes, Esther Álvarez and Isaac Vieco for their valuable technical support. E.M. is supported by the Asociación Fundación Española contra el Cáncer, JAP-AECC (2018/150). This study was supported by ISCIII (FIS) and FEDER (European Regional Development Fund): P117/01558 and Collaborative Project CIBERONC-CIBERBBN (ONC18PI03), NEN Association (Nico contra el cáncer infantil 2017- PVR00157). The funders had no involvement in the research process or the preparation and submission of the article.

Author contributions

E.M., S.M. and A.C. wrote the main manuscript, prepared the figures and carried out the image and data analysis and interpretation. S.M. and A.G. designed and fabricated the hydrogel models. R.B. contributed to data analysis and interpretation. S.N. performed the histopathological examination of the samples and the immunohistochemical analysis. J.S. and R.N. elaborated the concept, designed the study, reviewed the paper and suggested draft changes. All authors read and approved the final manuscript.

Competing interests

The authors declare no competing interests.

Additional information

Supplementary information is available for this paper at <https://doi.org/10.1038/s41598-020-62986-w>.

Correspondence and requests for materials should be addressed to J.S. or R.N.

Reprints and permissions information is available at www.nature.com/reprints.

Publisher's note Springer Nature remains neutral with regard to jurisdictional claims in published maps and institutional affiliations.



Open Access This article is licensed under a Creative Commons Attribution 4.0 International License, which permits use, sharing, adaptation, distribution and reproduction in any medium or format, as long as you give appropriate credit to the original author(s) and the source, provide a link to the Creative Commons license, and indicate if changes were made. The images or other third party material in this article are included in the article's Creative Commons license, unless indicated otherwise in a credit line to the material. If material is not included in the article's Creative Commons license and your intended use is not permitted by statutory regulation or exceeds the permitted use, you will need to obtain permission directly from the copyright holder. To view a copy of this license, visit <http://creativecommons.org/licenses/by/4.0/>.

© The Author(s) 2020

Supplementary Figure legends

Supplementary Figure 1. Variation in percentage of the Young's modulus at 37°C from the Young's Modulus calculated at room temperature in the three hydrogel types. b) Characterization of the Young's modulus of the composite hydrogels, cohort of HR-NB and orthotopic NB mice tumors. Comparative Young's modulus of 5% gelatin methacrylated with 0%, 1% and 2% methacrylated alginate in absence and presence of incubated SK-N-BE(2) cells. Measurements of each hydrogel were performed in quintuplicate. Values are plotted as mean and standard deviation. Statistical analysis using *t-student* test: ^{ns} *p*-value > 0.05, ^{**} *p*-value < 0.01, ^{***} *p*-value < 0.001, comparing SK-NB-E (2) and no cell-hydrogels, ^{####} *p*-value < 0.001, comparing NB patients vs SK-NB-E(2) hydrogels and ^{\$\$\$} *p*-value < 0.001, comparing orthotopic NB mice tumors vs SK-NB-E(2) hydrogels.

Supplementary Figure 2. Example of hydrogel cluster measurement using Panoramic Viewer. Red circle marks each hydrogel cluster. Hydrogel HE staining (15x).

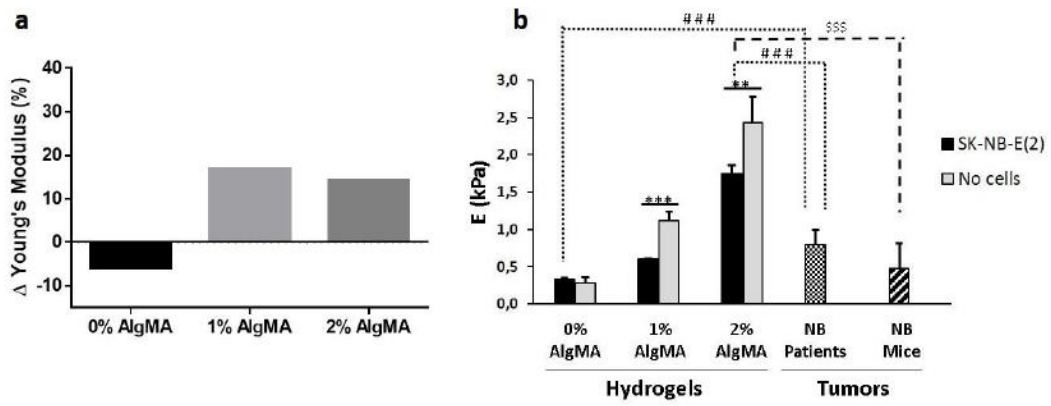
Supplementary Figure 3. Diagram of methodology used. 1. Hydrogel bioprinting; 2. Young's modulus measurement and paraffin embedding; 3. Immunohistochemistry; 4. Digitation and microscopic studies; 5. Analysis and quantification.

Supplementary Figure 4. Characterization of bioprinted hydrogels. Percentage of clusters (a1-a5), cluster density (b1-b5) and percentage of occupancy (c1-c5) for each cluster size (ranges: <400, 400-2.000, > 2,000 μm^2). (a, b, c: 1-3) Study over time within the same stiffness; (a, b, c: 4-5) Study of stiffness over the same timeframe. (d1-d2) Porosity of bioprinted hydrogels: d1) Study over time within the same stiffness; d2) Study of stiffness within the same timeframe. Values are plotted as mean and standard error of the mean.

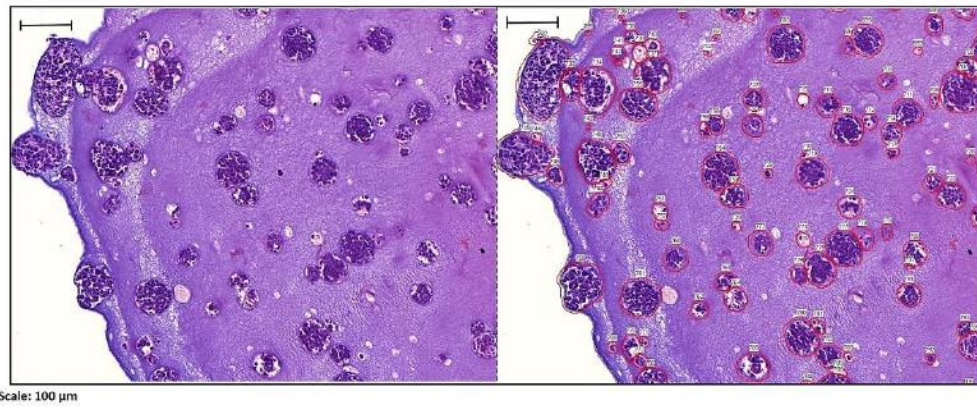
Supplementary Figure 5. Study of cell proliferation in each cluster size (ranges: <400, 400-2.000, > 2,000 μm^2). Percentage of negative and positive cells for a) Ki67 and b) PTBP1. Results

expressed as percentage cells represent total number of cells, differentiating between cluster size. White bars: negative cells; Black bars: positive cells. Statistical analysis using χ^2 test: * p -value < 0.05, ** p -value < 0.01, *** p -value < 0.001.

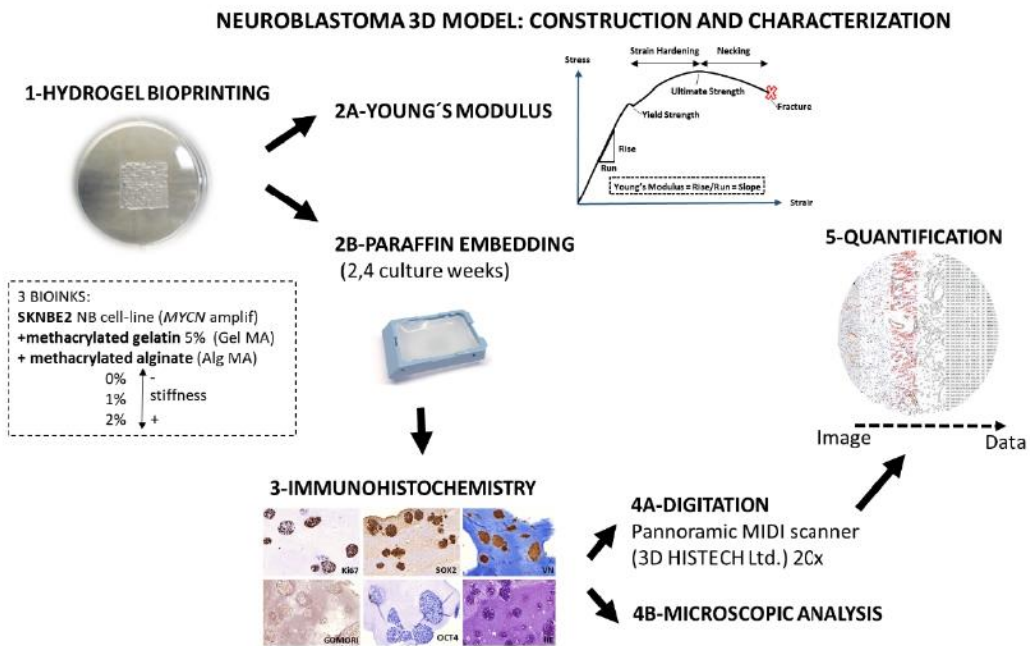
Supplementary Figures



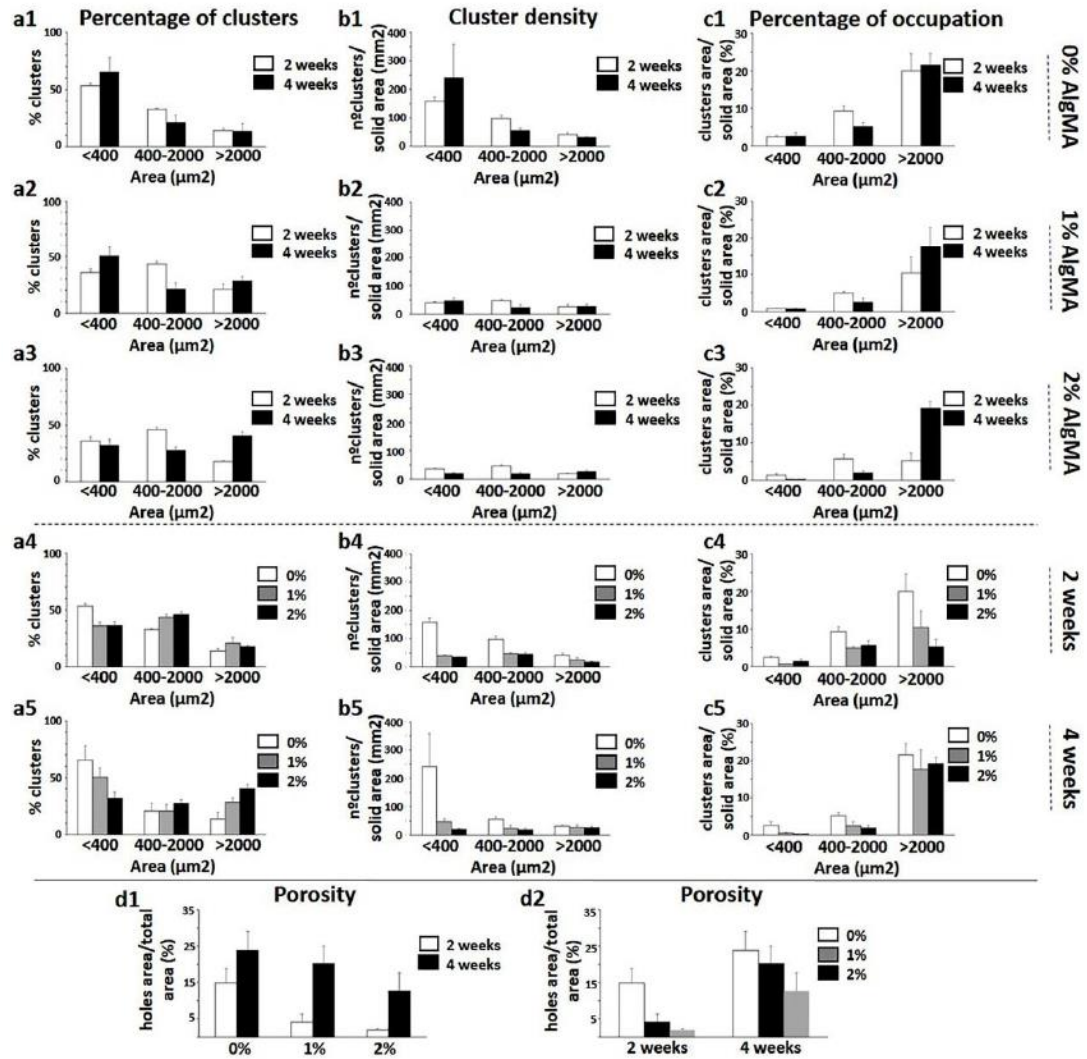
Supplementary Figure 1



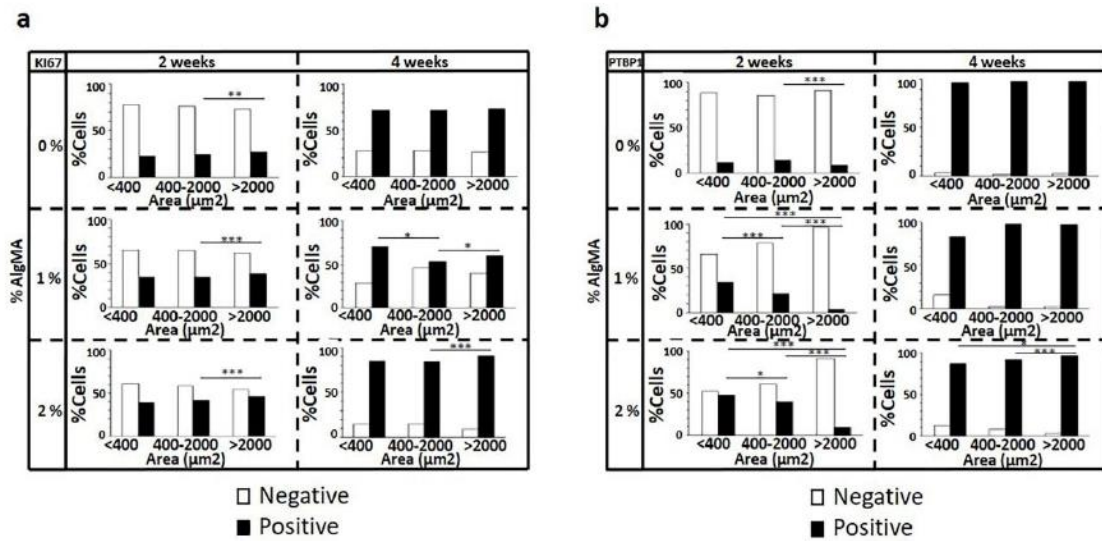
Supplementary Figure 2



Supplementary Figure 3



Supplementary Figure 4



Supplementary Figure 5

Article II: Digital Image Analysis Applied to Tumor Cell Proliferation, Aggressiveness, and Migration-Related Protein Synthesis in Neuroblastoma 3D Models.

Monferrer E*, Sanegre S*, Martín-Vañó S, García-Lizarribar A, Burgos-Panadero R, López-Carrasco A, Navarro S, Samitier J, Noguera R.

*Equal contribution

Int J Mol Sci. 2020. Nov 17; 21(22):8676. doi: 10.3390/ijms21228676.

MDPI, EISSN: 1422-0067

Impact factor 2020: 5.924

5-year impact factor 2020: 6.132

Biochemistry and Molecular Biology: Q1 / Chemistry, Multidisciplinary: Q2

Cites: 4



ARTICLE II



Article

Digital Image Analysis Applied to Tumor Cell Proliferation, Aggressiveness, and Migration-Related Protein Synthesis in Neuroblastoma 3D Models

Ezequiel Monferrer ^{1,2,†}, Sabina Sanegre ^{1,†}, Susana Martín-Vañó ^{1,2},
Andrea García-Lizarribar ^{3,4}, Rebeca Burgos-Panadero ^{1,2}, Amparo López-Carrasco ^{1,2},
Samuel Navarro ^{1,2}, Josep Samitier ^{3,4,5} and Rosa Noguera ^{1,2,*}

¹ Department of Pathology, Medical School, University of Valencia-INCLIVA Biomedical Health Research Institute, 46010 Valencia, Spain; ezequiel.mo.ga@gmail.com (E.M.); Sabina.sanegre@gmail.com (S.S.); Susana.Martin@uv.es (S.M.-V.); reburpa@alumni.uv.es (R.B.-P.); amparolopezcarrasco@gmail.com (A.L.-C.); samuel.navarro@uv.es (S.N.)

² Low Prevalence Tumors, Centro de Investigación Biomédica en Red de Cáncer (CIBERONC), Instituto de Salud Carlos III, 28029 Madrid, Spain

³ Institute for Bioengineering of Catalonia, Barcelona Institute of Science and Technology (IBEC-BIST), 08028 Barcelona, Spain; agarcial@ibecbarcelona.eu (A.G.-L.); jsamitier@ibecbarcelona.eu (J.S.)

⁴ Department of Electronics and Biomedical Engineering, University of Barcelona, 08028 Barcelona, Spain

⁵ Networking Biomedical Research Center in Bioengineering, Biomaterials and Nanomedicine (CIBER-BBN), 28029 Madrid, Spain

* Correspondence: rosa.noguera@uv.es

† These authors contributed equally to this work.

Received: 31 August 2020; Accepted: 16 November 2020; Published: 17 November 2020



Abstract: Patient-derived cancer 3D models are a promising tool that will revolutionize personalized cancer therapy but that require previous knowledge of optimal cell growth conditions and the most advantageous parameters to evaluate biomimetic relevance and monitor therapy efficacy. This study aims to establish general guidelines on 3D model characterization phenomena, focusing on neuroblastoma. We generated gelatin-based scaffolds with different stiffness and performed SK-N-BE(2) and SH-SY5Y aggressive neuroblastoma cell cultures, also performing co-cultures with mouse stromal Schwann cell line (SW10). Model characterization by digital image analysis at different time points revealed that cell proliferation, vitronectin production, and migration-related gene expression depend on growing conditions and are specific to the tumor cell line. Morphometric data show that 3D in vitro models can help generate optimal patient-derived cancer models, by creating, identifying, and choosing patterns of clinically relevant artificial microenvironments to predict patient tumor cell behavior and therapeutic responses.

Keywords: 3D cancer modeling; Ki67; vitronectin; DOCK8; KANK1; preclinical therapeutic studies

1. Introduction

Despite advances in treatment, cancer remains one of the leading causes of death worldwide due to its complexity. Developing physiologically accurate cancer models is therefore essential to uncover the keys to cancer progression and test new therapeutic approaches. As explants of small tumor samples, traditional bi-dimensional (2D) cell cultures have been among the most widely used tools as in vitro models for biomedical research, due to their simplicity and low cost. However, they are incapable of reflecting the effect of the tumor microenvironment or the multiple different cellular interactions that take place in this three-dimensional (3D) environment [1]. The extracellular matrix

(ECM), a vital part of the tumor microenvironment, is a 3D network present in all malignant tissues involved in different functions related to protection, nutrition, cell innervation, immune response, angiogenesis, fibrosis, and tissue regeneration [2–5]. It also participates in transmitting mechanical forces that support the tissue tensegrity system, activating cellular genetic and epigenetic mechanisms. ECM alterations can result in multiple dysfunctions [6], and although this network is not considered in standard cancer management practice today, there is growing evidence pointing to its key role in tumor progression and therapy resistance [7].

3D cell culture has attracted great attention in in vitro cancer modeling due to its ability to recapitulate the structural and functional aspect of the corresponding organs [1]. These models have already been used to study the impact of the ECM on different cancer cells, showing that ECM stiffness may enhance cell motility by modifying their morphological properties to an aggressive phenotype [8,9]. A variety of different tools and methods can be used to generate these 3D models depending on the desired characteristics [10]. Although 3D spheroids and organoids have been broadly used as cancer models for solid tumors, there is no scope for fine-tuning to modulate ECM composition and architecture. One of the most sophisticated methods to overcome the complexity and low reproducibility of 3D spheroids and organoids is 3D bioprinting technology, which allows direct and indirect cell incorporation into the bioink, accurate cell spatial distribution, and defined mesh structure patterning with the desired architectural features [11,12].

For many years, our research has focused on the role of the ECM in neuroblastoma (NB) [13–16] the most frequent extracranial solid tumor in childhood, typified by its highly variable prognosis [17]. A stiff ECM has been associated with NB aggressiveness, since malignant neuroblastic cells are highly sensitive to the biomechanical properties of their microenvironment [13–16,18]. Performing digital image analysis, we have successfully defined morphological patterns associated with ECM stiffness in NB, considering different components such as blood and lymph vessels, collagen fibers, glycosaminoglycans (GAGs), and glycoproteins such as fibronectin and vitronectin (VN) [13–16,19,20]. In recent years, we have also worked with 3D cell culture in bioprinted models, showing that the biomechanical forces imposed by the scaffolds have a great impact on malignant neuroblastic cell behavior [21,22].

The goal of translational research in oncology is to develop patient-derived cancer models to improve personalized therapy. This requires prior work with representative preliminary in vitro 3D models to establish and document the conditions modulating of the 3D cell culture behavior, as well as to assess drug response in preclinical therapeutic studies conducted on the most reliable models. In the present study, we generated 3D bioprinted gelatin-based models to perform 3D cell cultures. We selected two neuroblastoma cell lines with different genetic backgrounds and degrees of malignancy, with the previously used *MYCN*-amplified SK-N-BE(2) cells and *ALK*-mutated SH-SY5Y cells both representing high-risk neuroblastoma [23,24], and evaluated their behavior under different stiffness conditions. To develop a more physiologically relevant environment, we also co-cultured the NB lines with stromal Schwann cells (mouse Schwann cell line (SW10)). Including Schwann cells in the models allows the tumor cells to grow in a more biomimetic environment, since these cells are found at low proportions even in undifferentiated or poorly differentiated neuroblastoma with poor stroma, and are pivotal players in stroma synthesis, which helps determine aggressiveness in this pediatric cancer [25].

When choosing a model to carry out preclinical therapeutic studies, it is necessary to determine the optimal characteristics required from this model, taking into account the desired therapeutic approach and most useful related parameters to analyze. In this study, as a generic aggressiveness factor, we analyzed Ki67, a widely used marker for cell proliferation assessment in cancer studies [26,27]. Our previous studies highlighted territorial VN (tVN) as a relevant glycoprotein related to NB aggressiveness and stiffness [19,20]. VN also interacts with different ECM molecules and has an important role in metastasis through its RGD integrin binding domain, which allows tumor cells to migrate [28–30]. This makes VN a potential therapeutic target, assuming that inhibiting its interaction with tumor cell integrins and/or its ECM remodeling action could reduce tumor cell migration,

which prompted us to evaluate its presence in 3D NB models. We also studied the expression dynamics of two additional genes, DOCK8 and KANK1, having detected a common atypical segmental chromosomal aberration affecting these genes located in chromosome 9p in some high-risk NB patients, as well as in orthotopic mice models and 3D NB bioprinted models [22]. DOCK8 is involved in cytoskeleton remodeling, inducing migration in macrophages, Schwann precursor cells, T cells, and dendritic cells [31–34]. KANK1 participates in actin and microtubule regulation; however, its role in inhibiting or promoting migration depends on the system studied [35–38]. It has also been reported to play a role as a tumor suppressor gene [39,40].

In this study, we used morphometric digital analysis to identify cell characteristics and evaluate cell behavior on 3D scaffold-based NB models. Following on from our previous genetic studies [22], we have chosen replicates of the 3D cultured samples to characterize the expression pattern of the above-mentioned markers and pinpoint correlations with their genomic landscape. The specific parameters analyzed herein provide proof of concept of the wide spectrum of possibilities that these techniques offer to obtain clinically relevant in vitro models for preclinical therapeutic assessment.

2. Results

To assess whether 3D culture generates cell behavioral changes, we first characterized the three cell lines individually in 2D cultures. SK-N-BE(2) and SH-SY5Y cell lines presented Ki67 positivity (80 and 50%, respectively), and KANK1 was detected in all cells. However, DOCK8 staining was found to be negative (<1%) in these cell lines, and little VN was present in most cells (70%), although with different expression patterns; cell membrane and staining in neuritic prolongations in SK-N-BE(2) and perinuclear cytoplasmic staining in SH-SY5Y. SW10 cells presented low Ki67 positivity (<1%), but all cells were DOCK8 and KANK1 positive. VN was negative in SW10 cultures (<1%). Furthermore, to shed more light on cell behavior, synaptophysin (SYP) expression was used as a differential marker between SW10 and neuroblastic cells at 6 weeks in 3D cultures, since both SK-N-BE(2) and SH-SY5Y cell lines were 100% positive and SW10 negative (Figure 1B).

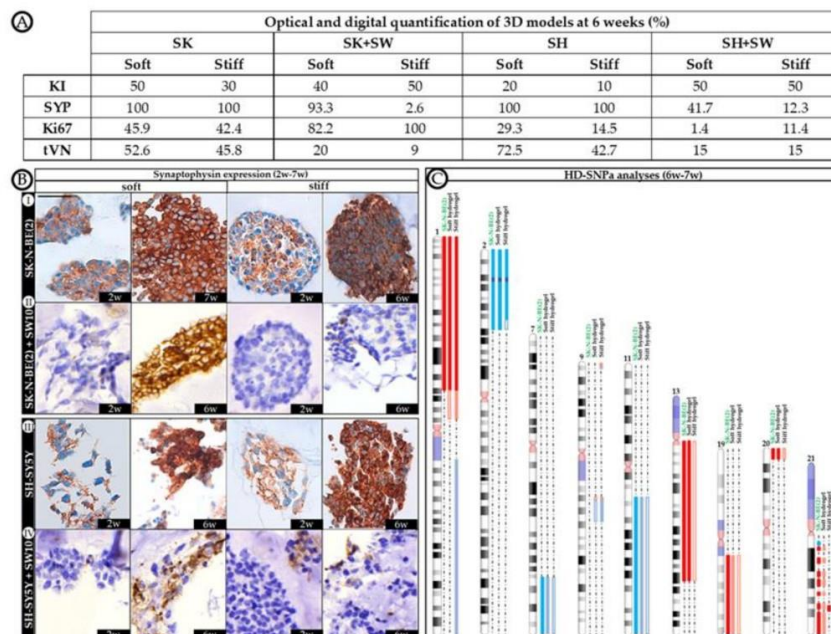


Figure 1. Morphological and genetic characterization of 3D models. (A) Optical and digital quantification of 3D models at 6 weeks. Quantifications were performed by digital image analysis, except for the karyorrhexis index (KI), which was obtained by optic microscopic assessment. Proportion of neuroblasts (data of neuroblasts in co-culture were obtained removing the proportion of non-expressing

synaptophysin cells, as we considered them SW10 cells) expressing synaptophysin (SYP), Ki67, tVN (territorial vitronectin strong staining expression) are detailed. **(B)** Immunostaining of synaptophysin in 3D models at short (2 weeks) and long (6–7 weeks) cell culture times. Scale bar 25 μm at top left of the first image. Same scale bar is valid for all images. **(C)** Genomic analyses. Schematic representation of the chromosomal aberrations differentially detected by HD-SNP α in soft and stiff hydrogels cultured with SK-N-BE(2) cell line over 6 weeks, and compared with SK-N-BE(2) cell line grown in 2D. For each altered chromosome, gains of genomic material are represented in blue, deletions in red, and *MYCN* amplification in purple. As the proportion of cells affected by the chromosomal aberrations decreases, their color becomes lighter. No genomic differences were observed between hydrogels grown with SK-N-BE(2) cell line alone and co-cultured with SW10 cell line in any of the studied conditions. Genomics of SH-SY5Y cells remained stable in every studied 3D condition, identical to that of 2D cultures [22].

2.1. Differential Effect of 3D Hydrogel Stiffness on Cell Proliferation in SK-N-BE(2) and SH-SY5Y NB Cell Lines

With the aim of characterizing the long-term effect of biomechanical properties on tumor aggressiveness, we cultured two different cell lines over long time spans in soft and stiff gelatin-based hydrogels to evaluate proliferation dynamics over time. We have previously shown that scaffolding stiffness increased SK-N-BE(2) cell proliferation during the 2nd to 4th week of culture [21]. Immunohistochemistry (IHC) analysis showed that proliferation dynamics differ completely from one cell line to another. SK-N-BE(2) cells appeared to be far more proliferative than SH-SY5Y cells in any condition studied, with a Ki67 proliferative index of 88.1% in stiff conditions at 4 weeks (Figure 2A). In particular, we could observe heightened proliferation of SK-N-BE(2) cells from the 2nd to 4th week (with proliferation indices of 17.9 to 70.1% and 34 to 88.1% for soft and stiff hydrogels, respectively), as previously described. Furthermore, as reported, this increase in proliferation was dependent on the stiffness of the substrate, with the neuroblasts on stiff hydrogels showing greater proliferation. Interestingly, we have now noticed that the SK-N-BE(2) cell proliferative index decreased from the 4th–5th week of culture, although this cell line remained proliferative even at the 12th week (15.7%). In comparison, SH-SY5Y cells displayed lower proliferative indices than SK-N-BE(2) cells, as already observed in 2D cultures (50 and 80% respectively), reaching up to 29.3% of proliferative cells in soft conditions at 6 weeks and with little proliferation observed after 12 weeks of culture (0.2%) (Figure 2C). SH-SY5Y cells in soft hydrogels achieved higher proliferative indices than in the stiffer ones, as opposed to SK-N-BE(2) cells.

2.2. The Contribution of Co-Cultured Stromal Schwann Cells to SK-N-BE(2) Proliferation Is Dependent on Substrate Stiffness

To recreate a more biomimetic tumor microenvironment, we co-cultured SK-N-BE(2) and SH-SY5Y NB cells with 10% Schwann cells and studied the contribution of the latter to NB cell line progression. Adding Schwann cells to SK-N-BE(2) cell cultures reduced proliferative indices in stiff hydrogels, while under soft hydrogel growth conditions the trend remained similar to that observed without co-culture (Figure 2B). However, the presence of Schwann cells in SH-SY5Y cell cultures hindered model proliferation, with 1.4% of Ki67 positive cells being the highest value observed across the time points studied (Figure 2D). Based on the SYP-positive population, we were able to determine the proportion of neuroblasts to total cells in co-cultured models from 6 weeks onwards, when genetic changes become more evident (Figure 1C). Furthermore, we determined the effect of SW10 cells on neuroblast proliferation according to the proportion of Ki67 positive neuroblasts (Figure 1A). Characterizing the neuroblast proportion in co-cultures at 6 weeks, we found that SK-N-BE(2) cells overtook the SW10 population proportionally in soft conditions (69.4% of neuroblasts). However, in stiff conditions, the proportion of neuroblasts remained very low (2.6%) and only overtook the Schwann cell population from 8 weeks onward (86.9% of neuroblasts).

Analyzing the specific effect of SW10 incorporation on neuroblast proliferation, we observed that SW10 increased the SK-N-BE(2) proliferation capacity (Figure 1A). Moreover, substrate stiffness determined the degree of proliferation in SK-N-BE(2) co-cultures, since only co-cultured neuroblasts in stiff conditions achieved full proliferation capacity (42.4% expected vs. 100% observed). SW10 cells reduced SH-SY5Y cell proliferation when co-cultured, especially in soft conditions (29.3% expected vs. 1.4% observed) and also reduced the proportion of neuroblasts (Figure 1A).

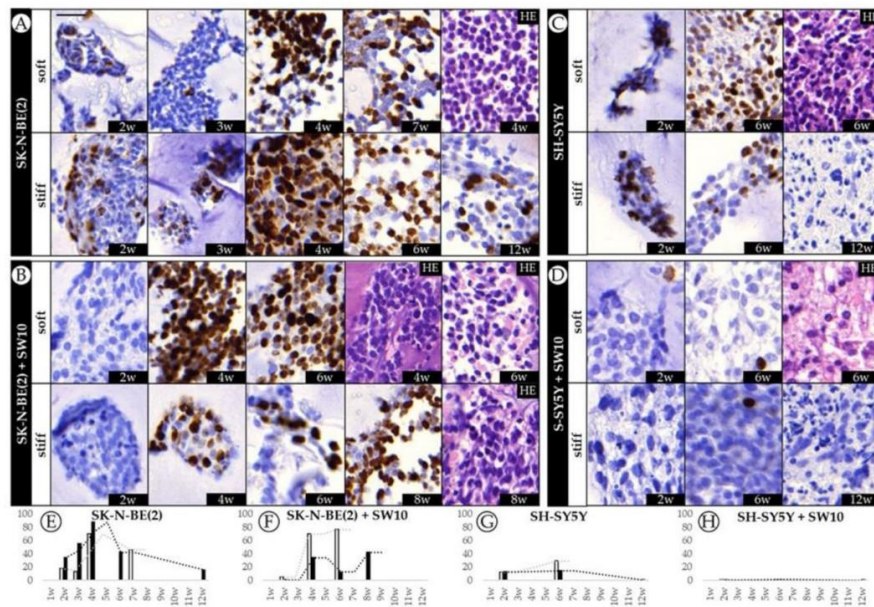


Figure 2. Dynamics of SK-N-BE(2) cell and SH-SY5Y cell proliferative indices over time. (A–D) Representative images of Ki67 expression at the time points studied (w: weeks) and hematoxylin eosin (HE) for each cell culture/co-culture in soft and stiff scaffolds. The images on the left correspond to the SK-N-BE(2) cell line cultivated (A) alone and (B) with mouse Schwann cell line (SW10); the images on the right represent the SH-SY5Y cell line cultivated (C) alone and (D) with SW10 cells. Scale bar 25 μ m at top left of the first image. Same scale bar is valid for all images. (E–H) Bar chart quantification of Ki67 staining (% of positive cells) for (E) SK-N-BE(2) cells and (F) SK-N-BE(2) cells plus SW10 cells in soft and stiff scaffolds, and for (G) SH-SY5Y cells and (H) SH-SY5Y cells plus SW10 cells in soft and stiff scaffolds. White and black bars: soft and stiff scaffolds, respectively. Dashed lines indicate moving average per stiffness condition. X axis: time in weeks (w) and Y axis: % of Ki67 positive cells.

2.3. Correlation between Mitosis–Karyorrhexis Index and Cell Number Differs with Growth Conditions

The cell proliferative index (Ki67 positivity) and cell number (number of cells, standardized by hydrogel area present at the slides) were established for comparison between conditions. In order to assess cell death, we determined the karyorrhexis index (the percentage of necrotic and apoptotic cells). Cell detachment was confirmed by the high number of cells found growing on the well surface when culture times were stopped in all conditions. In SK-N-BE(2) 3D hydrogels, as the proliferative index increased, the number of cells tended to stabilize. However, with similar proliferative indices, the number of cells was higher in soft than in stiff condition. In SK-N-BE(2) cell plus SW10 cell hydrogels, in general, there was a positive correlation between proliferation and cell number (the greater the proliferation, the higher the number of cells) (Figure 3). Interestingly, there was a correlation between the time and cell number, but not with proliferation, in both SH-SY5Y cells alone and SH-SY5Y cells plus SW10 cells: the longer the hydrogel culture time, the more cells were present. As opposed to SK-N-BE(2) models, stiffness increased the number of cells in SH-SY5Y cells alone and SH-SY5Y cells plus SW10 cells models. Finally, we found that high proliferative indices were observed in SK-N-BE(2)

both alone and co-cultured with SW10 did not yield an increase in the number of cells when compared with SH-SY5Y cultures.

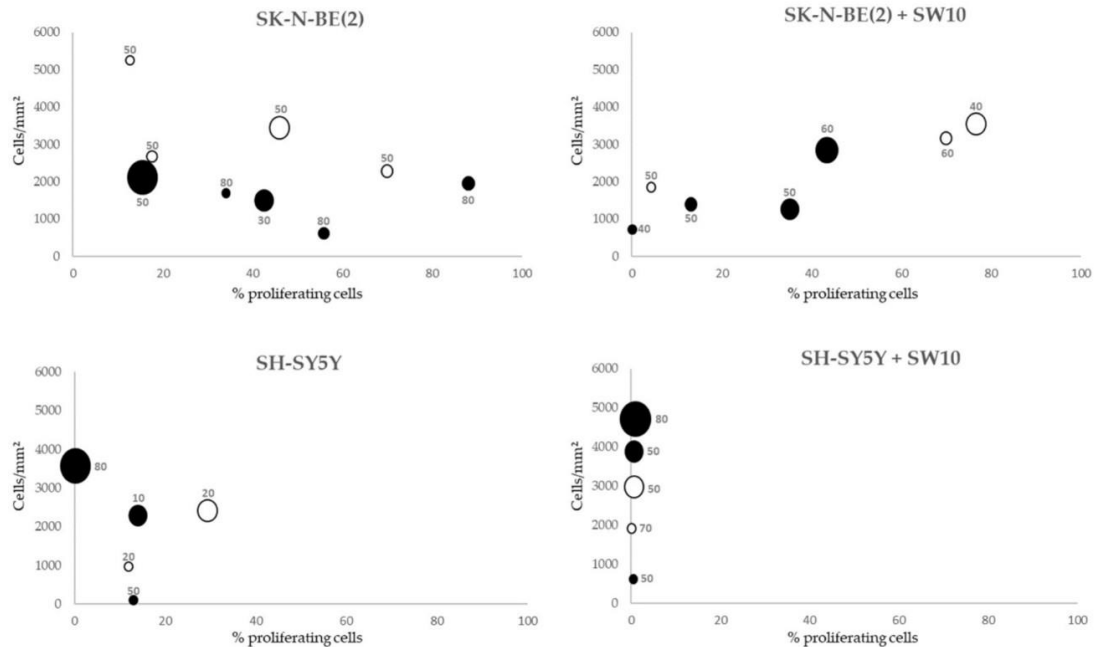


Figure 3. Correlation between proliferative index, cell number, and karyorrhexis index of each cell composition model and time of culture. White circles: soft models. Black circles: stiff models. Karyorrhexis index is shown for each culture condition. X axis: %Ki67 positive cells. Y axis: total number of cells/hydrogel area (mm²). Circle size is proportional to culture time (2 to 12 weeks).

According to the karyorrhexis index, SK-N-BE(2) cells presented a higher proportion of cell death ($55\pm 6\%$) than SH-SY5Y cells ($36\pm 13\%$) in their respective models, with the former reaching their maximum index in stiff conditions at the short cell culture time (80%). Furthermore, although the karyorrhexis index showed slight variations between both SK-N-BE(2) cell and SK-N-BE(2) cells and SW10 cell models in the different conditions, this index increased in SH-SY5Y cells plus SW10 cells models compared with SH-SY5Y cells models (Figure 3).

2.4. Differential 3D Culture Stimulation of tVN Expression Is Dependent on Cell Growth Conditions

Given that tVN is associated with an aggressive NB phenotype and proposed as a drug target, we aimed to characterize its dynamics over time. IHC results showed that tVN (high intensity staining) was greatly expressed in the cytoplasm and close pericellular space secreted by neuroblastic malignant cells in all 3D hydrogels regardless of their scaffold characteristics or cell composition, as opposed to 2D culture, where only neuroblasts expressed low cytoplasmic staining for VN. Interterritorial VN (low intensity staining) was considered as the ECM.

When SK-N-BE(2) cells were grown in 3D conditions, they reached high tVN expression levels (86.0 and 88.5% in soft and stiff hydrogels at the 2nd week) followed by a decrease in both soft and stiff conditions with just noticeable effect of stiffness on VN expression (Figure 4A). Although SH-SY5Y cells also increased their tVN expression when grown in 3D conditions (65.2 and 62.0% in soft and stiff hydrogels at the 2nd week), they mostly presented less tVN than SK-N-BE(2) cells. Interestingly, although SH-SY5Y stiff hydrogels followed a similar tVN expression dynamic as the SK-N-BE(2) ones over time, SH-SY5Y soft hydrogels slightly increased tVN expression from 2 to 6 weeks of cell culture (from 65.2 to 72.5%). In fact, at 6 weeks, there was a 30% difference in cell expression of tVN between soft and stiff scaffolds (Figure 4C).

SW10 cell co-culture reduced SK-N-BE(2) VN cell expression in all conditions when compared with SK-N-BE(2) cells grown alone. In both soft and stiff models VN expression was reduced from 2 to 6 weeks, particularly noticeable in the stiff ones. Remarkably, tVN expression increased at 8 weeks in cells grown in stiff hydrogels. In addition, SW10 cell co-culture contributed to the stiffness sensitivity of tVN malignant neuroblastic cell expression, which varied at each time point between soft and stiff hydrogels (Figure 4B). Adding SW10 cells also reduced SH-SY5Y cell VN expression, and as in SK-N-BE(2) cell plus SW10 cell hydrogels, soft and stiff models reduced in VN expression from 2 to 6 weeks with a final increase in tVN expression at 12 weeks in stiff hydrogels (Figure 4D).

Regarding neuroblast cell population assessment at 6 weeks co-culture (performed by SYP staining (Figure 1B)), we found that the tVN area was reduced in both cell lines when compared with cell lines cultured alone in both soft and stiff conditions (52.6% expected vs. 20% observed in soft and 45.8% expected vs. 9% observed in stiff conditions for SK-N-BE(2) and 72.5% expected vs. 15% observed in soft and 42.7% expected vs. 15% observed in stiff conditions for SH-SY5Y) (Figure 1A).

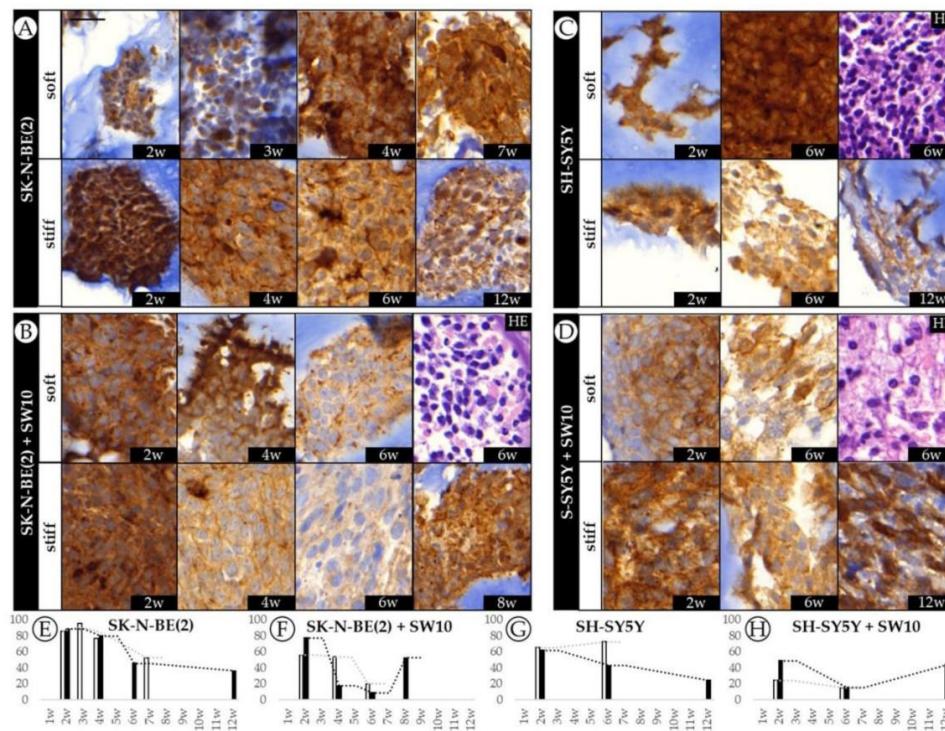


Figure 4. Dynamics of VN expression in SK-N-BE(2) and SH-SY5Y cell lines over time. (A–D) Representative images of VN expression at the time points studied (w: weeks) and hematoxylin eosin (HE) for each cell culture/co-culture in soft and stiff scaffolds. The images on the left correspond to the SK-N-BE(2) cell line cultivated (A) alone and (B) with SW10; the images on the right represent the SH-SY5Y cell line cultivated (C) alone and (D) with SW10 cells. Scale bar 25 μ m at top left of the first image. Same scale bar is valid for all images. (E–H) Bar chart quantification of VN staining (% of stained area) for SK-N-BE(2) cells (E) alone and (F) SK-N-BE(2) cells plus SW10 cells in soft and stiff scaffolds, and SH-SY5Y cells (G) alone and (H) S-SY5Y cells plus SW10 cells in soft and stiff scaffolds. White and black bars: soft and stiff scaffolds, respectively. Dashed lines indicate moving average per stiffness condition. X axis: time in weeks (w) and Y axis: % of VN stained area.

2.5. Co-Culture Condition with SW10 Modifies DOCK8 Expression Dynamics

Subjective quantification detected only very low levels of DOCK8 staining in both SK-N-BE(2) and SH-SY5Y 2D cell cultures and high expression in SW10 cells.

When we analyzed SK-N-BE(2) cells in 3D hydrogels, we also observed very low levels of DOCK8 expression, with an unexpected slight increase at 12 weeks in stiff hydrogels (Figure 5A). In addition, SH-SY5Y cells showed a remarkable increase in DOCK8 expression at 12 weeks in stiff hydrogels (42.2%), coinciding with the time point when there was almost no proliferation (0.2% of Ki67-positive cells).

Co-culture of SK-N-BE(2) cells with SW10 cells led to greater expression of DOCK8 in the hydrogel cells, decreasing over time (from 47.3 to 6.1% in soft and 58.6 to 0.8% in stiff hydrogels) in which the soft hydrogels were affected earlier (Figure 5B). Finally, when comparing SH-SY5Y to SH-SY5Y plus SW10, we observed that over 50% of cells expressed DOCK8 at every given condition of the latter models. Furthermore, with stiffness and time, DOCK8 positive cells in SH-SY5Y plus SW10 cells model were prominent at the outer edge of many necrotic clusters (4D).

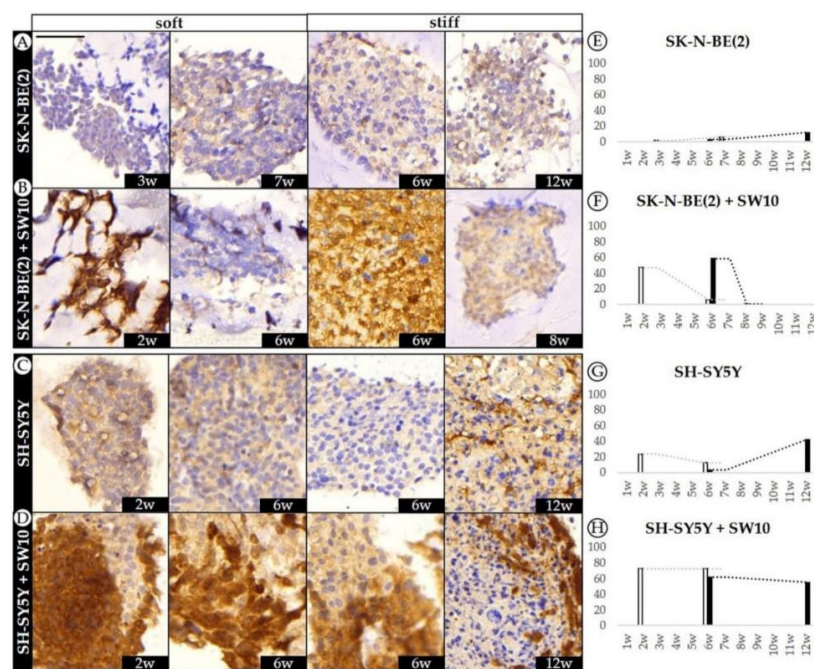


Figure 5. Dynamics of DOCK8 expression pattern in SK-N-BE(2) and SH-SY5Y over time. (A–D) Representative images of DOCK8 expression at the time points studied (w: weeks) in soft and stiff scaffoldings. Top images correspond to the SK-N-BE(2) cell line cultivated (A) alone and (B) with SW10; the images on the bottom represent the SH-SY5Y cell line cultivated (C) alone and (D) with SW10 cells. Scale bar 50 μ m at top left of the first image. Same scale bar is valid for all images. (E–H) Bar chart quantification of DOCK8 staining (% of positive cells) for SK-N-BE(2) cells (E) alone and (F) SK-N-BE(2) cells plus SW10 cells in soft and stiff scaffoldings, and SH-SY5Y cells (G) alone and (H) SH-SY5Y cells plus SW10 cells in soft and stiff scaffoldings. White and black bars: soft and stiff scaffoldings, respectively. Dashed lines indicate moving average per stiffness condition. X axis: time in weeks (w) and Y axis: % of positive DOCK8 cells.

2.6. Robust Expression of KANK1 in Models Including SH-SY5Y Cells Correlates Negatively with Proliferation

KANK1 was broadly expressed among NB cell lines SK-N-BE(2) and SH-SY5Y in 2D as well as in 3D hydrogels (Figure 6). SW10 cells also appeared positive in 2D cultures and 3D co-cultured hydrogels.

In SK-N-BE(2) cells, KANK1 expression increased 52.2% from 3rd to 7th week (from 21.6 to 73.8%), unveiling the effect of culturing time on KANK1 immunostaining in soft hydrogels. However, KANK1 expression remained high when comparing stiff hydrogels from 6th to 12th week with a decrease of only 2% (from 69.0 to 67.0%). Moreover, no significant difference in KANK1 expression was observed at the 6th week due to stiffness variation (Figure 6A). In 3D cultured SH-SY5Y cells, the proportion

of KANK1 highly positive cells was above 50% in all studied conditions, with a similar range to SK-N-BE(2) cells. We observed a slight increase of 8.6% in KANK1 expression comparing soft versus stiff hydrogels at 6 weeks (from 51.8 to 60.4% respectively). In addition, contrary to SK-N-BE(2) cell hydrogels, the proportion of KANK1 positive cells remained fairly constant over time in SH-SY5Y soft hydrogels (54.2 to 51.8% for 2 and 4 weeks, respectively) and displayed an increase of 13.8% of positive cells when grown in stiff hydrogels cultured up to 12 weeks (from 60.4 to 74.2%) (Figure 6C).

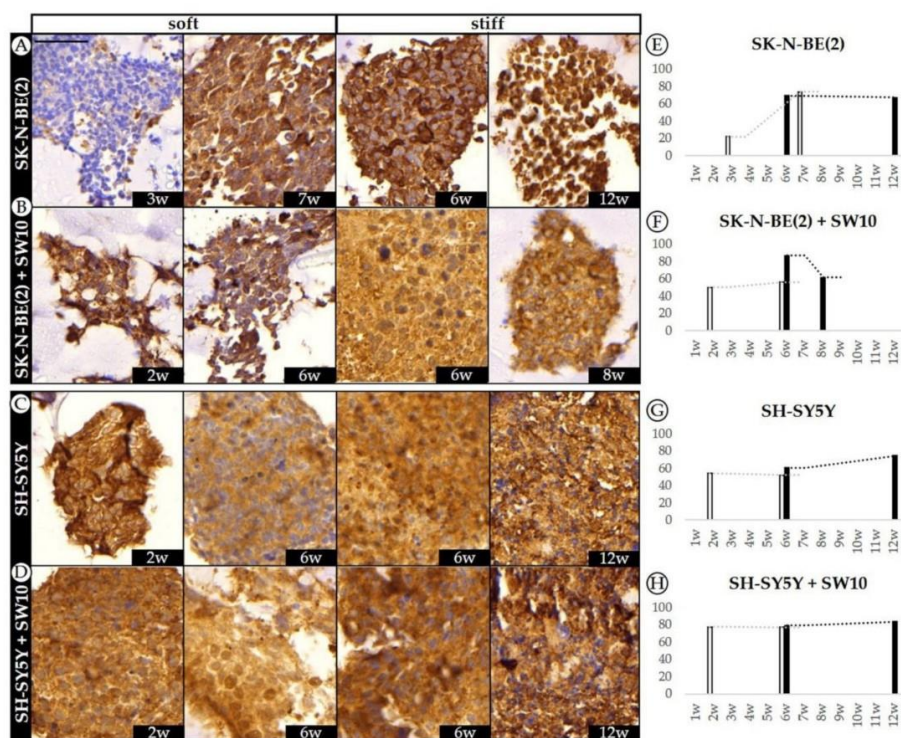


Figure 6. Dynamics of KANK1 expression pattern in SK-N-BE(2) and SH-SY5Y over time. (A–D) Representative images of KANK1 expression at the time points studied (w: weeks) in soft and stiff scaffoldings. The top images correspond to the SK-N-BE(2) cell line cultivated (A) alone and (B) with SW10; the images at the bottom represent the SH-SY5Y cell line cultivated (C) alone and (D) with SW10 cells. Scale bar 50 μ m at top left of the first image. Same scale bar is valid for all images. (E–H) Bar chart quantification of KANK1 staining (% of positive cells) for SK-N-BE(2) cells (E) alone and (F) SK-N-BE(2) cells plus SW10 cells in soft and stiff scaffolds, and SH-SY5Y cells (G) alone and (H) SH-SY5Y cells plus SW10 cells in soft and stiff scaffolds. White and black bars: soft and stiff scaffolds, respectively. Dashed lines indicate moving average per stiffness condition. X axis: time in weeks (w) and Y axis: % of KANK1 positive cells.

On addition of SW10 cells to SK-N-BE(2) cell line cultures, the observed culturing time effect in soft SK-N-BE(2) hydrogels was lost and KANK1 expression increased only slightly from 50 to 56%. Moreover, comparing KANK1 expression at 6 weeks of growth, we observed increasing KANK1 positive cells from 56.0 to 86.9% with stiffness. Although KANK1 expression appeared higher in stiff hydrogels, there was a decrease in expression over time from 86.9 to 61.4% when compared at 6 and 8 weeks, respectively (Figure 6B). In SH-SY5Y cells co-cultured with SW10 cells, KANK1 expression was increased in comparison with SH-SY5Y hydrogels. In these models, 3D hydrogel stiffness only slightly modified the cell expression of KANK1 with variations not higher than 6% even when comparing extreme conditions (soft hydrogel at 2 weeks versus stiff hydrogel at 12 weeks) (Figure 6D).

3. Discussion

Tumors are complex structures, made up of malignant cells coexisting within the stromal framework, including immune, lymphatic, and vascular endothelial cells [41,42]. The non-malignant cell population, together with the different molecules forming the stroma tissue such as GAGs, proteins, and glycoproteins, notably influence overall tumor cell behavior [42]. To study the effect of each of these components both individually and collectively, it is necessary to design artificial models that gradually increase in complexity. Three-dimensional bioprinting-related technologies already allow us to construct complex living structures with great precision, to the point of being able to generate tissue parts of functional organs such as the corneas or alveoli [43]. This technology is therefore ideal to improve current cancer modelling and for future development of artificial tumors with identical features to their *in vivo* counterparts. However, in order to faithfully recreate these tumors in 3D *in vitro* models, we must use biocompatible inks that enable not only malignant cell growth but also co-culture with non-malignant cells. The latter will contribute to synthesize and consolidate the tumor's own matrix, which will ultimately replace the fabricated scaffold [44]. We generated different co-cultures with Schwann stromal cells as a first approach to mimicking NB complexity, which allowed us to evaluate the effect of the Schwann cells by comparison with the non-co-culture models. Moreover, these models are useful for conducting preclinical therapeutic trials, as they can be used to establish analyzable parameters through which to characterize the pathophysiological importance of tumor components and evaluate treatment responses [45]. As proof of concept, we selected Ki67, SYP, VN, DOCK8, and KANK1 expression for study, to give us an overview of tumor cell behavior from different biological perspectives, such as proliferation, aggressiveness, and migration-related protein synthesis, as well as consequences in terms of ECM remodeling and gene tumor suppression [27,28,33,38]. Finally, it is worth underlining the importance of having used analytical methodology to interpret the immunocytochemical data and to link it with previous genetic results; we chose digital image analysis, as it provides objective, quantifiable, and automatized information previously validated by the pathologist's morphological assessment performed with digital imaging.

Ki67 evaluation revealed that SK-N-BE(2) cells proliferated more than SH-SY5Y cells on the models, indicating that the former exhibit a more aggressive phenotype. This is consistent with the presence of *MYCN* oncogene amplification in SK-N-BE(2) cells [46,47]. Moreover, the *ALK*-mutated SH-SY5Y cell line displayed low proliferation, but the cell population appeared similar to SK-N-BE(2), indicating good adaptation to the imposed growth conditions, since SH-SY5Y presented a lower karyorrhexis index than SK-N-BE(2), which could be related to an increased frequency of *ALK* mutations at a relapse of neuroblastoma. This finding highlights the importance of the ECM in tumor cell growth and behavior. Therefore, SH-SY5Y cells reach optimal growth in other models with different compositions [48,49] and including additional non-malignant cell populations in the models could help to generate the proper growth conditions for SH-SY5Y. SK-N-BE(2) and SH-SY5Y cells not only have diverse proliferation levels but also present dissimilar proliferation dynamics, since the substrate stiffness tends to increase proliferation in SK-N-BE(2) but not in SH-SY5Y. These data could be related to the differences observed in their genetic profile, which would indicate that stiffness has a strong effect on SK-N-BE(2). In fact, after 6 weeks of stiffness surroundings, new segmental chromosomal aberrations such as 9p (where DOCK8 and KANK1 genes are located) started to appear in SK-N-BE(2) but not in SH-SY5Y [22]. Further tests in other NB cell lines are warranted to evaluate whether the effect of stiffness on *MYCN*- and non-*MYCN*-amplified cells can be generalized. SW10 inclusion generally hindered proliferation in the models due to the fact that these cells are not as proliferative as NB tumor cells, and their presence thus reduced the overall proliferative index [50]. Nevertheless, differences found between the two co-cultures indicate that in soft hydrogels, SK-N-BE(2) cells can still grow and coexist with Schwann, but in stiff hydrogels, the Schwann cells overtake in proportion at 6 weeks of culture, with an increase in proliferative neuroblasts at 8 weeks of culture. Meanwhile, in SH-SY5Y cell co-cultures, there is a notable SW10-mediated proliferation decrease caused by the above-mentioned mechanisms. The data

presented suggest that the stiffness of the 3D hydrogels could determine the degree to which Schwann cells affect malignant cell proliferation and karyorrhexis [49].

Cell growth is the result of excess proliferation over karyorrhexis. However, given the high SK-N-BE(2) proliferative indices, we would expect greater population growth than observed when compared to SH-SY5Y cultures. One plausible explanation could be different cell detachment from the scaffold occurring during cell cultures. In addition, the reduced proportion of cells present in highly proliferative models can be explained by processes such as maximal proliferation, reduced clone adaptation, or an asynchronous balance between proliferation and karyorrhexis and/or cellular metabolism, since metabolic reprogramming must occur in order for cells to regulate cell growth, proliferation, and death [51]. Under this hypothesis, during the earliest cell culture time points, there would be a balance between proliferation of cells successfully adapting to the culture conditions and death of those unable to adapt. Subsequently, at longer cultivation times, cell metabolism would focus on other aggressive aspects such as migration, leaving proliferation aside. Nevertheless, this SK-N-BE(2) cell behavior would not accurately represent *in vivo* behavior without the presence of Schwann cells, highlighting the need to perform co-cultures in cancer models. Conversely, no correlation was found between proliferation and cell number in either SH-SY5Y model. Nonetheless, the time-related increase in cell numbers observed confirms the low cell proliferative index in these models and slow adaptation to imposed growth conditions, with less karyorrhexis and potentially lower cluster detachment events, which may account for the number of cells found in these models.

The high tVN expression found in 3D models demonstrates their usefulness compared to traditional models (VN expression in 2D cultures is scarce), as they better recreate the conditions found *in vivo*. The different tVN dynamics observed in 3D cultures seem to be determined by the specific needs of each cell line. Despite these slight variations, tVN expression is notable from the beginning of the cell culture in all the 3D models, exhibiting generally reduced (yet higher than in 2D culture) synthesis over time, which could be indicative of its key role not only in migration but also during the initial cell adaptation process. Interestingly, in the most clinically relevant models, those co-cultivated with SW10 cells, tVN expression levels are lower across all time points but increase at final culture times. This could be interpreted as an additional migration-related tVN role, which becomes apparent in those specific models, better recreating the metastatic pathways previously described in *in vivo* conditions [19].

Our results as regards DOCK8 expression dynamics support its cell migration role [31–33]. Data from SH-SY5Y cell and SH-SY5Y cell plus SW10 cell models correlate with a first stage of cell proliferation followed by a second stage where cells stop dividing in order to express migration-related mechanisms. Moreover, the elevated DOCK8 expression at longer culture time points in both SK-N-BE(2) and SH-SY5Y cells could also be indicative of cellular adaptation towards the migration process, which is further supported by the appearance of DOCK8 positive cells in the surroundings of necrotic clusters. On the other hand, taken together with Ki67 data, DOCK8 analysis in SW10 cell co-cultured models indicated that SK-N-BE(2) takes over in proportion in the conditions with low DOCK8 levels, as indicated by elevated proliferation and the proportion of SYP positive stained cells, which is also consistent with the fact that SK-N-BE(2) do not express high levels of DOCK8. When considering SH-SY5Y cell plus SW10 cell models, data confirm that SH-SY5Y cells have low proliferation capacity and that SW10 cells overtake in proportion. However, although we noted that SW10 cells expressed high amounts of DOCK8 in 2D cultures, we could not exclusively attribute the DOCK8 expression to SW10 cells, since some SH-SY5Y cells by themselves were also capable of expressing DOCK8.

KANK1 expression was found to be highly expressed in every condition, in a stable and robust way. The few differences observed between models show that scaffold stiffness and SW10 inclusion play different roles depending on the cultured tumor cell line. Although the KANK1 data could support the notion of a cell migration stage following on from a cell adaptation and proliferation process, the few variations found in KANK1 expression, together with its multiple functions, necessitate functional studies to determine the specific role that this gene plays in NB tumors.

Taken together, the data herein show that physiologically relevant 3D tissue-engineered neuroblastoma cell models can be successfully developed and characterized using gelatin-based scaffolds, demonstrating their potential as tools to elucidate cell behavior and for new drug development. Performing co-cultures with SW10 has been shown to modify malignant cell action towards improved pathophysiological mimicking [50]. These models will also allow us to increase the complexity of the system by adding other cell types, such as mesenchymal stem cells or cells of the immune system. This creates a more physiologically relevant *in vitro* scenario [44], always provided that the presence and behavior of each cell group included in the model can be identified and monitored. Further, the influence of cellular genetics during model development can be assessed in these platforms to predict the behavior of similar patient-derived cells. In the future, when optimal scaffolds can be generated for patient cell growth, these specifically adapted scaffold conditions will be required to carry out the corresponding preclinical therapeutic studies.

4. Materials and Methods

4.1. Cell Culture

SK-N-BE(2), SH-SY5Y human NB cell lines were chosen from a variety of available cell lines, since *MYCN*-amplified and *ALK*-mutated tumors represent 64% of high risk neuroblastoma (50 and 14%, respectively). SK-N-BE(2), SH-SY5Y, and SW10 mouse Schwann cell lines were acquired from American Type Culture Collection (ATCC, Manassas, VA, USA). NB cells were expanded in supplemented IMDM medium (Gibco, Life Technologies, Waltham, MA, USA) and SW10 in supplemented DMEM (Gibco, Life Technologies, Waltham, MA, USA) at 37 °C and 5% CO₂ atmosphere. Two dimensional cell cultures were grown in 8-well Cell Culture Slides (SPL Life Sciences, Waltham, MA, USA), until they reached 60% confluence before immunocytochemistry (ICC) analysis. Bioinks for 3D culture were formed by mixing SK-N-BE(2) or SH-SY5Y cells with the prepolymer solution at 37 °C to a final solution of 2×10^6 mL⁻¹, as previously reported [21], including in some cases, an additional 2×10^5 mL⁻¹ of SW10 cells. Hydrogels were cultured from 2 to 12 weeks in supplemented IMDM medium replaced every 2 or 3 days before immunohistochemistry (IHC) analysis.

4.2. Synthesis of Hydrogels

Composite hydrogels were synthesized using gelatin and alginate, as previously described [21,52]. Prepolymer solutions were prepared to obtain final concentrations of 5% *w/v* methacrylated gelatin (GelMA) and 0–0.5% (soft) or 1.5–2% (stiff) methacrylated alginate (AlgMA), according to the desired initial stiffness level. The bioink with the cells was loaded in a bioprinting syringe and gelified at –20 °C for 3 min before printing. All hydrogels were fabricated using a 3D bioprinter (3DDiscovery BioSafety, RegenHU, Villaz-St-Pierre, Switzerland; 365 nm, 3 W cm⁻²) and polymerized with UV light, as previously reported [21,52].

4.3. Immunocytochemistry and Immunohistochemistry

ICC stains were performed with anti-Ki67 (prediluted, Agilent Technologies, Santa Clara, CA, USA), anti-VN (1/100, Abcam, Cambridge, UK), anti-DOCK8 (1/700, Invitrogen, Life Technologies, Waltham, MA, USA), anti-KANK1 (1/1000, Invitrogen, Life Technologies, USA), and anti-SYP (prediluted, Dako, Glostrup, Denmark) antibodies. Anti-Ki67 labeling (nuclear staining) (Autostainer Link 48; Dako, Glostrup, Denmark), anti-VN labeling (cytoplasm and extracellular staining) (BenchMark XT, Ventana Medical Systems Inc., Tucson, AZ, USA), and anti-SYP labeling (cytoplasm staining) (Autostainer Link 48; Dako, Glostrup, Denmark) were automatically performed, while anti-DOCK8 (membrane, cytoplasm, and nuclear staining in normal cells) and anti-KANK1 (membrane, cytoplasm, and nuclear staining in normal cells) were done manually. Four percent formaldehyde and paraffin-embedded hydrogels were cut into 3 μm sections. IHC stains were performed as indicated above, including an antigen retrieval step using the corresponding buffer for each antibody (PT Link instrument,

Agilent, Santa Clara, CA, USA). All markers were evaluated by optical microscopy using the following criteria: negative (–, <1% positive cells); low positive (+, 1–20% positive cells); intermediate positive (++, 20–50% positive cells); high positive (+++, >50% positive cells); and by digital image analysis. Hematoxylin–eosin stained samples were used to evaluate karyorrhexis index and cell detachment from 3D hydrogels (after trypsinization of the wells used for 3D cultures) by optical microscopy evaluation.

4.4. Image Analysis

IHC stained slides were digitized with the whole-slide Panoramic MIDI scanner (3DHISTECH Ltd., Budapest, Hungary) at 20× magnification. Digital image analysis was performed on whole sample areas, excluding only detected artefacts and folded and/or broken regions, which were considered uninformative. Ki67, SYP, KANK1, and DOCK8 were analyzed automatically using Panoramic Viewer (PV) software (3DHISTECH), and their number of positive cells were determined by applying the NuclearQuant module. This module could be applied to non-nuclear stained samples by adjusting nucleus size settings to detect entire cells when required (nuclear radius 3–15 µm) and adjusting color deconvolution settings. HistoQuant module of PV was applied in VN-stained sections to obtain the areas of each VN intensity expression. All data obtained from PV modules were validated with pathologist’s morphological assessment of the digital image. Digitally obtained data and subsequent pathologist evaluation differed by only 5–10%.

4.5. Data Treatment

For Ki67, SYP, DOCK8, and KANK1 expression-related analysis, digital positive cell percentages were compared for each condition under study. We calculated the percentage of positive cells in each sample, considering as positive cells only those with digitally detected medium and high intensity expression. By considering low intensity expression as negative cells, we avoided including artifacts and unspecific staining areas in the analysis.

As previously described in our group [20], tVN intensity is higher than interterritorial VN. The tVN quantification was performed by calculating the percentage of strong staining intensity, territorial location, and H-score ≥ 180 from the total VN stain according to PV detection. Population cell growth was assessed correlating cell proliferative index (Ki67 positivity), cell number (number of cells, standardized by hydrogel area in mm² for comparison between conditions), and culturing time.

In order to characterize the SW10 vs. the neuroblast population, we used SYP as a differential marker between SW10 and neuroblastic cells since both SK-N-BE(2) and SH-SY5Y cell lines were 100% positive and SW10 negative. Since Ki67 and tVN are expressed only by the NB cells, we assumed that all the quantified staining belonged to NB cells. Therefore, we used the percentage of SYP to normalize the neuroblast population in co-cultured models and assessed the specific effect of SW10 in the neuroblastic cells (Figure 1A).

5. Conclusions

The tools presented in this study provide the data for successful development and characterization of pathophysiologically relevant 3D tissue-engineered neuroblastoma cell models. Through 3D bioprinted gelatin-based scaffolds, we were able to determine and study the effect of stiffness on SK-N-BE(2) and SH-SY5Y neuroblastoma cell lines. We generated the models using bioinks in order to study the more complex spheroid cells. Adding stromal SW10 cells in the bioink allowed co-culture with malignant neuroblastic cells, creating a biocompatible niche where cells could grow over long periods of time and recapitulate tumor-specific organization. We present robust and detailed phenotypic characterization of 3D models, based on objective immunostaining quantification using digital image analysis pipelines. As proof of concept, we selected Ki67, SYP, VN, DOCK8, and KANK1 expression, which are pivotal for study, as they provide an overview of tumor cell behavior from different biological perspectives such as proliferation, aggressiveness, and migration-related protein synthesis and consequences in terms of ECM remodeling and gene tumor suppression.

Author Contributions: Conceptualization, R.N. and J.S.; methodology, E.M., A.G.-L., and S.M.-V.; software, E.M. and S.S.; validation, R.N. and S.N.; formal analysis, E.M. and S.S.; investigation, E.M., S.S., S.M.-V., R.B.-P., and A.L.-C.; data curation, E.M. and S.S.; writing—original draft preparation, E.M., S.S.; writing—review and editing, R.N., S.N., A.L., R.B.-P., and S.M.-V.; supervision, R.N. All authors have read and agreed to the published version of the manuscript.

Funding: E.M. is supported by the Asociación Fundación Española contra el Cáncer, JAP-AECC (2018/150). This research was funded by ISCIII (FIS) and FEDER (European Regional Development Fund), grant number PI17/01558; Collaborative Project CIBERONC-CIBERBBN, grant number ONC18PI03 and NEN Association (Nico contra el cáncer infantil, grant number 2017-PVR00157). The APC was funded by CIBERONC (contract CB16/12/00484).

Acknowledgments: The authors thank Elisa Alonso, Miriam Funes, Esther Álvarez, Luis Alfaro, and Isaac Vieco-Martí for their valuable technical support and Kathryn Davies for English correction.

Conflicts of Interest: The authors declare no conflict of interest.

Abbreviations

ECM	extracellular matrix
IHC	immunohistochemistry
PV	Pannoramic Viewer
SW10	mouse Schwann cell line
SYP	synaptophysin
NB	neuroblastoma
VN	vitronectin
2D	2 dimensional
3D	3 dimensional

References

- Doyle, A.D.; Yamada, K.M. Mechanosensing via cell-matrix adhesions in 3D microenvironments. *Exp. Cell Res.* **2016**, *343*, 60–66. [[CrossRef](#)]
- Frantz, C.; Stewart, K.M.; Weaver, V.M. The extracellular matrix at a glance. *J. Cell Sci.* **2010**, *123*, 4195–4200. [[CrossRef](#)]
- Wells, R.G. The role of matrix stiffness in regulating cell behavior. *Hepatology* **2008**, *47*, 1394–1400. [[CrossRef](#)]
- Pickup, M.W.; Mouw, J.K.; Weaver, V.M. The extracellular matrix modulates the hallmarks of cancer. *EMBO Rep.* **2014**, *15*, 1243–1253. [[CrossRef](#)]
- Xiong, G.-F.; Xu, R. Function of cancer cell-derived extracellular matrix in tumor progression. *J. Cancer Metastasis Treat.* **2016**, *2*, 357. [[CrossRef](#)]
- Estofotele, C.F.; Botelho-Machado, C.; Taboga, S.R.; Zucoloto, S.; Polli-Lopes, A.C.; Gil, C.D. Effects of myenteric denervation on extracellular matrix fibers and mast cell distribution in normal stomach and gastric lesions. *Cancer Cell Int.* **2010**, *10*, 18. [[CrossRef](#)]
- Giraldo, N.A.; Sanchez-Salas, R.; Peske, J.D.; Vano, Y.; Becht, E.; Petitprez, F.; Validire, P.; Ingels, A.; Cathelineau, X.; Fridman, W.H.; et al. The clinical role of the TME in solid cancer. *Br. J. Cancer* **2019**, *120*, 45–53. [[CrossRef](#)]
- Kenny, P.A.; Bissell, M.J. Tumor reversion: Correction of malignant behavior by microenvironmental cues. *Int. J. Cancer* **2003**, *107*, 688–695. [[CrossRef](#)]
- Lejeune, M.; Álvaro, T. Clinicobiological, prognostic and therapeutic implications of the tumor microenvironment in follicular lymphoma. *Haematologica* **2009**, *94*, 16–21. [[CrossRef](#)]
- Lv, D.; Hu, Z.; Lu, L.; Lu, H.; Xu, X. Three-dimensional cell culture: A powerful tool in tumor research and drug discovery (Review). *Oncol. Lett.* **2017**, *14*, 6999–7010. [[CrossRef](#)]
- Fan, C.; Wang, D.-A. Macroporous Hydrogel Scaffolds for Three-Dimensional Cell Culture and Tissue Engineering. *Tissue Eng. Part B Rev.* **2017**, *23*, 451–461. [[CrossRef](#)]
- Huang, Y.; Zhang, X.-F.; Gao, G.; Yonezawa, T.; Cui, X. 3D bioprinting and the current applications in tissue engineering. *Biotechnol. J.* **2017**, *12*, 1600734. [[CrossRef](#)]

13. Tadeo, I.; Berbegall, A.P.; Castel, V.; García-Miguel, P.; Callaghan, R.; Pählman, S.; Navarro, S.; Noguera, R. Extracellular matrix composition defines an ultra-high-risk group of neuroblastoma within the high-risk patient cohort. *Br. J. Cancer* **2016**, *115*, 480–489. [[CrossRef](#)]
14. Tadeo, I.; Berbegall, A.P.; Navarro, S.; Castel, V.; Noguera, R. A stiff extracellular matrix is associated with malignancy in peripheral neuroblastic tumors. *Pediatr. Blood Cancer* **2017**, *64*, e26449. [[CrossRef](#)]
15. Tadeo, I.; Gamero-Sandemetrio, E.; Berbegall, A.P.; Gironella, M.; Ritort, F.; Cañete, A.; Bueno, G.; Navarro, S.; Noguera, R. Lymph microvascularization as a prognostic indicator in neuroblastoma. *Oncotarget* **2018**, *9*, 26157–26170. [[CrossRef](#)]
16. Tadeo, I.; Gamero-Sandemetrio, E.; Berbegall, A.P.; Navarro, S.; Cañete, A.; Noguera, R. 1p36 Deletion Results in a Decrease in Glycosaminoglycans Which Is Associated with Aggressiveness in Neuroblastic Tumors. *Histol. Histopathol.* **2018**, *33*, 487–495.
17. Park, J.R.; Eggert, A.; Caron, H. Neuroblastoma: Biology, Prognosis, and Treatment. *Hematol. Clin. N. Am.* **2010**, *24*, 65–86. [[CrossRef](#)]
18. Kruger, T.M.; Bell, K.J.; Lansakara, T.I.; Tivanski, A.V.; Doorn, J.A.; Stevens, L.L. A Soft Mechanical Phenotype of SH-SY5Y Neuroblastoma and Primary Human Neurons Is Resilient to Oligomeric A β (1–42) Injury. *ACS Chem. Neurosci.* **2020**, *11*, 840–850. [[CrossRef](#)]
19. Vicente-Munuera, P.; Burgos-Panadero, R.; Noguera, I.; Navarro, S.; Noguera, R.; Escudero, L.M. The topology of vitronectin: A complementary feature for neuroblastoma risk classification based on computer-aided detection. *Int. J. Cancer* **2019**, *146*, 553–565. [[CrossRef](#)]
20. Burgos-Panadero, R.; Noguera, I.; Cañete, A.; Navarro, S.; Noguera, R. Vitronectin as a molecular player of the tumor microenvironment in neuroblastoma. *BMC Cancer* **2019**, *19*, 479. [[CrossRef](#)]
21. Monferrer, E.; Martín-Vañó, S.; Carretero, A.; García-Lizarribar, A.; Burgos-Panadero, R.; Navarro, S.; Samitier, J.; Noguera, R. A three-dimensional bioprinted model to evaluate the effect of stiffness on neuroblastoma cell cluster dynamics and behavior. *Sci. Rep.* **2020**, *10*, 6370. [[CrossRef](#)] [[PubMed](#)]
22. López-Carrasco, A.; Martín-Vañó, S.; Burgos-Panadero, R.; Monferrer, E.; Berbegall, A.P.; Fernández-Blanco, B.; Navarro, S.; Noguera, R. Impact of Extracellular Matrix Stiffness on Genomic Heterogeneity in MYCN-Amplified Neuroblastoma Cell Line. *J. Exp. Clin. Cancer Res.* **2020**, *39*, 226. [[CrossRef](#)] [[PubMed](#)]
23. Brodeur, G.M.; Seeger, R.C.; Schwab, M.; Varmus, H.E.; Bishop, J.M. Amplification of N-myc in untreated human neuroblastomas correlates with advanced disease stage. *Science* **1984**, *224*, 1121–1124. [[CrossRef](#)] [[PubMed](#)]
24. Chen, Y.; Takita, J.; Nakagawara, A.; Hayashi, Y.; Mano, H.; Ogawa, S.; Choi, Y.L.; Kato, M.; Ohira, M.; Sanada, M.; et al. Oncogenic mutations of ALK kinase in neuroblastoma. *Nature* **2008**, *455*, 971–974. [[CrossRef](#)]
25. Bunimovich, Y.L.; Keskinov, A.A.; Shurin, G.V.; Shurin, M.R. Schwann cells: A new player in the tumor microenvironment. *Cancer Immunol. Immunother.* **2017**, *66*, 959–968. [[CrossRef](#)]
26. McCormick, D.; Chong, H.; Hobbs, C.; Datta, C.; Hall, P.A. Detection of the Ki-67 antigen in fixed and wax-embedded sections with the monoclonal antibody MIB1. *Histopathology* **1993**, *22*, 355–360. [[CrossRef](#)]
27. Scott, R.J.; Hall, P.A.; Haldane, J.S.; Van Noorden, S.; Price, Y.; Lane, D.P.; Wright, N.A. A comparison of immunohistochemical markers of cell proliferation with experimentally determined growth fraction. *J. Pathol.* **1991**, *165*, 173–178. [[CrossRef](#)]
28. Schneider, G.; Bryndza, E.; Poniewierska-Baran, A.; Serwin, K.; Suszynska, M.; Sellers, Z.P.; Merchant, M.L.; Kaliappan, A.; Ratajczak, J.; Kucia, M.; et al. Evidence that vitronectin is a potent migration-enhancing factor for cancer cells chaperoned by fibrinogen: A novel view of the metastasis of cancer cells to low-fibrinogen lymphatics and body cavities. *Oncotarget* **2016**, *7*, 69829–69843. [[CrossRef](#)]
29. Shi, K.; Lan, R.-L.; Tao, X.; Wu, C.-Y.; Hong, H.-F.; Lin, J.-H. Vitronectin significantly influences prognosis in osteosarcoma. *Int. J. Clin. Exp. Pathol.* **2015**, *8*, 11364–11371.
30. Felding-Habermann, B.; O’Toole, T.E.; Mueller, B.M.; Smith, J.W.; Fransvea, E.; Ruggeri, Z.M.; Ginsberg, M.H.; Hughes, P.E.; Pampori, N.; Shattil, S.J.; et al. Integrin activation controls metastasis in human breast cancer. *Proc. Natl. Acad. Sci. USA* **2001**, *98*, 1853–1858. [[CrossRef](#)]
31. Shiraiishi, A.; Uruno, T.; Sanematsu, F.; Ushijima, M.; Sakata, D.; Hara, T.; Fukui, Y. DOCK8 Protein Regulates Macrophage Migration through Cdc42 Protein Activation and LRAP35a Protein Interaction. *J. Biol. Chem.* **2017**, *292*, 2191–2202. [[CrossRef](#)] [[PubMed](#)]

32. Miyamoto, Y.; Torii, T.; Kawahara, K.; Tanoue, A.; Yamauchi, J. Dock8 interacts with Nck1 in mediating Schwann cell precursor migration. *Biochem. Biophys. Rep.* **2016**, *6*, 113–123. [[CrossRef](#)] [[PubMed](#)]
33. Harada, Y.; Tanaka, Y.; Terasawa, M.; Pieczyk, M.; Habiro, K.; Katakai, T.; Hanawa-Suetsugu, K.; Kukimoto-Niino, M.; Nishizaki, T.; Shirouzu, M.; et al. DOCK8 is a Cdc42 activator critical for interstitial dendritic cell migration during immune responses. *Blood* **2012**, *119*, 4451–4461. [[CrossRef](#)] [[PubMed](#)]
34. Xu, X.; Han, L.; Zhao, G.; Xue, S.; Gao, Y.; Xiao, J.; Zhang, S.; Chen, P.; Wu, Z.-Y.; Ding, J.; et al. LRCH1 interferes with DOCK8-Cdc42-induced T cell migration and ameliorates experimental autoimmune encephalomyelitis. *J. Exp. Med.* **2016**, *214*, 209–226. [[CrossRef](#)]
35. Li, C.-C.; Kuo, J.-C.; Waterman, C.M.; Kiyama, R.; Moss, J.; Vaughan, M. Effects of brefeldin A-inhibited guanine nucleotide-exchange (BIG) 1 and KANK1 proteins on cell polarity and directed migration during wound healing. *Proc. Natl. Acad. Sci. USA* **2011**, *108*, 19228–19233. [[CrossRef](#)]
36. Pu, J.; Shen, J.; Zhong, Z.; Yanling, M.; Gao, J. KANK1 regulates paclitaxel resistance in lung adenocarcinoma A549 cells. *Artif. Cells Nanomed. Biotechnol.* **2020**, *48*, 639–647. [[CrossRef](#)]
37. Bouchet, B.P.; Gough, R.E.; Ammon, Y.C.; van de Willige, D.; Post, H.; Jacquemet, G.; Altelaar, A.F.M.; Heck, A.J.R.; Goult, B.T.; Akhmanova, A. Talin-KANK1 Interaction Controls the Recruitment of Cortical Microtubule Stabilizing Complexes to Focal Adhesions. *eLife* **2016**, *5*, e18124. [[CrossRef](#)]
38. Kakinuma, N.; Roy, B.C.; Zhu, Y.; Wang, Y.; Kiyama, R. Kank regulates RhoA-dependent formation of actin stress fibers and cell migration via 14-3-3 in PI3K–Akt signaling. *J. Cell Biol.* **2008**, *181*, 537–549. [[CrossRef](#)]
39. Cui, Z.; Shen, Y.; Chen, K.H.; Mittal, S.K.; Yang, J.-Y.; Zhang, G. KANK1 inhibits cell growth by inducing apoptosis through regulating CXXC5 in human malignant peripheral nerve sheath tumors. *Sci. Rep.* **2017**, *7*, 40325. [[CrossRef](#)]
40. Gu, Y.; Zhang, M. Upregulation of the Kank1 gene inhibits human lung cancer progression in vitro and in vivo. *Oncol. Rep.* **2018**, *40*, 1243–1250. [[CrossRef](#)]
41. Noguera, R.; Nieto, O.A.; Tadeo, I.; Fariñas, F.; Alvaro, T. Extracellular matrix, biotensegrity and tumor microenvironment. An update and overview. *Histol. Histopathol.* **2012**, *27*, 693–705. [[PubMed](#)]
42. Burgos-Panadero, R.; Lucantoni, F.; Gamero-Sandemetrio, E.; De La Cruz-Merino, L.; Álvaro, T.; Noguera, R. The tumour microenvironment as an integrated framework to understand cancer biology. *Cancer Lett.* **2019**, *461*, 112–122. [[CrossRef](#)] [[PubMed](#)]
43. Zhang, B.; Xue, Q.; Li, J.; Ma, L.; Yao, Y.; Ye, H.; Cui, Z.; Yang, H. 3D bioprinting for artificial cornea: Challenges and perspectives. *Med. Eng. Phys.* **2019**, *71*, 68–78. [[CrossRef](#)] [[PubMed](#)]
44. Zhang, Y.S.; Duchamp, M.; Oklu, R.; Ellisen, L.W.; Langer, R.; Khademhosseini, A. Bioprinting the Cancer Microenvironment. *ACS Biomater. Sci. Eng.* **2016**, *2*, 1710–1721. [[CrossRef](#)]
45. Xu, X.; Farach-Carson, M.C.; Jia, X. Three-dimensional in vitro tumor models for cancer research and drug evaluation. *Biotechnol. Adv.* **2014**, *32*, 1256–1268. [[CrossRef](#)]
46. Cohn, S.L.; Pearson, A.D.J.; London, W.B.; Monclair, T.; Ambros, P.F.; Brodeur, G.M.; Faldum, A.; Hero, B.; Iehara, T.; Machin, D.; et al. The International Neuroblastoma Risk Group (INRG) Classification System: An INRG Task Force Report. *J. Clin. Oncol.* **2009**, *27*, 289–297. [[CrossRef](#)]
47. Brodeur, G.M. Neuroblastoma: Biological insights into a clinical enigma. *Nat. Rev. Cancer* **2003**, *3*, 203–216. [[CrossRef](#)]
48. Innala, M.; Riebe, I.; Kuzmenko, V.; Sundberg, J.; Gatenholm, P.; Hanse, E.; Johannesson, S. 3D Culturing and differentiation of SH-SY5Y neuroblastoma cells on bacterial nanocellulose scaffolds. *Artif. Cells Nanomed. Biotechnol.* **2013**, *42*, 302–308. [[CrossRef](#)]
49. Nolan, J.C.; Frawley, T.; Tighe, J.; Soh, H.; Curtin, C.; Piskareva, O. Preclinical models for neuroblastoma: Advances and challenges. *Cancer Lett.* **2020**, *474*, 53–62. [[CrossRef](#)]
50. Liu, S.; Tian, Y.; Chlenski, A.; Yang, Q.; Salwen, H.R.; Cohn, S.L. ‘Cross-talk’ between Schwannian stroma and neuroblasts promotes neuroblastoma tumor differentiation and inhibits angiogenesis. *Cancer Lett.* **2005**, *228*, 125–131. [[CrossRef](#)]
51. Zhu, J.; Thompson, C.B. Metabolic regulation of cell growth and proliferation. *Nat. Rev. Mol. Cell Biol.* **2019**, *20*, 436–450. [[CrossRef](#)] [[PubMed](#)]

52. García-Lizarribar, A.; Fernández-Garibay, X.; Velasco-Mallorquí, E.; Castaño, A.G.; Samitier, J.; Ramón-Azcón, J. Composite Biomaterials as Long-Lasting Scaffolds for 3D Bioprinting of Highly Aligned Muscle Tissue. *Macromol. Biosci.* **2018**, *18*, e1800167. [[CrossRef](#)]

Publisher's Note: MDPI stays neutral with regard to jurisdictional claims in published maps and institutional affiliations.



© 2020 by the authors. Licensee MDPI, Basel, Switzerland. This article is an open access article distributed under the terms and conditions of the Creative Commons Attribution (CC BY) license (<http://creativecommons.org/licenses/by/4.0/>).

Article III: Vitronectin-based hydrogels recapitulate neuroblastoma growth conditions

Monferrer E*, Dobre O*, Trujillo S, Azevedo González Oliva M, Trubert-Paneli A, Acevedo-León D, Noguera R, Salmerón-Sánchez M.

*Equal contribution

Front Cell Dev Biol. 2022. Oct 11; 10:988699. doi: 10.3389/fcell.2022.988699.

FRONTIERS MEDIA SA, EISSN: 2296-634X

Impact factor 2021: 6.081

5-year impact factor 2021: 6.576

Developmental Biology: Q1 / Cell Biology: Q2

Cites: 0

ARTICLE III



OPEN ACCESS

EDITED BY

Surabhi Sonam,
D Y Patil International University, India

REVIEWED BY

Jinseok Park,
Children's Hospital of Los Angeles,
United States
Nagaraj Balasubramanian,
Indian Institute of Science Education
and Research, India

*CORRESPONDENCE

Rosa Noguera,
Rosa.Noguera@uv.es
Manuel Salmeron-Sanchez,
Manuel.Salmeron-Sanchez@
glasgow.ac.uk

[†]These authors have contributed equally
to this work

SPECIALTY SECTION

This article was submitted to Cell
Adhesion and Migration,
a section of the journal
Frontiers in Cell and Developmental
Biology

RECEIVED 07 July 2022

ACCEPTED 20 September 2022

PUBLISHED 11 October 2022

CITATION

Monferrer E, Dobre O, Trujillo S,
González Oliva MA, Trubert-Paneli A,
Acevedo-León D, Noguera R and
Salmeron-Sanchez M (2022),
Vitronectin-based hydrogels
recapitulate neuroblastoma
growth conditions.
Front. Cell Dev. Biol. 10:988699.
doi: 10.3389/fcell.2022.988699

COPYRIGHT

© 2022 Monferrer, Dobre, Trujillo,
González Oliva, Trubert-Paneli,
Acevedo-León, Noguera and
Salmeron-Sanchez. This is an open-
access article distributed under the
terms of the [Creative Commons
Attribution License \(CC BY\)](https://creativecommons.org/licenses/by/4.0/). The use,
distribution or reproduction in other
forums is permitted, provided the
original author(s) and the copyright
owner(s) are credited and that the
original publication in this journal is
cited, in accordance with accepted
academic practice. No use, distribution
or reproduction is permitted which does
not comply with these terms.

Vitronectin-based hydrogels recapitulate neuroblastoma growth conditions

Ezequiel Monferrer^{1,2†}, Oana Dobre^{3†}, Sara Trujillo⁴,
Mariana Azevedo González Oliva³, Alexandre Trubert-Paneli³,
Delia Acevedo-León⁵, Rosa Noguera^{1,2*} and
Manuel Salmeron-Sanchez^{3*}

¹Department of Pathology Medical School, University of Valencia-INCLIVA Biomedical Health Research Institute, Valencia, Spain, ²Low Prevalence Tumors, Centro de Investigación Biomédica En Red de Cáncer (CIBERONC), Instituto de Salud Carlos III, Madrid, Spain, ³Centre for the Cellular Microenvironment, Advanced Research Centre, University of Glasgow, Glasgow, United Kingdom, ⁴INM—Leibniz Institute for New Materials, Saarbrücken, Germany, ⁵Clinical Analysis Service, Hospital Universitario Dr. Peset, Valencia, Spain

The tumor microenvironment plays an important role in cancer development and the use of 3D *in vitro* systems that decouple different elements of this microenvironment is critical for the study of cancer progression. In neuroblastoma (NB), vitronectin (VN), an extracellular matrix protein, has been linked to poor prognosis and appears as a promising therapeutic target. Here, we developed hydrogels that incorporate VN into 3D polyethylene glycol (PEG) hydrogel networks to recapitulate the native NB microenvironment. The stiffness of the VN/PEG hydrogels was modulated to be comparable to the *in vivo* values reported for NB tissue samples. We used SK-N-BE (2) NB cells to demonstrate that PEGylated VN promotes cell adhesion as the native protein does. Furthermore, the PEGylation of VN allows its crosslinking into the hydrogel network, providing VN retention within the hydrogels that support viable cells in 3D. Confocal imaging and ELISA assays indicate that cells secrete VN also in the hydrogels and continue to reorganize their 3D environment. Overall, the 3D VN-based PEG hydrogels recapitulate the complexity of the native tumor extracellular matrix, showing that VN-cell interaction plays a key role in NB aggressiveness, and that VN could potentially be targeted in preclinical drug studies performed on the presented hydrogels.

KEYWORDS

vitronectin, neuroblastoma, polyethylene-glycol, stiffness, extracellular matrix, digital image analysis

Introduction

The extracellular matrix (ECM) is a three-dimensional (3D) network that provides support and structure to tissues. The interaction between ECM, cells, tissue vascularization, lymphatic vessels, and nerve fibers is essential for tissue biotensegrity (transmission of mechanical forces and their stability). ECM alterations in structure, composition, stiffness or organization result in tissue dysfunction such as cell denervation, loss of regeneration potential, aberrant wound-healing capacity, and inflammation (Estofolete et al., 2010; Lu et al., 2011; Tomlin and Piccinini, 2018). Moreover, the ECM contributes to the biotensegrity of the tumor, leading to genetic and epigenetic modifications (Noguera et al., 2012; Tadeo et al., 2014). Hence, current oncology research focuses on the role of the ECM in cancer aggressiveness, progression, and therapy resistance (Jinka et al., 2012; Walker, Mojares and Del Río Hernández, 2018). The ECM glycoprotein vitronectin (VN) is an adhesive molecule that presents multiple binding domains; this allows VN to interact with different ECM molecules and integrins, which have been shown to promote tumor cell migration (Felding-Habermann et al., 2001; Shi et al., 2015; Schneider et al., 2016). Therefore, the inhibition of VN interactions with tumor cell integrins and/or its ECM remodeling action could impede cell migration and tumor spreading and provide an effective therapeutic approach. Previous studies on human neuroblastoma (NB) biopsies, one of the most common solid cancers in childhood (Maris et al., 2007; Kaatsch, 2010), have shown that ECM morphological patterns related to collagen fibers, glycosaminoglycans, and glycoproteins, as well as structural characteristics of their blood vascularization and lymph vessels, can define high-risk and even ultra-high-risk NB aggressiveness (Tadeo et al., 2016, 2017, 2018). In particular, our previous results highlighted VN as a relevant glycoprotein related to NB patients with poor prognosis (Burgos-Panadero, Noguera, et al., 2019; Vicente-Munuera et al., 2020). Our previous results with a clinical cohort and preclinical models (orthotopic xenograft VN knock-out (KO) mice and 3D bioprinted hydrogels with different stiffness) have also established that the interaction of VN, its ligands (e.g., α_v integrins), and genomic intratumor heterogeneity in *MYCN*-amplified NB cell line are related to increased ECM stiffness (Burgos-Panadero, Noguera, et al., 2019; López-Carrasco et al., 2020; Monferrer, Martín-Vañó, et al., 2020; Monferrer, Sanegre, et al., 2020; Vicente-Munuera et al., 2020). Furthermore, we performed preclinical therapeutic studies on NB monolayer cell cultures, targeting VN function blockade by employing cilengitide (α_v integrin antagonist) and combination therapy with etoposide-loaded (cytotoxin used in high-risk NB treatment) lipid nanoparticles (Burgos-Panadero et al., 2021). Despite our previous observations suggesting a high synergy between cilengitide and etoposide, the system did not recapitulate the VN expression pattern nor the 3D cell growth

observed in NB tumors. Considering all the presented arguments and the inefficiency of current models, a more reliable and physiologically relevant 3D NB *in vitro* model is needed.

In vivo models such as VN-KO NB mice xenografts have demonstrated that neuroblasts synthesize VN analogously to human NB tumors when growing in 3D conditions surrounded by the tumorous ECM (Burgos-Panadero, Noguera, et al., 2019) however, these *in vivo* models are challenging to produce, reproduce, and analyze. 3D *in vitro* models are versatile platforms that can be designed to closely recapitulate the cancer pathophysiology and study ECM-dependent tumor behavior (Kenny and Bissell, 2003; Denys et al., 2009; Lejeune and Álvaro, 2009; Imamura et al., 2015; Doyle and Yamada, 2016; Gao et al., 2017; Kuen et al., 2017); however, most models incorporate bioactive elements, such as gelatin, that can compete with the protein of interest and yield debased results. In contrast, polyethylene glycol (PEG) is a biocompatible and bioinert polymer that enables hydrogel formation by covalent biomolecule incorporation. Protein-based hydrogels can be designed with specific composition, properties, and biological functionality, allowing the study of the role of various biomolecules (Trujillo et al., 2020; Dobre et al., 2021). Here, we incorporated full-length VN in PEG hydrogels (VN/PEG) to create a tunable 3D cell culture platform that can recapitulate the NB microenvironment and simulate high-risk NB behavior.

In this work, we firstly characterized the bioactivity of the VN/PEG gels, their mechanical properties, and the viability of encapsulated SK-N-BE (2) cells. We subsequently investigated the relation between PEGylated and cellular VN to assess the behavior of SK-N-BE (2) in the system. Our results demonstrate the suitability of the engineered VN/PEG models to mimic NB behavior and their aptitude to be used as drug testing platforms.

Materials and methods

Vitronectin PEGylation

Vitronectin (VN, Peprotech, 1 mg) was PEGylated by modifying a previously published procedure (Almany and Seliktar, 2005). VN was dissolved in NaHCO₃ 0.1 M (pH 8.5). Subsequently, Maleimide-PEG-Succinimidyl Valerate (MAL-PEG-SVA, 3.4 kDa, LaysanBio) was mixed at a mass ratio VN:SVA 1:4 and incubated for 1 h at room temperature (RT) (Figure 1). The product of the reaction was dialyzed (Mini-A-Lyzer, MWCO 10 kDa, ThermoFisher) against PBS for 1 h at RT and stored at -20°C or immediately used. The degree of PEGylation for different VN:SVA ratios was measured by tracking the reduction in primary amines after the reaction using a 2,4,6-trinitrobenzene sulfonic acid (TNBSA, ThermoFisher) assay, which indicated an increase in the VN

degree of modification as the VN:SVA ratio increased (Supplementary Figure S1).

PEGylated VN bioactivity

Cell adhesion formation analysis in SK-N-BE (2) cells was performed to assess VN bioactivity compared to that of laminin (positive control) and ensure maintenance of VN bioactivity after PEGylation. First, protein solutions at $20 \mu\text{g ml}^{-1}$ were added on top of a sterile coverslip for 1 h at RT. Subsequently, 2×10^4 SK-N-BE (2) cells were seeded onto each protein coated coverslip substrate and cultured in growth media (Iscove's Modified Dulbecco's Media (IMDM)) without fetal bovine serum (FBS) to avoid unspecific focal adhesion formation. After 24 h, cells were fixed, permeabilized, and blocked for antibody incubation; primary mouse monoclonal-anti-vinculin antibody (Sigma, 1:400) was added and incubated for 1 h at RT, samples were washed thrice in PBST (0.1% Tween20 (Sigma)) before incubation of secondary Cy3 rabbit-anti-mouse antibody (Jackson ImmunoResearch, 1:200) and Alexa Fluor 488 Phalloidin 1:400, ThermoFisher) for 1 h at RT. Finally, samples were washed thrice in PBST and mounted with VECTASHIELD/DAPI mounting media (Vector Laboratories). Images were taken by a Zeiss Axio Observer. Z1 at $\times 63$ magnification (shown in Figure 2) and later assessed by CellProfiler 4.2.1 to measure focal adhesions size and density. We used a custom pipeline with different steps that include the identification of objects. For focal adhesion calculations, we set up a threshold for vinculin-stained images using an identified object function and calculate the focal adhesion area. At least five images per replicate were taken in three independent experiments.

Hydrogel formation

PEG hydrogels were formed using Michael-type addition reaction under physiological pH and temperature following a previously published protocol (Phelps et al., 2010). Briefly, a final concentration of $500 \mu\text{g ml}^{-1}$ of PEGylated VN was added to different amounts of 4-arm-PEG-MAL (PEG-MAL, 3 wt% or 10 wt%). The thiolated crosslinker was always added at the end, at a ratio 1:1 maleimide:thiol to ensure full crosslinking. The crosslinker used was a 9:1 mixture of PEG-dithiol (SH-PEG-SH, 2 kDa, LaysanBio) and protease-degradable peptide, flanked by two cysteine residues (VPM peptide, GCRDVPMSMRGGDRCG, purity 96.9%, Mw 1,696.96 Da, GenScript) (Figure 1). For cell seeding, the cell suspension was mixed with the VN and PEG-MAL before addition of the crosslinker. Once the crosslinker was added, samples were incubated for 30 min at 37°C to allow gelation. PEG only hydrogels were produced as negative controls. Some PEG hydrogels incorporated native VN (non-PEGylated) instead of PEGylated VN. The nomenclature used in this manuscript is x wt

% PEG for hydrogels without VN, x wt% VN/PEG for hydrogels with PEGylated VN, and x wt% PEG + VN for hydrogels with native VN, x being the percentage of PEG-MAL used.

Vitronectin release

VN release at 72 h was measured to demonstrate that PEGylated VN was covalently crosslinked to the PEG network; to assess this, plain hydrogels (3 and 10 wt% VN/PEG, PEG + VN or PEG only) were immersed for 72 h in PBS. Native VN was incorporated as previously indicated for PEGylated VN. Subsequently, hydrogels were embedded in optimal cutting temperature compound (OCT compound, VWR) and flash frozen in liquid nitrogen to preserve gel structure. Samples were stored at -80°C until use. A cryostat (Leica, -20°C) was used to cut the samples in $50 \mu\text{m}$ thick sections and presented on a microscope slide for immunostaining (Superfrost™ Plus, ThermoFisher). Five images were taken per replicate in triplicated samples, with the same exposure time, by a ZEISS AxioObserver Z.1 at $\times 40$ magnification and then quantified by QuPath 0.3.2 to calculate the VN area in relation to the total image area (%).

The media of each condition were systematically collected across 14 days of culture, concentrated with SpeedVac Vacuum Concentrator (ThermoFisher) until volumes were equivalent, and quantified by ELISA colorimetric assay for VN (R&D Systems) to assess the amount of cellular VN secreted in that culture period (Table 1). The optical density of each well was determined by a micro-plate reader set to 450 nm. Samples were measured in duplicate.

Vitronectin immunostaining

VN was detected *via* immunofluorescence in hydrogel cryosections. Sections were dehydrated with EtOH 100% for 10 min at RT, dried, and rehydrated with two PBS washes of 15 min. The sections were blocked for 30 min and incubated with the primary anti-VN antibody (Invitrogen, 1:200) for 1 h. The samples were washed three times in PBST and then incubated in secondary Cy3 anti-mouse antibody (Jackson ImmunoResearch, 1:200) for 1 h. Samples were washed, mounted, and imaged as previously described.

Mechanical properties

Nanoindentation measurements were performed using a Chiaro Nanoindenter (Optics 11) mounted on top of an inverted phase contrast microscope (Evos XL Core, ThermoFisher), following a previously described approach (Bartolozzi et al., 2020). Measurements were performed at RT

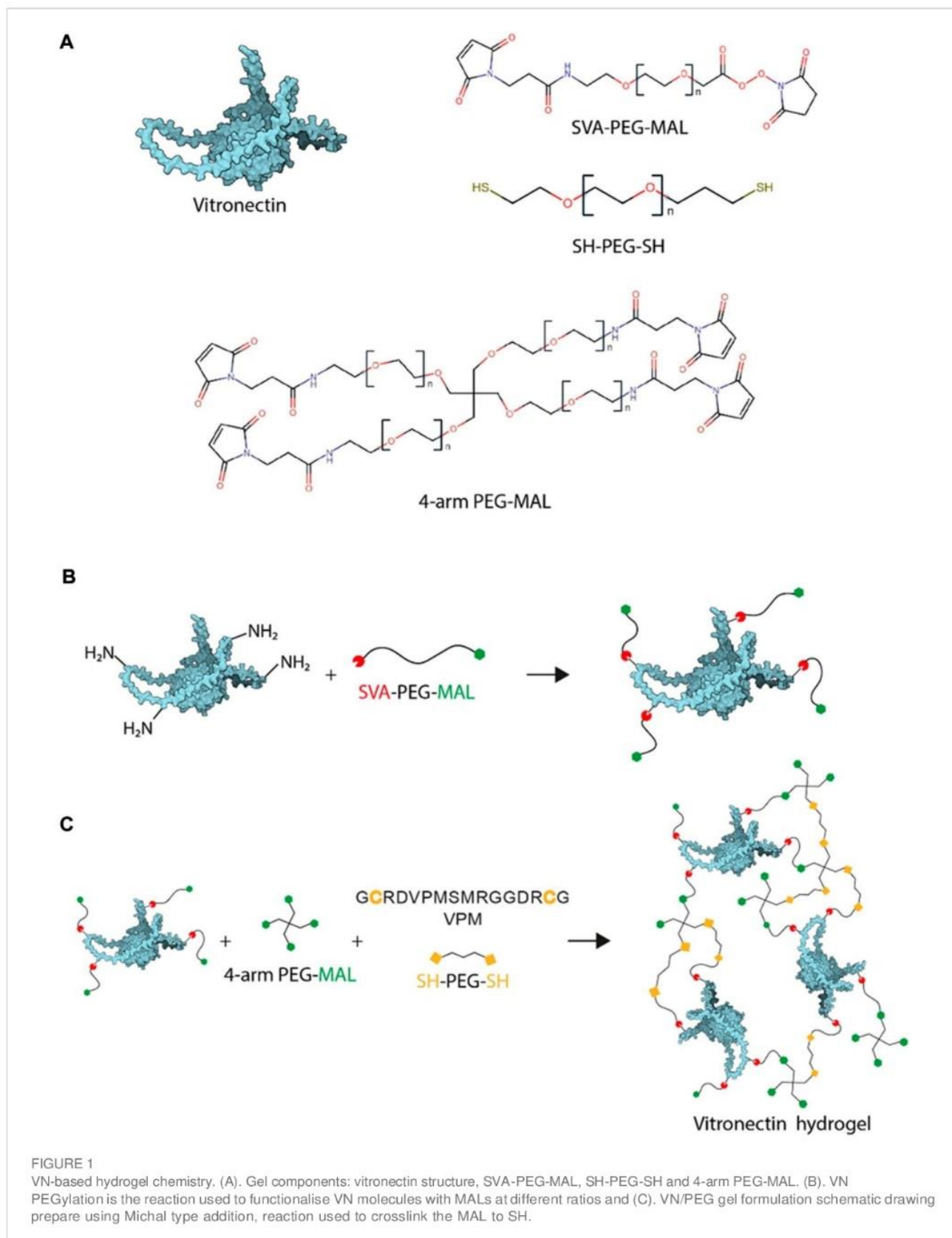


TABLE 1 Summary of ELISA assay for secreted VN detection in the culture media at different time points. VN detected values are referred as ng of VN secreted per hydrogel each day.

	Collection day	Hydrogels (n of samples)	ngVN/HG day
3 wt% PEG	3	12	1.29
	6	8	0.60
	7	8	—
	8	4	—
	10	4	—
	13	4	—
	14	4	—
3 wt% VN/PEG	3	12	0.95
	6	8	0.89
	7	8	—
	8	4	—
	10	4	—
	13	4	—
	14	4	—
10 wt% PEG	3	12	0.49
	6	8	—
	7	8	—
	8	4	—
	10	4	—
	13	4	—
	14	4	—
10 wt% VN/PEG	3	12	0.48
	6	8	—
	7	8	1.16
	8	4	—
	10	4	—
	13	4	—
	14	4	—

in culture media. The area of the sample was mapped defining square areas ($2,500 \mu\text{m}^2$, 25 measurements); a minimum of three maps per replicate were measured and at least two replicates per sample were tested. The selected cantilever had a stiffness of 0.46 Nm^{-1} and held a spherical tip of $52 \mu\text{m}$ radius. The collected curves were analyzed using a custom Python code (Ciccione et al., 2022). Curves were first aligned using a baseline detection method based on the histogram of the force signal (Duanis-Assaf, Razvag and Reches, 2019) and the corresponding indentation was calculated for each curve. The analysis was performed using the Hertz model for a spherical indenter to fit the curves obtained.

Cell culture

We chose SK-N-BE (2) *MYCN*-amplified human NB cell line to be encapsulated into the hydrogels since its genetic

characteristics are representative for 50% of high-risk NB cases (Otte et al., 2021). SK-N-BE (2) were acquired from American Type Culture Collection (ATCC, Manassas, VA, United States) and expanded in IMDM culture (Gibco, Thermofisher), supplemented with 10% FBS (Thermofisher), 1% Insulin-Transferrin-Selenium G Supplement (ITS, Thermofisher) and 1% penicillin/streptomycin (Thermofisher) at 37°C and 5% CO_2 atmosphere. Cells were seeded at 2×10^6 cells ml^{-1} and kept under culture conditions analogous to the expansion process. Hydrogels were cultured from 1 to 7 days; the media was exchanged every 3 days.

Live/dead viability assay

Cellular viability was tested by standard a LIVE/DEAD assay (ThermoFisher). Briefly, SK-N-BE (2) cells were encapsulated at 2×10^6 cells ml^{-1} to allow single-cell analysis. At each time point,

gels were washed twice with PBS, and calcein-AM (4 μ M) and Ethidium Homodimer-1 (2 μ M) were added for 15 min at 37°C; subsequently, gels were washed twice and imaged using a ZEISS AxioObserver Z.1. Samples were imaged on day 1, 5 and 7 at $\times 10$ magnification and analyzed by Fiji to project the overall viability (%), cluster size (μm^2), and cluster density; five images were taken per replicate in triplicated samples.

Statistical analysis

The statistical analysis was performed using GraphPad Prism 9.1.2 software. All *in vitro* experiments were carried out in triplicate unless stated otherwise. All graphs represent mean \pm standard deviation (SD) unless stated otherwise. The goodness of fit of all datasets was assessed *via* D'Agostino-Pearson Normality test or Shapiro-Wilk test. When comparing three or more groups: normal distributed populations were analyzed *via* analysis of variance test (ANOVA test) performing a Tukey's post hoc test to correct for multiple comparisons; when populations were not normally distributed, a Kruskal–Wallis test was used with a Dunn's post hoc test to correct for multiple comparisons. When comparing only two groups, parametric (normal distributed population, *t*-test) or nonparametric (Mann-Whitney test) tests were performed. Differences among groups are stated as follows: for *p*-values < 0.05 (*), when *p*-values < 0.01 (**), for *p*-values < 0.005 (***), for *p*-values < 0.001 (****), when differences between groups are not statistically significant (ns).

Results

PEGylation allows fabrication of hydrogels with functional full-length VN

Prior to hydrogel formation, VN was PEGylated *via* a Michael-type addition reaction by selective functionalization of the VN lysine residues with Maleimide-PEG-Succinimidyl Valerate (MAL-PEG-SVA). According to the results obtained from 2,4,6-Trinitrobenzene Sulfonic Acid (TNBS) assay, from the total VN amines, 99.1% \pm 1.1, 99.0% \pm 1.4 and 96.8% \pm 1.8 remained free after VN PEGylation with 1:10, 1:4 and 1:1 SVA:NH₂ molar ratios, respectively (Supplementary Figure S1). Since the reaction yield was less than 4%, we PEGylated VN with an excess of SVA, at mass ratio VN to MAL-PEG-SVA of 1:4 (approximately 1:60 M ratio) (Supplementary Figure S1) to ensure enough VN PEGylation.

If VN is covalently crosslinked there should not be any VN release, whereas the addition of native VN would cause significant release of VN by diffusion. To demonstrate that VN was crosslinked to the hydrogel network, we assessed the presence of PEGylated VN within the VN/PEG hydrogels after 3 days *via*

immunostaining and compared it to the native VN in the PEG + VN hydrogels (Figure 2A, Supplementary Figure S2). Hydrogels without VN did not show any staining (Supplementary Figure S2) and both VN/PEG and PEG + VN hydrogels showed VN detection at day 0, demonstrating that VN was initially loaded in the hydrogels. VN/PEG hydrogels did not release any VN after 3 days (Figure 2C), which was retained in the hydrogel in a concentration similar to the initial one (day 0). However, 3 wt% PEG + VN released approximately 70% of the initial VN after 3 days (Figure 2C). Interestingly, 10 wt% PEG + VN poorly incorporated VN when compared with 10 wt% VN/PEG.

We then demonstrated that PEGylation does not influence the biological activity of VN. We investigated focal adhesion formation of SK-N-BE (2) cells cultured over substrates coated with either laminin, native VN, or PEGylated VN (Figure 2B and Supplementary Figure S3). We observed comparable cell spreading area on all substrates. We have monitored SK-N-BE (2) cell attachment over time. We observed that culturing cells for 24 h will allow better cell adhesion compared to 4 h in culture. Also, we did not observe any differences in either size or number of focal adhesions between laminin, native and PEGylated VN (Figures 2D,E). These experiments demonstrate that cells interact with PEGylated VN using cell-adhesion domains that were not blocked by PEG.

VN does not modify initial hydrogel stiffness

Using PEG as a hydrogel network allows the physicochemical properties of the system to be controlled (Lutolf and Hubbell, 2003; Cambria et al., 2015; Goldshmid and Seliktar, 2017), (Figure 3). Increasing the amount of PEG in the system (from 3 to 10 wt%) increases the Young's modulus independently of the incorporation of VN in the hydrogel (Figure 3A) as shown for similar systems (Trujillo et al., 2020; Dobre et al., 2021). The 3 wt% PEG hydrogels had a Young's modulus of 0.81 ± 0.48 kPa and slightly increased to 1.03 ± 0.31 kPa upon incorporation of VN (3 wt% VN/PEG). 10 wt% PEG hydrogels showed an average Young's modulus of 3.99 ± 1.37 kPa; and 10 wt% VN/PEG displayed 4.12 ± 2.14 kPa. Importantly, these results are similar to NB stiffness, from 0.17 to 8.45 kPa (Bao et al., 2022), and show that VN incorporation into the hydrogels does not significantly modify hydrogel stiffness.

The degradability of the hydrogels was tuned by combining a protease degradable crosslinker (VPM peptide) with SH-PEG-SH in the synthesis of the hydrogels. Using 10 wt% cell-degradable VPM (Figure 1C), the mechanical properties of the hydrogels decreased after 7 days of culture (Figures 3B,C), 42% in 3 wt% PEG; 48% in 3 wt% VN/PEG; 69% in 10 wt% PEG and 68% in 10 wt% VN/PEG. The incorporation of VN in the hydrogels leads to an additional stiffness reduction when cells are encapsulated for both 3 and 10 wt% VN/PEG hydrogels. This

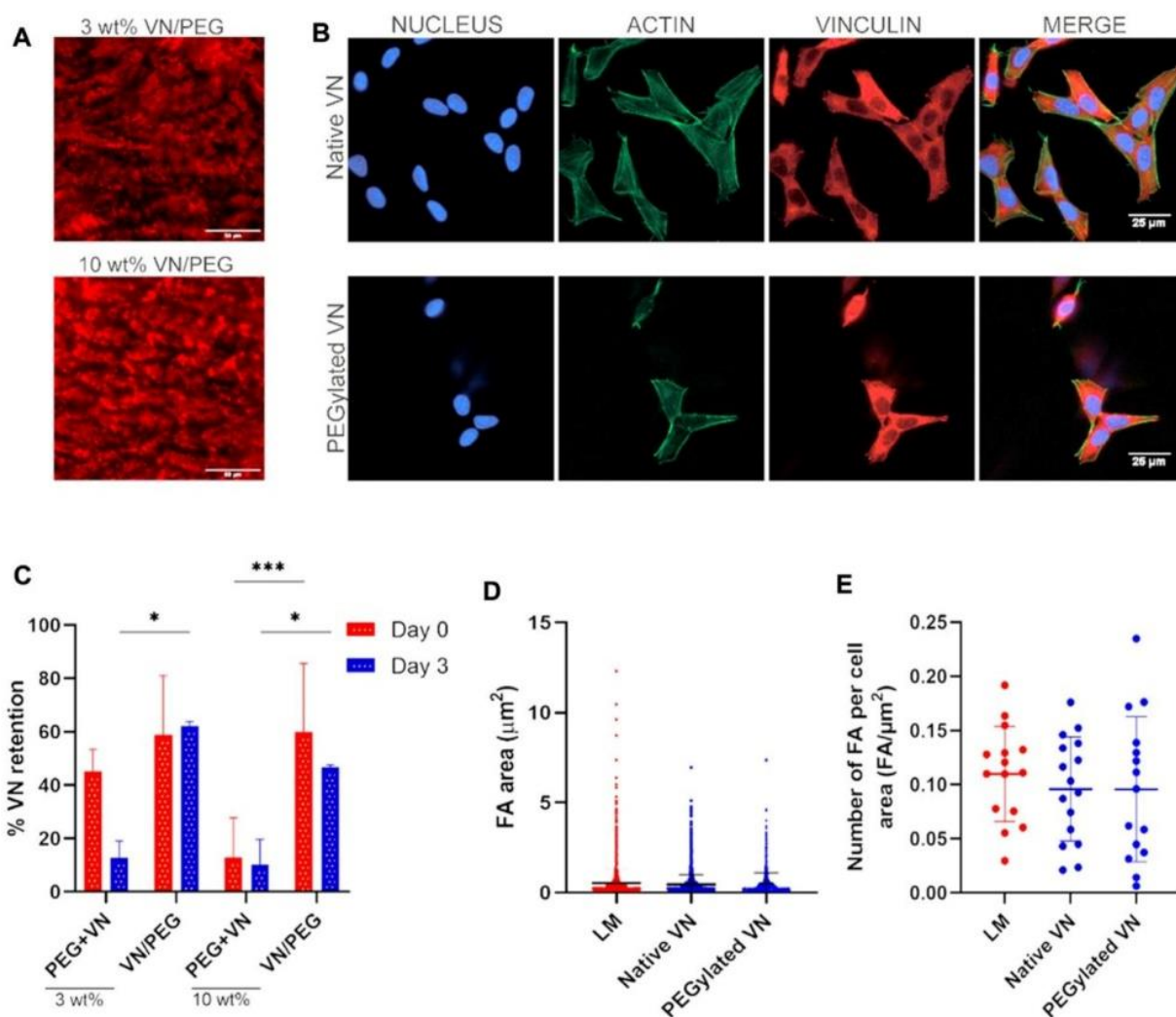


FIGURE 2
VN distribution and bioactivity after incorporation in the 3D hydrogel. (A). Immunofluorescence images of VN distribution in 3 and 10 wt% VN/PEG gel cryosections (scale bar 50 μm). VN was stained with a Cy3 secondary antibody, shown in red in the images. (B). Representative fluorescence images (nucleus in blue, actin in green and vinculin in red) of SK-N-BE (2) cells seeded on top of unmodified or PEGylated VN for 24 h (scale bar: 25 μm). Insets of FA images are shown in [Supplementary Figure S3](#). (C). Immunofluorescence images of VN distribution in 3 and 10 wt% VN/PEG gel cryosections were quantified by QuPath 0.3.2 to calculate VN retention after 3 days. (D). The area of the focal adhesions was found comparable between all conditions. (E). The same trend was observed after analysis focal adhesion density. For each experiment, 15 images (3 replicates, five images each) were analyzed per sample condition.

is likely due to the degradation of VN covalently linked to the PEG network by the cells, which further contributes to reduce the crosslinking density.

VN/PEG hydrogels support NB growth

VN incorporation in PEG hydrogels recapitulates part of the high-risk NB ECM, which influences cancer cell behavior, together with the stiffness of the microenvironment. As a proof of concept, VN concentration was kept constant at

500 $\mu\text{g ml}^{-1}$ in the VN/PEG hydrogels, and the stiffness was then modified.

Cell viability assays performed at 1, 5 and 7 days ([Figure 4](#)) revealed that approximately 80% of the encapsulated cells were viable after 7 days of culture regardless of the stiffness of the hydrogel ([Figures 4A,B](#)). Cell cluster formation was also observed, the size of which increased 2.5-fold from day 1 to day 7 in both 3 and 10 wt% VN/PEG ([Figure 4C](#)). Comparing stiffness conditions for each time point revealed no differences in cell cluster size, but the average cluster density was significantly lower in 10 wt% VN/PEG hydrogels ([Figures 4C,D](#)).

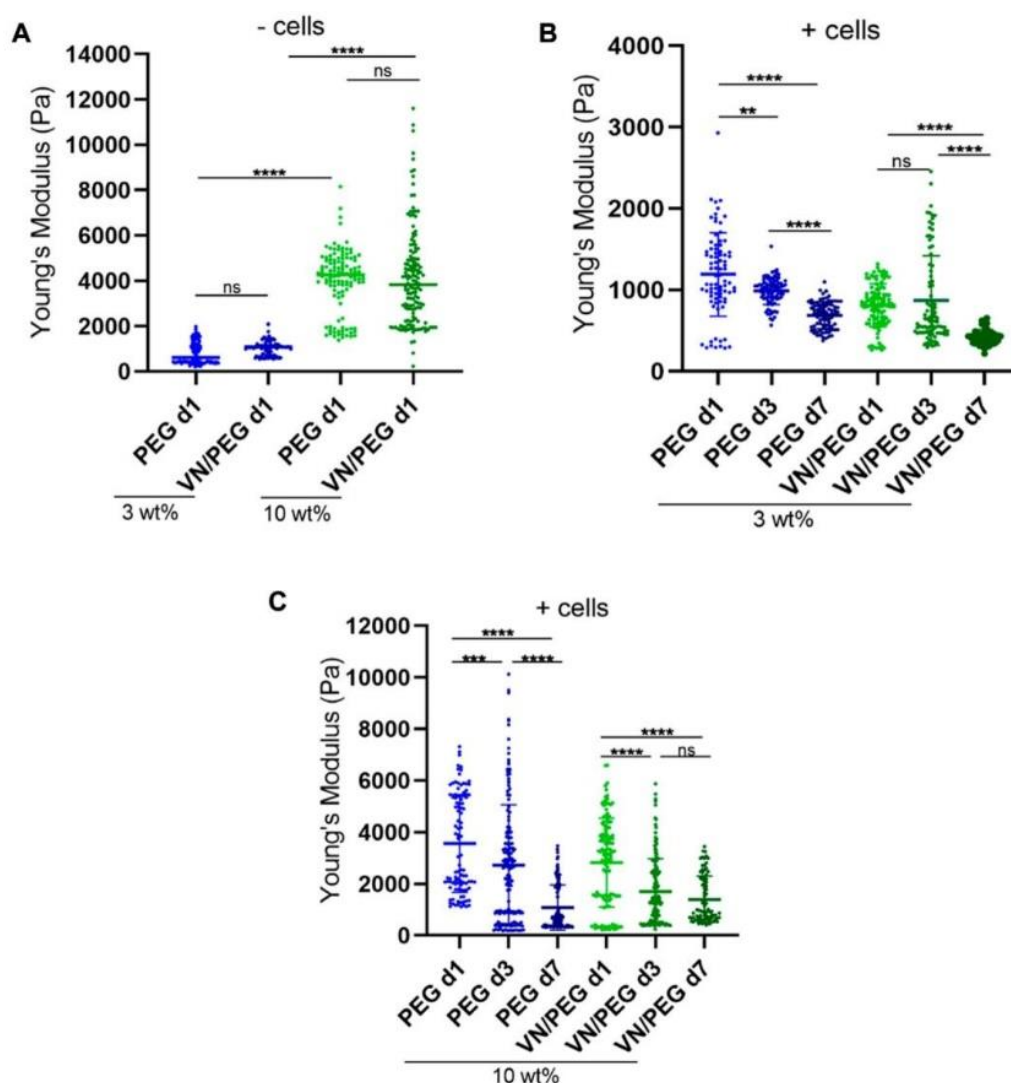


FIGURE 3 3D VN hydrogel with tunable stiffness. (A). Comparison between 3 and 10 wt% PEG gel stiffness with/without VN measured using nanoindentation. (B,C). *In situ* stiffness measurements of 3 (B) and 10 wt% (C) SK-N-BE (2)-loaded hydrogels at 1, 3, and 7 days. A minimum of three maps per replicate were measured and at least two replicates per sample were tested. ANOVA test was used for statistical analyzes.

SK-N-BE (2) cells synthesize VN in the 3D VN-based hydrogels

Since PEGylated VN is retained into VN/PEG hydrogels but not the native one, we checked whether VN synthesized by neuroblastic cells diffused out of the hydrogels into the culture media. Alternatively, cell-secreted VN might interact with other ECM proteins secreted by the cells within the hydrogel and still be retained in the 3D system contributing to the NB microenvironment: to evaluate this, a colorimetric ELISA assay for cell-secreted VN was performed. VN was mainly detected only when analyzing media from at least eight hydrogels cultured over 3 days (Table 1). Each hydrogel released from

0.48 to 1.29 ng VN day⁻¹, with 3 wt% PEG hydrogels showcasing the maximum release rate during the initial culture period. However, no statistical differences could be inferred between conditions (Table 1).

Then, the SK-N-BE (2) cells were incorporated in the 3 and 10 wt% PEG hydrogels with/without VN over 7 days and the VN was quantified using immunofluorescence (Figure 5). Confocal images confirmed SK-N-BE (2) VN synthesis, being slightly higher but not statistically significant in 3 than in 10% PEG hydrogels. Interestingly, the same tendency was observed when PEGylated VN was incorporated into the hydrogel. Despite no significant differences being found, VN/PEG hydrogels display higher VN integrated density

than PEG hydrogels (Figures 5A,B), suggesting that cells synthesize more VN in VN/PEG hydrogels or that the integrated VN density of VN/PEG hydrogels is the sum of the fluorescence signals from cell synthesized VN together with PEGylated VN.

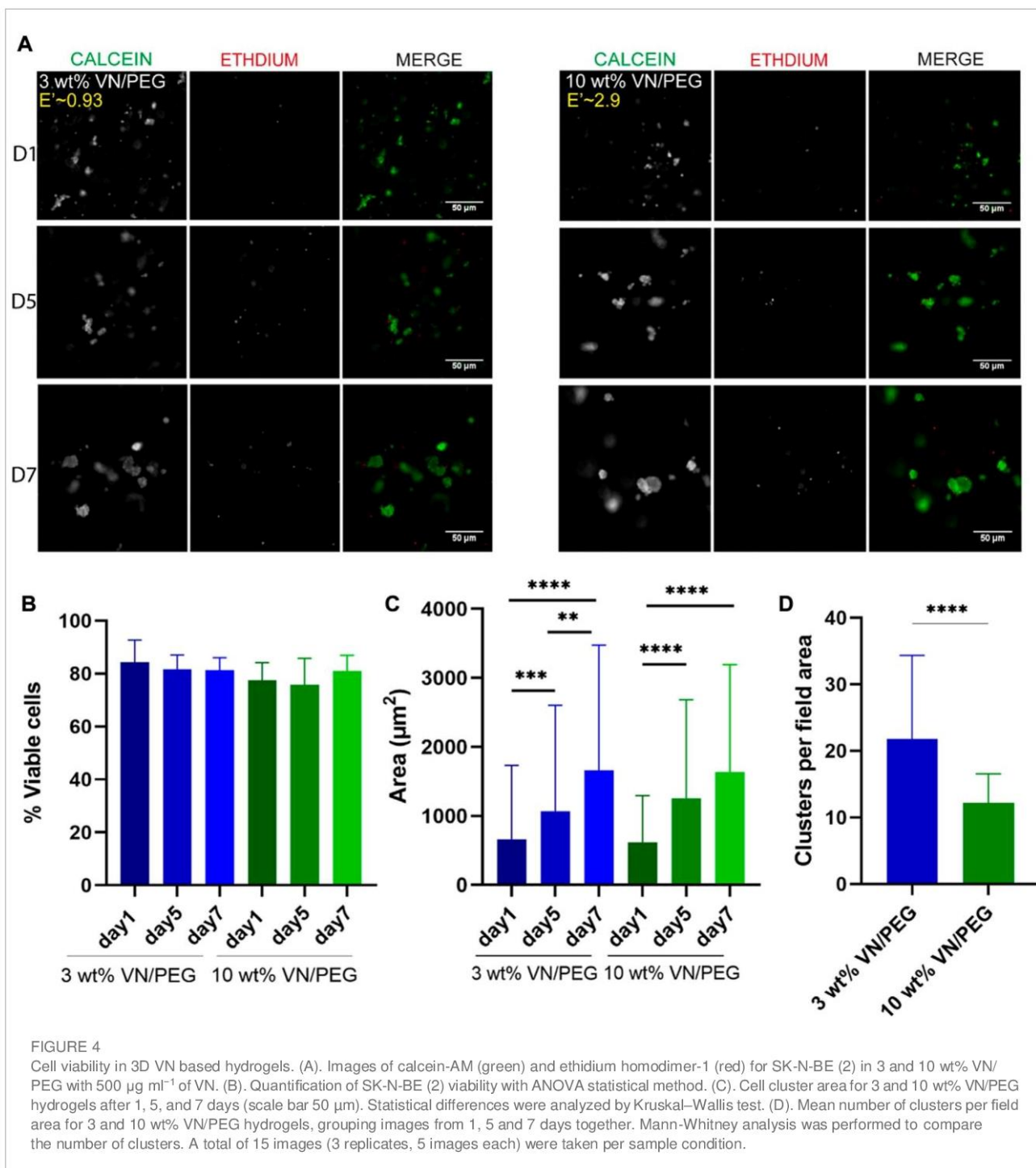
Discussion

The physics of cancer is an emerging field of oncology which highlights the mechanical properties of the tumor microenvironment (TME), focusing on the role of cell-ECM interactions in cancer disease and metastasis (Burgos-Panadero, Lucantoni, et al., 2019; Grant et al., 2022; Kpeglo et al., 2022; Liu et al., 2022; Xiao et al., 2022). As glycoproteins interact with integrins and are involved in cell adhesion and migration pathways, molecules similar to VN, such as FN have been used in cancer mechanotransduction studies (Missirlis and Spatz, 2014; Elosegui-Artola et al., 2016). In fact, VN has been shown to play a key role in NB aggressiveness (Burgos-Panadero, Noguera, et al., 2019; Vicente-Munuera et al., 2020), as such, we have developed a new platform based on PEG hydrogels that incorporate full-length VN and allows fully controllable mechanical properties to recreate high-risk NB behavior *in vitro* and to perform future patient-specific preclinical drug testing. Importantly, these models allow cell-cell and cell-ECM crosstalk that cannot be recreated by cell monolayer cultures (Burgos-Panadero et al., 2021), using a less demanding technology when compared with our previous bioprinted gelatin-based models (Monferrer, Martín-Vañó, et al., 2020; Monferrer, Sanegre, et al., 2020). Furthermore, PEG-based hydrogels allow for fine tuning properties for mechanical regulation, which, unlike gelatin models, can be decoupled from degradability and cell adhesion cues. In this way, PEG offers a bioinert synthetic platform that avoids confounding effects of the scaffold that may alter cell behavior, especially when performing drug targeted studies such as cilengitide to block cell-VN interaction. Hence, PEG allows system functionalization by adhesive peptide immobilization, full-length protein addition or growth factor incorporation; this enables step-by-step studies on artificial scaffolds with increasing complexity by independently adding bioactive components, such as collagen, that precisely recreate the TME, thus progressively evolving the model to a more relevant NB physiopathology. Maleimide groups were chosen as moieties to crosslink the hydrogels due to their higher affinity towards thiol groups as well as their shorter gelation times at physiological pH relative to hydrogels fabricated using acrylate groups (Phelps et al., 2012). Moreover, Michael-type addition has been previously used to form bioactive and biocompatible hydrogels (Phelps et al., 2015; Jansen et al., 2018).

Full-length proteins retain high biological activity after the PEGylation process when incorporated into hydrogel systems

(Almany and Seliktar, 2005; Seidlits et al., 2011; Francisco et al., 2014); however, no studies on VN PEGylation have been previously reported, consequently, we adapted a FN PEGylation protocol for targeting VN lysine residues (Trujillo et al., 2020). Despite the TNBS assay indicating low PEGylation efficiency (Supplementary Figure S1), data from hydrogel cryosections demonstrated that VN reaction with molar excess of MAL-PEG-SVA increases VN PEGylation efficiency, hence, full-length VN can be covalently incorporated into the PEG system (Supplementary Figure S2, Figures 2A–C). Full-length proteins have been incorporated at maximum final concentration of 1 mg ml⁻¹ (Trujillo et al., 2020). A constant final concentration of 500 µg ml⁻¹ of VN was used in our hydrogels. Regarding the relevance of the VN expression levels in NB (Burgos-Panadero, Noguera, et al., 2019; Vicente-Munuera et al., 2020), this system allowed us to regulate the desired amount of VN incorporated, so we can mimic multiple NB ECM conditions. Our cell adhesion studies demonstrated that SK-N-BE (2) adhere and form focal adhesions when seeded on laminin, native VN, and PEGylated VN (Figures 2B,D,E). These results confirm that PEGylation does not reduce VN biological activity, but more importantly, they demonstrate that neuroblastic cells interact with VN to a similar extent than other studied glycoproteins such as laminin, supporting the role of VN in cell migration (Alfano, Franco and Stoppelli, 2022). However, our results do not provide information about focal adhesion signaling activation, so further experiments such as phosphor-FAK focal adhesion protein assessment could deeper evaluate how cells interact with both PEGylated and native VN.

Stiffness is a well-known modulator of tumor behavior and is involved in NB aggressiveness as well as other cancers. However, the limited studies that measured the stiffness of human NB biopsies have reported contradictory results. According to the literature, the stiffness described in soft tissues such as nervous system components range from 0.1 to 1 kPa (Wolf et al., 2013), but human NB biopsies present broader values, from 0.17 to 8.45 kPa (Bao et al., 2022). Critically, the VN/PEG hydrogels reported here recapitulate a small range of physiological stiffness, from 0.42 ± 0.09 kPa to 4.12 ± 2.14 kPa (mean ± SD) (Figures 3A,B), so higher stiffness conditions could be tested in further studies. As previously reported, PEG composition ratios and cell degradation over time regulated hydrogel stiffness (Lutolf and Hubbell, 2003; Almany and Seliktar, 2005; Leslie-Barbick, Moon and West, 2012; Cambria et al., 2015; Jha et al., 2016). Moreover, the stiffness of similar acellular PEG hydrogels has been reported to be stable for up to 9 days (Dobre et al., 2021). In NB, high VN expression correlates with aggressiveness and high stiffness (Burgos-Panadero, Noguera, et al., 2019; Vicente-Munuera et al., 2020), however, VN incorporation did not modify hydrogels stiffness (Figure 3A), as occurs with the incorporation of other full-length proteins (Trujillo et al., 2020; Dobre et al., 2021), this could be due to its lower molecular weight and more globular conformation compared to other ECM proteins. *In vivo*, VN interacts with tumor cells and



fibers within the complex TME, which facilitates ECM remodeling and mediates tumor stiffness (Burgos-Panadero, Noguera, et al., 2019). In our models, VN is PEGylated and then covalently bound to a PEG network, so this approximation may not properly recapitulate the VN influence in NB stiffness determination. Nonetheless, our data suggests that VN may be responsible for defining part of the mechanical properties of the hydrogels, simultaneously making them more degradable since the stiffness

decreased more over time when VN was present in the hydrogels (Figures 3B,C). In this regard, VN has been reported to be degradable by matrix metalloproteinases such as MMP1, 2, 3, 7 and 9 (Imai, Shikata and Okada, 1995). Besides, VPM is also degraded by MMP1 and 2 (Foster et al., 2017). Therefore, the extra decrease in stiffness for VN/PEG hydrogels may be a combined effect of both VN and VPM degradation by the MMPs synthesized by SK-N-BE (2) (Roomi et al., 2013; Xiang et al., 2015; Mitchell and

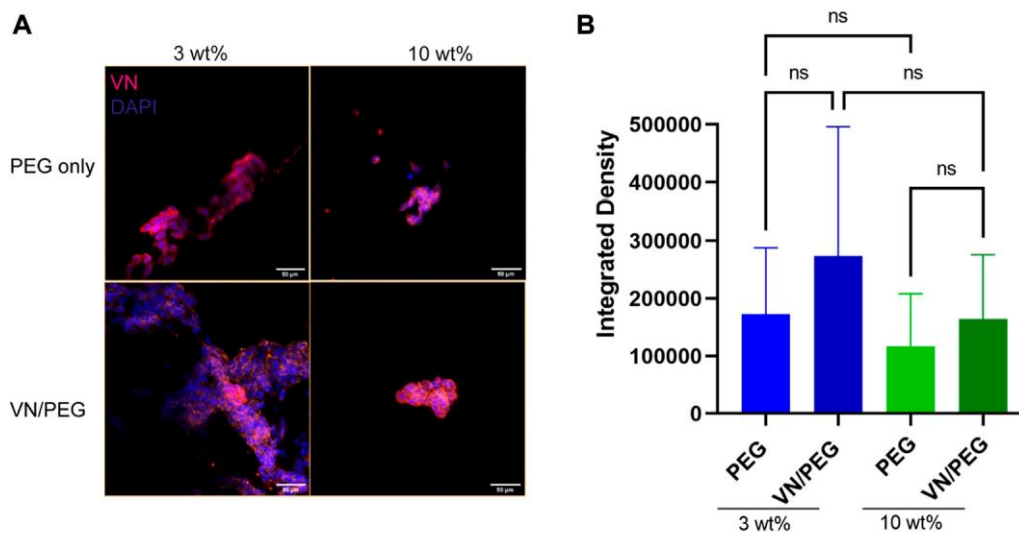


FIGURE 5

Distribution of VN secreted by the cells in 3D PEG and VN/PEG hydrogels. Immunofluorescence images of SK-N-BE (2) cultured for 7 days in 3 and 10 wt% PEG and VN/PEG. Images show nuclei (blue) and VN (magenta) (scale bar 50 μm). (B). Immunofluorescence quantification of VN secreted by cells in 3 and 10 wt% PEG with/without VN. We have represented in the graph the Integrated density (total raw intensity per image normalized by cell area). A total of 15 images (3 replicates, 5 images each) were taken per sample condition.

O'Neill, 2016). Importantly, the stiffness reduction of 10 wt% PEG and VN/PEG hydrogels was 20% higher than 3 wt% PEG and VN/PEG hydrogels, which may indicate that cells reacted to the stiff microenvironment by increasing their ECM degradation activity.

The incorporation of VN as the only bioactive molecule in this system allowed us the study of VN's specific role within the NB ECM, together with its stiffness. We found that SK-N-BE (2) cells presented the same viability and equivalent cluster growth rate in both stiffness conditions tested (Figures 4A–C), supporting the capability to model the NB cluster development although stiff conditions were more restrictive to cell aggregate allocation (Figure 4D). Thus, the stiff hydrogels provide higher confinement to the cells due to their small pore size which hinders rapid cell growth and migration. Nevertheless, this environment likely promotes metabolic adaptation leading to the increased degradation rate of the stiff hydrogels mentioned above (Figures 3B,C), being that cells may need to promote softer ECM conditions to grow efficiently.

Regarding the evaluation of cell secreted VN diffusion into the culture media, the ELISA kit displayed a VN limit detection of $<15,6 \text{ ng ml}^{-1}$ and so we were not able to detect VN in some samples (Table 1). We cannot confirm whether negative results were due to a lack in hydrogel number, culture time or VN cell synthesis. In fact, we should consider that cells may adapt their VN production overtime, so they could reduce or even stop their VN synthesis in order to prioritize other biological activities. We have demonstrated that SK-N-BE (2) cells synthesize VN, at least at initial culture times, even when it is already present in the environment (Table 1). More importantly, these results confirm

that we can detect VN release in the culture media. In healthy conditions, VN is mainly synthesized by hepatocytes, and it is released into the bloodstream. The mean concentration measured in plasma in healthy subjects has been reported as 200–300 $\mu\text{g ml}^{-1}$ (Clemetson, 1997), and various studies regarding VN concentration in different diseases have been performed (Boyd et al., 1993), so VN could become a liquid biopsy biomarker for high-risk NB. Additionally, confocal image analysis suggests that cells may produce slightly more VN in soft conditions due to less restrictive confinement (Figure 5). However, further experiments other than quantification of fluorescence (integrated density) will be necessary to determine if cells cultured within VN/PEG hydrogels secrete more VN compared to cells within PEG hydrogels. If higher VN integrated density is confirmed in VN/PEG hydrogels, the experiments should assess whether it is due to the presence of both synthesized and PEGylated VN (cells may preferentially grow on PEGylated VN spots or pericellularly reorganize PEGylated VN), or because an increased cell VN synthesis driven by PEGylated VN. Despite no statistical differences, the fact that VN expression is retained *in vitro* conditions indicates that VN/PEG hydrogels are susceptible for translational combinatory therapy studies as occurs with GD2 (KO et al., 2022).

Overall, these data demonstrate that full-length and functional VN can be incorporated into a synthetic hydrogel system that has controlled stiffness and degradation rates, mimicking part of the pathophysiology of high-risk NB tumors. Based on higher cluster and VN

integrated densities, together with increased degradation of the stiff hydrogels, we infer that 3 wt% VN/PEG conditions better recreate NB cell behavior. However, cell adaptive response depends on stiffness, time and the genetic background of the cell line, as previously suggested in the literature (López-Carrasco et al., 2020; Monferrer, Sanegre, et al., 2020), so further genetic and drug-testing studies on long-cultured models, using various *MYCN* amplified and/or *ALK* mutated NB cell lines, should be performed to confirm which model better recapitulates high-risk NB behavior. Finally, VN synthesis even in VN rich ECM conditions strengthen the relevance of testing VN targeted preclinical therapies in NB.

Data availability statement

The original contributions presented in the study are included in the article/Supplementary Materials, further inquiries can be directed to the corresponding authors.

Author contributions

EM: conceptualization, methodology, investigation, writing original draft. OD: conceptualization, methodology, investigation, editing original draft. ST: conceptualization, methodology. MG: methodology. AT-P: methodology. DA-L: methodology. RN: conceptualization, methodology, editing original draft, supervision, provide funding. MS-S: conceptualization, methodology, editing original draft, supervision, provide funding. All authors reviewed the manuscript.

Funding

EM is supported by the Asociación Fundación Española contra el Cáncer, JAP-AECC (2018/150). This research was funded by ISCIII (FIS) and FEDER (European Regional Development Fund), grant number PI20/01107; CIBERONC (contract CB16/12/00484). OD, MG, AT-P, and MS-S acknowledge support via an EPSRC Programme Grant (EP/P001114/1).

References

- Alfano, D., Franco, P., and Stoppelli, M. P. (2022). Modulation of cellular function by the urokinase receptor signalling: A mechanistic view. *Front. Cell Dev. Biol.* 10. doi:10.3389/fcell.2022.818616
- Almany, L., and Seliktar, D. (2005). Biosynthetic hydrogel scaffolds made from fibrinogen and polyethylene glycol for 3D cell cultures. *Biomaterials* 26 (15), 2467–2477. doi:10.1016/j.biomaterials.2004.06.047
- Bao, M., Chen, Y., Liu, J.-T., Bao, H., Wang, W.-B., Qi, Y.-X., et al. (2022). Extracellular matrix stiffness controls VEGF165 secretion and neuroblastoma angiogenesis via the YAP/RUNX2/SRSF1 axis. *Angiogenesis* 25 (1), 71–86. doi:10.1007/s10456-021-09804-7/FIGURES/7

Acknowledgments

We would like to thank Rodrigo-Navarro for helping us to draw the vitronectin structure and hydrogel chemical reaction shown in Figure 1.

Conflict of interest

The authors declare that the research was conducted in the absence of any commercial or financial relationships that could be construed as a potential conflict of interest.

Publisher's note

All claims expressed in this article are solely those of the authors and do not necessarily represent those of their affiliated organizations, or those of the publisher, the editors and the reviewers. Any product that may be evaluated in this article, or claim that may be made by its manufacturer, is not guaranteed or endorsed by the publisher.

Supplementary material

The Supplementary Material for this article can be found online at: <https://www.frontiersin.org/articles/10.3389/fcell.2022.988699/full#supplementary-material>

SUPPLEMENTARY FIGURE S1
PEGylated VN characterization using a TNBS assay. A. Standard curve of VN (left side) and VN free amines (in the middle) for different PEGylation ratios between VN:MAL and percentage of free amines for different PEGylation ratios shown on the right side.

SUPPLEMENTARY FIGURE S2
VN distribution and retention after incorporation in the 3D hydrogel. On the top, immunofluorescence images of 3 wt% PEG hydrogels and on the bottom, 10 wt% PEG cryosections. Columns represent PEG, PEG+VN (day 0 and 3) and VN/PEG (day 0 and 3) conditions (scale bar 50 μ m). Vitronectin was stained with a Cy3 secondary antibody, shown in red in the images.

SUPPLEMENTARY FIGURE S3
Insets of FA images (vinculin in red) of SK-N-BE(2) cells seeded on top of unmodified or PEGylated VN for 24h (scale bar: 25 μ m).

- Bartolozzi, A., Viti, F., De Stefano, S., Sbrana, F., Petecchia, L., Gavazzo, P., et al. (2020). Development of label-free biophysical markers in osteogenic maturation. *J. Mech. Behav. Biomed. Mater.* 103, 103581. doi:10.1016/j.jmbm.2019.103581

Boyd, N. A. M., Bradwell, A. R., and Thompson, R. A. (1993). Quantitation of vitronectin in serum: Evaluation of its usefulness in routine clinical practice. *J. Clin. Pathology* 46, 1042–1045. doi:10.1136/jcp.46.11.1042

Burgos-Panadero, R., Noguera, I., Cañete, A., Navarro, S., and Noguera, R. (2019). Vitronectin as a molecular player of the tumor microenvironment in neuroblastoma. *BMC cancer* 19 (1). doi:10.1186/s12885-019-5693-2

- Burgos-Panadero, R., El Moukhtari, S. H., Noguera, I., Rodríguez-Nogales, C., Martín-Vañó, S., Vicente-Munuera, P., et al. (2021). Unraveling the extracellular matrix-tumor cell interactions to aid better targeted therapies for neuroblastoma. *Int. J. Pharm.* 608, 121058. doi:10.1016/j.ijpharm.2021.121058
- Burgos-Panadero, R., Lucantoni, F., Gamero-Sandemetro, E., Cruz-Merino, L. d. I., Álvaro, T., and Noguera, R. (2019). The tumour microenvironment as an integrated framework to understand cancer biology. *Cancer Lett.* 461, 112–122. doi:10.1016/j.canlet.2019.07.010
- Cambria, E., Renggli, K., Ahrens, C. C., Cook, C. D., Kroll, C., Krueger, A. T., et al. (2015). Covalent modification of synthetic hydrogels with bioactive proteins via sortase-mediated ligation. *Biomacromolecules* 16 (8), 2316–2326. doi:10.1021/ACS.BIOMAC.5B00549
- Ciccione, G., Azevedo Gonzalez Oliva, M., Antonovaite, N., Lüchtfeld, I., Salmeron-Sanchez, M., and Vassalli, M. (2022). Experimental and data analysis workflow for soft matter nanoindentation. *JoVE* (179), e63401. doi:10.3791/63401
- Clemetson, K. J. (1997). *Blood glycoproteins*, 29. Amsterdam, Netherlands: ELSEVIER, 173–201. (PART B). doi:10.1016/S0167-7306(08)60622-5Blood glycoproteins~~~~
- Denys, H., Braems, G., Lambein, K., Pauwels, P., Hendrix, A., De Boeck, A., et al. (2009). The extracellular matrix regulates cancer progression and therapy response: Implications for prognosis and treatment. *Cpd* 15 (12), 1373–1384. doi:10.2174/138161209787846711
- Dobre, O., Oliva, M. A. G., Ciccione, G., Trujillo, S., Rodrigo-Navarro, A., Venters, D. C., et al. (2021). A hydrogel platform that incorporates laminin isoforms for efficient presentation of growth factors - neural growth and osteogenesis. *Adv. Funct. Mat.* 31 (21), 2010225. doi:10.1002/ADFM.202010225
- Doyle, A. D., and Yamada, K. M. (2016). Mechanosensing via cell-matrix adhesions in 3D microenvironments. *Exp. Cell Res.* 343 (1), 60–66. doi:10.1016/j.yexcr.2015.10.033
- Duanis-Assaf, T., Razzvag, Y., and Reches, M. (2019). ForSDAT: An automated platform for analyzing force spectroscopy measurements. *Anal. Methods* 11 (37), 4709–4718. doi:10.1039/C9AY01150A
- Elosegui-Artola, A., Oriá, R., Chen, Y., Kosmalska, A., Pérez-González, C., Castro, N., et al. (2016). Mechanical regulation of a molecular clutch defines force transmission and transduction in response to matrix rigidity. *Nat. Cell Biol.* 18 (5), 540–548. doi:10.1038/ncb3336
- Estofolete, C. F., Botelho-Machado, C., Taboga, S. R., Zucoloto, S., Polli-Lopes, A. C., and Gil, C. D. (2010). Effects of myenteric denervation on extracellular matrix fibers and mast cell distribution in normal stomach and gastric lesions. *Cancer Cell Int.* 10, 18. Available at: doi:10.1186/1475-2867-10-18
- Felding-Habermann, B., O'Toole, T. E., Smith, J. W., Fransvea, E., Ruggeri, Z. M., Ginsberg, M. H., et al. (2001). Integrin activation controls metastasis in human breast cancer. *Proc. Natl. Acad. Sci. U.S.A.* 98 (4), 1853–1858. doi:10.1073/PNAS.98.4.1853
- Foster, G. A., Headen, D. M., González-García, C., Salmerón-Sánchez, M., Shirwan, H., and García, A. J. (2017). Protease-degradable microgels for protein delivery for vascularization. *Biomaterials* 113, 170–175. doi:10.1016/j.biomaterials.2016.10.044
- Francisco, A. T., Hwang, P. Y., Jeong, C. G., Jing, L., Chen, J., and Setton, L. A. (2014). Photocrosslinkable laminin-functionalized polyethylene glycol hydrogel for intervertebral disc regeneration. *Acta biomater.* 10 (3), 1102–1111. doi:10.1016/j.actbio.2013.11.013
- Gao, S., Shen, J., Hornicek, F., and Duan, Z. (2017). Three-dimensional (3D) culture in sarcoma research and the clinical significance. *Biofabrication* 9, 032003. doi:10.1088/1758-5090/aa7f4b
- Goldshmid, R., and Seliktar, D. (2017). Hydrogel modulus affects proliferation rate and pluripotency of human mesenchymal stem cells grown in three-dimensional culture. *ACS Biomater. Sci. Eng.* 3 (12), 3433–3446. doi:10.1021/acsbomaterials.7b00266
- Grant, E., Bucklain, F. A., Ginn, L., Laity, P., Ciani, B., and Bryant, H. E. (2022). "Progesterone receptor expression contributes to gemcitabine resistance at higher ECM stiffness in breast cancer cell lines," *PLoS oneC. Trackman*. 17, e0268300. doi:10.1371/JOURNAL.PONE.0268300
- Imai, K., Shikata, H., and Okada, Y. (1995). Degradation of vitronectin by matrix metalloproteinases-1, -2, -3, -7 and -9. *FEBS Lett.* 369 (2–3), 249–251. doi:10.1016/0014-5793(95)00752-U
- Imamura, Y., Mukohara, T., Shimono, Y., Funakoshi, Y., Chayahara, N., Toyoda, M., et al. (2015). Comparison of 2D- and 3D-culture models as drug-testing platforms in breast cancer. *Oncol. Rep.* 33 (4), 1837–1843. doi:10.3892/OR.2015.3767
- Jansen, L. E., Negrón-Piñero, L. J., Galarza, S., and Peyton, S. R. (2018). Control of thiol-maleimide reaction kinetics in PEG hydrogel networks. *Acta biomater.* 70, 120–128. doi:10.1016/j.actbio.2018.01.043
- Jha, A. K., Tharp, K. M., Browne, S., Ye, J., Stahl, A., Yeghiazarians, Y., et al. (2016). Matrix metalloproteinase-13 mediated degradation of hyaluronic acid-based matrices orchestrates stem cell engraftment through vascular integration. *Biomaterials* 89, 136–147. doi:10.1016/j.biomaterials.2016.02.023
- Jinka, R., Kapoor, R., Sistla, P. G., Raj, T. A., and Pande, G. (2012). Alterations in cell-extracellular matrix interactions during progression of cancers. *Int. J. Cell Biol.* 2012, 1–8. doi:10.1155/2012/219196
- Kaatsch, P. (2010). Epidemiology of childhood cancer. *Cancer Treat. Rev.* 36 (4), 277–285. doi:10.1016/j.ctrv.2010.02.003
- Kenny, P. A., and Bissell, M. J. (2003). Tumor reversion: Correction of malignant behavior by microenvironmental cues. *Int. J. Cancer* 107 (5), 688–695. doi:10.1002/IJC.11491
- Kpeglo, D., Hughes, M. D. G., Dougan, L., Haddrick, M., Knowles, M. A., Evans, S. D., et al. (2022). Modeling the mechanical stiffness of pancreatic ductal adenocarcinoma. *Matrix Biol. plus* 14, 100109. doi:10.1016/j.mbplus.2022.100109
- Kuen, J., Darowski, D., Kluge, T., and Majety, M. (2017). Pancreatic cancer cell/fibroblast co-culture induces M2 like macrophages that influence therapeutic response in a 3D model. *PLoS one* 12 (7), e0182039. doi:10.1371/JOURNAL.PONE.0182039
- Lejeune, M., and Alvaro, T. (2009). Clinicobiological, prognostic and therapeutic implications of the tumor microenvironment in follicular lymphoma. *Haematologica* 94 (1), 16–21. doi:10.3324/HAEMATOL.2008.001255
- Leslie-Barbick, J. E., Moon, J. J., and West, J. L. (2012). Covalently-immobilized vascular endothelial growth factor promotes endothelial cell tubulogenesis in poly(ethylene glycol) diacrylate hydrogels. *J. Biomaterials Sci. Polym. Ed.* 20 (12), 1763–1779. doi:10.1163/156856208X38638110.1163/156856208X386381
- Liu, H.-H., Xu, Y., Li, C.-J., Hsu, S.-J., Lin, X.-H., Zhang, R., et al. (2022). An SCD1-dependent mechanoresponsive pathway promotes HCC invasion and metastasis through lipid metabolic reprogramming. *Mol. Ther.* 30, 2554–2567. doi:10.1016/j.ymt.2022.03.015
- López-Carrasco, A., Martín-Vañó, S., Burgos-Panadero, R., Monferrer, E., Berbegall, A. P., Fernández-Blanco, B., et al. (2020). Impact of extracellular matrix stiffness on genomic heterogeneity in MYCN-amplified neuroblastoma cell line. *J. Exp. Clin. Cancer Res.* 39 (1), 226. doi:10.1186/s13046-020-01729-1
- Lu, P., Takai, K., Weaver, V. M., and Werb, Z. (2011). Extracellular matrix degradation and remodeling in development and disease. *Cold Spring Harb. Perspect. Biol.* 3 (12), a005058. doi:10.1101/cshperspect.a005058
- Lutolf, M. P., and Hubbell, J. A. (2003). Synthesis and physicochemical characterization of end-linked poly(ethylene glycol)-co-peptide hydrogels formed by Michael-type addition. *Biomacromolecules*, 4, 713–722. doi:10.1021/BM025744E/ASSET/IMAGES/MEDIUM/BM025744EE00009
- Maris, J. M., Hogarty, M. D., Bagatell, R., and Cohn, S. L. (2007). Neuroblastoma. *Lancet* 369 (9579), 2106–2120. doi:10.1016/S0140-6736(07)60983-0
- McNerney, M., Karageorgos, S., Ferry, G., Wolpaw, A., Burudpakdee, C., Khurana, P., et al. (2022). TH-MYCN tumors, but not tumor-derived cell lines, are adrenergic lineage, GD2+, and responsive to anti-GD2 antibody therapy. *Oncotarget* 11 (1), doi:10.1080/2162402X.2022.2075204
- Missirlis, D., and Spatz, J. P. (2014). Combined effects of PEG hydrogel elasticity and cell-adhesive coating on fibroblast adhesion and persistent migration. *Biomacromolecules* 15 (1), 195–205. doi:10.1021/BM4014827/SUPPL_FILE/BM4014827_SI_001.PDF
- Mitchell, C. B., and O'Neill, G. M. (2016). Cooperative cell invasion: Matrix metalloproteinase-mediated incorporation between cells. *MBoC*, 27, 3284–3292. doi:10.1091/MBCE16-03-0194/ASSET/IMAGES/LARGE/MBCE16-03-3284-G008
- Monferrer, E., Martín-Vañó, S., Carretero, A., García-Lizarribar, A., Burgos-Panadero, R., Navarro, S., et al. (2020). A three-dimensional bioprinted model to evaluate the effect of stiffness on neuroblastoma cell cluster dynamics and behavior. *Sci. Rep.* 10 (11), 1–12. doi:10.1038/s41598-020-62986-w
- Monferrer, E., Sanegre, S., Martín-Vañó, S., García-Lizarribar, A., Burgos-Panadero, R., López-Carrasco, A., et al. (2020). Digital image analysis applied to tumor cell proliferation, aggressiveness, and migration-related protein synthesis in neuroblastoma 3D models. *Ijms* 21 (22), 8676–8692. doi:10.3390/IJMS21228676
- Noguera, R., Nieto, O. A., Tadeo, I., Fariñas, F., and Alvaro, T. (2012). Extracellular matrix, biotensegrity and tumor microenvironment. An update and overview. *Histol. Histopathol.* 27 (6), 693–705. doi:10.14670/HH-27.693
- Otte, J., Dyberg, C., Pepich, A., and Johnsen, J. I. (2021). MYCN function in neuroblastoma development. *Front. Oncol.* 10, 3210. doi:10.3389/fonc.2020.624079
- Phelps, E. A., Enemchukwu, N. O., Fiore, V. F., Sy, J. C., Murthy, N., Sulchek, T. A., et al. (2012). Maleimide cross-linked bioactive PEG hydrogel exhibits improved reaction kinetics and cross-linking for cell encapsulation and *in situ* delivery. *Adv. Mat.* 24 (1), 64–70. doi:10.1002/ADMA.201103574

- Phelps, E. A., Landázuri, N., Thulé, P. M., Taylor, W. R., and García, A. J. (2010). Bioartificial matrices for therapeutic vascularization. *Proc. Natl. Acad. Sci. U.S.A.* 107 (8), 3323–3328. doi:10.1073/PNAS.0905447107
- Phelps, E. A., Templeman, K. L., Thulé, P. M., and García, A. J. (2015). Engineered VEGF-releasing PEG-MAL hydrogel for pancreatic islet vascularization. *Drug Deliv. Transl. Res.* 5 (2), 125–136. doi:10.1007/S13346-013-0142-2
- Roomi, M. W., Kalinovsky, T., Roomi, N. W., Niedzwiecki, A., and Rath, M. (2013). Inhibition of the SK-N-MC human neuroblastoma cell line *in vivo* and *in vitro* by a novel nutrient mixture. *Oncol. Rep.* 29 (5), 1714–1720. doi:10.3892/OR.2013.2307/HTML
- Schneider, G., Bryndza, E., Poniewierska-Baran, A., Serwin, K., Suszyska, M., Sellers, Z. P., et al. (2016). Evidence that vitronectin is a potent migration-enhancing factor for cancer cells chaperoned by fibrinogen: A novel view of the metastasis of cancer cells to low-fibrinogen lymphatics and body cavities. *Oncotarget* 7 (43)–69843, 69829. doi:10.18632/ONCOTARGET.12003
- Seidlits, S. K., Drinnan, C. T., Petersen, R. R., Shear, J. B., Suggs, L. J., and Schmidt, C. E. (2011). Fibronectin-hyaluronic acid composite hydrogels for three-dimensional endothelial cell culture. *Acta biomater.* 7 (6), 2401–2409. doi:10.1016/J.ACTBIO.2011.03.024
- Shi, K., Lan, R.-L., Tao, X., Wu, C.-Y., Hong, H.-F., and Lin, J.-H. (2015). Vitronectin significantly influences prognosis in osteosarcoma. *Int. J. Clin. Exp. Pathol.* 8 (9), 11364–11371. eCollection 2015.
- Tadeo, I., Berbegall, A. P., Castel, V., García-Miguel, P., Callaghan, R., Pahlman, S., et al. (2016). Extracellular matrix composition defines an ultra-high-risk group of neuroblastoma within the high-risk patient cohort. *Br. J. Cancer* 115 (4), 480–489. doi:10.1038/BJC.2016.210
- Tadeo, I., Berbegall, A. P., Escudero, L. M., Á lvaro, T. s., and Noguera, R. (2014). Biotensegrity of the extracellular matrix: Physiology, dynamic mechanical balance, and implications in oncology and mechanotherapy. *Front. Oncol.* 4. doi:10.3389/fonc.2014.00039
- Tadeo, I., Berbegall, A. P., Navarro, S., Castel, V., and Noguera, R. (2017). A stiff extracellular matrix is associated with malignancy in peripheral neuroblastic tumors. *Pediatr. Blood Cancer* 64 (9), e26449. doi:10.1002/pbc.26449
- Tadeo, I., Gamero-Sandemetro, E., Berbegall, A. P., Gironella, M., Ritort, F., Cañete, A., et al. (2018). Lymph microvascularization as a prognostic indicator in neuroblastoma. *Oncotarget* 9 (40), 2617–26157. doi:10.18632/ONCOTARGET.25457
- Tomlin, H., and Piccinini, A. M. (2018). A complex interplay between the extracellular matrix and the innate immune response to microbial pathogens. *Immunology* 155 (2), 186–201. doi:10.1111/imm.12972
- Trujillo, S., Gonzalez-Garcia, C., Rico, P., Reid, A., Windmill, J., Dalby, M. J., et al. (2020). Engineered 3D hydrogels with full-length fibronectin that sequester and present growth factors. *Biomaterials* 252, 120104. doi:10.1016/J.BIOMATERIALS.2020.120104
- Vicente-Munuera, P., Burgos-Panadero, R., Noguera, I., Navarro, S., Noguera, R., and Escudero, L. M. (2020). The topology of vitronectin: A complementary feature for neuroblastoma risk classification based on computer-aided detection. *Int. J. Cancer* 146 (2), 553–565. doi:10.1002/IJC.32495
- Walker, C., Mojares, E., and del Río Hernández, A. (2018). Role of extracellular matrix in development and cancer progression. *Ijms* 19 (10), 3028. doi:10.3390/IJMS19103028
- Wolf, K., te Lindert, M., Krause, M., Alexander, S., te Riet, J., Willis, A. L., et al. (2013). Physical limits of cell migration: Control by ECM space and nuclear deformation and tuning by proteolysis and traction force. *J. Cell Biol.* 201 (7), 1069–1084. doi:10.1083/JCB.201210152
- Xiang, X., Mei, H., Zhao, X., Pu, J., Li, D., Qu, H., et al. (2015). miRNA-337-3p suppresses neuroblastoma progression by repressing the transcription of matrix metalloproteinase 14. *Oncotarget* 6 (26), 22452–22466. doi:10.18632/ONCOTARGET.4311
- Xiao, W., Pahlavanneshan, M., Eun, C.-Y., Zhang, X., DeKalb, C., Mahgoub, B., et al. (2022). Matrix stiffness mediates pancreatic cancer chemoresistance through induction of exosome hypersecretion in a cancer associated fibroblasts-tumor organoid biomimetic model. *Matrix Biol. plus* 14, 100111. doi:10.1016/J.MBPLUS.2022.100111

Supplementary figures

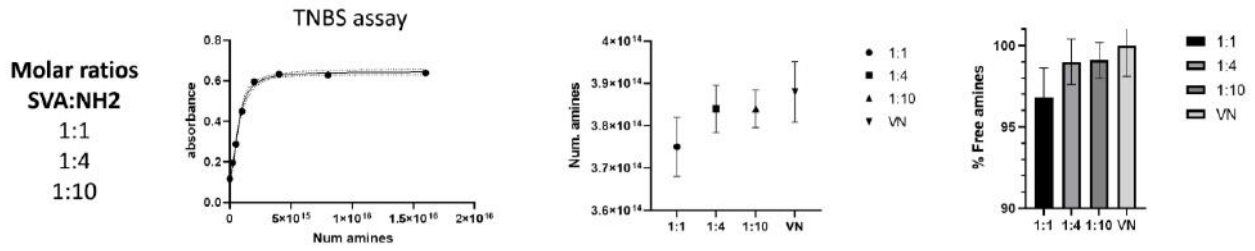


FIGURE S1 PEGylated VN characterization using a TNBS assay. A. Standard curve of VN (left side) and VN free amines (in the middle) for different PEGylation ratios between VN:MAL and percentage of free amines for different PEGylation ratios shown on the right side.

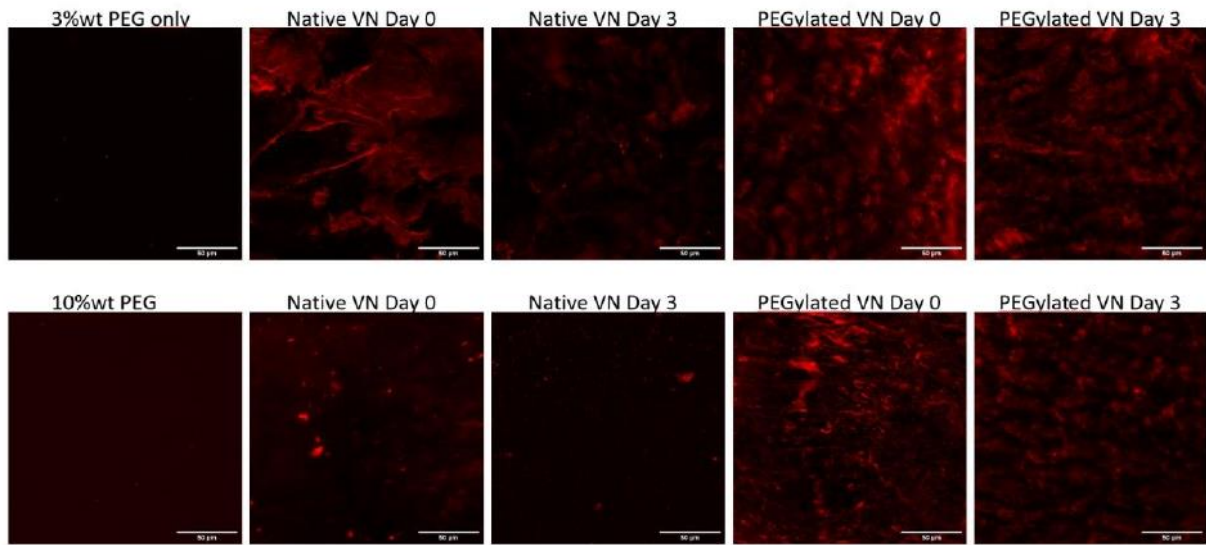


FIGURE S2 VN distribution and retention after incorporation in the 3D hydrogel. On the top, immunofluorescence images of 3 wt% PEG hydrogels and on the bottom, 10 wt% PEG cryosections. Columns represent PEG, PEG+VN (day 0 and 3) and VN/PEG (day 0 and 3) conditions (scale bar 50 μm). Vitronectin was stained with a Cy3 secondary antibody, shown in red in the images.

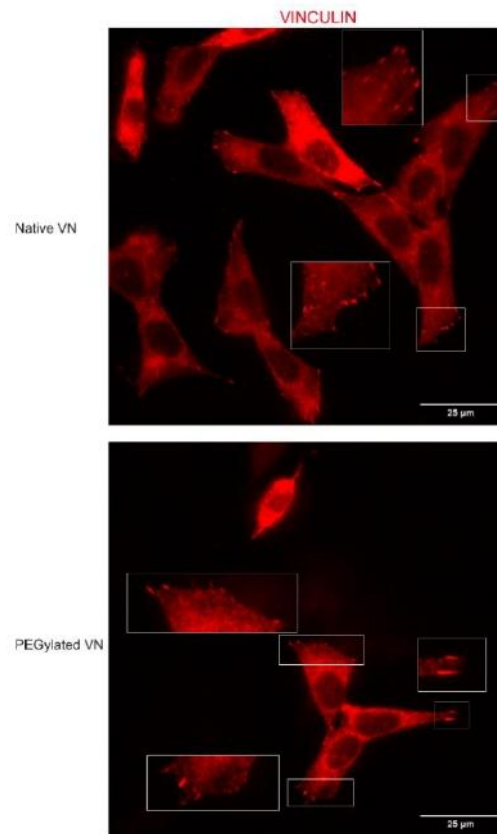


FIGURE S3

Insets of FA images (vinculin in red) of SK-N-BE(2) cells seeded on top of unmodified or PEGylated VN for 24h (scale bar: 25 μ m).

Additional scientific production that complements this thesis

Articles as a coauthor

- I. Integrated CGH/WES Analyses Advance Understanding of Aggressive Neuroblastoma Evolution: A Case Study. Corallo D, Zanon C, Pantile M, Tonini GP, Zin A, Francescato S, Rossi B, Trevisson E, Pinato C, **Monferrer E**, Noguera R, Aliño SF, Herrero MJ, Biffi A, Viscardi E, Aveic S. *Cells*. 2021 Oct 9; 10(10):2695.
- II. Immunometabolism Modulation in Therapy. **Monferrer E**, Sanegre S, Vieco-Martí I, López-Carrasco A, Fariñas F, Villatoro A, Abanades S, Mañes S, de la Cruz-Merino L, Noguera R, Álvaro Naranjo T. *Biomedicines*. 2021 Jul 9; 9(7):798.
- III. Metabolic Classification and Intervention Opportunities for Tumor Energy Dysfunction. **Monferrer E**, Vieco-Martí I, López-Carrasco A, Fariñas F, Abanades S, de la Cruz-Merino L, Noguera R, Álvaro Naranjo T. *Metabolites*. 2021 Apr 23; 11(5):264.
- IV. Impact of extracellular matrix stiffness on genomic heterogeneity in MYCN-amplified neuroblastoma cell line. López-Carrasco A, Martín-Vañó S, Burgos-Panadero R, **Monferrer E**, Berbegall AP, Fernández-Blanco B, Navarro S, Noguera R. *J Exp Clin Cancer Res*. 2020 Oct 28; 39(1):226.
- V. High Oct4 expression: implications in the pathogenesis of neuroblastic tumours. **Monferrer E**, Burgos-Panadero R, Blanquer-Maceiras M, Cañete A, Navarro S, Noguera R. *BMC Cancer*. 2019 Jan 3; 19(1):1.

Communications in scientific meetings

- I. Expresión y significado pronóstico de Oct4 en neuroblastoma. **Monferrer E**, Berbegall AP, Tadeo I, Navarro S, Noguera R. *XXVIII Congreso Nacional SEAP-IAP*. Valencia (Spain), May 2017.
- II. Evasión Inmunológica Del Neuroblastoma Mediante Expresión De OCT4. **Monferrer E**, Zúñiga V, Tadeo I, Navarro S, Noguera R. *XXXI Congreso Latinoamericano de Patología*. Cartagena de Indias (México), August 2017.

- III. Quantitative comparison and reproducibility of pathologist score and digital image analysis of the expression of S100A6 protein in neuroblastoma. Pérez A, **Monferrer E**, Mateu JM, Navarro S, Noguera R. *II Congreso Nacional de Jóvenes Investigadores en Biomedicina*. Valencia (Spain), November 2017.
- IV. Expression of Oct4 in neuroblastic tumors and its implications. **Monferrer E**, Tadeo I, Cañete A, Castel V, Navarro S, Noguera R. *II Congreso Nacional de Jóvenes Investigadores en Biomedicina*. Valencia (Spain), November 2017.
- V. High Oct4 Expression significance in neuroblastic tumors. **Monferrer E**, Tadeo I, Berbegall AP, Cañete A, Navarro S, Noguera R. *ANR Congress 2018*. San Francisco (California, United States of America), May 2018.
- VI. Characterization of cells distribution on Neuroblastoma-OnChip by morphometric techniques. Vieco-Martí I, Martín-Vañó S, **Monferrer E**, Carretero A, Navarro S, Samitier J, Noguera R. *VII Congreso de Investigación Biomédica (CIB2019)*. Valencia (Spain), February 2019.
- VII. Cellular dynamics as a function of time and stiffness in a 3D *in vitro* neuroblastoma model. **Monferrer E**, Martín-Vañó S, Carretero A, García-Lizarribar A, Navarro S, Samitier J, Noguera R. *III Congreso Nacional de Jóvenes Investigadores en Biomedicina*. Valencia (Spain), April 2019.
- VIII. 3D bioprinting models: applications and future perspectives. Berbel M, **Monferrer E**, Martín-Vañó S, Burgos-Panadero R, García-Lizarribar A, Samitier J, Noguera R. *Congreso Anual de Biotecnología (BAC2019)*. Madrid (Spain), July 2019.
- IX. Vitronectin and its receptors: human neuroblastoma 2D *in vitro* characterization. Burgos-Panadero R, **Monferrer E**, Noguera I, Navarro S, Noguera R. *SEHIT2019*. Murcia (Spain), September 2019.
- X. A 3D *in vitro* neuroblastoma model reveal stiffness-dependent vitronectin expression. **Monferrer E**, Martín-Vañó S, Carretero A, García-Lizarribar A, Burgos-Panadero R, Navarro S, Samitier J, Noguera R. *SEHIT2019*. Murcia (Spain), September 2019.
- XI. Gelatin-based hydrogels for neuroblastoma 3D bioprinting. **Monferrer E**, Martín-Vañó S, García-Lizarribar A, Burgos-Panadero R, Navarro S, Samitier J, Noguera R. *IIEJI CIBERONC*. Madrid (Spain), November 2019.

- XII. Bioprinted 3D models can reproduce different *in vivo* behaviors of neuroblastoma by adjusting the model stiffness and cultured cells. **Monferrer E**, Vieco-Martí I, Samitier J, Noguera R. *III EJI CIBERONC*. Online (Spain), December 2020.
- XIII. *In vitro* 3D bioprinted neuroblastoma: A tunable platform to assess extracellular matrix impact on growth and phenotypic cell behavior. **Monferrer E**, Martín-Vañó S, García-Lizarribar A, Samitier J, Navarro S, Noguera R. *ANR Congress 2021*. Online, January 2021.
- XIV. Vitronectin-based polyethylene glycol hydrogels as mimicking tools for neuroblastoma. **Monferrer E**, Dobre O, Azevedo M, Trujillo S, Salmerón-Sánchez M, Noguera R. *IV EJI CIBERONC*. Barcelona (Spain), December 2021.
- XV. Polyethylene glycol hydrogels including full-length vitronectin mimic neuroblastoma microenvironment. **Monferrer E**, Dobre O, Trujillo S, Azevedo M, Trubert-Paneli A, Acevedo-León D, Noguera R, Salmerón-Sánchez M. *SEHIT2022*. Granada (Spain), September 2022.
- XVI. Building silk-fibroin 3D hydrogels with enzymatically cross-linked vitronectin to study neuroblastoma aggressiveness. Vieco-Martí I, **Monferrer E**, López-Carrasco A, Granados-Aparici S, Navarro S, Noguera R. *SEHIT2022*. Granada (Spain), September 2022.
- XVII. Neuroblastoma 3D models: advantages of different hydrogel-based strategies. **Monferrer E**, Vieco-Martí I, López-Carrasco A, Granados-Aparici S, Navarro S, Samitier J, Salmerón-Sánchez, Noguera R. *Workshop of Experimental Models CIBERONC*. Pamplona (Spain), September 2022.

I. INTRODUCTION / STATE OF THE ART

1. Biotensegrity and mechanotransduction in euplastic and neoplastic human tissues

Attraction and repulsion physicochemical forces occurring in atomic and molecular interactions are the main responsible for shaping the universe as we know it and become equilibrated tensile and compressive forces to stabilize the architecture of complex structures [1,2]. In 1960s, this “tensional integrity” was renamed as tensegrity to initially refer to tensegral structures [1]. Currently, this concept defines a self-balancing principle in those structures built with discontinuous rigid struts connected by a continuous network of flexible tension ropes [3]. Despite being a relatively new structural concept, the universality of tensegrity is gradually being accepted and applied in architecture, engineering, or art among other fields, from micro to macro scale [4–6].

Tensegral models can also be applied to the field of biology (biotensegrity), referring to the functional homeostatic organization that support life at all detectable scales, from more complex biological systems to proteins or DNA [7,8]. It is easy to recognize biotensegrity in the human body through the arrangement of muscles, tendons, and bones forming an interconnected network of tension and compression elements, known as the musculoskeletal system, which provides structural stability and enables coordinated movement [7,9]. In fact, cells also obey the biotensegral self-balancing principle, since they are equipped with an internal biopolymeric structure, the cytoskeleton, which hard-wires cell membrane, nucleus, and organelles. Thus, the cytoskeleton gives shape, stability, and elastic rigidity to the cell through the mechanical balance between the tension traveling along the actin fibers and the compression exerted by the microtubules [9,10]. Also, the nucleus and its membrane have their own tensegrity system intertwined with the cytoskeleton tensegrity elements, which shapes the intracellular mechanotransduction pathways regulating chromatin organization and cell proliferation, differentiation, and apoptosis [9,10].

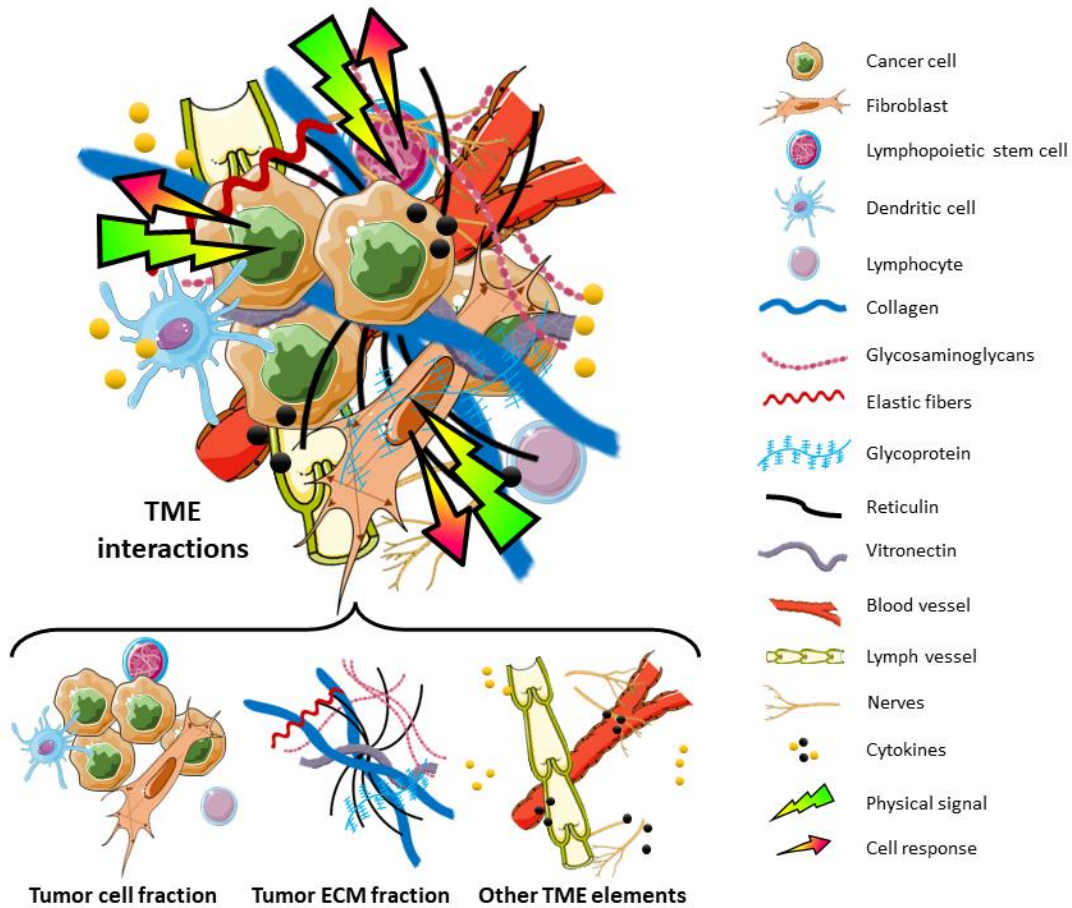
However, cellular biotensegrity is unable to ensure the proper functioning of a tissue by itself. Cells need to communicate with each other and with their surroundings, sensing chemical and mechanical cues and responding to them. In this sense, the biotensegrity of the cellular environment allows the mechanotransduction of the main

physical signals participating in cellular communication pathways [11,12]. The extracellular matrix (ECM) is the set of elements of the ground substance (which mainly act as forces that withstand intermittent compression) and fibrillary elements (which act as elements of continuous tension) that build up the environment that surrounds and supports the cells, joining the tissues of the body [8,13] (Figure 1). The ECM is a complex three-dimensional network that includes among many other elements, collagen, elastin, and fibrillin as fibrillary elements, and glycosaminoglycans, proteoglycans, fibronectin and vitronectin (VN) as non-fibrillary elements, and together with the cytoskeleton and the nucleus, it provides cells with an efficient communication system for the transmission of physical forces [14,15]. Interestingly, cell-ECM interaction conforms a biotensegrity system itself, where cell traction forces and points of resistance within the ECM are balanced [8]. In this regard, the cytoskeleton bridges biotensegral communication between the cell inner and the ECM by molecular assemblies known as focal adhesions (FAs) [16–18]. FAs consist of an agglomerate of integrin receptors that bind to specific ECM ligands through the extracellular domain, and to actin sites of the cytoskeleton via intracellular adapter proteins, such as talin, vinculin and paxillin [19,20]. Remarkably, since tensegrity components from ECM, cytoskeleton and nucleus are interconnected [21], intracellular force transmission might guarantee chromatin stability in stress conditions, thus ensuring physiological cell homeostasis and normal function [22]. When a mechanical cue is received, sensed mainly by FAs, it modifies the cytoskeletal scaffold, which triggers signal amplification and propagation through force-dependent signaling pathways that are sequentially activated until a response is induced. Furthermore, cell-cell junctions mediated mainly by cadherins allow neighboring cell arranged responses to signals affecting a single cell [23,24].

In addition, there are other elements embedded in the tissue ECM that also participate in biotensegral communication processes, setting up the tissue microenvironment (TME) (Figure 1). Thus, the tissue microenvironment is the entire ecosystem that surrounds and nourishes a tissue and includes non-tissue-specific cells (stromal cells, including immune cells), blood vessels, lymphatic vessels, nerves, and various molecules [25–27]. In this way, mechanosensing and mechanotransduction physiological processes occur in the three-dimensional space of the tissue

microenvironment. The biological significance of mechanotransduction is to promote coordinated cytoskeletal reorganizations that determine cell behavior such as gene expression or movement [8], but also redefine the whole tissue shape, which in turn depend on the stiffness and flexibility of the tissue microenvironment [28,29]. Indeed, the mechanical properties of the tissue microenvironment allow cells to remodel the ECM by exerting traction forces, both in homeostasis and in tissue disorders. Consequently, ECM alterations in structure, composition, stiffness, or organization may result in pathological events such as cell denervation, loss of regeneration potential, aberrant wound-healing capacity, and inflammation [30–32].

Figure 1. Representation of the interacting tumor microenvironment elements involved in biotensegrity mechanotransduction signaling. ECM: extracellular matrix, TME: tumor microenvironment.



In this regard, diseases display their own aberrant biotensegral systems, based on the abovementioned mechanisms, which drive illness evolution as occurs in cancer disease [33,34]. Non-cancerous cells within the TME lie among a network of ECM fibers, and are essential not only in tumor progression, but also even before tumorigenesis [35,36].

Specifically, stromal cells can deregulate tissue homeostasis, affecting architecture, adhesion, cell death and proliferation, thus shaping tumor aggressiveness, metastatic capacity, and therapy resistance [37]. Additionally, cancer cells also respond to TME mechanical cues in different ways, for example by promoting TME stiffening, further increasing tumor disorganization and cell motility [38]. Overall, tumor biotensegrity plays a key role in the pathogenesis and evolution of the malignant process, as important as the genetic instability of tumor cells [38]. In this way, several cancer studies highlight cell-ECM biotensegrity crosstalk as a major driving force in cell behavior by shifting cell adaptability towards a malignant phenotype [39–41], so the manipulation of ECM biotensegral system could be explored to develop new therapeutic approaches in cancer [8,42].

2. Cancer cell plasticity and adaptability

Cells continuously perceive their surrounding conditions through the different intermingled biotensegral systems, and generate a specific response linked to an adaptation process. Cellular plasticity is the ability of cells to modify their phenotype without genetic mutations to ensure their viability and functionality within the microenvironment where they are [43,44]. Although certain cell types such as stem cells may display greater plasticity in specific conditions [45,46], phenotype switching is a common process in all body tissues [47–49] and is also recognized as an essential phenomenon upon injury and disease, particularly in neoplasms [50,51]. Generally, malignant cells firstly encounter an acidic, hypoxic, and nutrient deficient TME, where they must then induce anchorage-independent growth to enter and survive in vessels until they finally colonize other organs with a completely new microenvironment [52]. Therefore, cancer cells need to rapidly adapt to different microenvironments during cancer progression to proliferate, invade, metastasize, and eventually resist drug therapy.

To do so, cells mostly exert their plasticity through metabolic reprogramming pathways, which can be driven or not by intrinsic TME epigenetic instability [53,54] (Figure 2). Metabolic reprogramming has been defined as the ability of cancer cells to redirect their bioenergetic pathways to meet the increased energy demand derived

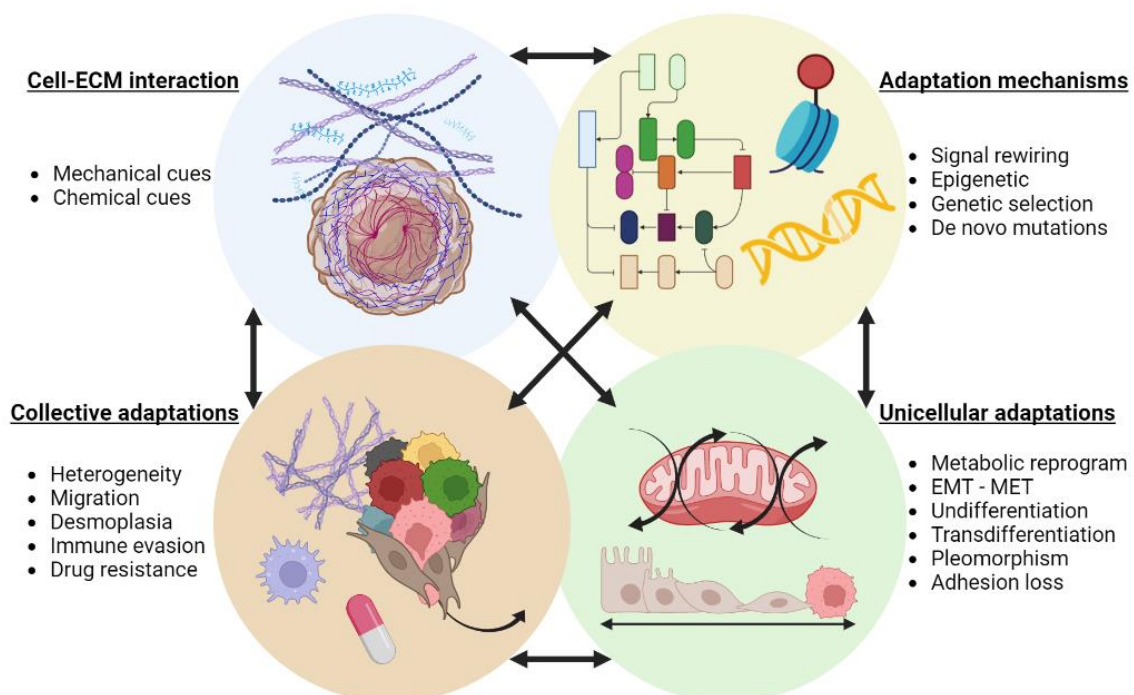
from its proliferation and growth activities, and it has become one of the 10 hallmarks of cancer [55,56]. The Warburg effect has been widely held to be the classical example of a cell-intrinsic reprogrammed metabolic pathway [57]. It refers to the tendency of tumor cells to increase glucose consumption through fermentation (a typical anaerobic process) even when oxygen is available, leading to aerobic glycolysis. In this way, cancer cells consume an elevated amount of glucose and contribute to TME acidosis by lactate production, which enhances ECM remodeling, angiogenesis, and tumor invasion [58,59].

Apart from carbohydrate, amino acid, and lipid metabolism plasticity [60], tumor cells can also undergo morphological and molecular adaptations affecting cell physics when responding to TME biotensegral cues. This is the case of the lower firmness of metastatic cells, that lose the consistency and tensegrity of their scaffold by reducing actin filaments and microtubules [61,62]. Similarly, ECM stiffness facilitates cells to rewire their epithelial cytoskeleton switching to a malignant (pseudomesenchymal) phenotype through epithelial-mesenchymal transition (EMT), which involves loss of both apical-basal polarity and cell-cell junctions [63,64] (Figure 2). Therefore, malignant cells become easily deformable, elastic, and mobile, which induces pleomorphism, enhances infiltration and enables metastasis [65]. Importantly, epithelial-mesenchymal transition is a completely reversible process as it occurs without genetic mutations, so cancer cells can display a hybrid phenotypic state (bridge cells) to invade other tissues and then revert to epithelial phenotype (mesenchymal-epithelial transition, MET) once they encounter the new environment [66]. Moreover, epigenetic reprogramming can also induce deeper cell fate changes by cell reprogramming processes such as dedifferentiation and transdifferentiation [67]. In this regard, partially differentiated cancer cells may dedifferentiate into cancer stem cells, which can perpetuate indefinitely and are mostly drug insensitive. Once a new pool of extremely plastic cancer stem cells has been generated, they can transdifferentiate into different cell lineages or even undergo phenotype mimicking adaptations, thus promoting tumor heterogeneity [53].

Remarkably, cell plasticity derives from the biotensegral intercommunication processes between the cell and its environment, so this phenomenon can also be understood as a process of collective adaptability within the tumor (Figure 2). For

instance, both ECM and cells regulate the mechanical forces exerted on cell–cell connections, which determine the size of those junctions thus affecting neighboring communication and organization [68,69]. Indeed, tumor cell cooperation may lead to a transient spatial rearrangement for collective migration of mobile and non-mobile cells as an entity, that may reveal worse clinical outcomes than single cells [70–72]. To ensure such a collective dissemination, cell clusters adapt to their respective TME by displaying aberrant polarity patterns, and/or remodeling the ECM in specific cases [73–75]. Among ECM modifications, desmoplasia induced by tumor stroma cells disturb tumor cell cytoskeleton homeostasis and the synthesis of ECM proteins [37]. This promotes ECM stiffening and subsequently upregulates malignant behaviors such as loss of euplastic tissue architecture and invasion. In addition, cell-ECM interplay generates molecular signals that shape the inflammatory polarization of immune cells within the TME and may induce tumor immune escape and immunotherapy resistance [76–79].

Figure 2. Interplay between tumor adaptation processes. Cell-ECM interaction (top-left) trigger cancer cell adaptation mechanisms (top-right), which subsequently induce unicellular adaptations (bot-right) coordinating collective adaptations (bot-left). Connecting arrows indicate bidirectional regulation between all adaptation processes. ECM: extracellular matrix, EMT: epithelial-mesenchymal transition, MET: mesenchymal-epithelial transition.



In a different way, TME biotensegrity may lead not only to phenotypic plasticity, but also to a genotypic adaptability. It is widely accepted that activating mutations in oncogenes and silencing mutations in tumor suppressor genes contribute to carcinogenesis, tumor malignancy, and even therapeutic resistance [80,81]. In addition, large cell population sizes, short cell generation time, and high mutation rates all contribute to rapidly increase tumor heterogeneity, thus preparing a clonal adaptive landscape within the tumor, which is responsive to TME signaling [82]. For example, the presence of therapeutic agents in TME causes clonal selection of resistant malignant cells, ensuring tumor survival [83,84]. However, TME conditions may not only exert positive selection of malignant mutations, but also promote the appearance of *de novo* genetic changes. This is the case of epigenetic instability followed by genetic instability, which intertwine in positive feedback during tumor progression [85]. In this sense, it has been seen that many inactivating mutations affecting genes that control the epigenome can disrupt DNA methylation patterns, histone modifications, and nucleosome positioning, which in turn may cause point mutations and disable DNA repair functions, thus increasing genetic alterations.

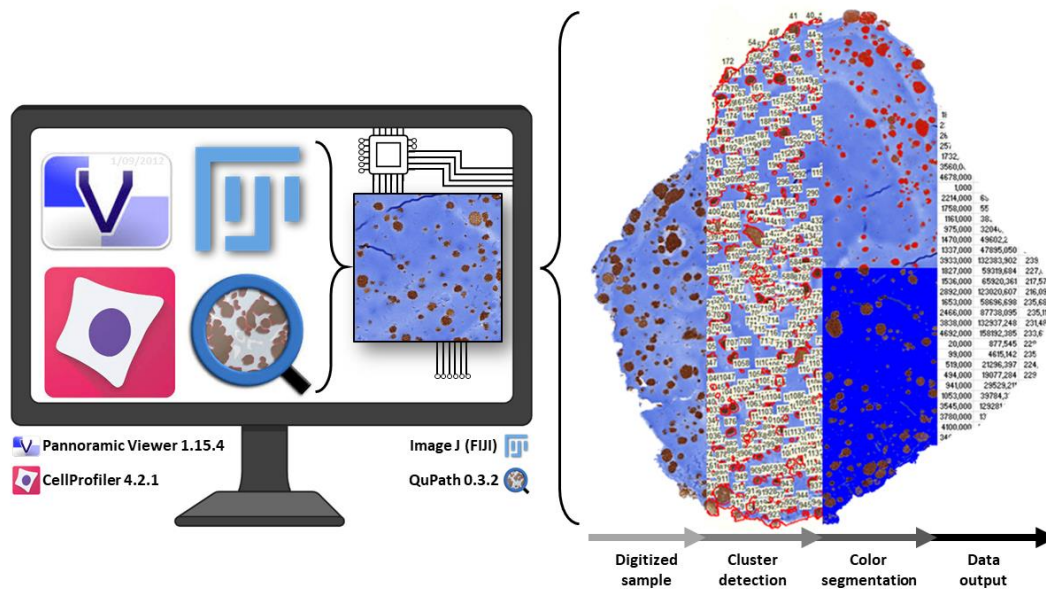
3. Precision diagnostics and therapeutics in oncology

The biotensegral comprehension of cancer is currently providing new insights related to the cell-TME crosstalk determining tumor dynamism and aggressiveness. Therefore, this perspective needs to be incorporated to translational research to release the clinical potential of the basic knowledge that it is being generated. Translational research translates basic science observations into knowledge that can be used to develop powerful targeted treatment options. Moreover, it also benefits from clinic information which turns into a basic knowledge refining, thus consolidating precision medicine strategies [86,87]. Translational oncology is inextricably linked to the clinical field, so cancer diagnosis and oncology research studies have been mostly supported by genetic and histological analysis performed on patient biopsies [88,89]. Histological evaluation is traditionally based on the characterization of stained tissue slides by a pathologist. In this regard, histochemistry (HC) and immunohistochemistry (IHC) are the main staining techniques routinely used in biomedicine due to their simplicity, robustness, and low cost [90,91]. Despite both HC and IHC are used to visualize biological structures within a

tissue section by different chemical reactions, only the latter involves the use of monoclonal and/or polyclonal antibodies. Depending on the protocol, these techniques provide color and contrast to specific TME elements. Remarkably, albeit tissue staining techniques can illustrate biotensegral related features within the tumor (e.g., ECM composition and organization), they were complex to evaluate, so the scientific community has begun to appreciate their importance with the rise of artificial intelligence (AI) and digital pathology in recent decades [92,93].

AI discipline combines computer science and robust datasets to enable problem-solving, thus boosting research forward. Cumulative advances in AI technologies have refined complex classification and prediction making processes that have revolutionized precision medicine [94,95]. In this way, there are several successful clinical applications of AI in oncology such as whole blood multicancer detection, virtual biopsies and advanced clinical decision support systems that combine genomics and clinomics [96]. For instance, machine learning and deep learning approaches are typically used in the digital pathology field to analyze whole slide images of stained tumor tissue. Regarding HC and IHC staining techniques, the implementation of novel image analysis tools provides information that complements clinical practice [97,98]. Indeed, stained histological sections can be converted into digital slides and then processed with image analysis tools, which translates the color pattern of the image into a numerical code of the quantified features (Figure 3). There are plenty of specific proprietary license (Pannoramic Viewer, Imaris) and versatile open-source image analysis softwares (FIJI, QuPath, CellProfiler) which can be chosen depending on the study requirements. Computation not only automates and speeds up data obtention, but also potentially increases the quality and diversity of the acquired information [99–101]. In this way, the greater precision and resolution of these technologies enables the analysis of new complex morphometric and topological features, such as fiber branching or intercellular distances [102,103]. Consequently, digital pathology expands data generation capacity in a reproducible way, decreasing human error and allowing measurement standardization, which in turn improves statistics and enhances the robustness of the conclusions of the studies [104].

Figure 3. Standard digital image analysis pipeline followed with the main four softwares used in this doctoral thesis.



Translational research has clinical objectives, so it demands studies in physiologically relevant samples. For this reason, oncology research is basically nourished by tumor samples from patients, since these contain the most precise information about the overall behavior of the disease. In fact, these studies have contributed to therapy development and improved the survival and life quality of many cancer patients, especially since digital pathology incorporation into the routine of laboratories and hospitals [105]. However, the increasing knowledge has revealed the complex functional interconnection between the multiple elements that constitute the tumor and its microenvironment, as well as the need to generate simplified study alternatives to understand the bases of specific pathogenic mechanisms.

Cancer *in vivo* models, most frequently murine models, have emerged as an alternative to rapidly obtain large number of highly mimetic tumor samples [106]. Two of the most widely used strategies are cell-line-derived and patient-derived xenografts (PDX). The former is based on the engraftment of established human cell lines, whereas the latter is generated by implantation of tumor fragments or disaggregated tumor cells, which are obtained from the material excised from patient [107,108]. Both models can be heterotopic, when inoculation is made in a different place from the original tumor site, or orthotopic, when engrafted into the analogous localization of the primary tumor.

Orthotopic models better imitate original TME conditions, so they exhibit greater pathophysiological relevance than heterotopic models [106]. Nevertheless, regardless the approximation, introducing cancer cells or tumor tissue in complex living organisms such as mice induce tumorigenesis within a biotensegrity network, thus providing cells with the signaling infrastructure they need to properly intercommunicate with TME. For this purpose, animals need to be immunocompromised, immunodeficient or humanized since their physiology differs from human and may impede tumor growth and immune system normal response [109–111]. Typically, these traits are generated by genetic editing tools, which allows upregulating or downregulating gene expression, or even adding (knockin) or removing (knockout, KO) specific genes related to different pathogenic pathways [112–114]. Also, murine models can be genetically engineered (GEMMs) to allow spontaneous murine tumor development within the native tissue and with appropriate immune response [115]. Therefore, tumors thus obtained develop under controlled experimental conditions, so samples display less intratumoral heterogeneity than in native conditions, being thus more reproducible and enhancing analysis robustness. Overall, *in vivo* models improve the comprehension of cellular processes occurring in a natural TME, relevant to therapy designing and response prediction [116–118]. However, working with animal models implies studying tumors with similar complexity to the patient samples, developed in non-human TME growth conditions and several ethics implications [119], which demands alternative ways to study cancer pathogenic basis.

In contrast, established human cell lines have traditionally been the most used *in vitro* experimental model in cancer research. Cell culture is the simplest and cheapest way to study cellular roles in cancer and is responsible for most of the knowledge generated in the oncology field [120]. In this way, the evaluation of multiple biomarkers, genetic aberrations, and therapeutic drugs has shed light on the biological processes driving cancer pathogenesis, aggressiveness, migration, and therapeutic resistance [121,122]. However, it consists of growing cancer cells in a monolayer on a rigid surface (plastic or glass), generally for long time periods under controlled experimental conditions, which typically induce cell phenotypic and genotypic alterations [123]. Moreover, cell line handling entails issues such as cross-contamination, which can generate controversial

results [124]. Nevertheless, the most important limitation is that cell cultures completely ignore TME role on cell behavior, so they cannot recapitulate the pathophysiological biotensegral conditions [124,125].

In the last decades, *in vitro* models have been evolving to 3D approaches, from spheroids to sophisticated cell culture scaffolds, with increasing TME mimicking capabilities [126,127]. Hence, when compared with monolayer cell cultures, 3D *in vitro* strategies better recreate *in vivo* drug availability and cell response, as well as tumor spreading patterns and gene expression profiles [127,128]. Multicellular tumor spheroids (MCS) are scaffold-free 3D cell aggregates that although the lack of ECM mimic *in vivo* cell-cell interactions and diffusional gradients, thus replicating hypoxia and necrosis found in the tumor center besides drug cytotoxicity [129,130]. MCS origin from either multiple cell compaction or by single cell proliferation in flotation conditions on non-adhesive surfaces [131]. However, several cell types are unable to form MCS. Also, the size and shape of MCS presents some limitations when simulating vascularized tumors and some metastasis initiations [131]. Advances in biomaterials have upgraded MCS into a more pathophysiological relevant models by incorporating synthetic and/or natural matrices which support 3D cell culture [129]. Generally, synthetic matrices are made of polymers, bioactive glasses, or self-assembled peptides, whereas natural matrices typically consist of ECM forming biomolecules [131]. Nevertheless, several approximations have engineered mixed matrices combining synthetic and natural components, increasing therefore the model capabilities. Scaffold-based models not only provide cell-ECM intercommunication, but also facilitates precisely fine-tuning ECM features such as composition, stiffness, and architecture, which in turn allows studying their role within the tumor pathophysiology [131]. Regarding their substrate properties, scaffold-based models can be defined as hydrogels, consisting of crosslinked networks of hydrophilic polymers that swell in water, or solid scaffolds, which provide fibrous or porous structures to support ECM deposition. Alternatively, naturally derived scaffolds can be generated by decellularizing ECM from the tissues, which keeps the natural architecture and removes the allogenic cellular antigens. Focusing on increasing manufacturing requirements, 3D culture platforms can be manually shaped, mold casted or 3D printed. In this way, as fabrication sophistication increases, 3D *in vitro*

tumor models become more accurate and complex, so they can better simulate specific features considering TME heterogeneity [132]. Notably, different stroma and tumor cells coexist within the TME, so native tumor conditions cannot be fully recreated by using 3D models containing just one cell type. *In vitro* 3D cell culture strategies abovementioned can overcome this issue by adopting multi-cell-type co-culturing, potentially mimicking *in vivo* spatial cell organization [133] and precisely recapitulating cancer hallmarks [56], that is, becoming tumor organoids (tumoroids) [134]. Also, novel microfluidic technologies can be combined with 3D cultures, particularly in casted and printed scaffolds, to elaborate complex and dynamic tumor-on-a-chip systems, gradually improving the pathophysiological relevance of the models [135].

4. Translational studies in neuroblastoma

Neuroblastoma (NB) represents 7% of childhood cancers worldwide, being therefore the most common solid extracranial tumor in pediatric age. It arises from malignant transformation of the neural crest sympathoadrenal lineage during embryonic development and is mainly diagnosed during the first 18 months of life [136,137]. Although it is mostly detected in adrenal gland (65%), NB can appear in any primary location throughout the sympathetic nervous system, such as in paraspinal ganglia of thorax, neck, and pelvis [137]. Metastatic disease is located in bone marrow, bone, liver, and lymph nodes, and rarely in the skin, brain, or lungs [138]. It is a clinically and biologically heterogeneous disease, causing 15% of cancer-related deaths in children [137,139]. In fact, patients with more benign NB subtypes have spontaneous regression of the disease even without treatment [140], while the more aggressive variants (high-risk, HR-NB) course with metastasis, resistance to existing multimodal therapies and display extremely low survival, below 40% [141,142]. Prognosis depends on many clinical (age and stage), histological (amount of stroma and differentiation degree) and genetic (*MYCN* oncogene amplification, 11q deletion and ploidy) factors, all included in the pre-treatment risk classification system developed by the International Neuroblastoma Risk Group (INRG) [143]. Additional genetic factors, such as recurrent numerical and segmental chromosome aberrations, and mutations have currently been described to upgrade this stratification and improve patient survival rates [144]. For

instance, typical segmental chromosome aberrations and several somatic alterations in *ATRX* or *TERT* genes associated with telomere elongation are linked to poor prognosis [145,146], as well as *ALK* oncogenic mutations. Remarkably, some of the latter have been described driving hereditary NB [144]. Still, despite growing knowledge and clinical advances, HR-NB patients keep on with particularly high mortality rates, highlighting the need to identify and validate new targeted therapies.

As in general cancer research, biotensegrity of NB has been traditionally poorly investigated, but it has now been recognized as one of the most basic mechanisms regulating tumor proliferation and treatment resistance. Our group has previously described some ECM morphological patterns together with vessel structural characteristics to be considered in the histopathologic analysis of NB [147]. In particular, our studies have pinpointed that crosslinked and branching reticulin fibers, scarce glycosaminoglycans and collagen type I fibers within or surrounding tumor niches and abundant pericellular and/or intracellular VN were related to a stiff ECM and poor prognosis in NB patients [102,148,149]. Indeed, these factors were found to define ultra HR-NB aggressiveness in samples from our patient cohorts when combined with abundant irregularly shaped vessels such as large blood vessels, intermediate lymphatic capillaries and small collector vessels [150–152].

Nevertheless, NB is an extremely complex and plastic tumor due to its intrinsic heterogeneity, so it can adapt and develop in different primary and metastatic environments [153,154]. As previously mentioned in Section 2., tumor malignant and non-malignant cells reprogram their metabolism in response to TME biotensegral cues, thus enabling coordinated cellular responses that remodels the TME according to tumor needs (e.g., regulating cell immune infiltration). Simultaneously, metabolic reprogramming gives rise to differential biomarker expression within the different cell populations of the tumor depending on their functional states. In this regard, cell undifferentiation markers such as OCT4 have revealed the presence of extremely plastic cells displaying a cancer stem cell-like phenotype, and their amount has been closely related to NB patients' survival by us and others [155–158]. In addition, this NB cells can transdifferentiate between an adrenergic (sympathetic) and mesenchymal (neural-crest-like) state, which is analogous to the abovementioned epithelial-to-mesenchymal

transition [159,160]. Thus, bridge cells present an intermediate phenotype that can be epigenetically regulated to foster different transcriptional outputs [161]. For instance, loss of GD2 lead this transition to mesenchymal state, which has been correlated with therapy resistance and relapse in NB [162]. Moreover, all these phenotypic plasticity processes are complemented by additional genotypic adaptability. Indeed, we have described that ECM stiffness triggers *de novo* genetic aberrations in genes such as *KANK1* and *DOCK8* [163], which regulate cytoskeleton organization and cell movement processes [164,165].

Altogether, NB exhibit formidable adaptability that not only facilitates tumor progression and survival, but also allows NB cell growth in *in vivo* and *in vitro* experimental environments. This capacity is widely shared by different cancers and has allowed biomedical research to develop current knowledge and therapies. There are more than 100 well-characterized established cell lines available for NB modeling [166], which are classified in three distinct phenotypes: N-type or neuroblastic cells (e.g., SH-SY5Y) are sympathoadrenal neuroblasts; S-type or substrate-adherent cells (e.g., LA1-5s) are non-neuronal precursor cells; and I-type or intermediate cells (e.g., SK-N-BE(2)) combine both previous phenotypes and exhibit cancer stem cell aggressive features [167]. NB cell lines as well as patient or model derived materials (cells or tissue) can be inoculated, mostly in mice, to produce a wide variety of syngeneic, transgenic, xenograft, and humanized *in vivo* models for neuroblastoma research and drug efficacy studies [168]. Additionally, a set of GEMMs have been developed specifically to induce NB after the TH-*MYCN* model, which was the first to demonstrate the *MYCN* role in NB pathogenesis, thus identifying the oncogene pathway as a potential therapeutic target [169]. In fact, some NB GEMMs have been developed from the TH-*MYCN*, including new relevant NB mutations, such as the TH-*MYCN*/*ALK*(F1174) model, which has been preclinically used to evaluate *ALK* inhibitors and elucidate the crosstalk between *ALK* and *MYCN* pathways in NB [170]. Depending on the strategy, models succeed recreating specific NB features related to histology traits, genetic aberrations, or invasion patterns. For instance, we have established VN-KO PDX NB murine models to investigate the implications of VN and its ligands in NB behavior [171]. However, limited engraftment rates, coupled with murine stromal elements in the samples, and the ethical efforts to

replace animals in biomedical experimentation have shifted the research focus towards 3D *in vitro* models.

In recent years, growing evidence on the implication of biotensegrity and TME in tumor pathogenesis has led to the development of new 3D cell culture strategies mimicking NB TME to facilitate their study [172,173]. Multiple NB cell lines have been used to establish MCS models, which have proved to simulate some tumor original features besides their suitability for stem cell research and therapy testing studies [174,175]. Analogous scenarios have been obtained with several 3D hydrogels fabricated with collagen, gelatin, or chitosan, adopted to carry out a set of NB behavior studies [176–178]. Further studies in hydrogel scaffolds have recreated natural cellular structures and interactions by co-culturing mesenchymal stem cells and human umbilical vein endothelial cells together with NB cells [179]. Recently, collagen-based solid scaffolds containing glycosaminoglycans or nanohydroxyapatite have been tested in NB research regarding bone and bone-marrow metastasis treatment [180]. Even so, these studies mostly focus on deciphering NB behavior or the effect of traditional cytotoxic or cytostatic therapeutic strategies by using more relevant NB models. Consequently, chemotherapy and radiotherapy continue acting not only on the malignant and stromal cells of the tumor, but also non-specifically injuring ECM elements, which can promote relapse or treatment resistance [181]. Therefore, modern oncology demands new and more precise therapeutic approaches, which should manipulate specific biotensegrity cues to reverse the malignant tumor phenotypes.

To meet this need, this thesis applies current digital image analysis tools to study the ECM as a therapeutic target in *in vitro* NB models, which are increasingly relevant due to tissue engineering advances [181]. In this sense, several studies in *in vitro* 3D NB models are presented here to discern some of the therapeutically targetable biotensegral aspects defining NB behavior. Specifically, this thesis evaluates the effect of the ECM stiffness (Article I), the influence of Schwann stroma cells (Article II) and the impact of certain non-cellular ECM elements such as VN (Article III) on NB cell behavior, as well as other uncommunicated results on malignant cell phenotypes obtained from the *in vitro* 3D NB models. Ultimately, it is expected that herein presented models can be optimized for developing new biotensegral-based therapies for HR-NB patients.

II. METHODOLOGY

1. Experiment guideline

Following the tumor biotensegrity principle, the experimentation herein provided aimed to unravel some basic aspects of the mechanical signal transmission and their influence on NB behavior, thus comparing monolayer cell culture approaches (without ECM) with 3D cell culture hydrogels (with soft or stiff ECM).

In this sense, uniaxial compression assays were performed in hydrogels, NB human and orthotopic NB mice samples to evaluate the ECM stiffness (Article I). Once hydrogels were basically characterized in a mechanical and morphological way, cell dynamics and behavior were evaluated by HC and IHC for each experimental condition (Article I, Article II and additional uncommunicated results). Further studies on 3D *in vitro* NB models assessed the influence of Schwann stroma cells on NB cell behavior, carrying out a deeper characterization for genetic alterations and VN synthesis (Article II). Finally, the study of VN impact on NB cell behavior was continued in Article III. VN inclusion pattern within the PEG scaffolds was defined, as well as its capability to promote cell adhesion or modify the mechanical properties of the models. Also, it was checked whether VN allowed NB cells growth and VN synthesis.

2. Cell cultures

Throughout this thesis focused on NB models, we have studied a total of three cell lines relevant to the pathophysiology of this tumor, two of them neuroblastic (SK-N-BE(2) and SH-SY5Y), and the other stromal (SW10). All three cell lines originally came from American Type Culture Collection (Manassas, VA, USA). SK-N-BE(2) *MYCN*-amplified and SH-SY5Y *ALK*-mutated human NB cell lines were chosen because their genetic features are representative for 50% and 14% of high-risk NB cases, respectively. We chose SW10 for coculture purposes since Schwannian stroma is related to patient prognosis [182]. SW10 mouse cells were used instead of a human Schwann cell line due to availability reasons.

NB cells were expanded in supplemented IMDM growth media and SW10 in supplemented DMEM at 37 °C and 5% CO₂ atmosphere as stated in the articles.

Monolayer and 3D cultures were kept under same culture conditions. Cells were incorporated to 3D hydrogels during their fabrication at 2×10^6 cells mL^{-1} for NB cells and at 2×10^5 cells mL^{-1} for SW10 cells. Cocultures with SW10 were grown in IMDM as NB cell line cultures. The media was replaced every 3 days in all culture procedures.

3. *In vitro* 3D platforms

Two different approaches for 3D NB modeling have been tested in this thesis. GelMA/AlgMA bioprinted hydrogels are described in Article I and Article II, whereas mold casted VN/PEG fabrication is shown in Article III. Briefly, hydrogels were synthesized combining an ECM-emulating material (gelatin methacrylate in GelMA/AlgMA and VN in VN/PEG) with a non-biodegradable component (alginate methacrylate in GelMA/AlgMA and PEG in VN/PEG). Previous PEGylation of VN was required before its incorporation to the PEG network. The bioinert compound (AlgMA or PEG) was used to adjust the mechanical properties of the hydrogel in both models. Importantly, UV light polymerization was applied for GelMA/AlgMA, but VN/PEG hydrogels were chemically crosslinked.

In Article I, GelMA/AlgMA hydrogels supported SK-N-BE(2) cell culture, while in Article II, GelMA/AlgMA were used to SW10 coculture with SK-N-BE(2) or SH-SY5Y. VN/PEG hydrogels were used to culture SK-N-BE(2) cells in Article III.

4. Ethics approval and consent to participate

Most of the experiments carried out in this thesis have been performed in 3D *in vitro* NB cell cultures, which do not imply ethical concerns. However, NB human and orthotopic NB mice samples were used in mechanical compression studies presented in Article I. These studies aimed to evaluate *in vivo* sample stiffness to ensure that 3D NB models herein developed properly recreated it *in vitro*. The use of these samples has been properly approved by the corresponding Ethical Committees.

Experimentation with human samples was approved by the Ethical Committee of the University of Valencia (reference B.0000339 29/01/2015). Participants or their family members/legal guardians provided written informed consent for studies performed in our laboratory.

Experimentation with animal samples were carried out in accordance with the standards and care approved by the institutional ethical animal care committee (reference 2015/VSC/PEA/00083).

5. Digital image analysis

Digital images were obtained from most of the studies carried out in this work, which were informatically processed and analyzed by custom mathematical algorithms. Digital image analysis was used to evaluate cell behavior and growth dynamics, morphological parameters, biomarker expression, as well as to determine hydrogel features.

Images mostly came from 3D models, but also from cytochemical (CC), immunocytochemical (ICC), and immunofluorescent (IF) stains performed on monolayer cell cultures. GelMA/AlgMA models were paraffin embedded, sectioned, HC or IHC stained and scanned (Article I and Article II, and other uncommunicated results). Depending on the experiment, some VN/PEG models were freshly stained by fluorescence and IF, while others were flash frozen in OCT, cryosectioned and IF stained. VN/PEG photographs were taken by fluorescence or confocal microscopy (Article III).

Different computer tools have been combined to obtain the results herein presented. HistoQuant and NuclearQuant modules of the Panoramic Viewer 1.15.4 software were adjusted to analyze HC and IHC images (Article I, Article II, and additional uncommunicated results). Fluorescence images were processed by FIJI to evaluate cell growth dynamics, by CellProfiler 4.2.1 to detect and measure focal adhesions, by QuPath 0.3.2 to evaluate VN incorporation within the PEG network, and with Imaris to assess the presence of VN in confocal microscopy images (Article III).

6. Statistics

D'Agostino-Pearson Normality test or Shapiro-Wilk test were performed on datasets. When comparing more than two groups, analysis of variance test (ANOVA test) with a Tukey's post hoc test was used for normal distributed populations, while Kruskal-Wallis test with a Dunn's post hoc test was used for not normal distributed populations. When comparing two groups, parametric (t-test) or nonparametric (Mann-Whitney test) tests were performed depending on dataset distribution. When data quality was not enough to perform quantitative statistical analysis, it was qualitatively assessed.

7. Thesis illustrations

The illustrative diagrams included in this work have been generated using the graphic resources provided by Servier Medical Art (smart.servier.com) or created with BioRender.com

III. HYPOTHESIS, AIMS AND JUSTIFICATION OF THE THESIS BY ARTICLE COMPENDIUM

1. Hypothesis

Considering that,

1.- The tension and compression physical forces that define biotensegrity display a stabilized three-dimensional distribution and are one of the main responsible elements for the functioning of biological tissues, including tumor tissues.

2.- Tumor plasticity allows cancer cells to adapt phenotypically and genotypically to the mechanotransduction signals it receives from the surroundings.

3.- The intercommunication between cellular and non-cellular elements within the tumor microenvironment promotes extracellular matrix remodeling and malignant cell fate, which define cancer aggressiveness and its drug response.

We hypothesize that, three-dimensional *in vitro* models with modulable biotensegral conditions trigger tumor cell plasticity and adaptability similar to *in vivo*, evinced by digital image analysis, which allows unraveling specific pathways that confer cancer aggressiveness and constitute potential excellent tools in preclinical tests.

2. Aims

General

The general purpose of this doctoral thesis is to apply the knowledge of the group on neuroblastoma extracellular matrix architecture to develop tumor-like *in vitro* microenvironments, with controllable mechanical properties, that mimic neuroblastoma pathophysiology, depicting the mechanical cues determining neuroblasts malignancy that can be therapeutically targeted.

Specifics

1.- *Studies in 3D in vitro gelatin/alginate hydrogels:*

- a. Bioprint 3D gelatin plus alginate biocompatible scaffolds for neuroblastoma cell culture.

- b. Determine the mechanical properties of the bioprinted hydrogels.
- c. Compare cell behavioral adaptations of two different aggressive neuroblastoma cell lines, SK-N-BE(2) and SH-SY5Y, when monocultured or co-cultured with stromal Schwann cells, in different stiffness conditions and culture time points.
- d. Quantify hydrogel degradation, cell cluster dynamics, migration-related protein synthesis, differentiation, and metabolism dynamics by digital image analysis to define neuroblastoma cell behavior.

2.- *Studies in 3D in vitro polyethylene glycol hydrogels:*

- e. Fabricate 3D polyethylene glycol biocompatible scaffolds that incorporate vitronectin to recapitulate high-risk neuroblastoma growth conditions.
- f. Ensure pathophysiological stiffness, functional vitronectin crosslinking and cell viability to validate the usefulness of the model.
- g. Characterize cell cluster growth and vitronectin synthesis adaptations related to stiffness, time of culture and the presence of crosslinked vitronectin.
- h. Evaluate vitronectin potential as a secreted biomarker and therapeutic target in high-risk neuroblastoma.

3. Justification of the article compendium

The present doctoral thesis research is presented as a compendium of three scientific publications with complementary work shared at scientific conferences. Additional uncommunicated relevant data is herein provided to further increase the knowledge of the mechanical transmission signals that occur within the 3D tumor microenvironment and drive neuroblastoma cell behavior, highlighting the potential of the *in vitro* models as drug-testing platforms.

The independent findings of these papers converge to reach the same goal: to establish general guidelines for optimal 3D modeling of tumor microenvironments, using high-risk neuroblastoma as tumor of reference, to obtain realistic cell culture *in vitro* platforms where to carry out biological and preclinical studies.

In article I, titled: **A three-dimensional bioprinted model to evaluate the effect of stiffness on neuroblastoma cell cluster dynamics and behavior**, we highlight the need of 3D conditions for cell culture and the role of the extracellular matrix stiffness when recapitulating the mechanical cues that trigger cell adaptation response over time, such as changes in proliferation and mRNA metabolism activity.

Article II, titled: **Digital image analysis applied to tumor cell proliferation, aggressiveness, and migration-related protein synthesis in neuroblastoma 3D models**, extends article I conclusions by evaluating migration-related protein synthesis. We evidence distinctive behavior of aggressive neuroblastoma cell lines depending on their genetic characteristics (*MYCN* amplification or *ALK* mutation), as well as the influence of stromal cells on cancer cells behavior, thus pinpointing the complexity of neuroblastoma.

In article III, titled: **Vitronectin-based hydrogels recapitulate neuroblastoma growth conditions**, we reproduce part of the high-risk neuroblastoma extracellular matrix by incorporating full-length vitronectin as the only bioactive molecule within the hydrogels, and seek to characterize the impact of this specific microenvironment on neuroblastoma cells.

IV. RESULTS AND DISCUSSION

1. Contribution of 3D scaffolding to NB biotensegrity mimicry

Environmental physical forces affecting cell cultures are unavoidable regardless the cell culture approach. In traditional cell monolayer cultures performed, cells typically need to adhere to the substrate to start proliferating. Indeed, culture devices are normally made of rigid plastic or glass, which have been proved to affect cytoskeletal organization, thus regulating cell adhesion, spreading, migration and proliferation [183,184]. Even when cells grow in floating conditions, they can sense physical forces from the liquid surrounding or from the neighboring cells when forming cell aggregates. However, none of this culture approaches fully resembles *in vivo* cell-cell or cell-ECM interactions. In this regard, 3D scaffolding strategies herein presented provide key improvements on pathophysiological signal mechanotransduction, and therefore on appropriate cell responses, thus overcoming some of the limitations of scaffold-free cell cultures. The following sections exhibit some of the technical aspects considered for the design of pathophysiological relevant hydrogels.

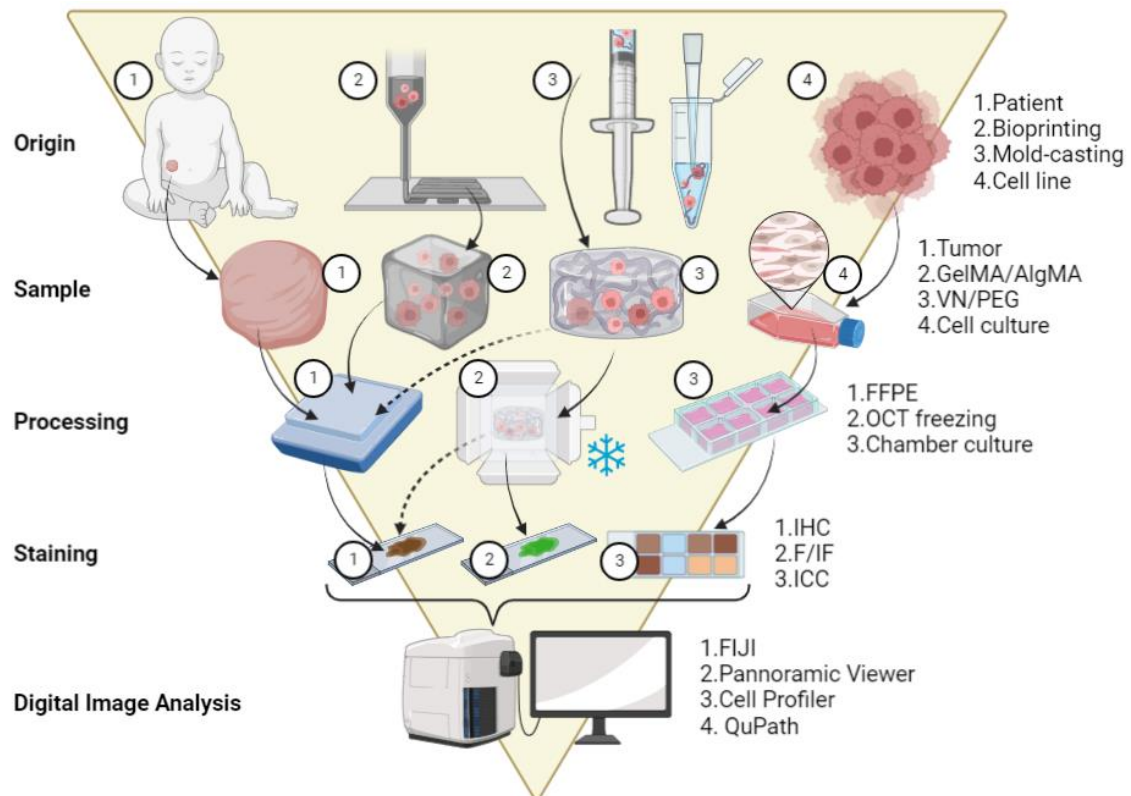
1.1. Technical features influencing 3D model designing

Tissue engineering brings together a set of sophisticated tools and techniques for biomimetic tissue fabrication. Since all the available strategies present several benefits and limitations, the choice usually depends on the purpose of the study and influences model designing. Regarding this, Figure 4 represents the main experimental workflow followed for evaluating the 3D *in vitro* NB models herein generated in comparison with traditional cell cultures and human NB biopsies.

1.1.1. *Architecture regarding fabrication procedure*

Biotensegrity elements are orchestrated within the tumor tissue forming dynamic and precise interactions. Therefore, compounds forming the scaffolds, as well as their disposition and assembling are key aspects to ensure biotensegrity resembling and influence cell distribution and signal transduction. Table 1 shows a comparison regarding the technical aspects of NB tumors development and the generation of the different scaffolds and traditional cell cultures herein performed.

Figure 4. Workflow from obtention to analysis of human NB biopsies and NB experimental models used in this thesis. AlgMA: alginate methacrylate, F: fluorescence, FFPE: formalin-fixed paraffin-embedded, GelMA: gelatin methacrylate, ICC: immunocytochemistry, IF: immunofluorescence, IHC: immunohistochemistry, OCT: optimal cutting temperature compound, PEG: polyethylene glycol, VN: vitronectin.



The architecture of the generated models has been defined to a greater or lesser extent depending on the manufacturing method. For instance, bioprinting technology used in GelMA/AlgMA hydrogels allowed to generate a precise and uniform structures by layer crosslinking; this facilitated the homogeneous distribution of cells and provided an optimal scaffolding for robust determination of the mechanical properties. Although it was not exploited during this project, bioprinting offers efficient ways not only to perform complex cell co-cultures that require different cell locations within the scaffold, but also to generate mechanical patterns with specific stiffness gradients.

Alternatively, using casting molds for hydrogel generation, as in the case of VN/PEG models, enabled to speed up the fabrication process, creating structures of limited complexity. In mold casting approach, cell distribution depended on user manual skills, thus originating hydrogel regions with different cell densities. Nevertheless, this uneven

cell distribution gives rise to a better representation of the intratumoral heterogeneity observed *in vivo*, so it could benefit studies on intratumoral differential cell behavior. In contrast to bioprinting, mechanical properties assessment in mold casted hydrogels depended on the specific structural quality of each individual sample. Hence, centric areas of the hydrogels were avoided during nanoindentation due to their irregular surface.

Table 1. Distinctive features of human NB biopsies and NB experimental models used in this thesis associated with sample origin. 3D: three-dimensional, AlgMA: alginate methacrylate, GelMA: gelatin methacrylate, NB: neuroblastoma, PEG-MAL: polyethylene glycol-maleimide, SH-PEG-SH: dithiol-polyethylene glycol, TME: tumor microenvironment, VN: vitronectin, VPM: peptide containing Val-Pro-Met amino acid sequence, ✖: not applicable, ✓: confirmed.

	NB	Monolayer cell culture	GelMA/AlgMA	VN/PEG
Fabrication				
<i>Procedure</i>	<i>In vivo</i> development	Cell seeding	3D bioprinting	Mold casting
<i>Components</i>	Full TME	Cells	Cells GelMA AlgMA	Cells PEG-MAL PEGylated VN Crosslinkers
<i>Stiffening</i>	TME features	✖	[AlgMA]	[PEG-MAL]
<i>Crosslinking</i>	✖	✖	UV light	VPM SH-PEG-SH
<i>Degradability</i>	✖	✖	GelMA	VPM Pegylated VN
Architecture				
<i>Form</i>	Variable	Flat	Cubic	Cylindric
<i>Accuracy</i>	✖	Absolute	Great	Acceptable
Cell population				
<i>Biocompatibility</i>	✓	✓	✓	✓
<i>Distribution</i>	Heterogeneous	Homogeneous	Homogeneous	Heterogeneous

Besides “macroscale” architectural features defining cell distribution or model morphology, other subtle but important structural aspects such as porosity, pore size, grain size and topography provide mechanical cues affecting cell cycle and mobility [185–187]. Albeit these variables have been partially explored in this thesis, they allow cell migration studies by adjusting scaffold composition, fabrication procedure and crosslinking methodology. Indeed, the scaffold composition was herein regulated giving rise to slightly different pore sizes as shown in Article I, and despite VN/PEG hydrogels are also expected to show different porosity in different compositions, it remains to be validated in this thesis.

1.1.2. Digital pathology as a unifying approach to sample analysis

When attempting to recreate *in vitro* a complex system such as cancer biotensegrity, a robust analysis method is needed to validate the model and perform reliable comparative studies between *in vitro* model and *in vivo* neoplastic tissue. Thus, sample processing and data analysis influence results obtention, so ideally both *in vivo* and *in vitro* samples should be processed identically. Sample processing and analysis differences between NB tumors, monolayer cell cultures and hydrogels used in this thesis are compared in Table 2.

Cancer biopsies are routinely processed in hospitals with optimized informative tools. Specifically, NB patient samples are normally touch imprinted for H-E staining or FISH and then divided in fragments for freezing or paraffin embedding. Frozen samples can be used for DNA extraction and subsequent genetic analysis, mechanical assessment or even for paraffin embedding, whereas paraffined samples are typically used for both DNA extraction and tissue staining approaches (HC, IHC, F, IF, FISH).

As well as NB samples, GelMA/AlgMA hydrogels were used for mechanical compression assessment, DNA extraction and subsequent SNP analysis (fresh samples) as well as for paraffin embedding and later HC and IHC staining. In contrast, despite fresh VN/PEG hydrogels could be mechanically assessed by nanoindentation and stained with F and IF techniques, they exhibit severe complications when DNA extraction or paraffin embedded. As previously reported [188], VN/PEG hydrogels were sensitive to standard paraffin processing, leading to scaffold structure distortion, entanglement with support

material and incomplete infiltration, which resulted in few non-informative sections. In fact, cell cultured VN/PEG models were frozen in OCT for later cryosectioning and staining, but still few samples preserved an optimal HC and IHC staining.

Table 2. Distinctive sample features according to processing and analysis of human NB biopsies and NB experimental models used in this thesis. AlgMA: alginate methacrylate, CC: cytochemistry, F: fluorescence, FFPE: formalin-fixed paraffin-embedded, FISH: fluorescence in situ hybridization, GelMA: gelatin methacrylate, HC: histochemistry, ICC: immunocytochemistry, IF: immunofluorescence, IHC: immunohistochemistry, NB: neuroblastoma, PEG: polyethylene glycol, VN: vitronectin, OCT: optimal cutting temperature compound, SNPa: single nucleotide polymorphism array, ✕: not applicable, ✓: applicable.

	NB	Monolayer cell culture	GelMA/AlgMA	VN/PEG
Processing				
<i>FFPE</i>	✓	✕	✓	Inefficient
<i>FFPE sectioning</i>	✓	✕	✓	Inefficient
<i>OCT freezing</i>	✓	✕	Not tested	✓
<i>Cryosectioning</i>	✓	✕	Not tested	Suboptimal
<i>DNA extraction</i>	✓	✓	✓	Inefficient
<i>Fresh</i>	✓	✓	✓	✓
Analysis				
<i>SNPa</i>	✓	✓	✓	✕
<i>Mechanical test</i>	Compression	✕	Compression	Nanoindentation
<i>Stains tested</i>	HC, IHC, F, IF, FISH	CC, ICC	HC, IHC	HC, IHC, F, IF
<i>Digital image analysis</i>	✓	✓	✓	✓

Regardless the method, all stains lead to digital images or photographs, which could be informatically segmented and evaluated. Figure 4 shows how different sample processing converge in digital image analysis. In this way, digital pathology tools gather different data outputs in a comparable way, also providing robust high throughput analysis. Additionally, digital image analysis perfectly fits in hospital routine, not only by complementing pathologist's assessment with objective quantification, but also

upscaling the accuracy and broadening the variables that can be analyzed. Remarkably, although digital image analysis is still a semiautomatic process, that is, it requires researcher supervision, this workflow is currently incorporating machine learning and deep learning pipelines from AI, thus moving digital image analysis towards full automatization.

1.1.3. Manufacturing cost demands model mimicry-technical balance and purpose fitness

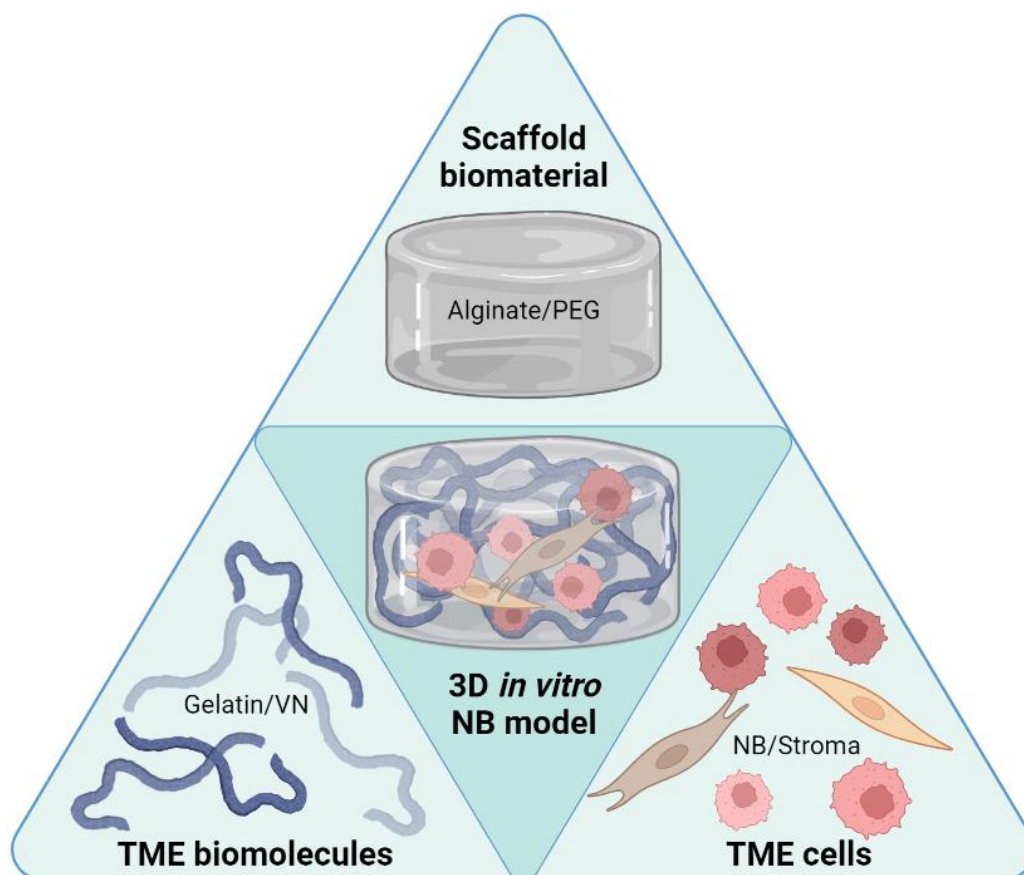
In the previous subsections it has been exposed the importance of the model architecture to recreate tumor biotensegrity, as well as the need to analyze its action mechanisms and its effects on the model behavior by using the adequate tools. However, technological requirements determine the experimentation cost, which might become a limiting factor as it influences the capability to obtain models with enough relevant biotensegrity.

Hydrogels herein presented have been generated with different manufacturing techniques (bioprinting in GelMA/AlgMA and mold casting in VN/PEG) and, in addition, they recreated different specific aspects of the NB biotensegrity (stiffness plus Schwann presence in GelMA/AlgMA and stiffness plus VN in VN/PEG). Regarding this, cost differences must be considered in addition to the advantages and limitations of each model. Bioprinting is a flexible and adjustable technology that would allow incorporating the biotensegral features developed in VN/PEG hydrogels. However, using such a cutting-edge technology would unnecessarily increase the production and experimentation costs, without a relevant neither evident improvement over molds. It is appropriate to adjust technical complexity and physiological relevance level according to the experimental requirements. Thus, using of simpler and cheaper models such as VN/PEG hydrogels better fits for preliminary studies, focused on exploring the basic mechanisms underpinning NB biotensegrity related to VN. In contrast, more expensive techniques such as bioprinting would be suitable for complex studies, where multiple biotensegral factors are considered to acquire a more realistic knowledge of the tumor pathophysiology.

1.2. Improvement of translational research focusing on ECM pathophysiological relevance

Three-dimensionality provided by hydrogels allows for vital cell-cell and cell-ECM interactions that do not take place in monolayer cell cultures. Moreover, multiple biological factors can be incorporated into hydrogels, individually or in combination, to gradually increase the pathophysiological relevance of the models. The study of biotensegrity pathways regulating neoplasia development such as NB is still an incipient field, so it requires simple models that isolate the role of the different participating elements. As indicated in the Introduction, section 4, more complex and relevant NB models than those presented here have been developed. Nevertheless, despite these highly relevant models are mostly used for testing traditional therapies, they would not be suitable for the specific biotensegral studies carried out in this work due to their many confounding variables.

Figure 5. Components used in this thesis for 3D *in vitro* NB model fabrication, classified according to tissue engineering triad. 3D: three-dimensional, NB: neuroblastoma, PEG: polyethylene glycol, TME: tumor microenvironment, VN: vitronectin.



Emulating the tissue engineering triad [189] shown in Figure 5, this thesis brings together basic regulation of scaffold mechanical properties, incorporation of functional

elements related to the pathophysiological relevance of the NB ECM, as well as coculture approaches to evaluate their effects on tumor cell behavior. Table 3 shows the pathophysiological improvements provided by the models in comparison to traditional cell culture. Importantly, stiffness regulation has been combined with stroma cells or VN incorporation, although new alternatives combining these three variables and others will be explored in future studies to further increase the biotensegrity pathophysiological relevance of the models.

Table 3. Comparison between the pathophysiological relevance of NB and that of the experimental models used in this thesis. 3D: three-dimensional, AlgMA: alginate methacrylate, ECM: extracellular matrix, GelMA: gelatin methacrylate, NB: neuroblastoma, PEG: polyethylene glycol, VN: vitronectin, TME: tumor microenvironment, ✕: not applicable/not tested.

	NB	Monolayer cell culture	GelMA/AlgMA	VN/PEG
Mechanics				
<i>Stiffness</i>	0.17-8.45 kPa	✕	0.32-9.10 kPa	0.33-5.45 kPa
<i>Degradability</i>	ECM remodeling	✕	Partial	Partial
ECM				
<i>Relevance</i>	Full	✕	Limited	Limited
<i>Composition</i>	Variable	✕	Gelatin (collagen)	VN
Cells				
<i>Interaction</i>	TME crosstalk	Monoculture	Mono/coculture	Monoculture
<i>Populations</i>	Neuroblastic	SK-N-BE(2)	SK-N-BE(2)	SK-N-BE(2)
		SH-SY5Y	SH-SY5Y	✕
	Schwannian	SW10	SW10	✕
	Endothelial	✕	✕	✕
	Immune	✕	✕	✕
<i>Initial density</i>	Unknown	$\sim 2 \times 10^5$ c/ml	$\sim 2 \times 10^6$ c/ml (NB) $\sim 2 \times 10^5$ c/ml (SW)	$\sim 2 \times 10^6$ c/ml
<i>Spatial growth</i>	3D	Flat	3D	3D
	Spheroidal mass	Monolayer	Clusters	Clusters

1.2.1. Mechanical properties of the hydrogels: Stiffness and degradability

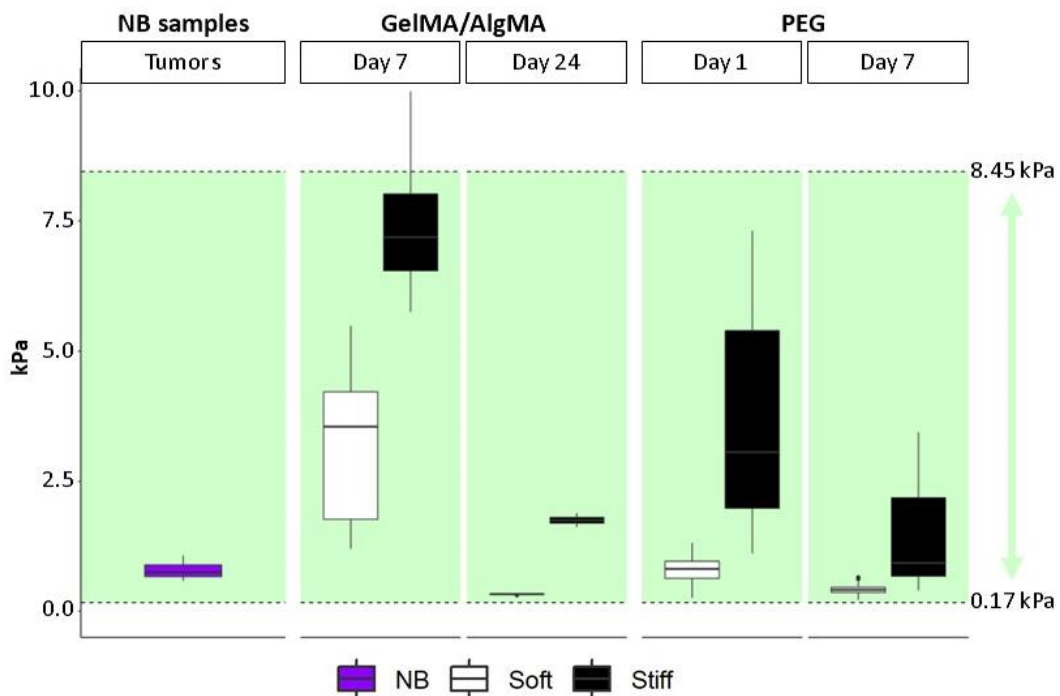
Hydrogels not only support cells and allow their three-dimensional growth, but also provide regulation of ECM compressive forces which cells interact with. As previously mentioned, stiffness participates in multiple aspects regulating cancer behavior and prognosis, such as tumor cell aggressiveness and motility. In fact, our previous results indicate that specific ECM and TME morphometric patterns lead to tumor stiffness related to worse prognosis in NB patients [102,148–150,152].

The mean stiffness of GelMA/AlgMA 3D cultures ranged from 3.16 ± 1.35 kPa to 7.66 ± 1.44 kPa in the initial measurements (7 days), and from 0.33 ± 0.01 kPa to 1.75 ± 0.11 kPa in the final ones (24 days). Regarding 3D cultures in VN/PEG hydrogels, stiffness ranged from 0.81 ± 0.26 kPa to 3.56 ± 1.89 kPa at the beginning of the experiment (1 day), and from 0.42 ± 0.09 kPa to 1.39 ± 0.91 kPa at the end (7 days) (Figure 6). Importantly, stiffness showed huge intraexperimental dispersion and enormous interexperimental variability due to procedural differences. For instance, GelMA/AlgMA models were designed to perform long-term cell cultures (weeks), whereas VN/PEG hydrogels were thought to last up to 7 days. In addition, GelMA/AlgMA initial and final measurements belong to two separate experimental setups, which could alter multiple subtle variables affecting the obtained stiffness values. What is more, GelMA/AlgMA and VN/PEG models were mechanically evaluated by uniaxial mechanical compression and nanoindentation respectively, and data processing specific pipelines could increase variability between models. Nevertheless, each experimental set was carried out and analyzed under identical conditions, thus facilitating the comparison between conclusions.

Apart from the abovementioned experimental variability sources, and the evident role of hydrogel components on scaffold stiffness, further tests revealed additional stiffness regulating factors, which are listed in Table 4. Among these, there are environmental factors such as room temperature and vibrations during mechanical assessment, which can alter data quality to a lesser or greater extent. Besides, cellularity reduced hydrogel stiffness in all experimental sets, doing so to a different extent in a cell-line dependent way. Overall, hydrogel stiffness mostly ranged within the NB

pathophysiological range, according to our measurements (0.79 ± 0.20 kPa) and those from literature (from 0.17 kPa to 8.45 kPa) [190] (Figure 6). On top of that, materials used for hydrogel fabrication offer greater versatility than is herein shown, so they would easily allow for stiffness range broadening if necessary for more specific studies.

Figure 6. Minimum to maximum stiffness range of the hydrogels herein developed at initial and final mechanical determination timepoints (days), compared with human NB stiffness. Purple NB box: stiffness range of NB samples from own patient cohorts. White Soft box: minimum stiffness found for each condition. Black Stiff box: maximum stiffness found for each condition. Green shadow: NB stiffness range according to literature. AlgMA: alginate methacrylate, GelMA: gelatin methacrylate, NB: neuroblastoma, PEG: polyethylene glycol.



Scaffold degradability is intrinsically linked to model stiffness since it modulates the cell ability to interact with their immediate surrounding. Scaffold degradation is a direct consequence of the cellular metabolism exerted on the hydrogel components, although it is also influenced by the structural stability of the constructs. Cell cultures and co-cultures carried out in GelMA/AlgMA hydrogels corroborated that degradation depends on the specific cell type, being higher when more metabolically active cells are cultured. The molecular target degraded by cells was gelatin in GelMA/AlgMA hydrogels, whereas it was the VPM protease degradable crosslinker in VN/PEG constructs. Degradable components were kept constant in both models, so it remains to be explored the effect

of scaffold degradability modification on model behavior. Nevertheless, a first approach was carried out in this thesis regarding VN incorporation as a forming biomolecule of VN/PEG hydrogels. Data from Article III revealed that VN increases hydrogel degradability, although it remains to be determined whether the mechanism of action is related to cell VN degradation and ECM remodeling, or to a boosting effect of VN on cell degradation activity.

Table 4. Parameters defining the variability of the hydrogel mechanical properties. ▲: increase, ▼: decrease, ✕: no effect.

	Effect on stiffness	Effect on degradation	Relevance
Composition			
<i>Stiffening elements</i>	▲	Variable	High
<i>Degradable molecules</i>	✕	▲	High
<i>Cell presence</i>	▼	▲	Intermediate
<i>Cell type</i>	Variable	Variable	Low
Experimentation			
<i>Human expertise</i>	Variable	Variable	Intermediate
<i>Data acquisition</i>	Variable	✕	High
Environment			
<i>Temperature</i>	Variable	Variable	Low
<i>Vibration</i>	Variable	Variable	Intermediate

Even though no exhaustive studies have been done on the intrinsic structural stability of the models presented in this work, the acquired experience indicates that GelMA/AlgMA hydrogels are more stable than VN/PEG hydrogels. Indeed, most cell cultures performed in the former remained stable after 6 weeks, some of them even exceeding 10 weeks of incubation. In contrast, VN/PEG experiments were carried out up to 7 days, at the end of which, various soft structures exhibited evident signs of degradation.

Critically, recent studies demonstrate that tissues and ECMs exhibit complex mechanical behaviors that cannot be fully understood with elastic hydrogels [191,192]. Thus, the ECM stiffness dogma established over the past two decades is now evolving towards more accurate research, which aims to resemble tissue and ECM viscoelasticity

and mechanical plasticity properties within the different tissue engineering applications [193–195]. Indeed, viscoelasticity has been proved to play a key role not only in euplastic cell behavior and tissue functioning, but also in neoplastic [196–198]. Consequently, further mechanical assessment of NB biopsies and the NB models herein presented should be carried out to check if NB viscoelasticity and plasticity are being properly recreated or if the models need to be adjusted.

1.2.2. Scaffolding functionalization with gelatin and VN

It is important to bear in mind that, even if scaffolds perfectly mimic tumor ECM mechanical properties, bioactive materials would be still required so that cells could interact with the scaffold, thus acting accordingly to the perceived cues. In other words, in the absence of a functional ECM, many of the biochemical and biotensegral signals occurring *in vivo* will not take place, thus preventing key aspects such as cancer cell migration due to cell encapsulation and isolation. However, although including multiple biocomponents in the constructs allows for *in vitro* ECM pathophysiological relevance enrichment, this may increase production time and costs, as well as impair the analytical process in certain studies. Alternatively, both natural (Alginate) and synthetic (PEG) inert materials have been herein combined with biofunctional components (Gelatin, VMP and VN), resulting in simple but functional biotensegral environments allowing basic cell-ECM interactions.

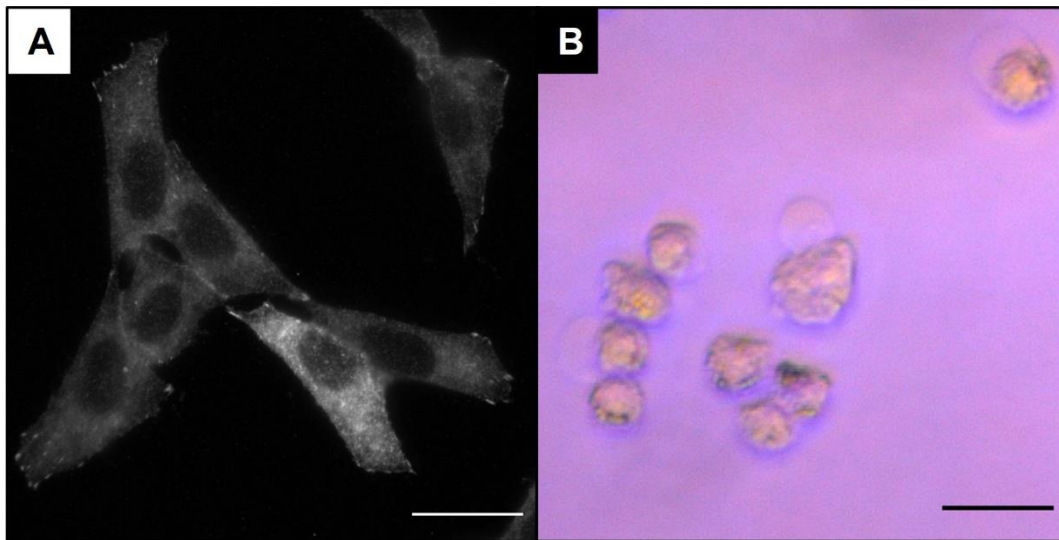
The way how these bioactive components are included in the final constructs depends on the specific fabrication process, which may also determine the capability to progressively improve the pathophysiological relevance of the model. In GelMA/AlgMA hydrogels, gelatin methacrylate allows its photopolymerization together with the alginate methacrylate [199], whereas the VN of VN/PEG models underwent a PEGylation process to chemically react with PEG molecules and form stable polymer networks [200,201]. Theoretically, both approaches would allow improving the model pathophysiological relevance by incorporating many methacrylate or PEGylated biomolecules, respectively. Although there are no studies that fully illustrate the potential and limitations of such a multiple biomolecule incorporation, component distribution and final construct stability are supposed to be the most critical parameters

to achieve a truly pathophysiological ECM *in vitro*. Besides, biomolecules could be also trapped inside the hydrogels without molecular modification, but it would be necessary to ensure retention efficiency and check whether the interactions between the forming components generate a functional biotensegral network.

Collagen and VN are ubiquitous components forming connective tissue [202,203], so they are suitable for relevant ECM *in vitro* mimicry. Regarding their specific usefulness in HR-NB modeling, both type I collagen fibers and VN are involved in stiffness regulation and aggressiveness determination of this malignancy [102,148]. Noticeably, gelatin is denatured collagen [199], so it lacks the fibrous structure and organization of the native molecule. Furthermore, methacrylation and subsequent photopolymerization could originate protein aberrant organizations different from those found *in vivo*. Nevertheless, this biomolecule disorganization could favor recreating the scarcity of type I collagen fibers observed in HR-NB ECM [102] while providing functional RGD domains that can be recognized by cells. In contrast, VN was included as a full-length protein with its native structure intact, and although it was PEGylated, studies reported in Article III showed that its functionality was not affected. Moreover, HR-NB VN pattern relates to the glycoprotein amount and its location relative to cells rather than its self-organization [148], so it would be expected that the resulting VN disposition derived from VN/PEG hydrogel fabrication would not alter its pathophysiological role. VN induced cell spreading in cultures performed on coverslips, but not in hydrogels (Figure 7), which could indicate that VN organization indeed altered VN function. However, this phenomenon could also be explained by an insufficient incubation time or even because scaffold viscoplasticity, porosity and/or degradability confined the cells [191].

Based on the knowledge generated in the laboratory regarding the ECM role in HR-NB aggressiveness, building additional scaffolds incorporating reticulin fibers or GAGs, independently and combined with the already tested biomolecules, would be useful to further unravel the mechanisms underlying NB development. Particularly, designing complex *in vitro* HR-NB ECMs would allow to identify specific cell-ECM interactions, as well as their role in environmental remodeling caused by the degradation of the fabricated ECM and the synthesis of natural ECM, both products of cellular activity.

Figure 7. SK-N-BE(2) morphology depending on the VN-enriched substrate. A: flattened cells cultured on VN-coated coverslips for 24h. B: rounded cells cultured in VN/PEG hydrogels for 24h. Scale bar 20 μ m.



1.2.3. Hydrogel cell hosting capacity

Last but not least, cell survival and growth are mandatory for relevant tumor modeling, as these are basic hallmarks of cancer [56]. In fact, aforementioned biomechanical and biofunctional model features are thought to provide cells with the environment they need to behave as they do *in vivo*.

Following literature guidelines, all hydrogels were initially seeded with approximately 2×10^6 cells/ml (Table 3), that is, about 10^5 cells/hydrogel [177–179]. GelMA/AlgMA models were independently used for SK-N-BE(2) and SH-SY5Y cell cultures, as well as the corresponding individual cocultures with SW10 schwannian cell line. Critically, SW10 cells were added at a final solution of 2×10^5 cells/ml, due to their scarcity in HR-NB [204]. Besides that, despite only SK-N-BE(2) cell culture was tested in VN/PEG hydrogels, this platform would presumably support NB related coculture likewise similar PEG platforms do for organoid culture [205,206].

Cells underwent outstanding stressful conditions during hydrogel fabrication, which could impair their viability. For instance, GelMA/AlgMA cell-laden bioinks were placed at -20°C for 3 minutes before bioprinting, and then irradiated several times with UV light at room temperature for hydrogel polymerization. Albeit VN/PEG hydrogel fabrication was performed in more gentle conditions, cells also spend a lot of time at room temperature before polymerization step. Moreover, both models were kept without cell

culture media until complete scaffold stabilization. Nevertheless, hydrogel fabrication was performed according to previously reported optimized protocols, thus reducing the negative impact on the cells [207,208]. In fact, all hydrogels proved to be biocompatible since they displayed great cell viability and proliferation even at long-term cultures, and genetic analysis performed on GelMA/AlgMA platforms revealed no mutations caused by UV exposition [163].

Differences between SK-N-BE(2) and SH-SY5Y cell genetic backgrounds defined their particular responses to the same environmental conditions. Significantly, there is still almost 40% of HR-NB cases that are not represented by these cell lines, and more importantly, NB TME conditions exhibit high inter- and intratumor variability. Therefore, NB cell lines other than those herein presented should be studied in multiple scaffolds to define behavioral changes regarding little and large genetic background variations. In addition, SW10 coculture modified NB cell activity, both suggesting that other NB cell lines would probably behave different when cocultured with Schwann cells and pinpointing the importance of the stromal cells on malignant cell behavior [182]. In this regard, NB TME also contains scarce but important immune cells, so human Schwann cells rather than mouse SW10 as well as few immune cells should be incorporated to NB models to promote *in vivo* like cell dynamics.

2. Biomarkers unraveling the mechanotransduction impact in the models

Models presented in this thesis succeed in partially mimicking HR-NB TME. Consequently, cultured cells underwent phenotypical adaptations in response to biotensegral cues provided by hydrogels. Mechanotransduction signaling starts with cell-ECM crosstalk and is subsequently transmitted through cellular cytoskeleton to the nucleus, so cells can reorganize their vital information to adapt themselves to their environment. Therefore, biomarkers related to ECM and cytoskeleton reorganization have been studied to shed light on mechanotransduction cell responses driving NB aggressiveness.

2.1. KANK1 and DOCK8 proteins as intracellular biotensegrity modulators

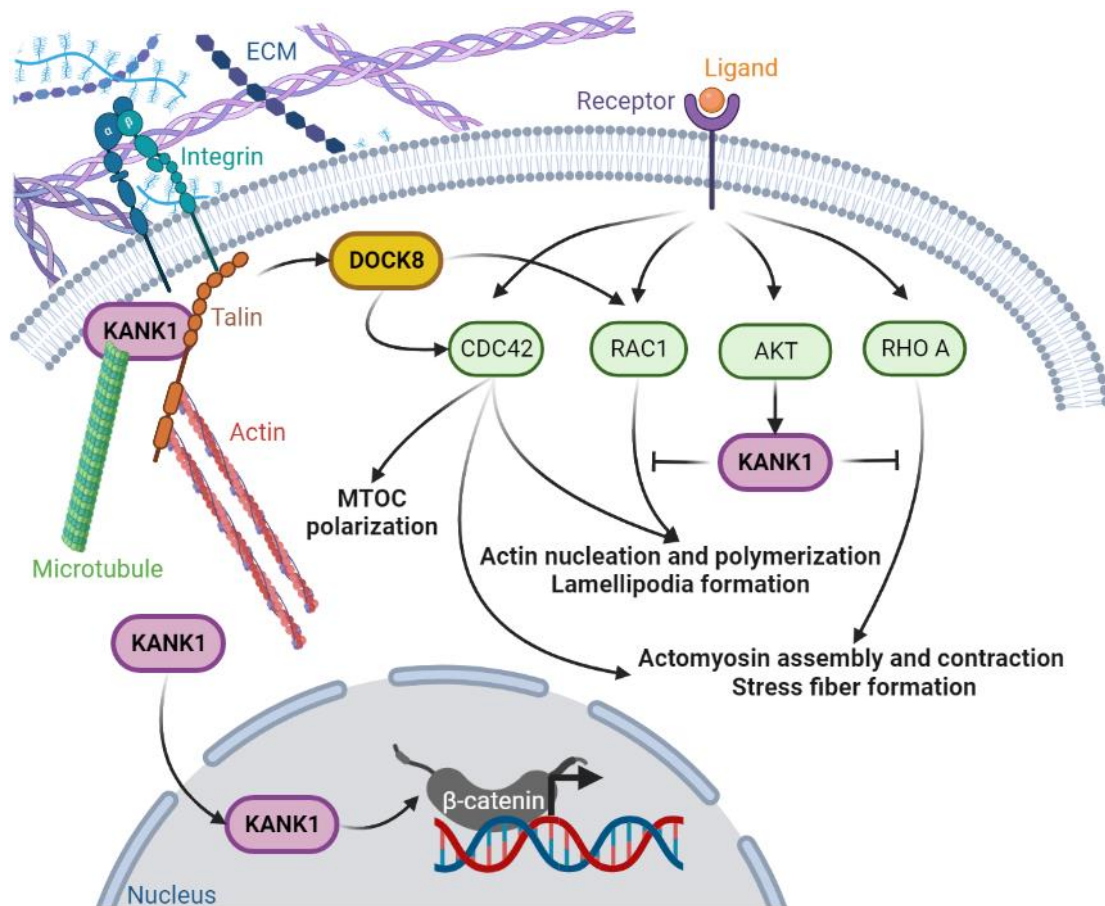
High density SNP and NGS techniques are routinely applied to identify genomic alterations such as segmental chromosomal aberrations, which are critical in NB prognosis. For instance, our group described that almost 40% cases within a HR-NB cohort presented atypic 9p- aberrations including *KANK1* and/or *DOCK8* genes [163], which are related with biotensegral cell cytoskeleton reorganization and migration responses. Interestingly, albeit little is known about the role of these genes in NB, similar 9p- aberrations and *DOCK8* inactivating mutations have previously been reported in almost 40% cases within a set of relapsed NB [209]. Therefore, further genetic analysis was performed, and confirmed those aberrations in our VN-KO PDX NB mice models and in stiff long cultured bioprinted hydrogels, so *KANK1* and *DOCK8* were deeper characterized by IHC.

KANK1 protein participates in actin and microtubule regulation. Specifically, it bridges the interaction between the integrin/actin-binding protein talin and the cortical microtubule-stabilizing complex, thus mediating the first mechanotransduction steps involved in cell-ECM crosstalk related to focal adhesion formation [164,210]. *KANK1* can be also activated through PI3K/Akt signaling pathway and impede RhoA and Rac1 activities, which inhibits actin polymerization and lamellipodia formation [211,212]. In addition, *KANK1* nucleus import has been positively correlated with the activation of β -catenin dependent transcription [213], and it has also been described as a tumor suppressor gene [214,215]. *KANK1* general interventions within the different biotensegral pathways are schematically represented in Figure 8; their effect on migration regulation may vary depending on the system [216,217].

Despite results in Article II showed broad *KANK1* expression among both monolayer and 3D cell cultures, the latter was more dynamic regarding the number of high intensity positive cells. Hydrogel specific features such as stiffness and coculture with SW10 led *KANK1* expression changes in 3D cell cultures that were not found in monolayer cell cultures. In addition, the role of each feature affecting *KANK1* expression in hydrogels varied depending on the system hallmarks, thus increasing model complexity and pathophysiological relevance. For instance, systems including SK-N-BE(2) cells were

more dynamic than those with SH-SY5Y cells, thus suggesting that the latter were less sensitive to stiffness and SW10 presence. Indeed, 9p- aberrations only appeared in SK-N-BE(2) cells, but not in SH-SY5Y. Critically, only one of two copies of KANK1 were lost when 9p- occurred, and the allele frequency increased with longer culture times and greater stiffness. In this regard, genetic and IHC analysis showed up cell adaptive clonal evolution driven by tumor biotensegrity cues and suggested KANK1 as a potential biotensegral biomarker to be considered in NB diagnosis and treatment, but further studies need to be addressed to fully understand its implications.

Figure 8. Biotensegral pathways related to cytoskeletal signal mechanotransduction and reorganization involving KANK1 and DOCK8 proteins. ECM: extracellular matrix, MTOC: microtubule organizing center.



DOCK8 is a guanine nucleotide exchange factor, the impact of which has been widely described in immune cells. It typically activates CDC42 but also Rac1 pathways, thus inducing migration in dendritic cells, T cells, macrophages and Schwann precursor cells [165,218–220]. Besides, it is involved in microtubule organizing center (MTOC) polarization, which is critical for NK cell cytotoxicity [221]. DOCK8 role in cytoskeleton reorganization is depicted in Figure 8.

Contrary to KANK1 expression results, little or none DOCK8 expression was detected in monolayer NB cell cultures, but it was greatly expressed in SW10. When performing cell cultures in 3D conditions, every model behaved differently, with huge variations between them. 3D culture conditions did not modify DOCK8 expression in SK-N-BE(2) cells, but increased it in SH-SY5Y. Moreover, despite SW10 coculture could have triggered some DOCK8 expression in NB cell lines, neuroblastic/schwannian cell population fluctuation notably influenced overall DOCK8 expression in the models. Hence, DOCK8 analysis performed in cocultured models supported the idea of malignant cell clonal selection favoring the progression of the better adapted cells. Regarding 9p-genetic aberration predominance, same dynamics of KANK1 apply to DOCK8, so further studies need to be performed to understand whether DOCK8 plays a key role on NB aggressiveness and metastasis due to its low expression.

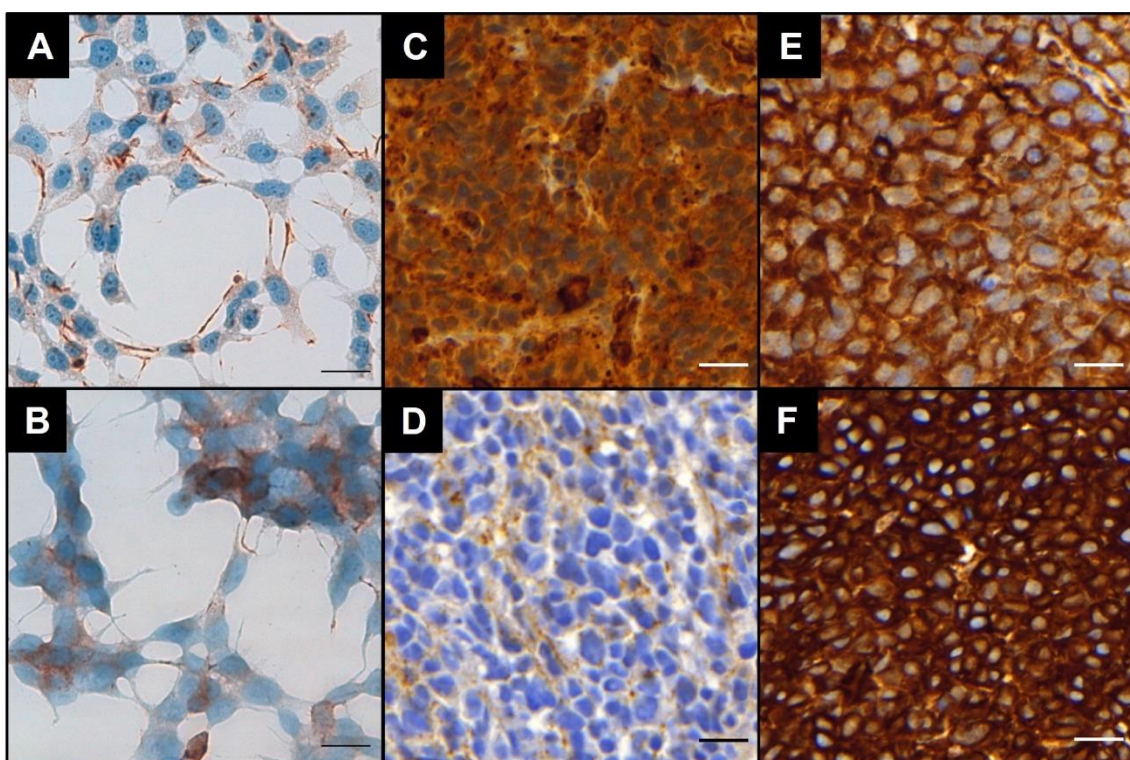
2.2. VN as a potential therapeutic target involved in cell-ECM crosstalk

Cells not only reorganize themselves in response to biotensegral signals, but also alter the ECM surrounding them. In this sense, tumor cells can both realign existing ECM components and synthesize new ones [222–224]. Regarding VN ECM glycoprotein, several *in vitro* studies demonstrated that cells could degrade and reshape it affecting cell-substrate interactions [225,226] and NB cell adherence to VN was proved in Article III. Furthermore, we have previously described that NB cells synthesize VN, not only in *in vitro* cell cultures, but also in *in vivo* samples from NB patients and VN-KO PDX NB mice models [148] (Figure 9). Subsequently, VN has been linked to NB prognosis and suggested as a potential therapeutic target involved in tumor biotensegrity [227].

Although different NB cell lines exhibit distinctive VN expression patterns [148], 3D culture conditions provided by hydrogels totally reshaped VN synthesis and distribution. Whereas almost non VN was detected in SW10 monolayer cultures, most NB cells presented low VN staining, mainly located in the cell membrane and neuritic prolongations of SK-N-BE(2), or perinuclear cytoplasmatic in SH-SY5Y (Figure 9). In contrast, spatial growth within hydrogels rapidly promoted high cytoplasmic and pericellular VN expression in all designed systems (Figure 10), which gradually decreased over time. Detailed results on VN synthesis patterns published in Article II and III

highlighted the complexity of the cell-ECM biotensegrity crosstalk, being that VN dynamics were regulated by a synergistic effect of the different features defining the hydrogels. For instance, NB cell lines increased their VN expression in a different extent depending on their genetic background, and stiffness induced non predictable changes by itself.

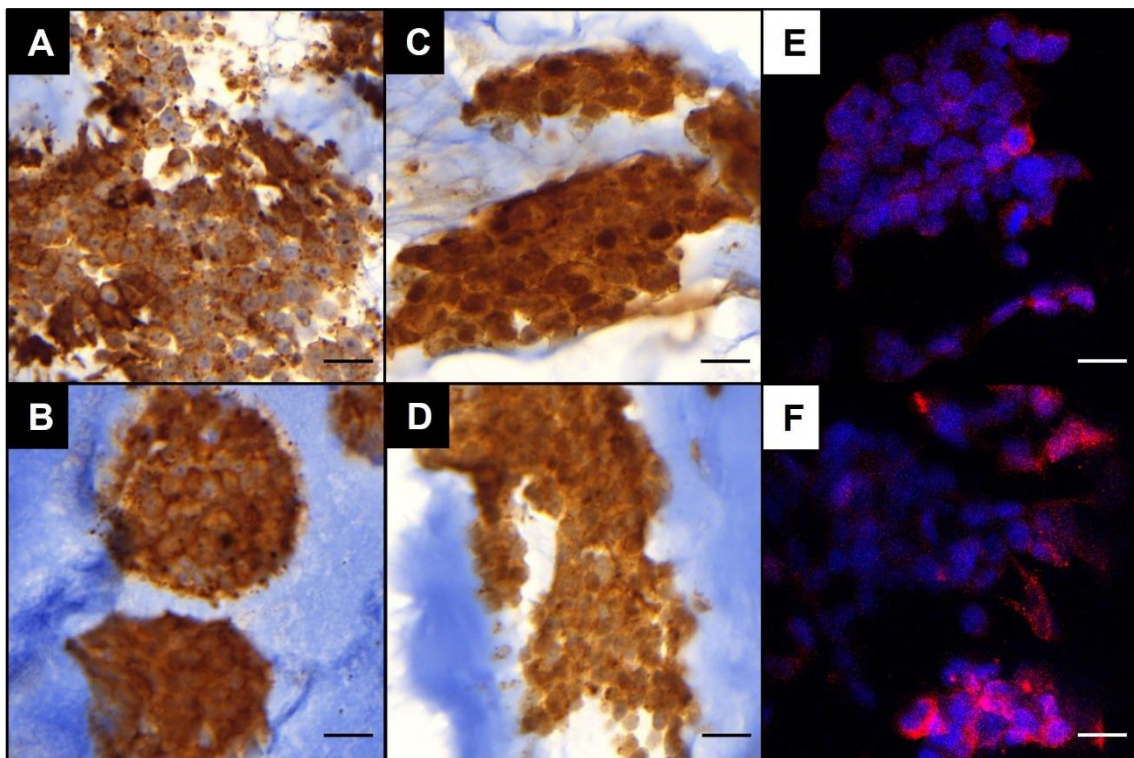
Figure 9. VN synthesis in NB cell lines, human NB biopsies, and VN-KO PDX NB samples. A: SK-N-BE(2) monolayer culture, B: SH-SY5Y monolayer culture, C: *MYCN* amplified NB, D: non *MYCN* amplified NB, E: VN-KO PDX sample from SK-N-BE(2) inoculation, F: VN-KO PDX sample from SH-SY5Y inoculation. Scale bar 20µm. KO: knockout, NB: neuroblastoma, PDX: patient derived xenograft, VN: vitronectin.



Additional studies on GelMA/AlgMA models revealed that biotensegral cues differently promoted VN synthesis regarding the size of cell aggregates, being that bigger cell clusters exhibited VN expression in a greater extent [228]. What is more, SW10 incorporation initially evened model VN pattern towards full low intensity (Figure 11), contrary to pure NB cell cultures, which expressed a variety of VN intensities within the cell clusters [228]. These findings suggest large cell cluster activity shifting towards a high VN migratory phenotype, and are in line with previous knowledge about Schwann cells triggering NB maturation [229] and their relationship with NB better prognosis [182]. Nevertheless, despite SW10 coculture initially reduced VN synthesis in a

multiparameter-dependent way, they seemed to favor cell adaptation towards a high VN expression phenotype in long term cocultures (Figure 11), which may be related to cell migration responses.

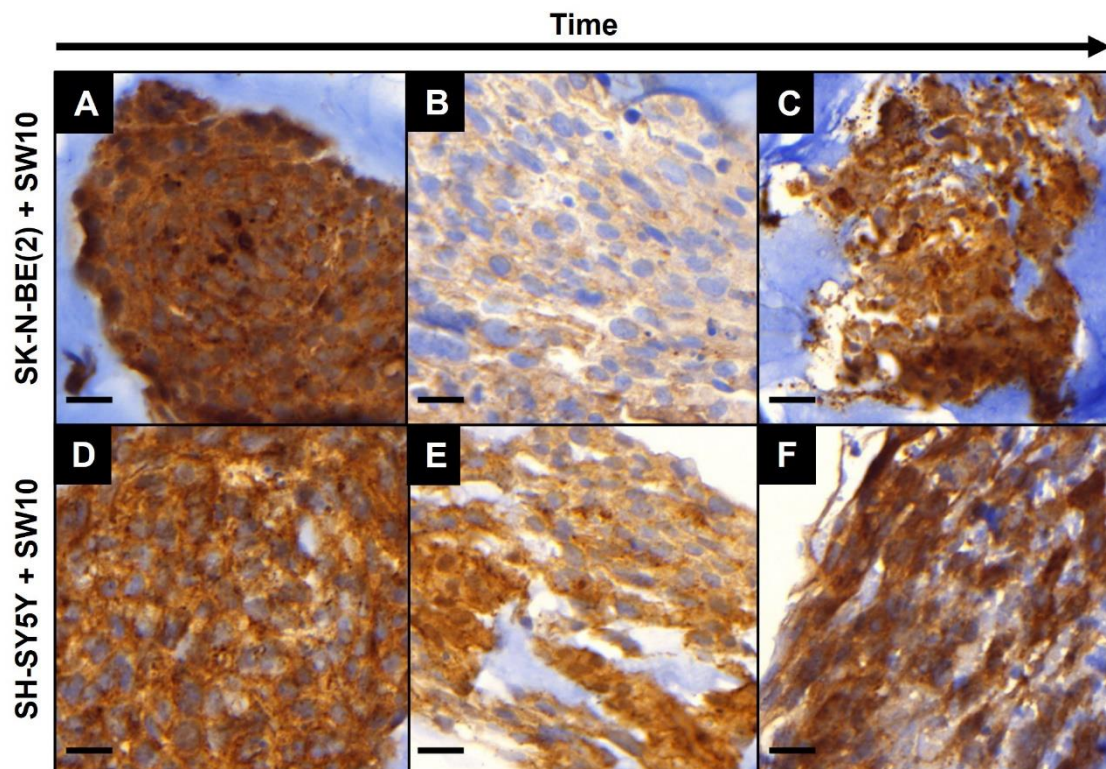
Figure 10. VN synthesis in GelMA/AlgMA and PEG hydrogels. A, B: SK-N-BE(2) cultures in soft (A) and stiff (B) GelMA/AlgMA hydrogels, C, D: SH-SY5Y cultures in soft (C) and stiff (D) GelMA/AlgMA hydrogels, E, F: SK-N-BE(2) cultures in soft (E) and (F) PEG hydrogels. VN staining is both brown (A-D) or red (E, F). Scale bar 20 μ m. AlgMA: alginate methacrylate, GelMA: gelatin methacrylate, PEG: polyethylene glycol, VN: vitronectin.



However, those approximations consisted in VN free substrates, and only synthesized VN was found within cell clusters. For better resembling *in vivo* conditions in Article III, VN was included in PEG hydrogels to assess how VN availability in the ECM influence cell biotensegral responses. Interestingly, cells did not stop VN synthesis despite it was already in their surroundings (Article III), thus indicating a dynamic VN turnover intrinsically linked to ECM remodeling, which in turn, may promote cell aggressiveness and migration. Moreover, VN immobilization within the PEG net revealed that synthesized VN could escape from the hydrogels and be detected as a soluble molecule. Results in Article III also indicated that VN not only did not directly increase sample stiffness upon incorporation but generally favored VN/PEG hydrogel degradation by the

cells during the first 7 days of culture. Unfortunately, no longer cultures were studied. These results obtained from short term cultures in this 3D models suggest that the abovementioned association between VN and NB stiffness discovered in our lab may not necessarily describe VN driving tumor stiffening, but stiffness boosting VN expression, so further studies need to be carried out to elucidate the nature of these association. Alternatively, like other proteins used in PEG systems [208,230], VN has been artificially incorporated into a non-biological scaffold, so it could be aberrantly arranged being unable to drive any hydrogel stiffening.

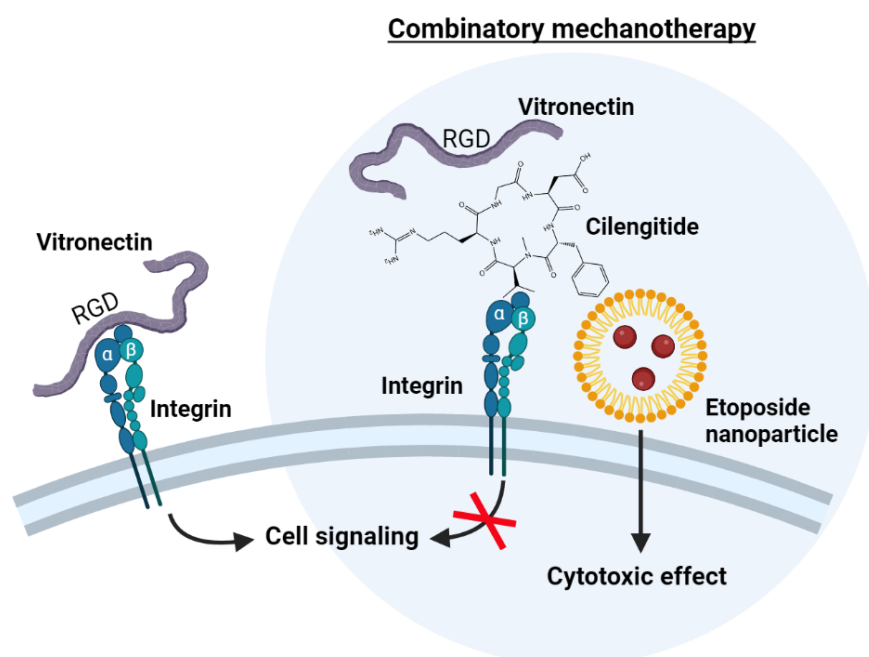
Figure 11. VN synthesis evolution in SK-N-BE(2) plus SW10 and SH-SY5Y plus SW10 GelMA/AlgMA hydrogels. A-C: SK-N-BE(2) plus SW10 cultures expressing VN at 2 (A), 6 (B) and 8 (C) weeks. D-F: SH-SY5Y plus SW10 cultures expressing VN at 2 (D), 6 (E) and 12 (F) weeks. Scale bar 20 μ m. AlgMA: alginate methacrylate, GelMA: gelatin methacrylate, VN: vitronectin.



Altogether, VN results support hydrogels as a more biomimetic models for tumors than monolayer cell cultures being that the latter displayed cell flattened shape non observed neither *in vivo* nor hydrogels and could not retain any VN pericellularly. Critically, this work also evidences the limitations of working with a single ECM molecule, thus pinpointing the need of progressively increasing *in vitro* ECM complexity according to the *in vivo* interplay between ECM elements. Nevertheless, herein presented results

opens new diagnostic alternatives in NB by using VN both as a soluble biomarker and as a therapeutic target. Usefulness of targeting VN in NB treatment rely on its RGD domain interacting with cell integrins such as $\alpha_v\beta_3$ and $\alpha_v\beta_5$ to drive mechanotransduction signaling promoting cancer invasion, angiogenesis, and aggressiveness [231,232]. Regarding this, several anti-integrin antibodies such as vitaxin, abituzumab and cilengitide have been tested in different cancer preclinical studies, where they presented anti-metastasis or anti-angiogenesis activity [233,234]. Moreover, due to ECM-integrin crosstalk not only occurs within the tumors, new advances on coated nanoparticles have improved cancer treatments based on integrin targeting [235,236]. Indeed, our lab has proposed the use of nanoparticles for the combination of cilengitide and etoposide (a broadly used drug for NB chemotherapy) as a molecular mechanotherapeutic alternative for targeting VN-cell interaction in NB (Figure 12), with already promising results in NB monolayer cell cultures, published in a scientific paper [227], and VN-KO PDX murine models, the results of which were presented in two final degree works [237,238].

Figure 12. Mechanotherapeutic approach for NB designed in our laboratory using cilengitide and etoposide. Cell integrins recognize VN through its RGD domine to trigger signaling mechanotransduction. Cilengitide compete with VN, blocking integrin-VN interaction. Lipid nanoparticles increase etoposide delivery accuracy, reducing off-target cytotoxicity. Synergy between both approximations were designed to increase therapy effectiveness while minimizing the adverse effects. NB: neuroblastoma, VN: vitronectin.



Besides, this therapeutic approximation is meant to be further tested in NB hydrogels. In this way, NB models herein presented are expected to provide further insights on the specific VN biotensegral pathways influencing NB aggressiveness and metastasis, thus allowing to design new therapies complementing the current ones as well as reducing their negative impact on the patients.

3. Cell plasticity promotes dynamic adaptation in response to biotensegral stimuli

The classical hallmarks of cancer have traditionally referred to the uncontrollable and limitless cell growth capacity to explain tumor malignancy [239]. Moreover, recent studies have contributed to the field with new emerging hallmarks such as cell senescence, further highlighting the importance of cell growth in tumor progression, but also other dimensions such as phenotypic plasticity and epigenetic reprogramming have been recognized, thus supporting metabolism deregulation as a major driving force of cell adaptation [56]. Therefore, once both biotensegral stimuli and cell-ECM crosstalk occurring in NB hydrogels related to KANK1, DOCK8 and VN expression were herein demonstrated, several parameters related to cell expansion, turnover, differentiation, and activity were evaluated to better understand neuroblastic cell behavior shifts driven by mechanical forces.

3.1. Cell growth dynamics

Cancer cell density has been broadly studied in monolayer and 3D *in vitro* cell cultures as well as in *in vivo* models. It has been reported to influence population growth rate [240,241], speed up cell adaptation to the environment [240] and promote cancer cell transdifferentiation [242], metastasis [241,243,244] and drug resistance [245]. Furthermore, cell density has also been associated with NB metabolism adaptation and cell growth arrest [246]. Consequently, cell population evolution studies focused on cellularity and organization were carried out as a first approximation to describe malignancy and pathophysiological relevance in the presented NB 3D models.

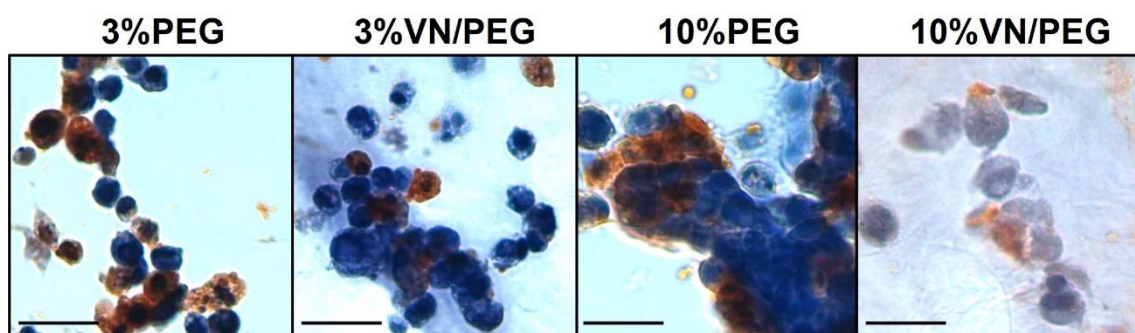
Albeit cells were initially inoculated as a monodispersed suspension, cell growth derived in cell cluster formation in all studied hydrogels. Scaffold cytocompatibility allowed clusters to grow over time regardless hydrogel characteristics, and they did so without a specific distribution within the hydrogels. Interestingly, obtained results robustly showed a stiffness effect on cluster growth dynamics. In fact, soft conditions harbored higher cluster densities, and despite cluster growth rate was initially similar in both soft and stiff conditions, the latter promoted large cluster formation in long term cultures. Additionally, only soft GelMA/AlgMA hydrogels presented loose irregular clusters, contrary to rounded compact ones found in stiff GelMA/AlgMA and VN/PEG hydrogels.

Apart from cell density, cell turnover was characterized through proliferation and survival biomarkers to further elucidate cell growth dynamics. Ki-67 antibody specifically recognizes a nuclear antigen present in proliferating cells [247], so it has been widely used among other cell-cycle regulatory proteins to determine proliferative state in many cancers, and it has typically been associated with poor prognosis [248–251]. On top of that, cell survival/death imbalance also regulates tumorigenesis [252] and can define malignancy in opposite ways [56,253]. Besides the intuitive link between aberrantly high cell survival and limited cell death rate in tumor proliferation, cell death events such as necrosis [254–256], but also apoptosis [253] and senescence [56], can paradoxically contribute to tumor progression. Indeed, the global proportion of mitotic and karyorrhectic cells within NB (Mitosis-Karyorrhexis Index, MKI) is a well-established scoring for NB aggressiveness that considers the combination of both cell proliferation and imminent cell death [257–259]. Therefore, cell pro-survival proteins such as Bcl-2 and pro-apoptotic such as Bax [260–262] and Caspase-3 [263–265] have been broadly studied in cancer prognosis as well as in the hydrogels presented in this thesis.

Ki-67 IHC results on SK-N-BE(2) models from Article I and Article II showed stiffness and time boosting cell proliferation rate up to certain point, after which it gradually decreased regardless the stiffness. Interestingly, analysis carried out in Article I differentiating between cell cluster sizes revealed no Ki-67 expression variations associated with cluster size. Regarding cell survival biomarkers, all GelMA/AlgMA

hydrogels mainly displayed Bcl-2 expression rather than Bax, despite stiffness enhanced both protein expressions (Article I). Analogously, few Caspase-3 IHC carried out in VN/PEG hydrogels further supported cell survival since little apoptosis was detected (Figure 13). Finally, high MKI scoring was confirmed in all hydrogels, being karyorrhexis more prevalent than mitosis. Despite remarkable differences were noticed, neither time nor stiffness could be associated with MKI variability. Critically, results from Article II evinced distinct aggressive NB cell lines presenting intrinsic specific behaviors, which in turn were differently regulated by culture conditions. Contrary to SK-N-BE(2), SH-SY5Y GelMA/AlgMA models from Article II exhibited general scant Ki-67 expression, particularly in stiff conditions, and became negative after long cell culture times. Regarding MKI, SH-SY5Y displayed high scoring as SK-N-BE(2) did, but it was significantly lower. Besides, 3D culture conditions triggered some phenotypic features different from those found in monolayer cell cultures. For instance, although MKI scores were found similar in monolayer and hydrogel cultures, the former exhibited greater expression of all Ki-67, Bcl-2 and Bax biomarkers. Finally, SW10 incorporation affected model growth and MKI in distinct ways depending on the NB cell line and the stiffness, so albeit no studies were herein performed regarding survival and apoptosis biomarkers in hydrogels presenting SW10 cells, these features would also be probably affected by coculture conditions.

Figure 13. Caspase-3 expression in PEG hydrogels. Scale bar 20 μ m. PEG: polyethylene glycol, VN: vitronectin.



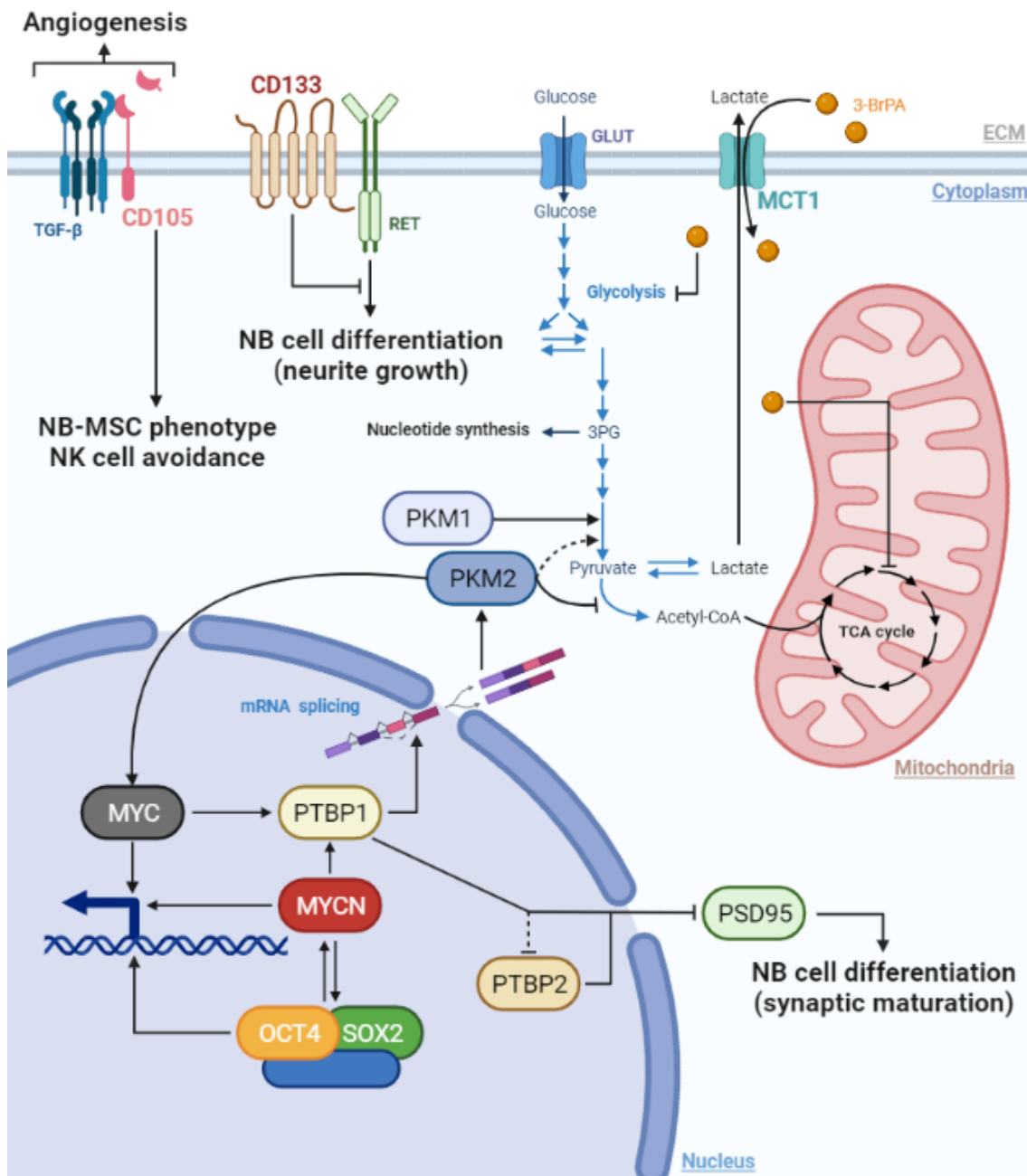
In vivo HR-NB tumors are large cellular masses rather than stroma bodies with multiple cell clusters. Theoretically, either long enough culture times or suitably higher initial cell density in the hydrogels should allow bigger cell mass formation likewise NB tumors, but model limitations on TME mimicry would probably impede proper cell

survival within such a cell mass. Nevertheless, each cluster within the hydrogels resembled the basic morphological aspects of NB cell organization, thus allowing hydrogels to be considered as scaffolds containing multiple tiny tumors. Furthermore, NB models have been proved to bear cell replication, support cell survival, and maintain HR-NB features such as MKI, which are related to tumor aggressiveness. Altogether, NB cell line specific growth dynamics have been modulated by adjusting stiffness and Schwann cell presence. In this way, hydrogels have shown biotensegrity favoring or hindering tumor progression depending on the cell line, as well as its crosstalk with other cell populations, thus regulating the effect of Schwann cells, which typically shift NB behavior towards more favorable prognosis [182]. Importantly, studies carried out herein ignored temporal and spatial topography of other biomarker expression complementary to those examined for cell proliferation and survival, so Ki-67 negative cells here classified as non-proliferative could be indeed proliferating by other mechanisms [266], thus both increasing the aggressiveness potential of the model as well as the complexity to evaluate it.

3.2. Differentiation and metabolism dynamics

Cell turnover is intrinsically intertwined with inner cell pathways regulating cell differentiation and metabolism status. For instance, cancer cells typically present undifferentiated pluripotent phenotypes likewise stem cells, which allow them to become invasive, proliferative, and potentially immortal. Accordingly, stem cell-related genes have been studied to understand and reverse cancer malignancy [267–269], and some have been related to undifferentiation and prognosis in NB [270–273]. Together with MYC and Klf-4, OCT4 and SOX2 are part of the so-called Yamanaka factors, which allow differentiated cell reprogramming towards a pluripotent stem cell phenotype [274]. Both OCT4 and SOX2 are transcription factors involved in embryonic stem cell pluripotency which act within a trimeric complex. Critically for NB, this complex has been described to exhibit a positive feedback loop with MYCN, which is decisive in HR-NB presenting *MYCN* amplification [275] (Figure 14).

Figure 14. NB cell molecular pathways related to differentiation, glucose metabolism and TME reshape. 3-BrPA: 3-bromopyruvate, ECM: extracellular matrix, MSC: mesenchymal stromal cell, NB: neuroblastoma, NK: natural killer, TCA: tricarboxylic acid.

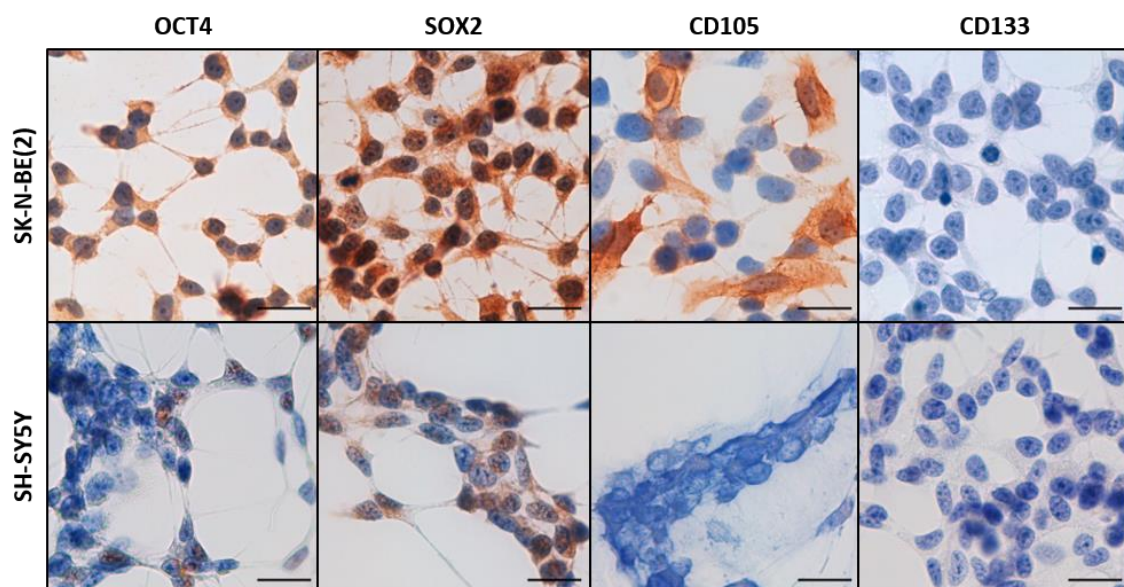


In contrast, CD105 is a polyvalent glycoprotein typically exhibited by endothelial cells that act as both TGF- β coreceptor and cytokine, and is strongly involved in angiogenesis, but also in many other signaling pathways such as maintaining cancer stem cell and epithelial-mesenchymal transition phenotypes when MYC is also involved [269,271,276]. Particularly, CD105 expression in NB cell lines have been correlated with mesenchymal stromal cell (MSC)-like phenotype and NK immune cell avoidance [277]

(Figure 14), which provides an alternative way to modulate immunometabolism in cancer from those we previously reported in a scientific review [76]. Regarding CD133 transmembrane glycoprotein, it has been described to mediate apical plasma membrane organization in epithelial cells, early retinal development, and MAPK and Akt signaling pathways. What is more, CD133 has also been associated with RET tyrosine kinase in neurite outgrowth suppression in NB cells [278] (Figure 14).

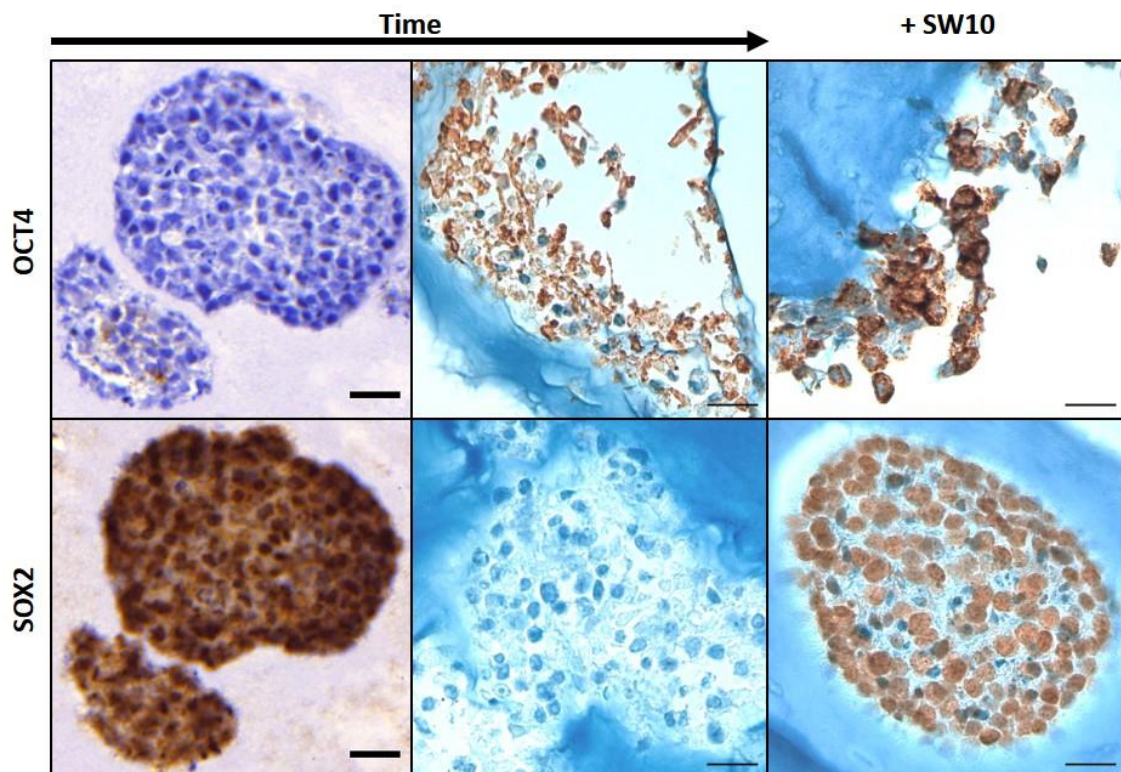
We have previously assessed *OCT4*, *CD105* and *CD133* expression in own cohorts of NB patients, the results of which are published in a journal article [155] and in a doctoral thesis [171]. Similarly, we have carried out additional *SOX2* evaluation in human NB samples, the results of which are still uncommunicated. In a complementary way, we also have evaluated *OCT4*, *SOX2*, *CD105* and *CD133* expression patterns in the GelMA/AlgMA models from Article I and Article II included in this thesis compendium, but the resulting findings are also still uncommunicated. Therefore, our uncommunicated results showed SK-N-BE(2) cells to express both cytoplasmic and nuclear moderate OCT4 and high SOX2 in monolayer cultures, whereas CD105 staining suggested some cells presenting MSC-like phenotype as previously described [277] (Figure 15). When SH-SY5Y traditional cultures were evaluated different cell expression was found; they mostly exhibit low nuclear OCT4 and SOX2 staining, but negative CD105 expression related to the aforesaid MSC-like phenotype [277] (Figure 15).

Figure 15. Expression of stem cell markers in monolayer cell cultures. Scale bar 20 μ m.



Intriguingly, 3D conditions promoted complementary OCT4 and SOX2 expressions in SK-N-BE(2); OCT4 remained mainly negative until long term cultures where it became positive, whereas SOX2 turned greatly positive in almost all conditions, but negative on those when OCT4 was found positive (Figure 16). However, SW10 incorporation in SK-N-BE(2) hydrogels promoted OCT4 expression, while maintaining SOX2 positivity (Figure 16). In contrast, SH-SY5Y cells almost became OCT4 and SOX2 negative when cultured within the hydrogels, regardless SW10 presence. Furthermore, CD105 was negative in all hydrogel conditions tested, as well as CD133, which was negative even in monolayer cultures (Figure 15). In line with literature [275], SK-N-BE(2) *MYCN* amplified cells, but not SH-SY5Y, expressed both OCT4 and SOX2 when cocultured with SW10 within hydrogels, thus highlighting the importance of a relevant *in vitro* pathophysiological TME to induce stem cell behavior like the found *in vivo*. In addition, albeit CD105 was previously found in SK-N-BE(2) presenting MSC-like phenotypes [277], and CD133 expression has been correlated with *MYCN* amplification in NB aggressiveness [279], the absence of both biomarkers in the studied hydrogels indicate that NB model conditions can be further improved to better recreate *in vivo* NB stem cell-behavior.

Figure 16. OCT4 and SOX2 expression variation in SK-N-BE(2) GelMA/AlgMA hydrogels due to culture time and SW10 incorporation. Scale bar 20 μ m.

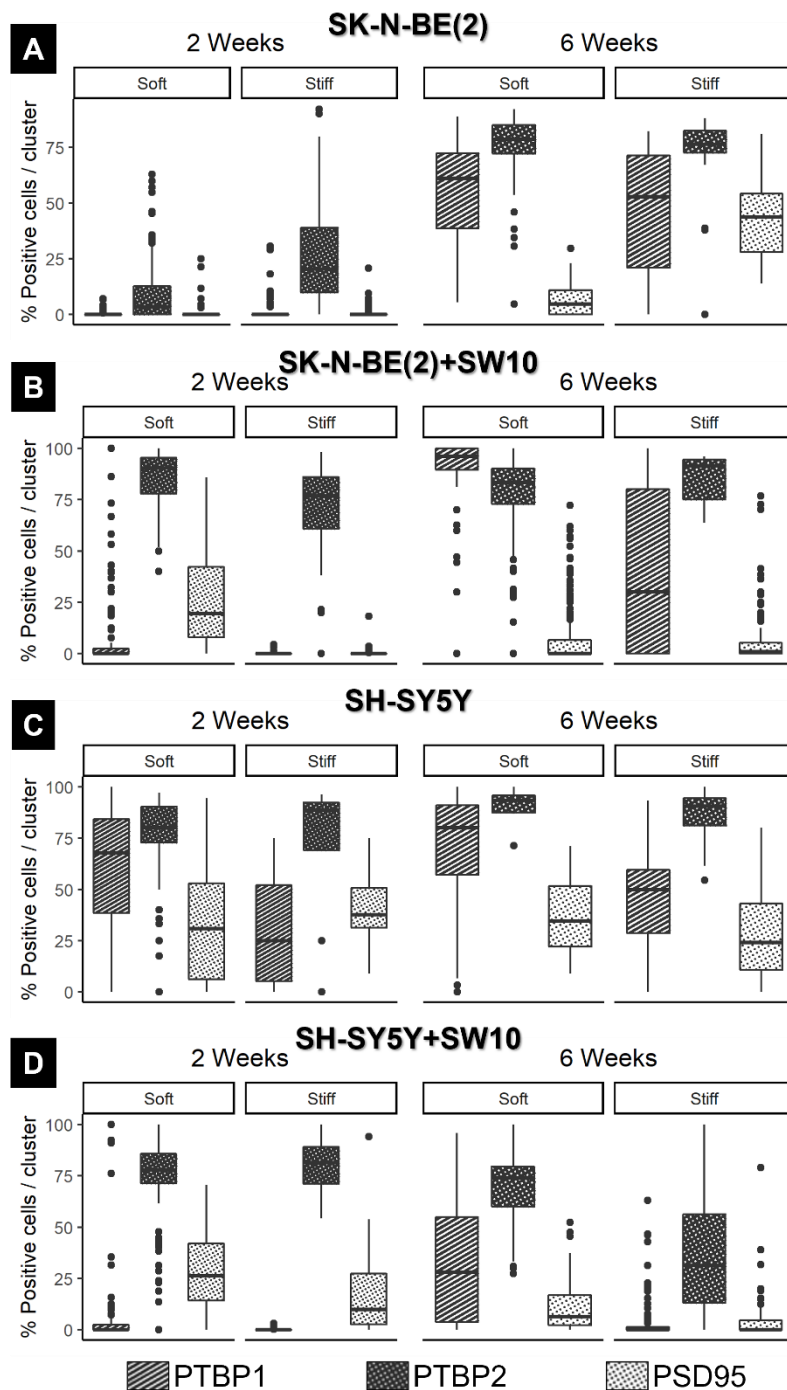


Considering NB arising from the neural crest, NB cell lines are primitive neuronal cells with sympathoadrenal lineage rather than pure stem cells, which indeed, can undergo full neuronal differentiation [280,281]. Moreover, INRG NB pretreatment classification system associates NB cell differentiation with better prognosis, so studying biomarkers specifically regulating neuronal differentiation would provide complementary information to the abovementioned stem cell biomarkers. In this sense, broadly studied in NB, MYC and MYCN transcription factors [282–284] positively regulate PTBP1 transcription. PTBP1 is a splicing factor which contributes to cancer malignancy by regulating apoptosis, proliferation, and migration, either by itself or in combination with its homologue PTBP2, which is exclusively expressed in the nervous system [285–287]. Critically for NB cells, PTBP1 and PTBP2 are key regulators in neuronal differentiation and maturation [288,289] (Figure 14). In fact, PTBP1 is highly expressed in non-neuronal cells and neural progenitor cells, but it is downregulated during neuronal differentiation, leading to neuron specific splicing patterns and the accumulation of PTBP2 [290,291] (Figure 14). Nevertheless, PTBP1 and PTBP2 inhibit PSD-95 expression, which is a postsynaptic scaffolding protein that allows postsynaptic clustering of crucial synaptic proteins [288,291]. Accordingly, further neuronal maturation undergoes with PTBP1 and PTBP2 downregulation, thus allowing PSD-95 expression necessary to synaptic maturation and plasticity [288,291] (Figure 14).

Therefore, we performed complementary differentiation studies by evaluating PTBP1 and PTBP2 on mainly HR-NB human samples, but also in few *in vivo* VN-KO PDX NB murine models and in *in vitro* GelMA/AlgMA hydrogels with either SK-N-BE(2) and SH-SY5Y pure cultures or cocultured with SW10 cells. Those results were presented in a final degree work [292], and showed the implication of PTBP1 and PTBP2 in NB aggressiveness. What is more, PTBP2 was suggested as a potential biomarker to distinct undifferentiated NB with low PTBP2 expression, from poorly differentiated NB with high PTBP2 expression, which may have important implications in NB pretreatment risk classification [292]. Subsequently, additional characterization of PTBP1 was carried out in SK-N-BE(2) cell line and GelMA/AlgMA hydrogels, the results of which were published in Article I. Once high PTBP1 positivity found in Article I and uncommunicated data confirmed neuronal progenitor cell status in both NB monolayer cell cultures, extensive

PTBP1, PTBP2 and PSD-95 markers were evaluated in GelMA/AlgMA models from Article I and Article II to assess whether NB cells differentiated towards a neuronal phenotype when exposed to hydrogel conditions or remained undifferentiated (Figure 17).

Figure 17. Box plot of PTBP1, PTBP2 and PSD-95 expression in GelMA/AlgMA hydrogels revealing NB maturation dynamics. A, B: SK-N-BE(2) (A) and SK-N-BE(2) + SW10 (B) hydrogels show low PTBP1 increasing with time (A, B), PTBP2 increasing with time (A) and SW10 presence (B), and low PSD-95 (A, B). C, D: SH-SY5Y (C) and SH-SY5Y + SW10 (D) hydrogels show high PTBP1 decreasing with stiffness (C, D) and SW10 presence (D), PTBP2 high expression (C, D), and low/intermediate PSD-95 positivity (C, D).

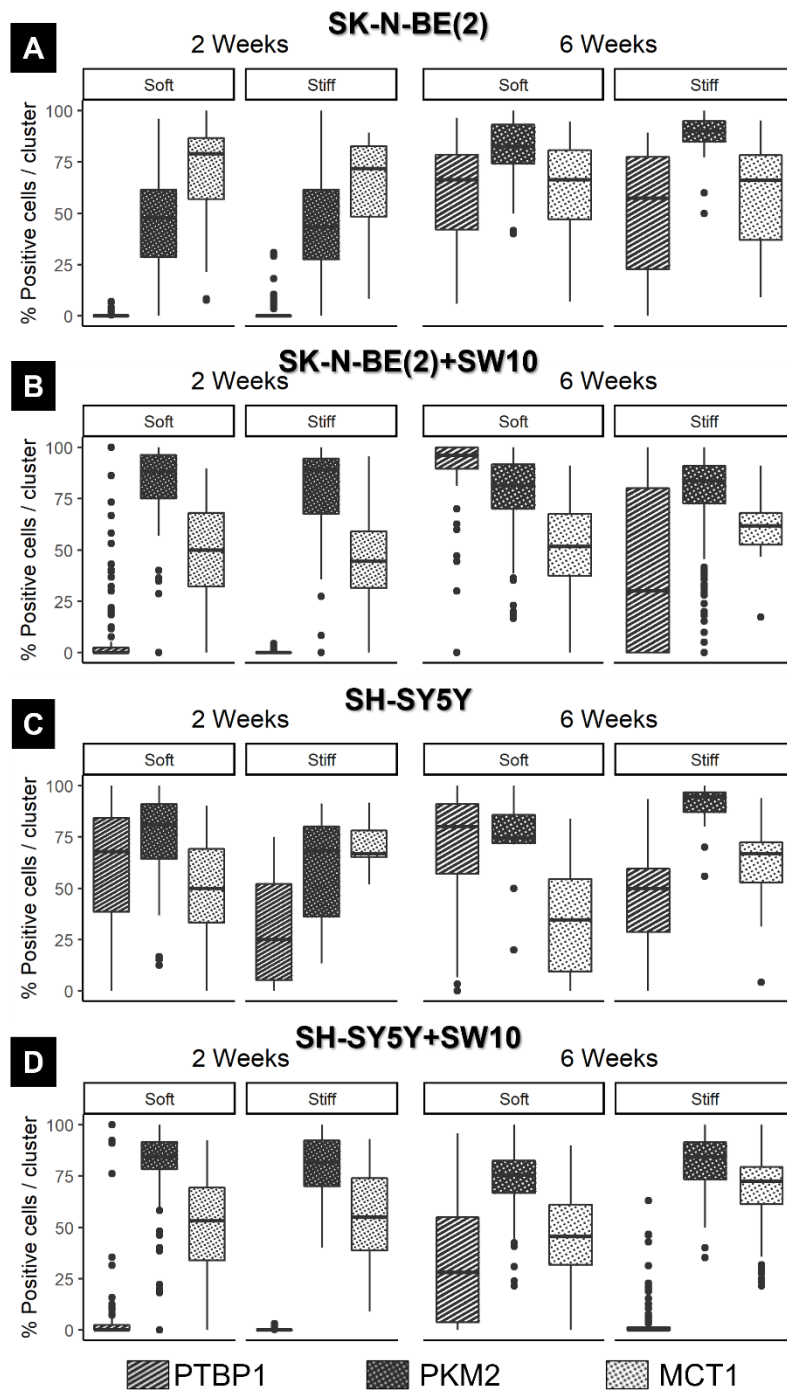


Partially published PTBP1 data showed SK-N-BE(2) hydrogels initially presented low PTBP1 values, which increased with time regardless stiffness (Figure 17A) and SW10 presence (Figure 17B). Similarly, uncommunicated results indicated that PTBP2 was lower in early SK-N-BE(2) cultures and increased with time regardless stiffness (Figure 17A). However, it was expressed in a greater extent than PTBP1 in all conditions, and SW10 greatly promoted PTBP2 expression from early culture times (Figure 17B). By contrast, SH-SY5Y models displayed high PTBP1 expression decreasing with stiffness (Figure 17C) and SW10 presence (Figure 17D), whereas PTPB2 was found highly positive in almost all conditions. These findings are in line with the NB sympathoadrenal lineage [280,281], and strengthen the studies reporting the Schwann cell role in NB cell maturation [229]. Additionally, uncommunicated scant PSD-95 expression confirmed that hydrogel conditions allowed cells remaining immature for NB tumor modelling (Figure 17), despite extra PSD-95 expression found in SH-SY5Y hydrogels suggests that SH-SY5Y may be more prone to mature than SK-N-BE(2), at least in the herein studied hydrogel conditions.

Simultaneously, PTBP1 also shifts pyruvate kinase PKM1 isoform prevalence towards PKM2 isoform [293,294] (Figure 14). PKM2 has been proposed to regulate *MYC* gene transcription, which further contributes to cell response adaptability and pinpoints the tight connection between differentiation and metabolic pathways [295,296] (Figure 14). Nevertheless, PKM2 is a less active glycolysis enzyme than PKM1 isoform, so its canonical impact on cell metabolism results in pyruvate formation impairment and glycolytic intermediates accumulation, which respectively favors lactate production related to Warburg effect and nucleotide biosynthesis pathways [296,297] (Figure 14), as we previously reported in a scientific review [60]. Despite we did not previously evaluated PKM2 in human nor PDX NB samples, we did so in GelMA/AlgMA hydrogels due to its direct implication on cancer malignancy, the results of which have not been communicated yet. We found that PKM2 was robustly expressed in all conditions, thus supporting cell malignant behavior (Figure 18). In fact, despite PKM2 levels increased with time in SK-N-BE(2) cultures, it remained almost constant in the remaining time points regardless variations in stiffness, SW10 presence or the NB cell line cultured (Figure 18), and although low PTBP1 levels did not correlate with lower PKM2 values,

other hnRNP proteins could be also promoting PKM2 isoform splicing as it has previously been described [293].

Figure 18. Box plot of PTBP1, PKM2 and MCT1 expression in GelMA/AlgMA hydrogels revealing NB glucose metabolism dynamics. A, B: SK-N-BE(2) (A) and SK-N-BE(2) + SW10 (B) hydrogels show low PTBP1 increasing with time (A, B), PKM2 increasing with time (A) and invariable robust expression (B), and MCT1 expression slightly decreasing with time (A) and greatly with SW10 presence (B). C, D: SH-SY5Y (C) and SH-SY5Y + SW10 (D) hydrogels show high PTBP1 decreasing with stiffness (C, D) and SW10 presence (D), PKM2 robust expression (C, D), and MCT1 increasing with stiffness (C, D) and barely decreasing with time (C).



In parallel, since lactate is an acidic molecule, cells maintain their intracellular pH homeostasis by secreting it to the ECM through monocarboxylate transporters (MCT). Particularly, MCT1 mediates bidirectional transport of lactate and albeit it has been associated with poor outcome in several cancer types, it also has been therapeutically used since it can internalize lactate analogs such as 3-bromopyruvate (3-BrPA) [298–300] (Figure 14). 3-BrPA is a cytotoxic compound that not only inhibits glycolysis, but also mitochondrial oxidative phosphorylation (Figure 14), so it has become a promising antitumor drug [301,302]. Importantly for HR-NB patients, SK-N-BE(2) and SH-SY5Y among other NB cell lines, have been described to express MCT1 and respond to 3-BrPA treatment [303–305]. Therefore, MCT1 presence was evaluated for the first time in our lab in GelMA/AlgMA NB models, but results remain uncommunicated. Albeit subsequent quantification confirmed all hydrogels expressing moderate/high MCT1 values, hydrogel features differently regulated MCT1 dynamics (Figure 18). SK-N-BE(2) hydrogels generally showed greater MCT1 expression than SH-SY5Y models, but it slightly decreased with culture time (Figure 18A) and specially with SW10 incorporation (Figure 18B). However, MCT1 tended to be enhanced by stiffness and mostly repressed with time in SH-SY5Y hydrogels (Figure 18C), with no obvious effect due to SW10 incorporation (Figure 18D). In this way, MCT1 variations may suggest different 3-BrPA sensitivities, but further studies on these NB hydrogels are needed to confirm whether moderate MCT1 expression found is enough to obtain an optimum cytotoxic effect after 3-BrPA inoculation.

Altogether, NB mimicking platforms developed in this thesis have pinpointed the interconnection existing between multiple TME biotensegral pathways, and how their complex crosstalk differently drives cell behavior depending on the system characteristics. In this regard, herein reported hydrogels provide improved translational knowledge and technological infrastructure which brings new paradigms particularly to the oncology field, but also to general biology in a wider extent.

In the following sections it will be detailed how findings obtained from 3D NB models have direct relevant implications on NB diagnosis and therapy landscapes and lays the foundation for analogous biological applications, thus potentially becoming the warhorse of current and future precision medicine.

4. Model contribution to precision diagnostic and therapy

4.1. Current translational upgrades

Developed scaffolded hydrogel systems provide a simplified, unexpensive and controllable experimental setup. Moreover, hydrogel 3D *in vitro* cultures not only are more relevant than monolayer cell cultures, but also allow recreating some features from mice models [163], so they are in line with the 3R's principles, critical in experimental designing [119]. Besides, herein reported hydrogels exhibit enough pathophysiological and biotensegral relevance to be used as first-approach preclinical platforms for drug testing and screening. Indeed, their biotensegral mimicry would allow testing the effect of mechanotransduction signals on cell response to current cytotoxic approaches, but also assess new therapy alternatives implementing mechanotransduction targets.

Furthermore, phenotypic and genotypic data from the NB hydrogels herein presented partially define NB cell behavior and has generated specific knowledge about the impact of several biotensegral cues on NB aggressiveness. In detail, biotensegral mechanotransduction has been evinced as the backbone supporting and regulating a multi-process network related to cell survival, maturation, and energy metabolism, which in turn are interconnected to define tumor malignancy. Despite some of the biomarkers studied in this thesis are not common in the current diagnostic practice, their assessment would entail a more exhaustive evaluation of the patients, thus being easier to adapt the treatment choice to the patient specific needs.

Mechanical, genetic and digital image studies carried out in this thesis have converged in an optimized workflow, which efficiently allows deepening into the regulatory mechanisms underpinning HR-NB aggressiveness, but also elucidate the biological processes occurring in other malignancies and non-malignant systems. Remarkably, since informatic tools such as digital image analysis are increasingly complementing pathology evaluation within the oncology field, the application of these technologies on hydrogel characterization favors the incorporation of these kind of preclinical models into the pathology routine.

4.2. Potential translational upgrades

Once a particular scaffold has been well characterized and proved to properly mimic some basic TME features, it needs to be tested with a set of cancer cell lines in pure cell cultures as well as in different coculture setups to fully understand model performance. Subsequently, hydrogels would become powerful informative and predictive tools for clinical *ex vivo* applications as we have previously reported in collaborative studies [306]. Accordingly, cells from tumor biopsies could be cultured in hydrogel conditions, thus generating *in vitro* fast-growing patient-derived samples that would potentially provide clues about patient evolution and treatment response. Particularly, besides genetic characterization [163], we have performed both IHC (Article I and Article II) and soluble (Article III) biomarker detection, which respectively correlate with clinical analysis performed on tissue samples and liquid biopsies. Therefore, comparative studies between *in vivo* patient samples and *in vitro* patient-derived hydrogels could contribute to both cancer research and precision medicine strategies.

In addition, tissue engineering versatility enable completely redesigning the elaborated platforms from the scratch, being able to vary both the biochemical composition of the scaffolding and its architecture, depending on the experimental requirements. On top of that, cell populations chosen for culture provide further dimensions on model evolution, so that more complex and accurate systems can be obtained. In this sense, 3D culture platforms open up new possibilities with specific constructs for studying cell migration, drug response, the mechanotransduction pathways underlying distinct ECM and TME elements or the cell-cell crosstalk in more realistic coculture scenarios. For instance, hydrogel scaffolds can be engineered to incorporate microfluidic systems, thus potentially becoming either organ-on-chip or tumor-on-chip devices which almost limitless applications on basic, translational, and clinical research [307].

Hydrogels can also be exploited in alternative ways, especially when combined with digital image analysis approaches. As an example, hydrogels can be designed to induce specific cell morphological changes or cell death, which can be recognized visually in scanned images. Therefore, virtual image banks containing multiple images of these induced events can be generated by scanning stained hydrogel slides. Subsequently,

thus generated image banks could be used to train AI algorithms with deep learning approaches to accurately recognize the desired morphological features in *in vivo* samples. In this sense, hydrogels would become data generation tools that would contribute to pathologist assessment accuracy and sample characterization.

V. CONCLUSIONS / CONCLUSIONES

Biotensegrity perspective applied to the oncology research focus not only in malignant cells, but in the interplay of all the elements and variables within the tumor ecosystem. In this way, biotensegrity approaches study the multiple and complex interactions existing between all tumor cells, amorphous substance, fibers, vascular and nervous structures, as well as signaling molecules. Together, these interactions define tumor physics as a key regulator of cancer aggressiveness and highlights its potential as a therapeutic target. Applied to children with high-risk neuroblastoma, the biotensegral perspective aims to find new factors that improve pretreatment risk classification and may be useful for the development of alternative mechanotherapies.

The research carried out in this doctoral thesis, which has used *in vitro* three-dimensional cell culture models to study biotensegrity and its implication in neuroblastoma aggressiveness, has reached the following conclusions:

1. Following the tissue engineering basic principles, we have successfully combined inert structural materials, such as alginate and polyethylene glycol, with biofunctional elements present in the extracellular matrix, such as gelatin (disorganized collagen) and vitronectin. As a result, we generated biocompatible structures with well-defined mechanical properties, which allow maintaining both short- and long-term tumor cell cultures and cocultures (up to 84 days).

2. The morphometric tools that we have computationally developed for the analysis of tumor biopsies can be adjusted to characterize the herein designed hydrogels in an objective and accurate way. Besides cell morphology and protein expression patterns, digital image analysis allowed us to identify cell focal adhesions, determine cell viability within the models, evaluate cell growth dynamics, and characterize vitronectin topography once incorporated into polyethylene glycol scaffolds.

3. Compared to monolayer cell cultures, partially biomimetic extracellular matrix provided by hydrogels acts as a key biotensegral element, thus redefining neuroblast cell behavior while maintaining aggressiveness features such as high mitosis-karyorrhexis index.

4. Recreating basic aspects of the extracellular matrix biotensegrity in a simplified environment facilitates obtaining specific knowledge about tumor clone evolution. The

extracellular matrix stiffness influences some cancer cells adaptation and survival, promoting their cell proliferation, the selection of segmental chromosomal alterations and the appearance of new ones, also reducing model cell cluster total density.

5. The incorporation of Schwann stroma cells into our neuroblastoma models modifies the system behavior as they affect neuroblastoma pathophysiology. Cocultures herein carried out presented dynamics consistent with less aggressiveness, such as reduced proliferation and vitronectin expression.

6. Vitronectin is a key glycoprotein for high-risk neuroblastoma cells. We have demonstrated that neuroblastic cells can adhere to it and that its presence favors hydrogel degradation under the studied conditions. Despite vitronectin expression variations have been found, it has been synthesized by neuroblasts in all experimental conditions, even in those models that were fabricated with vitronectin. In fact, the detection of vitronectin secreted into the culture medium suggests this molecule as a potential biomarker for aggressiveness in neuroblastoma.

7. Overall, extracellular matrix stiffness, stroma cells presence, vitronectin incorporation, and the specific characteristics of both neuroblastic cell lines tested in this thesis establish dynamic synergies, which depend on the system features, and modulate cell growth, metabolism and clonality. These synergies adapt according to model evolution.

9. The versatility of the three-dimensional platforms generated for cell culture, together with the multidisciplinary nature of this research allow using them to deepen neuroblastoma knowledge, as well as in other oncology and biology applications.

Finally, extrapolating our results to general oncology, we declare that the generated models mimic specific aspects of biotensegrity related to tumor aggressiveness, so that they offer direct applications in translational preclinical research and precision medicine, such as both digital pathology and artificial intelligence tools development, as well as molecular mechanotherapies to improve survival and life quality of cancer patients.

El estudio de la oncología desde la perspectiva de la biotensegridad otorga la merecida importancia a todos los elementos y variables presentes en el ecosistema tumoral, no solo a las células malignas. De este modo, se estudian las múltiples y complejas interacciones existentes entre todas las células presentes en el tumor, la sustancia amorfa, las fibras, las estructuras vasculares y nerviosas, así como las moléculas señalizadoras. Todas ellas en conjunto definen la física del tumor como elemento regulador de la agresividad tumoral, con el objetivo de utilizarla como diana terapéutica. Aplicada a los niños con neuroblastoma de alto riesgo, la perspectiva biotensegral busca encontrar nuevos factores que mejoren la clasificación de riesgo pretratamiento y puedan ser útiles para el desarrollo de mecanoterapias alternativas.

La investigación realizada en esta tesis doctoral, que ha utilizado modelos *in vitro* de cultivo celular tridimensionales para estudiar la biotensegridad en relación con la agresividad del neuroblastoma, ha llegado a las siguientes conclusiones:

1. Siguiendo los principios básicos de la ingeniería tisular, hemos combinado con éxito materiales estructurales inertes, como el alginato y el polietilenglicol, con elementos biofuncionales presentes en la matriz extracelular, como la gelatina (colágeno desorganizado) y la vitronectina, para generar estructuras biocompatibles, con propiedades mecánicas bien definidas, y que permiten mantener cultivos y cocultivos celulares tumorales a corto y largo plazo (hasta 84 días).
2. El conjunto de herramientas morfométricas desarrolladas computacionalmente para el análisis de biopsias tumorales es ajustable para caracterizar de forma objetiva y precisa los modelos generados. Además de la morfología celular y los patrones de expresión proteica, el análisis de imagen digital ha permitido la identificación de adhesiones focales, la determinación de la viabilidad celular en los modelos, de las dinámicas de crecimiento celular y la caracterización topográfica de la vitronectina incorporada en los hidrogeles de polietilenglicol.
3. En comparación con los cultivos en monocapa, la matriz extracelular parcialmente biomimética provista por los hidrogeles actúa como elemento biotensegral clave, que redefine el comportamiento de las células neuroblásticas, a la vez que mantiene características de agresividad como el elevado índice de mitosis-cariorraxis.

4. Recrear de forma simplificada aspectos básicos de la biotensegridad de la matriz extracelular permite obtener conocimiento específico sobre la evolución de clones tumorales. La rigidez de la matriz extracelular influye de manera crucial en el proceso de adaptación y supervivencia de determinadas células cancerosas, promoviendo su proliferación celular, la selección de alteraciones cromosómicas segmentarias y aparición de nuevas, reduciendo la densidad total de agrupaciones celulares mantenidas por los modelos.
5. La incorporación de células estromales schwannianas en los modelos de neuroblastoma generados modifica el comportamiento del sistema con repercusiones equivalentes a la fisiopatología descrita en neuroblastoma. Los cocultivos realizados presentaron dinámicas acordes con una menor agresividad, como una reducida proliferación y expresión de vitronectina.
6. La vitronectina es una glicoproteína clave para las células de neuroblastoma de alto riesgo. Hemos demostrado que las células neuroblásticas son capaces de adherirse a ella y que su presencia favorece la degradación de los hidrogeles en las condiciones estudiadas. Además, pese a las variaciones de expresión descritas, ha sido sintetizada por los neuroblastos en todas las condiciones experimentales, incluso en aquellos modelos que se fabricaron incluyendo vitronectina. De hecho, la detección de vitronectina secretada al medio de cultivo sugiere esta molécula como potencial biomarcador de agresividad en neuroblastoma.
7. En conjunto, la rigidez de la matriz extracelular, la presencia de células estromales, la vitronectina incorporada y las características específicas de las líneas celulares neuroblásticas testadas establecen sinergias dinámicas dependientes de las características del sistema y modulan el crecimiento, el metabolismo y la clonalidad celular. Dichas sinergias responden adaptándose a la evolución temporal del modelo.
8. La versatilidad de las plataformas tridimensionales generadas para el cultivo celular, y la multidisciplinariedad del proceso de investigación llevado a cabo en esta tesis permiten su aprovechamiento para profundizar en el conocimiento del neuroblastoma, así como en otras áreas de la oncología y la biología en todas sus aplicaciones.

Finalmente, extrapolando nuestros resultados a nivel general de la oncología, afirmamos que los modelos generados mimetizan aspectos concretos de la biotenseguridad relacionados con la agresividad tumoral, de modo que ofrecen aplicaciones directas en la investigación preclínica traslacional y la medicina de precisión, como el ensayo y desarrollo de herramientas de patología digital, inteligencia artificial y mecanoterapias moleculares con la finalidad de mejorar la supervivencia y la calidad de vida de los pacientes oncológicos.

REFERENCES

1. Buckminster, F.R. Tensile-integrity structures 1962.
2. Yamada, T.; Richiert, D.; Tumminia, S.J.; Russell, P. The tensegrity model applied to the lens: a hypothesis for the presence of the fiber cell ball and sockets. *Med. Hypotheses* 2000, *55*, 36–39, doi:10.1054/MEHY.1999.0994.
3. Motro, R. *Tensegrity : structural systems for the future*; Kogan Page Science, 2003; ISBN 1 9039 9637 6.
4. Liu, Y.; Bi, Q.; Yue, X.; Wu, J.; Yang, B.; Li, Y. A review on tensegrity structures-based robots. *Mech. Mach. Theory* 2022, *168*, 104571, doi:10.1016/J.MECHMACHTHEORY.2021.104571.
5. Tibert, G. Deployable Tensegrity Structures for Space Applications, KTH, 2002.
6. Obara, P.; Tomasik, J. Active Control of Stiffness of Tensegrity Plate-like Structures Built with Simplex Modules. *Mater. (Basel, Switzerland)* 2021, *14*, doi:10.3390/MA14247888.
7. Ingber, D.E. Tensegrity: the architectural basis of cellular mechanotransduction. *Annu. Rev. Physiol.* 1997, *59*, 575–599, doi:10.1146/ANNUREV.PHYSIOL.59.1.575.
8. Tadeo, I.; Berbegall, A.P.; Escudero, L.M.; Álvaro, T.; Noguera, R. Biotensegrity of the extracellular matrix: Physiology, dynamic mechanical balance, and implications in oncology and mechanotherapy. *Front. Oncol.* 2014, *4 MAR*, 39, doi:10.3389/FONC.2014.00039.
9. Chen, C.S.; Ingber, D.E. Tensegrity and mechanoregulation: from skeleton to cytoskeleton. *Osteoarthr. Cartil.* 1999, *7*, 81–94, doi:10.1053/JOCA.1998.0164.
10. Swanson, R.L. Biotensegrity: a unifying theory of biological architecture with applications to osteopathic practice, education, and research--a review and analysis. *J. Am. Osteopath. Assoc.* 2013, *113*, 34–52, doi:10.7556/JAOA.2013.113.1.34.
11. Jaalouk, D.E.; Lammerding, J. Mechanotransduction gone awry. *Nat. Rev. Mol. Cell Biol.* 2009, *10*, 63–73, doi:10.1038/NRM2597.
12. Duncan, R.L.; Turner, C.H. Mechanotransduction and the functional response of

- bone to mechanical strain. *Calcif. Tissue Int.* 1995, 57, 344–358, doi:10.1007/BF00302070.
13. Noguera, R.; Nieto, O.A.; Tadeo, I.; Fariñas, F.; Álvaro, T. Extracellular matrix, biotensegrity and tumor microenvironment. An update and overview. *Histol. Histopathol.* 2012, 27, 693–705, doi:10.14670/HH-27.693.
 14. Lovett, D.B.; Shekhar, N.; Nickerson, J.A.; Roux, K.J.; Lele, T.P. Modulation of Nuclear Shape by Substrate Rigidity. *Cell. Mol. Bioeng.* 2013, 6, 230–238, doi:10.1007/S12195-013-0270-2.
 15. Wang, N.; Tytell, J.D.; Ingber, D.E. Mechanotransduction at a distance: mechanically coupling the extracellular matrix with the nucleus. *Nat. Rev. Mol. Cell Biol.* 2009 101 2009, 10, 75–82, doi:10.1038/nrm2594.
 16. Martino, F.; Perestrelo, A.R.; Vinarský, V.; Pagliari, S.; Forte, G. Cellular mechanotransduction: From tension to function. *Front. Physiol.* 2018, 9, 824, doi:10.3389/FPHYS.2018.00824.
 17. Seong, J.; Wang, N.; Wang, Y. Mechanotransduction at focal adhesions: from physiology to cancer development. *J. Cell. Mol. Med.* 2013, 17, 597, doi:10.1111/JCMM.12045.
 18. Geiger, B.; Spatz, J.P.; Bershadsky, A.D. Environmental sensing through focal adhesions. *Nat. Rev. Mol. Cell Biol.* 2009, 10, 21–33, doi:10.1038/NRM2593.
 19. Wu, C. Focal adhesion: a focal point in current cell biology and molecular medicine. *Cell Adh. Migr.* 2007, 1, 13–18, doi:10.4161/CAM.1.1.4081.
 20. Palumbo, S.; Benvenuti, E.; Fraldi, M. Actomyosin contractility and buckling of microtubules in nucleation, growth and disassembling of focal adhesions. *Biomech. Model. Mechanobiol.* 2022, doi:10.1007/S10237-022-01584-3.
 21. Lombardi, M.L.; Jaalouk, D.E.; Shanahan, C.M.; Burke, B.; Roux, K.J.; Lammerding, J. The interaction between nesprins and sun proteins at the nuclear envelope is critical for force transmission between the nucleus and cytoskeleton. *J. Biol. Chem.* 2011, 286, 26743–26753, doi:10.1074/JBC.M111.233700.

22. Swift, J.; Ivanovska, I.L.; Buxboim, A.; Harada, T.; Dingal, P.C.D.P.; Pinter, J.; Pajerowski, J.D.; Spinler, K.R.; Shin, J.W.; Tewari, M.; et al. Nuclear lamin-A scales with tissue stiffness and enhances matrix-directed differentiation. *Science* 2013, *341*, doi:10.1126/SCIENCE.1240104.
23. Lecuit, T.; Yap, A.S. E-cadherin junctions as active mechanical integrators in tissue dynamics. *Nat. Cell Biol.* 2015 *175* 2015, *17*, 533–539, doi:10.1038/ncb3136.
24. Maruthamuthu, V.; Sabass, B.; Schwarz, U.S.; Gardel, M.L. Cell-ECM traction force modulates endogenous tension at cell-cell contacts. *Proc. Natl. Acad. Sci. U. S. A.* 2011, *108*, 4708–4713, doi:10.1073/PNAS.1011123108.
25. Rani, B.; Cao, Y.; Malfettone, A.; Tomuleasa, C.; Fabregat, I.; Giannelli, G. Role of the tissue microenvironment as a therapeutic target in hepatocellular carcinoma. *World J. Gastroenterol.* 2014, *20*, 4128, doi:10.3748/WJG.V20.I15.4128.
26. Whiteside, T.L. The tumor microenvironment and its role in promoting tumor growth. *Oncogene* 2008, *27*, 5904, doi:10.1038/ONC.2008.271.
27. Majewska, A.; Wilkus, K.; Brodaczewska, K.; Kieda, C. Endothelial Cells as Tools to Model Tissue Microenvironment in Hypoxia-Dependent Pathologies. *Int. J. Mol. Sci.* 2021, *22*, 1–25, doi:10.3390/IJMS22020520.
28. Huang, S.; Ingber, D.E. The structural and mechanical complexity of cell-growth control. *Nat. Cell Biol.* 1999 *15* 1999, *1*, E131–E138, doi:10.1038/13043.
29. Twiss, F.; De Rooij, J. Cadherin mechanotransduction in tissue remodeling. *Cell. Mol. Life Sci.* 2013, *70*, 4101–4116, doi:10.1007/S00018-013-1329-X.
30. Estofolete, C.F.; Botelho-Machado, C.; Taboga, S.R.; Zucoloto, S.; Polli-Lopes, A.C.; Gil, C.D. Effects of myenteric denervation on extracellular matrix fibers and mast cell distribution in normal stomach and gastric lesions. *Cancer Cell Int.* 2010, *10*, doi:10.1186/1475-2867-10-18.
31. Lu, P.; Takai, K.; Weaver, V.M.; Werb, Z. Extracellular matrix degradation and remodeling in development and disease. *Cold Spring Harb. Perspect. Biol.* 2011, *3*, doi:10.1101/CSHPERSPECT.A005058.

32. Tomlin, H.; Piccinini, A.M. A complex interplay between the extracellular matrix and the innate immune response to microbial pathogens. *Immunology* 2018, *155*, 186, doi:10.1111/IMM.12972.
33. Burgos-Panadero, R.; Lucantoni, F.; Gamero-Sandemetrio, E.; Cruz-Merino, L. de la; Álvaro, T.; Noguera, R. The tumour microenvironment as an integrated framework to understand cancer biology. *Cancer Lett.* 2019, *461*, 112–122, doi:10.1016/j.canlet.2019.07.010.
34. Sanegre, S.; Lucantoni, F.; Burgos-Panadero, R.; de La Cruz-Merino, L.; Noguera, R.; Naranjo, T.Á. Integrating the tumor microenvironment into cancer therapy. *Cancers (Basel)*. 2020, *12*, 1–24, doi:10.3390/cancers12061677.
35. Tlsty, T.D.; Coussens, L.M. Tumor stroma and regulation of cancer development. *Annu. Rev. Pathol.* 2006, *1*, 119–150, doi:10.1146/ANNUREV.PATHOL.1.110304.100224.
36. Tlsty, T.D. Stromal cells can contribute oncogenic signals. *Semin. Cancer Biol.* 2001, *11*, 97–104, doi:10.1006/SCBI.2000.0361.
37. Pupa, S.M.; Ménard, S.; Forti, S.; Tagliabue, E. New insights into the role of extracellular matrix during tumor onset and progression. *J. Cell. Physiol.* 2002, *192*, 259–267, doi:10.1002/JCP.10142.
38. Dufort, C.C.; Paszek, M.J.; Weaver, V.M. Balancing forces: architectural control of mechanotransduction. *Nat. Rev. Mol. Cell Biol.* 2011, *12*, 308–319, doi:10.1038/NRM3112.
39. Romani, P.; Valcarcel-Jimenez, L.; Frezza, C.; Dupont, S. Crosstalk between mechanotransduction and metabolism. *Nat. Rev. Mol. Cell Biol.* 2021, *22*, 22–38, doi:10.1038/S41580-020-00306-W.
40. Moreira, A.M.; Pereira, J.; Melo, S.; Fernandes, M.S.; Carneiro, P.; Seruca, R.; Figueiredo, J. The Extracellular Matrix: An Accomplice in Gastric Cancer Development and Progression. *Cells* 2020, *9*, doi:10.3390/CELLS9020394.
41. Jang, I.; Beningo, K.A. Integrins, CAFs and Mechanical Forces in the Progression of

- Cancer. *Cancers (Basel)*. 2019, *11*, doi:10.3390/CANCERS11050721.
42. Abdollahiyan, P.; Oroojalian, F.; Baradaran, B.; de la Guardia, M.; Mokhtarzadeh, A. Advanced mechanotherapy: Biotensegrity for governing metastatic tumor cell fate via modulating the extracellular matrix. *J. Control. Release* 2021, *335*, 596–618, doi:10.1016/J.JCONREL.2021.06.002.
 43. Tata, P.R.; Rajagopal, J. Cellular plasticity: 1712 to the present day. *Curr. Opin. Cell Biol.* 2016, *43*, 46–54, doi:10.1016/J.CEB.2016.07.005.
 44. Clairambault, J.; Shen, S. Cell plasticity in cancer cell populations. *F1000Research* 2020, *9*, doi:10.12688/F1000RESEARCH.24803.1.
 45. Wilmut, I.; Sullivan, G.; Chambers, I. The evolving biology of cell reprogramming. *Philos. Trans. R. Soc. B Biol. Sci.* 2011, *366*, 2183, doi:10.1098/RSTB.2011.0051.
 46. Filip, S.; Mokrý, J.; English, D.; Vojáček, J. Stem cell plasticity and issues of stem cell therapy. *Folia Biol* 2005, *51*, 180–187.
 47. Merrell, A.J.; Stanger, B.Z. Adult cell plasticity in vivo: de-differentiation and transdifferentiation are back in style. *Nat. Rev. Mol. Cell Biol.* 2016, *17*, 413–425, doi:10.1038/NRM.2016.24.
 48. Fagotto, F. EpCAM as Modulator of Tissue Plasticity. *Cells* 2020, *Vol. 9*, Page 2128 2020, *9*, 2128, doi:10.3390/CELLS9092128.
 49. Sakers, A.; De Siqueira, M.K.; Seale, P.; Villanueva, C.J. Adipose-tissue plasticity in health and disease. *Cell* 2022, *185*, 419–446, doi:10.1016/J.CELL.2021.12.016.
 50. Yuan, S.; Norgard, R.J.; Stanger, B.Z. Cellular Plasticity in Cancer. *Cancer Discov.* 2019, *9*, 837–851, doi:10.1158/2159-8290.CD-19-0015.
 51. Qin, S.; Jiang, J.; Lu, Y.; Nice, E.C.; Huang, C.; Zhang, J.; He, W. Emerging role of tumor cell plasticity in modifying therapeutic response. *Signal Transduct. Target. Ther.* 2020 *51* 2020, *5*, 1–36, doi:10.1038/s41392-020-00313-5.
 52. Schild, T.; Low, V.; Blenis, J.; Gomes, A.P. Unique Metabolic Adaptations Dictate Distal Organ-Specific Metastatic Colonization. *Cancer Cell* 2018, *33*, 347–354, doi:10.1016/j.ccell.2018.02.001.

53. Friedmann-Morvinski, D.; Verma, I.M. Dedifferentiation and reprogramming: origins of cancer stem cells. *EMBO Rep.* 2014, *15*, 244, doi:10.1002/EMBR.201338254.
54. Ohshima, K.; Morii, E. Metabolic Reprogramming of Cancer Cells during Tumor Progression and Metastasis. *Metabolites* 2021, *11*, 1–23, doi:10.3390/METABO11010028.
55. Jacquet, P.; Stéphanou, A. Metabolic Reprogramming, Questioning, and Implications for Cancer. *Biology (Basel)*. 2021, *10*, 1–7, doi:10.3390/BIOLOGY10020129.
56. Hanahan, D. Hallmarks of Cancer: New Dimensions. *Cancer Discov.* 2022, *12*, 31–46, doi:10.1158/2159-8290.CD-21-1059.
57. Warburg, O. On the origin of cancer cells. *Science* 1956, *123*, 309–314, doi:10.1126/SCIENCE.123.3191.309.
58. Yoshida, G.J. Metabolic reprogramming: The emerging concept and associated therapeutic strategies. *J. Exp. Clin. Cancer Res.* 2015, *34*, 1–10, doi:10.1186/S13046-015-0221-Y.
59. Boedtkjer, E.; Pedersen, S.F. The Acidic Tumor Microenvironment as a Driver of Cancer. *Annu. Rev. Physiol.* 2020, *82*, 103–126, doi:10.1146/ANNUREV-PHYSIOL-021119-034627.
60. Monferrer, E.; Vieco-Martí, I.; López-Carrasco, A.; Fariñas, F.; Abanades, S.; de la Cruz-Merino, L.; Noguera, R.; Álvaro Naranjo, T. Metabolic Classification and Intervention Opportunities for Tumor Energy Dysfunction. *Metabolites* 2021, *11*, doi:10.3390/metabo11050264.
61. Cross, S.E.; Jin, Y.S.; Rao, J.; Gimzewski, J.K. Nanomechanical analysis of cells from cancer patients. *Nat. Nanotechnol.* 2007, *2*, 780–783, doi:10.1038/nnano.2007.388.
62. Lekka, M.; Laidler, P.; Gil, D.; Lekki, J.; Stachura, Z.; Hryniewicz, A.Z. Elasticity of normal and cancerous human bladder cells studied by scanning force microscopy.

- Eur. Biophys. J.* 1999, 28, 312–316, doi:10.1007/S002490050213.
63. Lee, J.M.; Dedhar, S.; Kalluri, R.; Thompson, E.W. The epithelial-mesenchymal transition: new insights in signaling, development, and disease. *J. Cell Biol.* 2006, 172, 973–981, doi:10.1083/JCB.200601018.
 64. Guarino, M.; Rubino, B.; Ballabio, G. The role of epithelial-mesenchymal transition in cancer pathology. *Pathology* 2007, 39, 305–318, doi:10.1080/00313020701329914.
 65. Suresh, S. Biomechanics and biophysics of cancer cells. *Acta Biomater.* 2007, 3, 413–438, doi:10.1016/J.ACTBIO.2007.04.002.
 66. Jonckheere, S.; Adams, J.; De Groote, D.; Campbell, K.; Berx, G.; Goossens, S. Epithelial-Mesenchymal Transition (EMT) as a Therapeutic Target. *Cells Tissues Organs* 2022, 211, 157–182, doi:10.1159/000512218.
 67. Selvaraj, V.; Plane, J.M.; Williams, A.J.; Deng, W. Switching cell fate: the remarkable rise of iPS cells and lineage reprogramming technologies. *Trends Biotechnol.* 2010, 28, 214, doi:10.1016/J.TIBTECH.2010.01.002.
 68. Z, L.; JL, T.; DM, C.; MT, Y.; NJ, S.; SA, R.; CM, N.; CS, C. Mechanical tugging force regulates the size of cell-cell junctions. *Proc. Natl. Acad. Sci. U. S. A.* 2010, 107, doi:10.1073/PNAS.0914547107.
 69. Le Duc, Q.; Shi, Q.; Blonk, I.; Sonnenberg, A.; Wang, N.; Leckband, D.; De Rooij, J. Vinculin potentiates E-cadherin mechanosensing and is recruited to actin-anchored sites within adherens junctions in a myosin II-dependent manner. *J. Cell Biol.* 2010, 189, 1107–1115, doi:10.1083/JCB.201001149.
 70. Friedl, P.; Wolf, K. Tumour-cell invasion and migration: diversity and escape mechanisms. *Nat. Rev. Cancer* 2003, 3, 362–374, doi:10.1038/NRC1075.
 71. Lintz, M.; Muñoz, A.; Reinhart-King, C.A. The Mechanics of Single Cell and Collective Migration of Tumor Cells. *J. Biomech. Eng.* 2017, 139, 0210051, doi:10.1115/1.4035121.
 72. Pasquier, J.; Abu-Kaoud, N.; Al Thani, H.; Rafii, A. Epithelial to Mesenchymal

- Transition in a Clinical Perspective. *J. Oncol.* 2015, 2015, doi:10.1155/2015/792182.
73. Saéñz-de-Santa-María, I.; Celada, L.; Chiara, M.D. The Leader Position of Mesenchymal Cells Expressing N-Cadherin in the Collective Migration of Epithelial Cancer. *Cells* 2020, Vol. 9, Page 731 2020, 9, 731, doi:10.3390/CELLS9030731.
74. Friedl, P.; Alexander, S. Cancer invasion and the microenvironment: plasticity and reciprocity. *Cell* 2011, 147, 992–1009, doi:10.1016/J.CELL.2011.11.016.
75. Cheung, K.J.; Ewald, A.J. A collective route to metastasis: Seeding by tumor cell clusters. *Science* 2016, 352, 167–169, doi:10.1126/SCIENCE.AAF6546.
76. Monferrer, E.; Sanegre, S.; Vieco-Martí, I.; López-Carrasco, A.; Fariñas, F.; Villatoro, A.; Abanades, S.; Mañes, S.; de la Cruz-Merino, L.; Noguera, R.; et al. Immunometabolism Modulation in Therapy. *Biomedicines* 2021, 9, doi:10.3390/biomedicines9070798.
77. Gordon-Weeks, A.; Yuzhalin, A.E. Cancer Extracellular Matrix Proteins Regulate Tumour Immunity. *Cancers (Basel)*. 2020, 12, 1–25, doi:10.3390/CANCERS12113331.
78. Ahmad, R.S.; Eubank, T.D.; Lukomski, S.; Boone, B.A. Immune Cell Modulation of the Extracellular Matrix Contributes to the Pathogenesis of Pancreatic Cancer. *Biomolecules* 2021, 11, 901, doi:10.3390/BIOM11060901.
79. Weng, C.Y.; Kao, C.X.; Chang, T.S.; Huang, Y.H. Immuno-Metabolism: The Role of Cancer Niche in Immune Checkpoint Inhibitor Resistance. *Int. J. Mol. Sci.* 2021, 22, 1–24, doi:10.3390/IJMS22031258.
80. Zhu, K.; Liu, Q.; Zhou, Y.; Tao, C.; Zhao, Z.; Sun, J.; Xu, H. Oncogenes and tumor suppressor genes: Comparative genomics and network perspectives. *BMC Genomics* 2015, 16, 1–11, doi:10.1186/1471-2164-16-S7-S8.
81. Lee, E.Y.H.P.; Muller, W.J. Oncogenes and Tumor Suppressor Genes. *Cold Spring Harb. Perspect. Biol.* 2010, 2, doi:10.1101/CSHPERSPECT.A003236.
82. Fortunato, A.; Boddy, A.; Mallo, D.; Aktipis, A.; Maley, C.C.; Pepper, J.W. Natural

- Selection in Cancer Biology: From Molecular Snowflakes to Trait Hallmarks. *Cold Spring Harb. Perspect. Med.* 2017, 7, doi:10.1101/CSHPERSPECT.A029652.
83. Worsley, C.M.; Mayne, E.S.; Veale, R.B. Clone wars: the evolution of therapeutic resistance in cancer. *Evol. Med. Public Heal.* 2016, 2016, 180, doi:10.1093/EMPH/EOW015.
 84. Anupriya, S.; Chakraborty, A.; Patnaik, S. Clonal evolution and expansion associated with therapy resistance and relapse of Colorectal Cancer. *Mutat. Res. Mutat. Res.* 2022, 108445, doi:10.1016/J.MRREV.2022.108445.
 85. You, J.S.; Jones, P.A. Cancer genetics and epigenetics: two sides of the same coin? *Cancer Cell* 2012, 22, 9–20, doi:10.1016/J.CCR.2012.06.008.
 86. Doroshow, J.H.; Kummar, S. Translational research in oncology—10 years of progress and future prospects. *Nat. Rev. Clin. Oncol.* 2014 1111 2014, 11, 649–662, doi:10.1038/nrclinonc.2014.158.
 87. Zhang, B.; Ao, B.; Lu, X.; Yang, S.; Bao, P.; Wang, H.; Li, R.; Huang, Y. Global research trends on precision oncology: A systematic review, bibliometrics, and visualized study. *Medicine (Baltimore)*. 2022, 101, e31380, doi:10.1097/MD.00000000000031380.
 88. Robb, J.A.; Gulley, M.L.; Fitzgibbons, P.L.; Kennedy, M.F.; Cosentino, L.M.; Washington, K.; Dash, R.C.; Branton, P.A.; Jewell, S.D.; Lapham, R.L. A Call to Standardize Preanalytic Data Elements for Biospecimens. *Arch. Pathol. Lab. Med.* 2014, 138, 526, doi:10.5858/ARPA.2013-0250-CP.
 89. Kim, H.S.; Minna, J.D.; White, M.A. GWAS meets TCGA to illuminate mechanisms of cancer predisposition. *Cell* 2013, 152, 387–389, doi:10.1016/J.CELL.2013.01.027.
 90. Lavis, L.D. Histochemistry: Live and in Color. *J. Histochem. Cytochem.* 2011, 59, 139, doi:10.1369/0022155410395760.
 91. Duraiyan, J.; Govindarajan, R.; Kaliyappan, K.; Palanisamy, M. Applications of immunohistochemistry. *J. Pharm. Bioallied Sci.* 2012, 4, S307, doi:10.4103/0975-

- 7406.100281.
92. Sussman, L.; Garcia-Robledo, J.E.; Ordóñez-Reyes, C.; Forero, Y.; Mosquera, A.F.; Ruíz-Patiño, A.; Chamorro, D.F.; Cardona, A.F. Integration of artificial intelligence and precision oncology in Latin America. *Front. Med. Technol.* 2022, 4, doi:10.3389/FMEDT.2022.1007822.
 93. Janowczyk, A.; Baumhoer, D.; Dirnhofer, S.; Grobholz, R.; Kipar, A.; de Leval, L.; Merkler, D.; Michielin, O.; Moch, H.; Perren, A.; et al. Towards a national strategy for digital pathology in Switzerland. *Virchows Arch.* 2022, doi:10.1007/S00428-022-03345-0.
 94. Vigneswaran, W.T.; Campbell, D.N.; Pappas, G.; Wiggins, J.W.; Wolfe, R.W.; Clarke, D.R. Use of artificial intelligence for the preoperative diagnosis of pulmonary lesions. *Ann. Thorac. Surg.* 1989, 48, 556–559, doi:10.1016/S0003-4975(10)66862-2.
 95. Nafe, R.; Choritz, H. Introduction of a neuronal network as a tool for diagnostic analysis and classification based on experimental pathologic data. *Exp. Toxicol. Pathol.* 1992, 44, 17–24, doi:10.1016/S0940-2993(11)80132-6.
 96. Shreve, J.T.; Khanani, S.A.; Haddad, T.C. Artificial Intelligence in Oncology: Current Capabilities, Future Opportunities, and Ethical Considerations. *Am. Soc. Clin. Oncol. Educ. book. Am. Soc. Clin. Oncol. Annu. Meet.* 2022, 42, 1–10, doi:10.1200/EDBK_350652.
 97. Huang, J.; Mei, L.; Long, M.; Liu, Y.; Sun, W.; Li, X.; Shen, H.; Zhou, F.; Ruan, X.; Wang, D.; et al. BM-Net: CNN-Based MobileNet-V3 and Bilinear Structure for Breast Cancer Detection in Whole Slide Images. *Bioeng. (Basel, Switzerland)* 2022, 9, 261, doi:10.3390/BIOENGINEERING9060261.
 98. Qaiser, T.; Lee, C.-Y.; Vandenberghe, M.; Yeh, J.; Gavrielides, M.A.; Hipp, J.; Scott, M.; Reischl, J. Usability of deep learning and H&E images predict disease outcome-emerging tool to optimize clinical trials. *NPJ Precis. Oncol.* 2022, 6, doi:10.1038/S41698-022-00275-7.
 99. Hamilton, P.W.; Bankhead, P.; Wang, Y.; Hutchinson, R.; Kieran, D.; Mcart, D.G.;

- James, J.; Salto-Tellez, M. Digital pathology and image analysis in tissue biomarker research. 2014, doi:10.1016/j.ymeth.2014.06.015.
100. Laurinavicius, A.; Laurinaviciene, A.; Dasevicius, D.; Elie, N.; Plancoulaine, B.; Bor, C.; Herlin, P. Digital image analysis in pathology: Benefits and obligation. *Anal. Cell. Pathol.* 2012, *35*, 75–78, doi:10.3233/ACP-2011-0033.
101. Baxi, V.; Edwards, R.; Montalto, M.; Saha, S. Digital pathology and artificial intelligence in translational medicine and clinical practice. *Mod. Pathol.* 2021 *351* 2021, *35*, 23–32, doi:10.1038/s41379-021-00919-2.
102. Tadeo, I.; Berbegall, A.P.; Navarro, S.; Castel, V.; Noguera, R. A stiff extracellular matrix is associated with malignancy in peripheral neuroblastic tumors. *Pediatr. Blood Cancer* 2017, *64*, e26449, doi:10.1002/pbc.26449.
103. Sabri, S.; Richelme, F.; Pierres, A.; Benoliel, A.M.; Bongrand, P. Interest of image processing in cell biology and immunology. *J. Immunol. Methods* 1997, *208*, 1–27, doi:10.1016/S0022-1759(97)00115-4.
104. Rizzardi, A.E.; Johnson, A.T.; Vogel, R.I.; Pambuccian, S.E.; Henriksen, J.; Pn Skubitz, A.; Metzger, G.J.; Schmechel, S.C. Quantitative comparison of immunohistochemical staining measured by digital image analysis versus pathologist visual scoring. *Diagn. Pathol.* 2012, *20*, 7–42, doi:10.1186/1746-1596-7-42.
105. Cronin, K.A.; Susan, |; Mph, S.; Firth Bs, A.U.; Phd, S.; Henley, | S Jane; Recinda, |; Sherman Mph, L.; Siegel Mph, R.L.; Anderson, R.N.; et al. Annual report to the nation on the status of cancer, part 1: National cancer statistics. *Cancer* 2022, doi:10.1002/CNCR.34479.
106. Zhan, B.; Wen, S.; Lu, J.; Shen, G.; Lin, X.; Feng, J.; Huang, H. Identification and causes of metabonomic difference between orthotopic and subcutaneous xenograft of pancreatic cancer. *Oncotarget* 2017, *8*, 61264, doi:10.18632/ONCOTARGET.18057.
107. Day, C.P.; Merlino, G.; Van Dyke, T. Preclinical mouse cancer models: a maze of opportunities and challenges. *Cell* 2015, *163*, 39–53,

- doi:10.1016/J.CELL.2015.08.068.
108. Lai, Y.; Wei, X.; Lin, S.; Qin, L.; Cheng, L.; Li, P. Current status and perspectives of patient-derived xenograft models in cancer research. *J. Hematol. Oncol.* 2017, *10*, doi:10.1186/S13045-017-0470-7.
 109. Collins, A.T.; Lang, S.H. A systematic review of the validity of patient derived xenograft (PDX) models: the implications for translational research and personalised medicine. *PeerJ* 2018, *6*, doi:10.7717/PEERJ.5981.
 110. Okada, S.; Vaeteewoottacharn, K.; Kariya, R. Application of Highly Immunocompromised Mice for the Establishment of Patient-Derived Xenograft (PDX) Models. *Cells* 2019, *8*, doi:10.3390/CELLS8080889.
 111. Zhou, Q.; Facciponte, J.; Jin, M.; Shen, Q.; Lin, Q. Humanized NOD-SCID IL2rg^{-/-} mice as a preclinical model for cancer research and its potential use for individualized cancer therapies. *Cancer Lett.* 2014, *344*, 13–19, doi:10.1016/J.CANLET.2013.10.015.
 112. Tratar, U.L.; Horvat, S.; Cemazar, M. Transgenic mouse models in cancer research. *Front. Oncol.* 2018, *8*, 268, doi:10.3389/FONC.2018.00268.
 113. Mou, H.; Kennedy, Z.; Anderson, D.G.; Yin, H.; Xue, W. Precision cancer mouse models through genome editing with CRISPR-Cas9. *Genome Med.* 2015, *7*, 1–11, doi:10.1186/S13073-015-0178-7.
 114. Platt, R.J.; Chen, S.; Zhou, Y.; Yim, M.J.; Swiech, L.; Kempton, H.R.; Dahlman, J.E.; Parnas, O.; Eisenhaure, T.M.; Jovanovic, M.; et al. CRISPR-Cas9 knockin mice for genome editing and cancer modeling. *Cell* 2014, *159*, 440–455, doi:10.1016/J.CELL.2014.09.014.
 115. Kersten, K.; Visser, K.E.; Miltenburg, M.H.; Jonkers, J. Genetically engineered mouse models in oncology research and cancer medicine. *EMBO Mol. Med.* 2017, *9*, 137–153, doi:10.15252/EMMM.201606857.
 116. Talmadge, J.E.; Singh, R.K.; Fidler, I.J.; Raz, A. Murine Models to Evaluate Novel and Conventional Therapeutic Strategies for Cancer. *Am. J. Pathol.* 2007, *170*,

- 793, doi:10.2353/AJPATH.2007.060929.
117. Zuber, J.; Radtke, I.; Pardee, T.S.; Zhao, Z.; Rappaport, A.R.; Luo, W.; McCurrach, M.E.; Yang, M.M.; Dolan, M.E.; Kogan, S.C.; et al. Mouse models of human AML accurately predict chemotherapy response. *Genes Dev.* 2009, *23*, 877, doi:10.1101/GAD.1771409.
118. Zeng, Z.; Gu, S.S.; Wong, C.J.; Yang, L.; Ouardaoui, N.; Li, D.; Zhang, W.; Brown, M.; Liu, X.S. Machine learning on syngeneic mouse tumor profiles to model clinical immunotherapy response. *Sci. Adv.* 2022, *8*, eabm8564, doi:10.1126/SCIADV.ABM8564.
119. Díaz, L.; Zambrano, E.; Flores, M.E.; Contreras, M.; Crispín, J.C.; Alemán, G.; Bravo, C.; Armenta, A.; Valdés, V.J.; Tovar, A.; et al. Ethical Considerations in Animal Research: The Principle of 3R's. *Rev. Invest. Clin.* 2020, *73*, 199–209, doi:10.24875/RIC.20000380.
120. Klinghammer, K.; Walther, W.; Hoffmann, J. Choosing wisely - Preclinical test models in the era of precision medicine. *Cancer Treat. Rev.* 2017, *55*, 36–45, doi:10.1016/J.CTRV.2017.02.009.
121. Yang, W.; Soares, J.; Greninger, P.; Edelman, E.J.; Lightfoot, H.; Forbes, S.; Bindal, N.; Beare, D.; Smith, J.A.; Thompson, I.R.; et al. Genomics of Drug Sensitivity in Cancer (GDSC): a resource for therapeutic biomarker discovery in cancer cells. *Nucleic Acids Res.* 2013, *41*, doi:10.1093/NAR/GKS1111.
122. Pijuan, J.; Barceló, C.; Moreno, D.F.; Maiques, O.; Sisó, P.; Marti, R.M.; Macià, A.; Panosa, A. In vitro cell migration, invasion, and adhesion assays: From cell imaging to data analysis. *Front. Cell Dev. Biol.* 2019, *7*, 107, doi:10.3389/FCELL.2019.00107.
123. Ben-David, U.; Siranosian, B.; Ha, G.; Tang, H.; Oren, Y.; Hinohara, K.; Strathdee, C.A.; Dempster, J.; Lyons, N.J.; Burns, R.; et al. Genetic and transcriptional evolution alters cancer cell line drug response. *Nature* 2018, *560*, 325–330, doi:10.1038/S41586-018-0409-3.
124. Gillet, J.P.; Varma, S.; Gottesman, M.M. The clinical relevance of cancer cell lines.

- J. Natl. Cancer Inst.* 2013, *105*, 452–458, doi:10.1093/JNCI/DJT007.
125. Nishida-Aoki, N.; Gujral, T.S. Emerging approaches to study cell-cell interactions in tumor microenvironment. *Oncotarget* 2019, *10*, 785–797, doi:10.18632/ONCOTARGET.26585.
126. Pape, J.; Emberton, M.; Cheema, U. 3D Cancer Models: The Need for a Complex Stroma, Compartmentalization and Stiffness. *Front. Bioeng. Biotechnol.* 2021, *9*, 276, doi:10.3389/FBIOE.2021.660502.
127. Rodrigues, J.; Heinrich, M.A.; Teixeira, L.M.; Prakash, J. 3D In Vitro Model (R)evolution: Unveiling Tumor–Stroma Interactions. *Trends in Cancer* 2021, *7*, 249–264, doi:10.1016/j.trecan.2020.10.009.
128. Jubelin, C.; Muñoz-Garcia, J.; Griscom, L.; Cochonneau, D.; Ollivier, E.; Heymann, M.F.; Vallette, F.M.; Oliver, L.; Heymann, D. Three-dimensional in vitro culture models in oncology research. *Cell Biosci.* 2022 *121* 2022, *12*, 1–28, doi:10.1186/S13578-022-00887-3.
129. Cui, X.; Hartanto, Y.; Zhang, H. Advances in multicellular spheroids formation. *J. R. Soc. Interface* 2017, *14*, doi:10.1098/RSIF.2016.0877.
130. Zanoni, M.; Piccinini, F.; Arienti, C.; Zamagni, A.; Santi, S.; Polico, R.; Bevilacqua, A.; Tesei, A. 3D tumor spheroid models for in vitro therapeutic screening: a systematic approach to enhance the biological relevance of data obtained. *Sci. Reports* 2016 *61* 2016, *6*, 1–11, doi:10.1038/srep19103.
131. Lin, R.Z.; Chang, H.Y. Recent advances in three-dimensional multicellular spheroid culture for biomedical research. *Biotechnol. J.* 2008, *3*, 1172–1184, doi:10.1002/BIOT.200700228.
132. Albritton, J.L.; Miller, J.S. 3D bioprinting: improving in vitro models of metastasis with heterogeneous tumor microenvironments. *Dis. Model. Mech.* 2017, *10*, 3, doi:10.1242/DMM.025049.
133. Xin, X.; Yang, H.; Zhang, F.; Yang, S.T. 3D cell coculture tumor model: A promising approach for future cancer drug discovery. *Process Biochem.* 2019, *78*, 148–160,

- doi:10.1016/J.PROCBIO.2018.12.028.
134. Tatullo, M.; Marrelli, B.; Benincasa, C.; Aiello, E.; Makeeva, I.; Zavan, B.; Ballini, A.; De Vito, D.; Spagnuolo, G. Organoids in Translational Oncology. *J. Clin. Med.* 2020, *Vol. 9*, Page 2774 2020, 9, 2774, doi:10.3390/JCM9092774.
 135. Gunti, S.; Hoke, A.T.K.; Vu, K.P.; London, N.R. Organoid and Spheroid Tumor Models: Techniques and Applications. *Cancers (Basel)*. 2021, *13*, 1–18, doi:10.3390/CANCERS13040874.
 136. Kaatsch, P. Epidemiology of childhood cancer. *Cancer Treat. Rev.* 2010, *36*, 277–285, doi:10.1016/J.CTRV.2010.02.003.
 137. Maris, J.M.; Hogarty, M.D.; Bagatell, R.; Cohn, S.L. Neuroblastoma. *Lancet (London, England)* 2007, *369*, 2106–2120, doi:10.1016/S0140-6736(07)60983-0.
 138. DuBois, S.G.; Kalika, Y.; Lukens, J.N.; Brodeur, G.M.; Seeger, R.C.; Atkinson, J.B.; Haase, G.M.; Black, C.T.; Perez, C.; Shimada, H.; et al. Metastatic sites in stage IV and IVS neuroblastoma correlate with age, tumor biology, and survival. *J. Pediatr. Hematol. Oncol.* 1999, *21*, 181–189, doi:10.1097/00043426-199905000-00005.
 139. Vandesompele, J.; Roy, N. Van; Gele, M. Van; Ve Laureys, G.; Ambros, P.; Heimann, P.; Devalck, C.; Schuurin, E.; Brock, P.; Otten, J.; et al. Genetic Heterogeneity of Neuroblastoma Studied by Comparative Genomic Hybridization. *Genes Chromosom. Cancer* 1998, *23*, 141–152, doi:10.1002/(SICI)1098-2264(199810)23:2.
 140. D’Angio, G.J.; Evans, A.E.; Koop, C.E. Special pattern of widespread neuroblastoma with a favourable prognosis. *Lancet (London, England)* 1971, *1*, 1046–1049, doi:10.1016/S0140-6736(71)91606-0.
 141. De Bernardi, B.; Nicolas, B.; Boni, L.; Indolfi, P.; Carli, M.; Di Montezemolo, L.C.; Donfrancesco, A.; Pession, A.; Provenzi, M.; Di Cataldo, A.; et al. Disseminated neuroblastoma in children older than one year at diagnosis: comparable results with three consecutive high-dose protocols adopted by the Italian Co-Operative Group for Neuroblastoma. *J. Clin. Oncol.* 2003, *21*, 1592–1601, doi:10.1200/JCO.2003.05.191.

142. Matthay, K.K.; Villablanca, J.G.; Seeger, R.C.; Stram, D.O.; Harris, R.E.; Ramsay, N.K.; Swift, P.; Shimada, H.; Black, C.T.; Brodeur, G.M.; et al. Treatment of high-risk neuroblastoma with intensive chemotherapy, radiotherapy, autologous bone marrow transplantation, and 13-cis-retinoic acid. Children's Cancer Group. *N. Engl. J. Med.* 1999, *341*, 1165–1173, doi:10.1056/NEJM199910143411601.
143. Ambros, P.; Ambros, I.; Brodeur, G.; Haber, M.; Khan, J.; Nakagawara, A.; Schleiermacher, G.; Speleman, F.; Spitz, R.; London, W.; et al. International consensus for neuroblastoma molecular diagnostics: report from the International Neuroblastoma Risk Group (INRG) Biology Committee. *Br. J. Cancer* 2009, *100*, 1471–1482, doi:10.1038/sj.bjc.6605014.
144. Mossé, Y.P.; Laudenslager, M.; Longo, L.; Cole, K.A.; Wood, A.; Attiyeh, E.F.; Laquaglia, M.J.; Sennett, R.; Lynch, J.E.; Perri, P.; et al. Identification of ALK as a major familial neuroblastoma predisposition gene. *Nature* 2008, *455*, 930–935, doi:10.1038/NATURE07261.
145. van Gerven, M.R.; Bozsaky, E.; Matser, Y.A.H.; Vosseberg, J.; Taschner-Mandl, S.; Koster, J.; Tytgat, G.A.M.; Molenaar, J.J.; van den Boogaard, M. Mutational spectrum of ATRX aberrations in neuroblastoma and associated patient and tumor characteristics. *Cancer Sci.* 2022, *113*, 2167–2178, doi:10.1111/CAS.15363.
146. Peifer, M.; Hertwig, F.; Roels, F.; Dreidax, D.; Gartlgruber, M.; Menon, R.; Krämer, A.; Roncaioli, J.L.; Sand, F.; Heuckmann, J.M.; et al. Telomerase activation by genomic rearrangements in high-risk neuroblastoma. *Nature* 2015, *526*, 700–704, doi:10.1038/NATURE14980.
147. Tadeo, I.; Piqueras, M.; Montaner, D.; Villamón, E.; Berbegall, A.P.; Cañete, A.; Navarro, S.; Noguera, R. Quantitative modeling of clinical, cellular, and extracellular matrix variables suggest prognostic indicators in cancer: a model in neuroblastoma. *Pediatr. Res.* 2014 *752* 2013, *75*, 302–314, doi:10.1038/pr.2013.217.
148. Burgos-Panadero, R.; Noguera, I.; Cañete, A.; Navarro, S.; Noguera, R. Vitronectin as a molecular player of the tumor microenvironment in neuroblastoma. *BMC Cancer* 2019, *19*, doi:10.1186/S12885-019-5693-2.

149. Vicente-Munuera, P.; Burgos-Panadero, R.; Noguera, I.; Navarro, S.; Noguera, R.; Escudero, L.M. The topology of vitronectin: A complementary feature for neuroblastoma risk classification based on computer-aided detection. *Int. J. Cancer* 2020, *146*, 553, doi:10.1002/IJC.32495.
150. Tadeo, I.; Bueno, G.; Berbegall, A.P.; Milagro Fernández-Carrobles, M.; Castel, V.; García-Rojo, M.; Navarro, S.; Noguera, R. Vascular patterns provide therapeutic targets in aggressive neuroblastic tumors. *Oncotarget* 2016, *7*, 19935–19947, doi:10.18632/oncotarget.7661.
151. Tadeo, I.; Gamero-Sandemetrio, E.; Berbegall, A.P.; Gironella, M.; Ritort, F.; Cañete, A.; Bueno, G.; Navarro, S.; Noguera, R. Lymph microvascularization as a prognostic indicator in neuroblastoma. *Oncotarget* 2018, *9*, 26157, doi:10.18632/ONCOTARGET.25457.
152. Tadeo, I.; Berbegall, A.P.; Castel, V.; García-Miguel, P.; Callaghan, R.; Pålman, S.; Navarro, S.; Noguera, R. Extracellular matrix composition defines an ultra-high-risk group of neuroblastoma within the high-risk patient cohort. *Br. J. Cancer* 2016, *115*, 480–489, doi:10.1038/bjc.2016.210.
153. Lundberg, K.I.; Treis, D.; Johnsen, J.I. Neuroblastoma Heterogeneity, Plasticity, and Emerging Therapies. *Curr. Oncol. Rep.* 2022, *24*, 1053–1062, doi:10.1007/S11912-022-01270-8.
154. Gautier, M.; Thirant, C.; Delattre, O.; Janoueix-Lerosey, I. Plasticity in neuroblastoma cell identity defines a noradrenergic-to-mesenchymal transition (Nmt). *Cancers (Basel)*. 2021, *13*, doi:10.3390/CANCERS13122904.
155. Monferrer, E.; Burgos-Panadero, R.; Blanquer-Maceiras, M.; Cañete, A.; Navarro, S.; Noguera, R. High Oct4 expression: Implications in the pathogenesis of neuroblastic tumours. *BMC Cancer* 2019, *19*, doi:10.1186/s12885-018-5219-3.
156. Yang, S.; Zheng, J.; Ma, Y.; Zhu, H.; Xu, T.; Dong, K.; Xiao, X. Oct4 and Sox2 are overexpressed in human neuroblastoma and inhibited by chemotherapy. *Oncol. Rep.* 2012, *28*, 186–192, doi:10.3892/OR.2012.1765.
157. Long, W.; Zhao, W.; Ning, B.; Huang, J.; Chu, J.; Li, L.; Ma, Q.; Xing, C.; Wang, H.Y.;

- Liu, Q.; et al. PHF20 collaborates with PARP1 to promote stemness and aggressiveness of neuroblastoma cells through activation of SOX2 and OCT4. *J. Mol. Cell Biol.* 2018, *10*, 147–160, doi:10.1093/JMCB/MJY007.
158. Monajemzadeh, M.; Soleimani, V.; Vasei, M.; Koochakzadeh, L.; Karbakhsh, M. Expression and prognostic significance of Oct4 and Nanog in neuroblastoma. *APMIS* 2014, *122*, 734–741, doi:10.1111/apm.12207.
159. van Groningen, T.; Akogul, N.; Westerhout, E.M.; Chan, A.; Hasselt, N.E.; Zwijnenburg, D.A.; Broekmans, M.; Stroeken, P.; Haneveld, F.; Hooijer, G.K.J.; et al. A NOTCH feed-forward loop drives reprogramming from adrenergic to mesenchymal state in neuroblastoma. *Nat. Commun.* 2019 *101* 2019, *10*, 1–11, doi:10.1038/s41467-019-09470-w.
160. Van Groningen, T.; Koster, J.; Valentijn, L.J.; Zwijnenburg, D.A.; Akogul, N.; Hasselt, N.E.; Broekmans, M.; Haneveld, F.; Nowakowska, N.E.; Bras, J.; et al. Neuroblastoma is composed of two super-enhancer-associated differentiation states. *Nat. Genet.* 2017, *49*, 1261–1266, doi:10.1038/NG.3899.
161. Ponzoni, M.; Bachetti, T.; Corrias, M.V.; Brignole, C.; Pastorino, F.; Calarco, E.; Bensa, V.; Giusto, E.; Ceccherini, I.; Perri, P. Recent advances in the developmental origin of neuroblastoma: an overview. *J. Exp. Clin. Cancer Res.* 2022, *41*, 1–28, doi:10.1186/S13046-022-02281-W.
162. KO, M.; S, K.; GM, F.; AJ, W.; C, B.; P, K.; CN, T.; R, V.; A, V.; MD, H.; et al. TH-MYCN tumors, but not tumor-derived cell lines, are adrenergic lineage, GD2+, and responsive to anti-GD2 antibody therapy. *Oncoimmunology* 2022, *11*, doi:10.1080/2162402X.2022.2075204.
163. López-Carrasco, A.; Martín-Vañó, S.; Burgos-Panadero, R.; Monferrer, E.; Berbegall, A.P.; Fernández-Blanco, B.; Navarro, S.; Noguera, R. Impact of extracellular matrix stiffness on genomic heterogeneity in MYCN-amplified neuroblastoma cell line. *J. Exp. Clin. Cancer Res.* 2020, *39*, doi:10.1186/s13046-020-01729-1.
164. Bouchet, B.P.; Gough, R.E.; Ammon, Y.C.; van de Willige, D.; Post, H.; Jacquemet,

- G.; Maarten Altelaar, A.F.; Heck, A.J.R.; Goult, B.T.; Akhmanova, A. Talin-KANK1 interaction controls the recruitment of cortical microtubule stabilizing complexes to focal adhesions. *Elife* 2016, 5, doi:10.7554/ELIFE.18124.
165. Miyamoto, Y.; Torii, T.; Kawahara, K.; Tanoue, A.; Yamauchi, J. Dock8 interacts with Nck1 in mediating Schwann cell precursor migration. *Biochem. Biophys. Reports* 2016, 6, 113–123, doi:10.1016/J.BBREP.2016.03.013.
166. Thiele, C.J. Neuroblastoma Cell Lines. In (Ed.) *Masters, J. Human Cell Culture*; Kluwer Academic Publishers: Lancaster, UK, 1998; Vol. 1, pp. 21–53 ISBN 3014020575.
167. Walton, J.D.; Kattan, D.R.; Thomas, S.K.; Spengler, B.A.; Guo, H.F.; Biedler, J.L.; Cheung, N.K. V.; Ross, R.A. Characteristics of Stem Cells from Human Neuroblastoma Cell Lines and in Tumors. *Neoplasia* 2004, 6, 838, doi:10.1593/NEO.04310.
168. Ornell, K.J.; Coburn, J.M. Developing preclinical models of neuroblastoma: driving therapeutic testing. *BMC Biomed. Eng.* 2019 11 2019, 1, 1–18, doi:10.1186/S42490-019-0034-8.
169. Weiss, W.A.; Aldape, K.; Mohapatra, G.; Feuerstein, B.G.; Bishop, J.M. Targeted expression of MYCN causes neuroblastoma in transgenic mice. *EMBO J.* 1997, 16, 2985–2995, doi:10.1093/EMBOJ/16.11.2985.
170. Berry, T.; Luther, W.; Bhatnagar, N.; Jamin, Y.; Poon, E.; Sanda, T.; Pei, D.; Sharma, B.; Vetharoy, W.R.; Hallsworth, A.; et al. The ALK(F1174L) mutation potentiates the oncogenic activity of MYCN in neuroblastoma. *Cancer Cell* 2012, 22, 117–130, doi:10.1016/J.CCR.2012.06.001.
171. Panadero, B.; Rebeca Búsqueda de dianas terapéuticas en los puntos de contacto de la célula tumoral con su matriz extracelular en tumores neuroblásticos, Universitat de Valencia: Valencia, 2020.
172. Corallo, D.; Frabetti, S.; Candini, O.; Gregianin, E.; Dominici, M.; Fischer, H.; Aveic, S. Emerging Neuroblastoma 3D In Vitro Models for Pre-Clinical Assessments., doi:10.3389/fimmu.2020.584214.

173. Nolan, J.C.; Frawley, T.; Tighe, J.; Soh, H.; Curtin, C.; Piskareva, O. Preclinical models for neuroblastoma: Advances and challenges. *Cancer Lett.* 2020, *474*, 53–62, doi:10.1016/j.canlet.2020.01.015.
174. Craig, B.T.; Rellinger, E.J.; Alvarez, A.L.; Dusek, H.L.; Qiao, J.; Chung, D.H. Induced differentiation inhibits sphere formation in neuroblastoma. *Biochem. Biophys. Res. Commun.* 2016, *477*, 255–259, doi:10.1016/J.BBRC.2016.06.053.
175. Baek, N.H.; Seo, O.W.; Kim, M.S.; Hulme, J.; An, S.S.A. Monitoring the effects of doxorubicin on 3D-spheroid tumor cells in real-time. *Onco. Targets. Ther.* 2016, *9*, 7207–7218, doi:10.2147/OTT.S112566.
176. Curtin, C.; Nolan, J.C.; Conlon, R.; Deneweth, L.; Gallagher, C.; Tan, Y.J.; Cavanagh, B.L.; Asraf, A.Z.; Harvey, H.; Miller-Delaney, S.; et al. A physiologically relevant 3D collagen-based scaffold–neuroblastoma cell system exhibits chemosensitivity similar to orthotopic xenograft models. *Acta Biomater.* 2018, *70*, 84–97, doi:10.1016/j.actbio.2018.02.004.
177. Roehm, K.D.; Madihally, S. V Bioprinted chitosan-gelatin thermosensitive hydrogels using an inexpensive 3D printer. *Biofabrication* 2017, *10*, 015002, doi:10.1088/1758-5090/aa96dd.
178. Marrella, A.; Dondero, A.; Aiello, M.; Casu, B.; Olive, D.; Regis, S.; Bottino, C.; Pende, D.; Meazza, R.; Caluori, G.; et al. Cell-laden hydrogel as a clinical-relevant 3D model for analyzing neuroblastoma growth, immunophenotype, and susceptibility to therapies. *Front. Immunol.* 2019, *10*, doi:10.3389/fimmu.2019.01876.
179. Campos, D.F.D.; Marquez, A.B.; O’seanain, C.; Fischer, H.; Blaeser, A.; Vogt, M.; Corallo, D.; Aveic, S. Exploring cancer cell behavior in vitro in three-dimensional multicellular bioprintable collagen-based hydrogels. *Cancers (Basel)*. 2019, *11*, doi:10.3390/cancers11020180.
180. C, G.; C, M.; FJ, O.; O, P. Three-dimensional In Vitro Biomimetic Model of Neuroblastoma using Collagen-based Scaffolds. *J. Vis. Exp.* 2021, doi:10.3791/62627.

181. Moysidou, C.M.; Barberio, C.; Owens, R.M. Advances in Engineering Human Tissue Models. *Front. Bioeng. Biotechnol.* 2021, 8, 1566, doi:10.3389/FBIOE.2020.620962.
182. Shimada, H.; Ambros, I.M.; Dehner, L.P.; Hata, J.; Joshi, V. V; Roald, B.; Stram, D.O.; Gerbing, R.B.; Lukens, J.N.; Matthay, K.K.; et al. The International Neuroblastoma Pathology Classification (the Shimada system). *Cancer* 1999, 86, 364–72, doi:10.1002/(SICI)1097-0142(19990715)86:2<364::AID-CNCR21>3.0.CO;2-7.
183. Doss, B.L.; Pan, M.; Gupta, M.; Greci, G.; Mège, R.M.; Lim, C.T.; Sheetz, M.P.; Voituriez, R.; Ladoux, B. Cell response to substrate rigidity is regulated by active and passive cytoskeletal stress. *Proc. Natl. Acad. Sci. U. S. A.* 2020, 117, 12817–12825, doi:10.1073/PNAS.1917555117.
184. Yang, Y.; Wang, K.; Gu, X.; Leong, K.W. Biophysical Regulation of Cell Behavior—Cross Talk between Substrate Stiffness and Nanotopography. *Engineering* 2017, 3, 36–54, doi:10.1016/J.ENG.2017.01.014.
185. Murphy, C.M.; O’Brien, F.J. Understanding the effect of mean pore size on cell activity in collagen-glycosaminoglycan scaffolds. *Cell Adh. Migr.* 2010, 4, 377, doi:10.4161/CAM.4.3.11747.
186. Murphy, C.M.; Haugh, M.G.; O’Brien, F.J. The effect of mean pore size on cell attachment, proliferation and migration in collagen–glycosaminoglycan scaffolds for bone tissue engineering. *Biomaterials* 2010, 31, 461–466, doi:10.1016/J.BIOMATERIALS.2009.09.063.
187. Chen, X.; Fan, H.; Deng, X.; Wu, L.; Yi, T.; Gu, L.; Zhou, C.; Fan, Y.; Zhang, X. Scaffold Structural Microenvironmental Cues to Guide Tissue Regeneration in Bone Tissue Applications. *Nanomater.* 2018, Vol. 8, Page 960 2018, 8, 960, doi:10.3390/NANO8110960.
188. Ruan, J.L.; Tulloch, N.L.; Muskheli, V.; Genova, E.E.; Mariner, P.D.; Anseth, K.S.; Murry, C.E. An Improved Cryosection Method for Polyethylene Glycol Hydrogels Used in Tissue Engineering. *Tissue Eng. Part C. Methods* 2013, 19, 794,

- doi:10.1089/TEN.TEC.2012.0460.
189. Almouemen, N.; Kelly, H.M.; O’Leary, C. Tissue Engineering: Understanding the Role of Biomaterials and Biophysical Forces on Cell Functionality Through Computational and Structural Biotechnology Analytical Methods. *Comput. Struct. Biotechnol. J.* 2019, *17*, 591, doi:10.1016/J.CSBJ.2019.04.008.
 190. Bao, M.; Chen, Y.; Liu, J.-T.; Bao, H.; Wang, W.-B.; Qi, Y.-X.; Lv, F. Extracellular matrix stiffness controls VEGF165 secretion and neuroblastoma angiogenesis via the YAP/RUNX2/SRSF1 axis. *Angiogenes.* 2021, *2021*, *1*, 1–16, doi:10.1007/S10456-021-09804-7.
 191. Chaudhuri, O.; Cooper-White, J.; Janmey, P.A.; Mooney, D.J.; Shenoy, V.B. Effects of extracellular matrix viscoelasticity on cellular behaviour. *Nat.* 2020, *584*, 535–546, doi:10.1038/s41586-020-2612-2.
 192. Elosegui-Artola, A. The extracellular matrix viscoelasticity as a regulator of cell and tissue dynamics. *Curr. Opin. Cell Biol.* 2021, *72*, 10–18, doi:10.1016/J.CEB.2021.04.002.
 193. Chaudhuri, O.; Gu, L.; Klumpers, D.; Darnell, M.; Bencherif, S.A.; Weaver, J.C.; Huebsch, N.; Lee, H.P.; Lippens, E.; Duda, G.N.; et al. Hydrogels with tunable stress relaxation regulate stem cell fate and activity. *Nat. Mater.* 2016, *15*, 326–334, doi:10.1038/NMAT4489.
 194. Miri, A.K.; Heris, H.K.; Mongeau, L.; Javid, F. Nanoscale viscoelasticity of extracellular matrix proteins in soft tissues: A multiscale approach. *J. Mech. Behav. Biomed. Mater.* 2014, *30*, 196–204, doi:10.1016/J.JMBBM.2013.10.022.
 195. De Hilster, R.H.J.; Sharma, P.K.; Jonker, M.R.; White, E.S.; Gercama, E.A.; Roobeek, M.; Timens, W.; Harmsen, M.C.; Hylkema, M.N.; Burgess, J.K. Human lung extracellular matrix hydrogels resemble the stiffness and viscoelasticity of native lung tissue. *Am. J. Physiol. Lung Cell. Mol. Physiol.* 2020, *318*, L698–L704, doi:10.1152/AJPLUNG.00451.2019.
 196. Mierke, C.T. Viscoelasticity Acts as a Marker for Tumor Extracellular Matrix Characteristics. *Front. cell Dev. Biol.* 2021, *9*, doi:10.3389/FCELL.2021.785138.

197. Yan, H.; Ramirez-Guerrero, D.; Lowengrub, J.; Wu, M. Stress generation, relaxation and size control in confined tumor growth. *PLoS Comput. Biol.* 2021, *17*, doi:10.1371/JOURNAL.PCBI.1009701.
198. Hajjarian, Z.; Brachtel, E.F.; Tshikudi, D.M.; Nadkarni, S.K. Mapping Mechanical Properties of the Tumor Microenvironment by Laser Speckle Rheological Microscopy. *Cancer Res.* 2021, *81*, 4874–4885, doi:10.1158/0008-5472.CAN-20-3898.
199. Nichol, J.W.; Koshy, S.T.; Bae, H.; Hwang, C.M.; Yamanlar, S.; Khademhosseini, A. Cell-laden microengineered gelatin methacrylate hydrogels. *Biomaterials* 2010, *31*, 5536–5544, doi:10.1016/J.BIOMATERIALS.2010.03.064.
200. Phelps, E.A.; Templeman, K.L.; Thulé, P.M.; García, A.J. Engineered VEGF-releasing PEG-MAL hydrogel for pancreatic islet vascularization. *Drug Deliv. Transl. Res.* 2015, *5*, 125, doi:10.1007/S13346-013-0142-2.
201. Phelps, E.A.; Landázuri, N.; Thulé, P.M.; Taylor, W.R.; García, A.J. Bioartificial matrices for therapeutic vascularization. *Proc. Natl. Acad. Sci. U. S. A.* 2010, *107*, 3323–3328, doi:10.1073/PNAS.0905447107.
202. Gelse, K.; Pöschl, E.; Aigner, T. Collagens - Structure, function, and biosynthesis. *Adv. Drug Deliv. Rev.* 2003, *55*, 1531–1546, doi:10.1016/j.addr.2003.08.002.
203. Schwartz, I.; Seger, D.; Shaltiel, S. Vitronectin. *Int. J. Biochem. Cell Biol.* 1999, *31*, 539–544, doi:10.1016/S1357-2725(99)00005-9.
204. Ambros, I.M.; Ambros, P.F. Schwann cells in neuroblastoma. *Eur. J. Cancer* 1995, *31A*, 429–434, doi:10.1016/0959-8049(95)00051-J.
205. Cruz-Acuña, R.; Quirós, M.; Huang, S.; Siuda, D.; Spence, J.R.; Nusrat, A.; García, A.J. PEG-4MAL hydrogels for human organoid generation, culture, and in vivo delivery. *Nat. Protoc.* 2018 *139* 2018, *13*, 2102–2119, doi:10.1038/s41596-018-0036-3.
206. Wilson, R.L.; Swaminathan, G.; Ettayebi, K.; Bomidi, C.; Zeng, X.L.; Blutt, S.E.; Estes, M.K.; Grande-Allen, K.J. Protein-Functionalized Poly(ethylene glycol) Hydrogels as

- Scaffolds for Monolayer Organoid Culture. *Tissue Eng. Part C. Methods* 2021, 27, 12, doi:10.1089/TEN.TEC.2020.0306.
207. García-Lizarribar, A.; Fernández-Garibay, X.; Velasco-Mallorquí, F.; Castaño, A.G.; Samitier, J.; Ramon-Azcon, J.; García-Lizarribar, A.; Fernández Garibay, X.; Velasco Mallorquí, F.; Castaño, A.G.; et al. Composite Biomaterials as Long-Lasting Scaffolds for 3D Bioprinting of Highly Aligned Muscle Tissue. *Macromol. Biosci.* 2018, 18, 1800167, doi:10.1002/MABI.201800167.
208. Trujillo, S.; Gonzalez-Garcia, C.; Rico, P.; Reid, A.; Windmill, J.; Dalby, M.J.; Salmeron-Sanchez, M. Engineered 3D hydrogels with full-length fibronectin that sequester and present growth factors. *Biomaterials* 2020, 252, 120104, doi:10.1016/J.BIOMATERIALS.2020.120104.
209. Schramm, A.; Köster, J.; Assenov, Y.; Althoff, K.; Peifer, M.; Mahlow, E.; Odersky, A.; Beisser, D.; Ernst, C.; Henssen, A.G.; et al. Mutational dynamics between primary and relapse neuroblastomas. *Nat. Genet.* 2015, 47, 872–877, doi:10.1038/NG.3349.
210. Yu, M.; Le, S.; Ammon, Y.C.; Goult, B.T.; Akhmanova, A.; Yan, J. Force-Dependent Regulation of Talin-KANK1 Complex at Focal Adhesions. *Nano Lett.* 2019, 19, 5982–5990, doi:10.1021/ACS.NANOLETT.9B01732.
211. Kakinuma, N.; Roy, B.C.; Zhu, Y.; Wang, Y.; Kiyama, R. Kank regulates RhoA-dependent formation of actin stress fibers and cell migration via 14-3-3 in PI3K-Akt signaling. *J. Cell Biol.* 2008, 181, 537–549, doi:10.1083/JCB.200707022.
212. Roy, B.C.; Kakinuma, N.; Kiyama, R. Kank attenuates actin remodeling by preventing interaction between IRSp53 and Rac1. *J. Cell Biol.* 2009, 184, 253–267, doi:10.1083/JCB.200805147.
213. Wang, Y.; Kakinuma, N.; Zhu, Y.; Kiyama, R. Nucleo-cytoplasmic shuttling of human Kank protein accompanies intracellular translocation of beta-catenin. *J. Cell Sci.* 2006, 119, 4002–4010, doi:10.1242/JCS.03169.
214. Gu, Y.; Zhang, M. Upregulation of the Kank1 gene inhibits human lung cancer progression in vitro and in vivo. *Oncol. Rep.* 2018, 40, 1243–1250,

- doi:10.3892/OR.2018.6526.
215. Cui, Z.; Shen, Y.; Chen, K.H.; Mittal, S.K.; Yang, J.Y.; Zhang, G.J. KANK1 inhibits cell growth by inducing apoptosis through regulating CXXC5 in human malignant peripheral nerve sheath tumors. *Sci. Reports* 2017 71 2017, 7, 1–13, doi:10.1038/srep40325.
 216. Li, C.C.; Kuo, J.C.; Waterman, C.M.; Kiyama, R.; Moss, J.; Vaughan, M. Effects of brefeldin A-inhibited guanine nucleotide-exchange (BIG) 1 and KANK1 proteins on cell polarity and directed migration during wound healing. *Proc. Natl. Acad. Sci. U. S. A.* 2011, 108, 19228–19233, doi:10.1073/PNAS.1117011108.
 217. Pu, J.; Shen, J.; Zhong, Z.; Yanling, M.; Gao, J. KANK1 regulates paclitaxel resistance in lung adenocarcinoma A549 cells. *Artif. cells, nanomedicine, Biotechnol.* 2020, 48, 639–647, doi:10.1080/21691401.2020.1728287.
 218. Harada, Y.; Tanaka, Y.; Terasawa, M.; Pieczyk, M.; Habiro, K.; Katakai, T.; Kyoko, H.S.; Mutsuko, K.N.; Nishizaki, T.; Shirouzu, M.; et al. DOCK8 is a Cdc42 activator critical for interstitial dendritic cell migration during immune responses. *Blood* 2012, 119, 4451–4461, doi:10.1182/BLOOD-2012-01-407098.
 219. Xu, X.; Han, L.; Zhao, G.; Xue, S.; Gao, Y.; Xiao, J.; Zhang, S.; Chen, P.; Wu, Z.Y.; Ding, J.; et al. LRCH1 interferes with DOCK8-Cdc42-induced T cell migration and ameliorates experimental autoimmune encephalomyelitis. *J. Exp. Med.* 2017, 214, 209–226, doi:10.1084/JEM.20160068.
 220. Shiraishi, A.; Uruno, T.; Sanematsu, F.; Ushijima, M.; Sakata, D.; Hara, T.; Fukui, Y. DOCK8 Protein Regulates Macrophage Migration through Cdc42 Protein Activation and LRAP35a Protein Interaction. *J. Biol. Chem.* 2017, 292, 2191–2202, doi:10.1074/JBC.M116.736306.
 221. Zhang, Q.; Jing, H.; Su, H.C. Recent Advances in DOCK8 Immunodeficiency Syndrome. *J. Clin. Immunol.* 2016, 36, 441–449, doi:10.1007/S10875-016-0296-Z.
 222. Wolf, K.; Friedl, P. Mapping proteolytic cancer cell-extracellular matrix interfaces. *Clin. Exp. Metastasis* 2009, 26, 289–298, doi:10.1007/S10585-008-9190-2.

223. Dinca, S.C.; Greiner, D.; Weidenfeld, K.; Bond, L.; Barkan, D.; Jorczyk, C.L. Novel mechanism for OSM-promoted extracellular matrix remodeling in breast cancer: LOXL2 upregulation and subsequent ECM alignment. *Breast Cancer Res.* 2021, *23*, doi:10.1186/S13058-021-01430-X.
224. Koikawa, K.; Ohuchida, K.; Takesue, S.; Ando, Y.; Kibe, S.; Nakayama, H.; Endo, S.; Abe, T.; Okumura, T.; Horioka, K.; et al. Pancreatic stellate cells reorganize matrix components and lead pancreatic cancer invasion via the function of Endo180. *Cancer Lett.* 2018, *412*, 143–154, doi:10.1016/J.CANLET.2017.10.010.
225. Toromanov, G.; Gugutkov, D.; Gustavsson, J.; Planell, J.; Salmerón-Sánchez, M.; Altankov, G. Dynamic Behavior of Vitronectin at the Cell-Material Interface. *ACS Biomater. Sci. Eng.* 2015, *1*, 927–934, doi:10.1021/ACSBIMATERIALS.5B00147.
226. Buzza, M.S.; Zamurs, L.; Sun, J.; Bird, C.H.; Smith, A.I.; Trapani, J.A.; Froelich, C.J.; Nice, E.C.; Bird, P.I. Extracellular matrix remodeling by human granzyme B via cleavage of vitronectin, fibronectin, and laminin. *J. Biol. Chem.* 2005, *280*, 23549–23558, doi:10.1074/JBC.M412001200.
227. Burgos-Panadero, R.; El Moukhtari, S.H.; Noguera, I.; Rodríguez-Nogales, C.; Martín-Vañó, S.; Vicente-Munuera, P.; Cañete, A.; Navarro, S.; Blanco-Prieto, M.J.; Noguera, R. Unraveling the extracellular matrix-tumor cell interactions to aid better targeted therapies for neuroblastoma. *Int. J. Pharm.* 2021, *608*, doi:10.1016/J.IJPHARM.2021.121058.
228. Monferrer, E.; Martí-Vañó, S.; Carretero, A.; García-Lizarribar, A.; Burgos-Panadero, R.; Navarro, S.; Samitier, J.; Noguera, R. A 3D in vitro neuroblastoma model reveal stiffness-dependent vitronectin expression. *Histol. Histopathol.* 2019, *34*, 60, doi:10.14670/HH-sehit19.
229. Liu, S.; Tian, Y.; Chlenski, A.; Yang, Q.; Salwen, H.R.; Cohn, S.L. ‘Cross-talk’ between Schwannian stroma and neuroblasts promotes neuroblastoma tumor differentiation and inhibits angiogenesis. *Cancer Lett.* 2005, *228*, 125–131, doi:10.1016/J.CANLET.2005.01.056.
230. Dobre, O.; Oliva, M.A.G.; Ciccone, G.; Trujillo, S.; Rodrigo-Navarro, A.; Venters,

- D.C.; Llopis-Hernandez, V.; Vassalli, M.; Gonzalez-Garcia, C.; Dalby, M.J.; et al. A Hydrogel Platform that Incorporates Laminin Isoforms for Efficient Presentation of Growth Factors – Neural Growth and Osteogenesis. *Adv. Funct. Mater.* 2021, *31*, 2010225, doi:10.1002/ADFM.202010225.
231. Ahmad, K.; Lee, E.J.; Shaikh, S.; Kumar, A.; Rao, K.M.; Park, S.Y.; Jin, J.O.; Han, S.S.; Choi, I. Targeting integrins for cancer management using nanotherapeutic approaches: Recent advances and challenges. *Semin. Cancer Biol.* 2021, *69*, 325–336, doi:10.1016/J.SEMCANCER.2019.08.030.
232. Eliceiri, B.P.; Cheresh, D.A. The role of alphav integrins during angiogenesis: insights into potential mechanisms of action and clinical development. *J. Clin. Invest.* 1999, *103*, 1227–1230, doi:10.1172/JCI6869.
233. Raab-Westphal, S.; Marshall, J.F.; Goodman, S.L. Integrins as Therapeutic Targets: Successes and Cancers. *Cancers (Basel)*. 2017, *9*, doi:10.3390/CANCERS9090110.
234. Gutheil, J.C.; Campbell, T.N.; Pierce, P.R.; Watkins, J.D.; Huse, W.D.; Bodkin, D.J.; Cheresh, D.A. Targeted antiangiogenic therapy for cancer using Vitaxin: a humanized monoclonal antibody to the integrin alphavbeta3. *Clin. Cancer Res.* 2000, *6*, 3056–3061.
235. Zhao, Y.Z.; Lin, Q.; Wong, H.L.; Shen, X.T.; Yang, W.; Xu, H.L.; Mao, K.L.; Tian, F.R.; Yang, J.J.; Xu, J.; et al. Glioma-targeted therapy using Cilengitide nanoparticles combined with UTMD enhanced delivery. *J. Control. Release* 2016, *224*, 112–125, doi:10.1016/J.JCONREL.2016.01.015.
236. Kang, W.; Svirskis, D.; Sarojini, V.; McGregor, A.L.; Bevitt, J.; Wu, Z. Cyclic-RGDyC functionalized liposomes for dual-targeting of tumor vasculature and cancer cells in glioblastoma: An in vitro boron neutron capture therapy study. *Oncotarget* 2017, *8*, 36614, doi:10.18632/ONCOTARGET.16625.
237. Sánchez Sánchez, M. Preliminary study of combined mechano-cytotoxic therapy in an in vivo model of high-risk neuroblastoma, Universitat Politècnica de València: Valencia, 2021.
238. Stoks, M. Patología digital aplicada a tumores heterotópicos murinos, Universitat

- Politécnica de València: Valencia, 2022.
239. Hanahan, D.; Weinberg, R.A. The hallmarks of cancer. *Cell* 2000, *100*, 57–70, doi:10.1016/S0092-8674(00)81683-9.
240. Enrico Bena, C.; Del Giudice, M.; Grob, A.; Gueudré, T.; Miotto, M.; Gialama, D.; Osella, M.; Turco, E.; Ceroni, F.; De Martino, A.; et al. Initial cell density encodes proliferative potential in cancer cell populations. *Sci. Reports* 2021 *11* 2021, *11*, 1–11, doi:10.1038/s41598-021-85406-z.
241. Gregório, A.C.; Fonseca, N.A.; Moura, V.; Lacerda, M.; Figueiredo, P.; Simões, S.; Dias, S.; Moreira, J.N. Inoculated Cell Density as a Determinant Factor of the Growth Dynamics and Metastatic Efficiency of a Breast Cancer Murine Model. *PLoS One* 2016, *11*, e0165817, doi:10.1371/JOURNAL.PONE.0165817.
242. Pernicová, Z.; Slabáková, E.; Fedr, R.; Šimečková, Š.; Jaroš, J.; Suchánková, T.; Bouchal, J.; Kharashvili, G.; Král, M.; Kozubík, A.; et al. The role of high cell density in the promotion of neuroendocrine transdifferentiation of prostate cancer cells. *Mol. Cancer* 2014, *13*, 1–16, doi:10.1186/1476-4598-13-113.
243. Jayatilaka, H.; Umanson, F.G.; Shah, V.; Meirson, T.; Russo, G.; Starich, B.; Tyle, P.; Lee, J.S.H.; Khatau, S.; Gil-Henn, H.; et al. Tumor cell density regulates matrix metalloproteinases for enhanced migration. *Oncotarget* 2018, *9*, 32556, doi:10.18632/ONCOTARGET.25863.
244. Sharif, G.M.; Wellstein, A. Cell density regulates cancer metastasis via the Hippo pathway. *Futur. Oncol.* 2015, *11*, 3253, doi:10.2217/FON.15.268.
245. De Anta, J.M.; Real, F.X.; Mayol, X. Low tumor cell density environment yields survival advantage of tumor cells exposed to MTX in vitro. *Biochim. Biophys. Acta - Gen. Subj.* 2005, *1721*, 98–106, doi:10.1016/J.BBAGEN.2004.10.006.
246. Spassieva, S.D.; Rahmaniyan, M.; Bielawski, J.; Clarke, C.J.; Kravka, J.M.; Obeid, L.M. Cell density-dependent reduction of dihydroceramide desaturase activity in neuroblastoma cells. *J. Lipid Res.* 2012, *53*, 918–928, doi:10.1194/JLR.M019075.
247. Gerdes, J.; Schwab, U.; Lemke, H.; Stein, H. Production of a mouse monoclonal

- antibody reactive with a human nuclear antigen associated with cell proliferation. *Int. J. cancer* 1983, *31*, 13–20, doi:10.1002/IJC.2910310104.
248. De Azambuja, E.; Cardoso, F.; De Castro, G.; Colozza, M.; Mano, M.S.; Durbecq, V.; Sotiriou, C.; Larsimont, D.; Piccart-Gebhart, M.J.; Paesmans, M. Ki-67 as prognostic marker in early breast cancer: a meta-analysis of published studies involving 12,155 patients. *Br. J. Cancer* 2007, *96*, 1504–1513, doi:10.1038/SJ.BJC.6603756.
249. Luo, Y.; Zhang, X.; Mo, M.; Tan, Z.; Huang, L.; Zhou, H.; Wang, C.; Wei, F.; Qiu, X.; He, R.; et al. High Ki-67 Immunohistochemical Reactivity Correlates With Poor Prognosis in Bladder Carcinoma: A Comprehensive Meta-Analysis with 13,053 Patients Involved. *Medicine (Baltimore)*. 2016, *95*, doi:10.1097/MD.0000000000003337.
250. Nakamura, N.; Yamamoto, H.; Yao, T.; Oda, Y.; Nishiyama, K.I.; Imamura, M.; Yamada, T.; Nawata, H.; Tsuneyoshi, M. Prognostic significance of expressions of cell-cycle regulatory proteins in gastrointestinal stromal tumor and the relevance of the risk grade. *Hum. Pathol.* 2005, *36*, 828–837, doi:10.1016/J.HUMPATH.2005.03.012.
251. Graham, D.; Magee, H.; Kierce, B.; Ball, R.; Dervan, P.; O'Meara, A. Evaluation of Ki-67 reactivity in neuroblastoma using paraffin embedded tissue. *Pathol. Res. Pract.* 1995, *191*, 87–91, doi:10.1016/S0344-0338(11)80557-1.
252. Fairlie, W.D.; Lee, E.F. Co-Operativity between MYC and BCL-2 Pro-Survival Proteins in Cancer. *Int. J. Mol. Sci.* 2021, *22*, 1–28, doi:10.3390/IJMS22062841.
253. Morana, O.; Wood, W.; Gregory, C.D. The Apoptosis Paradox in Cancer. *Int. J. Mol. Sci.* 2022, *Vol. 23, Page 1328* 2022, *23*, 1328, doi:10.3390/IJMS23031328.
254. Liu, Z.G.; Jiao, D. Necroptosis, tumor necrosis and tumorigenesis. *Cell Stress* 2020, *4*, 1, doi:10.15698/CST2020.01.208.
255. Bredholt, G.; Mannelqvist, M.; Stefansson, I.M.; Birkeland, E.; Bø, T.H.; Øyan, A.M.; Trovik, J.; Kalland, K.H.; Jonassen, I.; Salvesen, H.B.; et al. Tumor necrosis is an important hallmark of aggressive endometrial cancer and associates with

- hypoxia, angiogenesis and inflammation responses. *Oncotarget* 2015, 6, 39676, doi:10.18632/ONCOTARGET.5344.
256. Ling, Y.H.; Chen, J.W.; Wen, S.H.; Huang, C.Y.; Li, P.; Lu, L.H.; Mei, J.; Li, S.H.; Wei, W.; Cai, M.Y.; et al. Tumor necrosis as a poor prognostic predictor on postoperative survival of patients with solitary small hepatocellular carcinoma. *BMC Cancer* 2020, 20, 1–9, doi:10.1186/S12885-020-07097-5.
257. Gestblom, C.; Hoehner, J.C.; Pålman, S. Proliferation and apoptosis in neuroblastoma: subdividing the mitosis-karyorrhexis index. *Eur. J. Cancer* 1995, 31, 458–463, doi:10.1016/0959-8049(95)00006-5.
258. Bhardwaj, N.; Rohilla, M.; Trehan, A.; Bansal, D.; Kakkar, N.; Srinivasan, R. Mitosis-Karyorrhexis Index evaluation by digital image visual analysis for application of International Neuroblastoma Pathology Classification in FNA biopsy. *Cancer Cytopathol.* 2022, 130, 128–135, doi:10.1002/CNCY.22520.
259. Feng, L.; Qian, L.; Yang, S.; Ren, Q.; Zhang, S.; Qin, H.; Wang, W.; Wang, C.; Zhang, H.; Yang, J. Prediction for Mitosis-Karyorrhexis Index Status of Pediatric Neuroblastoma via Machine Learning Based 18F-FDG PET/CT Radiomics. *Diagnostics (Basel, Switzerland)* 2022, 12, doi:10.3390/DIAGNOSTICS12020262.
260. Schuyer, M.; Van der Burg, M.E.L.; Henzen-Logmans, S.C.; Fieret, J.H.; Klijn, J.G.M.; Look, M.P.; Foekens, J.A.; Stoter, G.; Berns, E.M.J.J. Reduced expression of BAX is associated with poor prognosis in patients with epithelial ovarian cancer: a multifactorial analysis of TP53, p21, BAX and BCL-2. *Br. J. Cancer* 2001 859 2001, 85, 1359–1367, doi:10.1054/bjoc.2001.2101.
261. Kulsoom, B.; Shamsi, T.S.; Afsar, N.A.; Memon, Z.; Ahmed, N.; Hasnain, S.N. Bax, Bcl-2, and Bax/Bcl-2 as prognostic markers in acute myeloid leukemia: are we ready for Bcl-2-directed therapy? *Cancer Manag. Res.* 2018, 10, 403–416, doi:10.2147/CMAR.S154608.
262. Katkoori, V.R.; Suarez-Cuervo, C.; Shanmugam, C.; Jhala, N.C.; Callens, T.; Messiaen, L.; III, J.P.; Bumpers, H.L.; Meleth, S.; Grizzle, W.E.; et al. Bax expression is a candidate prognostic and predictive marker of colorectal cancer. *J.*

- Gastrointest. Oncol.* 2010, *1*, 76–89, doi:10.3978/J.ISSN.2078-6891.2010.019.
263. Yang, X.; Zhong, D.N.; Qin, H.; Wu, P.R.; Wei, K.L.; Chen, G.; He, R.Q.; Zhong, J.C. Caspase-3 over-expression is associated with poor overall survival and clinicopathological parameters in breast cancer: a meta-analysis of 3091 cases. *Oncotarget* 2018, *9*, 8629, doi:10.18632/ONCOTARGET.23667.
264. Huang, K.H.; Fang, W.L.; Li, A.F.Y.; Liang, P.H.; Wu, C.W.; Shyr, Y.M.; Yang, M.H. Caspase-3, a key apoptotic protein, as a prognostic marker in gastric cancer after curative surgery. *Int. J. Surg.* 2018, *52*, 258–263, doi:10.1016/J.IJSU.2018.02.055.
265. Huang, Q.; Li, F.; Liu, X.; Li, W.; Shi, W.; Liu, F.F.; O’Sullivan, B.; He, Z.; Peng, Y.; Tan, A.C.; et al. Caspase 3-mediated stimulation of tumor cell repopulation during cancer radiotherapy. *Nat. Med.* 2011, *17*, 860, doi:10.1038/NM.2385.
266. Gaglia, G.; Kabraji, S.; Rammos, D.; Dai, Y.; Verma, A.; Wang, S.; Mills, C.E.; Chung, M.; Bergholz, J.S.; Coy, S.; et al. Temporal and spatial topography of cell proliferation in cancer. *Nat. Cell Biol.* 2022 *243* 2022, *24*, 316–326, doi:10.1038/s41556-022-00860-9.
267. Zhou, H.M.; Zhang, J.G.; Zhang, X.; Li, Q. Targeting cancer stem cells for reversing therapy resistance: mechanism, signaling, and prospective agents. *Signal Transduct. Target. Ther.* 2021 *61* 2021, *6*, 1–17, doi:10.1038/s41392-020-00430-1.
268. Kim, Y.S.; Potashnikova, D.M.; Gisina, A.M.; Kholodenko, I. V.; Kopylov, A.T.; Tikhonova, O. V.; Kurbatov, L.K.; Saidova, A.A.; Tvorogova, A. V.; Kholodenko, R. V.; et al. TRIM28 Is a Novel Regulator of CD133 Expression Associated with Cancer Stem Cell Phenotype. *Int. J. Mol. Sci.* 2022, *23*, doi:10.3390/IJMS23179874.
269. Hu, J.; Guan, W.; Yan, L.; Ye, Z.; Wu, L.; Xu, H.; Angelini, F. Cancer Stem Cell Marker Endoglin (CD105) Induces Epithelial Mesenchymal Transition (EMT) but Not Metastasis in Clear Cell Renal Cell Carcinoma. 2019, doi:10.1155/2019/9060152.
270. Yang, S.; Zheng, J.; Ma, Y.; Zhu, H.; Xu, T.; Dong, K.; Xiao, X. Oct4 and Sox2 are overexpressed in human neuroblastoma and inhibited by chemotherapy. *Oncol. Rep.* 2012, doi:10.3892/or.2012.1765.

271. Ćavar, S.; Jelašić, D.; Seiwert, S.; Milošević, M.; Hutinec, Z.; Mišić, M. Endoglin (CD 105) as a potential prognostic factor in neuroblastoma. *Pediatr. Blood Cancer* 2015, *62*, 770–775, doi:10.1002/PBC.25427.
272. Tong, Q.-S.; Zheng, L.-D.; Tang, S.-T.; Ruan, Q.-L.; Liu, Y.; Li, S.-W.; Jiang, G.-S.; Cai, J.-B. Expression and clinical significance of stem cell marker CD133 in human neuroblastoma. *World J. Pediatr.* 2008, *4*, 58–62, doi:10.1007/S12519-008-0012-Z.
273. Takenobu, H.; Shimosato, O.; Nakamura, T.; Ochiai, H.; Yamaguchi, Y.; Ohira, M.; Nakagawara, A.; Kamijo, T. CD133 suppresses neuroblastoma cell differentiation via signal pathway modification. *Oncogene* 2011 *30* 2010, *30*, 97–105, doi:10.1038/onc.2010.383.
274. Li, T.; Hao, L.; Li, J.; Du, C.; Wang, Y. Insight into vitronectin structural evolution on material surface chemistries: The mediation for cell adhesion. *Bioact. Mater.* 2020, *5*, 1044–1052, doi:10.1016/J.BIOACTMAT.2020.06.021.
275. Kaneko, Y.; Suenaga, Y.; Islam, S.M.R.; Matsumoto, D.; Nakamura, Y.; Ohira, M.; Yokoi, S.; Nakagawara, A. Functional interplay between MYCN, NCYM, and OCT4 promotes aggressiveness of human neuroblastomas. *Cancer Sci* 2015, *106*, 840–847, doi:10.1111/cas.12677.
276. Bellón, T.; Corbi, A.; Lastres, P.; Calés, C.; Cebrián, M.; Vera, S.; Cheifetz, S.; Massague, J.; Letarte, M.; Bernabéu, C. Identification and expression of two forms of the human transforming growth factor- β -binding protein endoglin with distinct cytoplasmic regions. *Eur. J. Immunol.* 1993, *23*, 2340–2345, doi:10.1002/EJL.1830230943.
277. Canzonetta, C.; Pelosi, A.; DI Matteo, S.; Veneziani, I.; Tumino, N.; Vacca, P.; Munari, E.; Pezzullo, M.; Theuer, C.; De Vito, R.; et al. Identification of neuroblastoma cell lines with uncommon TAZ+/mesenchymal stromal cell phenotype with strong suppressive activity on natural killer cells. *J. Immunother. Cancer* 2021, *9*, e001313, doi:10.1136/JITC-2020-001313.
278. Takenobu, H.; Shimosato, O.; Nakamura, T.; Ochiai, H.; Yamaguchi, Y.; Ohira, M.;

- Nakagawara, A.; Kamijo, T. CD133 suppresses neuroblastoma cell differentiation via signal pathway modification. *Oncogene* 2011 301 2010, 30, 97–105, doi:10.1038/onc.2010.383.
279. Zhong, Z.-Y.; Shi, B.-J.; Zhou, H.; Wang, W.-B. CD133 expression and MYCN amplification induce chemoresistance and reduce average survival time in pediatric neuroblastoma. *J. Int. Med. Res.* 2018, 46, 1209–1220, doi:10.1177/0300060517732256.
280. Tsubota, S.; Kadomatsu, K. Origin and mechanism of neuroblastoma. *Oncoscience* 2017, 4, 70, doi:10.18632/ONCOSCIENCE.360.
281. Shipley, M.M.; Mangold, C.A.; Szpara, M.L. Differentiation of the SH-SY5Y Human Neuroblastoma Cell Line. *J. Vis. Exp.* 2016, 2016, 53193, doi:10.3791/53193.
282. Campbell, K.; Shyr, D.; Bagatell, R.; Fischer, M.; Nakagawara, A.; Nieto, A.C.; Brodeur, G.M.; Matthay, K.K.; London, W.B.; DuBois, S.G. Comprehensive evaluation of context dependence of the prognostic impact of MYCN amplification in neuroblastoma: A report from the International Neuroblastoma Risk Group (INRG) project. *Pediatr. Blood Cancer* 2019, 66, e27819, doi:10.1002/PBC.27819.
283. Yang, X.H.; Tang, F.; Shin, J.; Cunningham, J.M. A c-Myc-regulated stem cell-like signature in high-risk neuroblastoma: A systematic discovery (Target neuroblastoma ESC-like signature). *Sci. Reports* 2017 71 2017, 7, 1–15, doi:10.1038/s41598-017-00122-x.
284. Le Grand, M.; Mukha, A.; Püschel, J.; Valli, E.; Kamili, A.; Vittorio, O.; Dubrovskaya, A.; Kavallaris, M. Interplay between MycN and c-Myc regulates radioresistance and cancer stem cell phenotype in neuroblastoma upon glutamine deprivation. *Theranostics* 2020, 10, 6411–6429, doi:10.7150/THNO.42602.
285. Zhu, W.; Zhou, B. lun; Rong, L. juan; Ye, L.; Xu, H. juan; Zhou, Y.; Yan, X. jun; Liu, W. dong; Zhu, B.; Wang, L.; et al. Roles of PTBP1 in alternative splicing, glycolysis, and oncogenesis. *J. Zhejiang Univ. Sci. B* 2020, 21, 122, doi:10.1631/JZUS.B1900422.

286. Cheung, H.C.; Hai, T.; Zhu, W.; Baggerly, K.A.; Tsavachidis, S.; Krahe, R.; Cote, G.J. Splicing factors PTBP1 and PTBP2 promote proliferation and migration of glioma cell lines. *Brain* 2009, *132*, 2277–2288, doi:10.1093/BRAIN/AWP153.
287. Guo, J.; Jia, J.; Jia, R. PTBP1 and PTBP2 impaired autoregulation of SRSF3 in cancer cells. *Sci. Rep.* 2015, *5*, doi:10.1038/SREP14548.
288. Li, Q.; Zheng, S.; Han, A.; Lin, C.H.; Stoilov, P.; Fu, X.D.; Black, D.L. The splicing regulator PTBP2 controls a program of embryonic splicing required for neuronal maturation. *Elife* 2014, *2014*, 1201, doi:10.7554/ELIFE.01201.001.
289. Zhang, M.; Ergin, V.; Lin, L.; Stork, C.; Chen, L.; Zheng, S. Axonogenesis Is Coordinated by Neuron-Specific Alternative Splicing Programming and Splicing Regulator PTBP2. *Neuron* 2019, *101*, 690-706.e10, doi:10.1016/J.NEURON.2019.01.022.
290. Makeyev, E. V.; Zhang, J.; Carrasco, M.A.; Maniatis, T. The MicroRNA miR-124 promotes neuronal differentiation by triggering brain-specific alternative pre-mRNA splicing. *Mol. Cell* 2007, *27*, 435–448, doi:10.1016/J.MOLCEL.2007.07.015.
291. Zheng, S.; Gray, E.E.; Chawla, G.; Porse, B.T.; O’Dell, T.J.; Black, D.L. Pcd-95 is post-transcriptionally repressed during early neural development by PTBP1 and PTBP2. *Nat. Neurosci.* 2012, *15*, 381, doi:10.1038/NN.3026.
292. Campillos Palomares, L. Papel de las proteínas de unión al tracto de polipirimidina en la diferenciación de neuroblastos malignos, Universidad Católica de Valencia: Valencia, 2021.
293. David, C.J.; Chen, M.; Assanah, M.; Canoll, P.; Manley, J.L. HnRNP proteins controlled by c-Myc deregulate pyruvate kinase mRNA splicing in cancer. *Nature* 2010, *463*, 364–368, doi:10.1038/NATURE08697.
294. Zhang, S.; Wei, J.S.; Li, S.Q.; Badgett, T.C.; Song, Y.K.; Agarwal, S.; Coarfa, C.; Tolman, C.; Hurd, L.; Liao, H.; et al. MYCN controls an alternative RNA splicing program in high-risk metastatic neuroblastoma. *Cancer Lett.* 2016, *371*, 214–224, doi:10.1016/J.CANLET.2015.11.045.

295. Yang, W.; Xia, Y.; Hawke, D.; Li, X.; Liang, J.; Xing, D.; Aldape, K.; Hunter, T.; Alfred Yung, W.K.; Lu, Z. PKM2 phosphorylates histone H3 and promotes gene transcription and tumorigenesis. *Cell* 2012, *150*, 685–696, doi:10.1016/J.CELL.2012.07.018.
296. Wiese, E.K.; Hitosugi, T. Tyrosine Kinase Signaling in Cancer Metabolism: PKM2 Paradox in the Warburg Effect. *Front. cell Dev. Biol.* 2018, *6*, doi:10.3389/FCELL.2018.00079.
297. Christofk, H.R.; Vander Heiden, M.G.; Harris, M.H.; Ramanathan, A.; Gerszten, R.E.; Wei, R.; Fleming, M.D.; Schreiber, S.L.; Cantley, L.C. The M2 splice isoform of pyruvate kinase is important for cancer metabolism and tumour growth. *Nature* 2008, *452*, 230–233, doi:10.1038/NATURE06734.
298. Skaripa-Koukelli, I.; Hauton, D.; Walsby-Tickle, J.; Thomas, E.; Owen, J.; Lakshminarayanan, A.; Able, S.; McCullagh, J.; Carlisle, R.C.; Vallis, K.A. 3-Bromopyruvate-mediated MCT1-dependent metabolic perturbation sensitizes triple negative breast cancer cells to ionizing radiation. *Cancer Metab.* 2021 *91* 2021, *9*, 1–17, doi:10.1186/S40170-021-00273-6.
299. Pereira-Vieira, J.; Azevedo-Silva, J.; Preto, A.; Casal, M.; Queirós, O. MCT1, MCT4 and CD147 expression and 3-bromopyruvate toxicity in colorectal cancer cells are modulated by the extracellular conditions. *Biol. Chem.* 2019, *400*, 787–799, doi:10.1515/HSZ-2018-0411.
300. Birsoy, K.; Wang, T.; Possemato, R.; Yilmaz, O.H.; Koch, C.E.; Chen, W.W.; Hutchins, A.W.; Gultekin, Y.; Peterson, T.R.; Carette, J.E.; et al. MCT1-mediated transport of a toxic molecule is an effective strategy for targeting glycolytic tumors. *Nat. Genet.* 2012, *45*, doi:10.1038/ng.2471.
301. Fan, T.; Sun, G.; Sun, X.; Zhao, L.; Zhong, R.; Peng, Y. Tumor Energy Metabolism and Potential of 3-Bromopyruvate as an Inhibitor of Aerobic Glycolysis: Implications in Tumor Treatment. *Cancers (Basel)*. 2019, *11*, doi:10.3390/CANCERS11030317.
302. Abbaszadeh, H.; Valizadeh, A.; Mahdavinia, M.; Teimoori, A.; Pipelzadeh, M.H.;

- Zeidooni, L.; Alboghobeish, S. 3-Bromopyruvate potentiates TRAIL-induced apoptosis in human colon cancer cells through a reactive oxygen species- and caspase-dependent mitochondrial pathway. *Can. J. Physiol. Pharmacol.* 2019, *97*, 1176–1184, doi:10.1139/CJPP-2019-0131.
303. Gan, L.; Ren, Y.; Lu, J.; Ma, J.; Shen, X.; Zhuang, Z. Synergistic Effect of 3-Bromopyruvate in Combination with Rapamycin Impacted Neuroblastoma Metabolism by Inhibiting Autophagy. *Onco. Targets. Ther.* 2020, *13*, 11125–11137, doi:10.2147/OTT.S273108.
304. Matsushita, K.; Uchida, K.; Saigusa, S.; Ide, S.; Hashimoto, K.; Koike, Y.; Otake, K.; Inoue, M.; Tanaka, K.; Kusunoki, M. Glycolysis inhibitors as a potential therapeutic option to treat aggressive neuroblastoma expressing GLUT1. *J. Pediatr. Surg.* 2012, *47*, 1323–1330, doi:10.1016/J.JPESURG.2011.12.007.
305. Bean, J.F.; Qiu, Y.Y.; Yu, S.; Clark, S.; Chu, F.; Madonna, M.B. Glycolysis inhibition and its effect in doxorubicin resistance in neuroblastoma. *J. Pediatr. Surg.* 2014, *49*, 981–984, doi:10.1016/J.JPESURG.2014.01.037.
306. Corallo, D.; Zanon, C.; Pantile, M.; Tonini, G.P.; Zin, A.; Francescato, S.; Rossi, B.; Trevisson, E.; Pinato, C.; Monferrer, E.; et al. Integrated cgh/wes analyses advance understanding of aggressive neuroblastoma evolution: A case study. *Cells* 2021, *10*, doi:10.3390/cells10102695.
307. Leung, C.M.; de Haan, P.; Ronaldson-Bouchard, K.; Kim, G.A.; Ko, J.; Rho, H.S.; Chen, Z.; Habibovic, P.; Jeon, N.L.; Takayama, S.; et al. A guide to the organ-on-a-chip. *Nat. Rev. Methods Prim.* 2022 *21* 2022, *2*, 1–29, doi:10.1038/s43586-022-00118-6.

APPENDIX

This appendix provides the following scientific works shared in scientific meetings, the results of which complement this thesis albeit they have not been exposed in detail.

- I. Evasión Inmunológica Del Neuroblastoma Mediante Expresión De OCT4. **Monferrer E**, Zúñiga V, Tadeo I, Navarro S, Noguera R. *XXXI Congreso Latinoamericano de Patología*. Cartagena de Indias (México), August 2017.
- II. Quantitative comparison and reproducibility of pathologist score and digital image analysis of the expression of S100A6 protein in neuroblastoma. Pérez A, **Monferrer E**, Mateu JM, Navarro S, Noguera R. *II Congreso Nacional de Jóvenes Investigadores en Biomedicina*. Valencia (Spain), November 2017.
- III. A 3D in vitro neuroblastoma model reveals stiffness-dependent vitronectin expression. **Monferrer E**, Martín-Vañó S, Carretero A, García-Lizarribar A, Burgos-Panadero R, Navarro S, Samitier J, Noguera R. *SEHIT2019*. Murcia (Spain), September 2019.
- IV. Vitronectin and its receptors: human neuroblastoma 2D in vitro characterization. Burgos-Panadero R, **Monferrer E**, Noguera I, Navarro S, Noguera R. *SEHIT2019*. Murcia (Spain), September 2019.
- V. Building silk-fibroin 3D hydrogels with enzymatically cross-linked vitronectin to study neuroblastoma aggressiveness. Vieco-Martí I, **Monferrer E**, López-Carrasco A, Granados-Aparici S, Navarro S, Noguera R. *SEHIT2022*. Granada (Spain), September 2022.

Notes:

- Results on PTPB1, PTPB2, PSD-95, PKM2 and MCT1, which are related to neuroblastoma cell neuronal differentiation and glucose metabolism, are being communicated in this thesis for the first time. These results are expected to be shared in ANR 2023 scientific meeting. Manuscript ongoing.
- Appendix work V. constitutes preliminary data from a new neuroblastoma model based on gelatin and silk fibroin, which are being developed in the framework of a different doctoral thesis in our lab.

I. Evasión Inmunológica Del Neuroblastoma Mediante Expresión De OCT4. Monferrer E, Zúñiga V, Tadeo I, Navarro S, Noguera R. XXXI Congreso Latinoamericano de Patología. Cartagena de Indias (México), August 2017.

Nº 162



Evasión Inmunológica Del Neuroblastoma Mediante Expresión De OCT4

Ezequiel Monferrer Garzarán¹, Víctor Zúñiga Zaragoza¹, Irene Tadeo Cervera¹, Samuel Navarro Fos^{1,2}, Rosa Noguera Salvá^{1,2}

¹Departamento de Patología, Facultad de Medicina y Odontología/INCLIVA, Universidad de Valencia, España
²CIBER de Cáncer, Madrid, España



Antecedentes Objetivos

La expresión de Oct4 en las células madre del cáncer (CSCs) se ha relacionado con la patogénesis, el desarrollo y la persistencia de diferentes tumores. Además, la infiltración de subpoblaciones linfocitarias específicas para Oct4 en algunos de ellos, plantea un papel clave de este marcador en el reconocimiento in vivo del cáncer. En los tumores neuroblásticos (TNBs) no hay descritos estudios concluyentes de la expresión de Oct4 ni de su papel en relación al infiltrado celular inmune, razón por la que hemos considerado interesante su estudio.

- Determinar el patrón de expresión de Oct4 en los TNBs en función de su histopatología.
- Describir la conexión existente entre el infiltrado celular inmune y la presencia de células Oct4 positivas en los tumores neuroblásticos.

Material y Métodos

1. Micromatrices de tejido (TMA):

- 618 TNBs incluidos en TMA desde 1996 a 2016.



Tinción inmunohistoquímica

Tipo celular	Marcaadores	Casa comercial	Dilución
Células madre	Oct4	Roche	PD ¹
Linfocitos T	CD4, CD7, CD8	Dako	ND ¹ , ND, 1:50
Linfocitos B	CD20	Dako	1:100
Células supresoras mieloides	CD11b, CD11c	Novus Biologicals	1:100
Macrófagos	CD68, CD163	Dako, Novus Biologicals	1:500, 1:10
Leucocitos	CD45	Dako	1:100

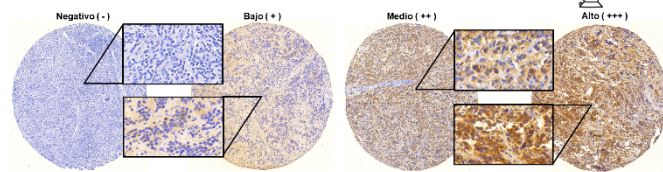
¹ No estudiado por la casa comercial;
² No estudiado

Digitalización

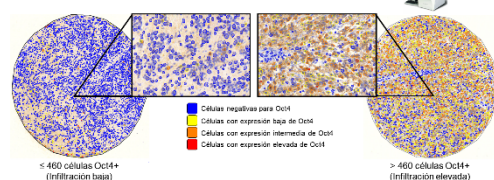


2. Análisis de expresión de Oct4:

- Visual → Evaluación de intensidad del marcador por célula y proporción celular que presenta expresión.

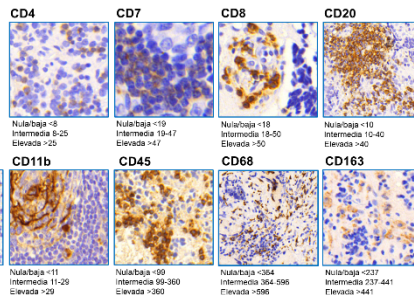


- Automático → Módulo NuclearQuant del software Panoramic Viewer.



3. Análisis de expresión de marcadores inmunes:

- Procedimiento análogo al descrito para Oct4.
- El grado de infiltración celular inmune se divide en 3 rangos:



Resultados

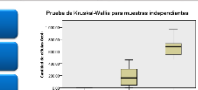
Relación entre el análisis visual y automático para Oct4

Intensidad por evaluación visual	Células Oct4+ (evaluación automática)
Negativo (0)	0
Baja (+)	1460
Medio (++)	461-673
Alto (+++)	671-987

Nota 1: El rango de número de células Oct4+ para los diferentes niveles de intensidad de expresión de Oct4 se muestra en la tabla.

Prueba de Chi-cuadrado para muestras independientes

Intensidad	Grado de infiltración
Nula	0.000
Baja	0.000
Medio	0.000
Alto	0.000

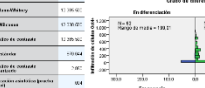


Patrón de expresión de Oct4 en los TNBs

Grupo Histopatológico	Casos totales	Casos Oct4+
NE-ONBnd (sin diferenciación)	61	29/61 (47.5%)
NE-ONBnd (pobremente diferenciado)	214	112/214 (52.3%)
NE-ONBnd (en diferenciación)	42	12/42 (28.57%)
ONB-ONBnd (en diferenciación)	17	0

Nota 2: El número de casos con expresión de Oct4 en cada grupo histopatológico NE-ONBnd, ONB-ONBnd, ONB-ONBnd y ONB-ONBnd se muestra en la tabla.

Prueba U de Mann-Whitney para muestras independientes



Clasificación histopatológica de los TNBs atendiendo a la categoría (diferenciación: los NE y ONBnd de los ON y ONBnd) y a los diferentes grados de diferenciación posibles dentro de cada grupo categorial (indiferenciado, pobremente diferenciado y en diferenciación). Considerando los casos totales existentes para cada uno de los cuatro grupos histopatológicos resultantes, se calculó el porcentaje de TNBs que presentaban expresión de Oct4. Estadísticamente, los resultados muestran una correlación significativa con un p<0.004 entre la mayor presencia de células Oct4+ y los casos de TNBs sin diferenciación.

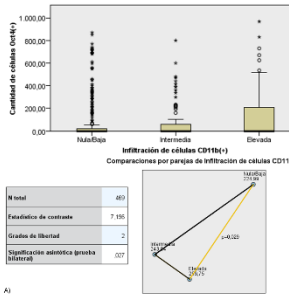
4. Análisis estadístico:

- Software SPSS Statistics (p<0.05).
- Se realizan dos tipos de aproximaciones:

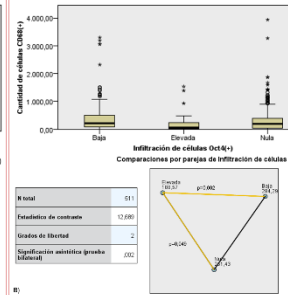


Correlación entre marcadores celulares

Prueba de Kruskal-Wallis para muestras independientes



Prueba de Kruskal-Wallis para muestras independientes



A) Relación de marcadores inmunes en rangos frente a la expresión cuantitativa de Oct4:

- La infiltración de células inmunes se considera nula o baja, intermedia o elevada.
- CD31b presenta relación significativa con la expresión de Oct4, independientemente del grado de infiltración (p=0.029).
- Los resultados muestran una correlación significativa con un p<0.004 entre la mayor presencia de células Oct4+ y los casos de TNBs sin diferenciación.

Conclusiones

- Oct4 se expresa en mayor proporción cuanto más indiferenciado sea el TNB.
- La expresión de Oct4 facilita la evasión del sistema inmune en los TNBs, favoreciendo la presencia de células supresoras mieloides (CD11b+) y reduciendo la presencia de macrófagos (CD68+).

II. Quantitative comparison and reproducibility of pathologist score and digital image analysis of the expression of S100A6 protein in neuroblastoma. Pérez A, Monferrer E, Mateu JM, Navarro S, Noguera R. *II Congreso Nacional de Jóvenes Investigadores en Biomedicina*. Valencia (Spain), November 2017.



Quantitative comparison and reproducibility of pathologist score and digital image analysis of the expression of S100A6 protein in neuroblastoma

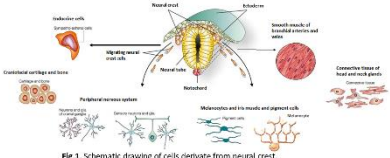
Pérez, A.¹; Monferrer, E.¹; Mateu, J.¹; Navarro, S.^{1,2}; Noguera, R.^{1,2}
¹Department of Pathology, Medical School, University of Valencia / INCLIVA.
²CIBER of Cancer (CIBERONC), Madrid



Facultat de Medicina i Odontologia

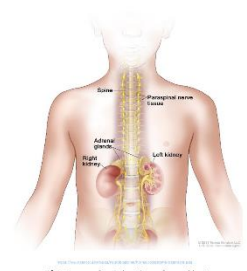
Background of S100A6 protein in Neuroblastoma

- **S100 family of proteins** is normally expressed in cells derived from the neural crest (Schwann cells and melanocytes), macrophages and dendritic cells, among others (Fig.1).
- Aberrant expression of S100 family members has been reported in **many types of cancers**.
- S100 calcium-binding A6 (**S100A6**) protein may function in Ca2+ signaling (Fig.2).
- Some studies have described subpopulations of neuroblastic-like cells that express GD2 and S100A6, **related to a low risk Neuroblastic tumors (NBT)**¹.
- Additionally, an important role of calcium signaling has been observed in the response of NBT to **chemotherapy**².



Background of Neuroblastic tumors

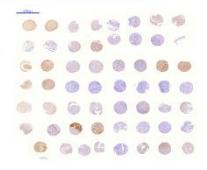
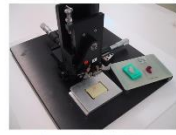
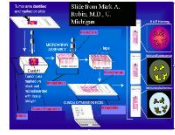
- **Most frequent** extracranial childhood tumor.
- Originates in the neural crest tissue and it can occur anywhere along the **sympathetic nervous system (Fig.3)**.
- The clinical signs and symptoms are very **heterogeneous**.
- Composed by neuroblasts and stroma cells (Schwann cells, immune cells, stem cells and other cells).
- Cause of **15% childhood cancer death**³.
- More than 90% of the affected are children are **younger than 5 years**.



Aims: To assess the quantitative digital image analysis of S100A6 protein expression in NBT.

Materials and methods

- We investigated the expression of S100A6 protein in **482 NBT** included in tissue microarrays (TMAs).
- Construction of **TMAs** was done using MTA-1 (Beecher Instruments-Silver Spring) (Fig.4-6).
- Immunohistochemistry (IHC) with **anti-S100A6 polyclonal antibody** (Rabbit Anti-Human S100A6 Code No. A 5115, DAKO) at a dilution 1:200.



- Panoramic MIDI scanner was used for digitalization (Fig.7).
- The expression levels were measured using the software **Pannoramic Viewer** with the NuclearQuant algorithm. The percentage of positive cells related to negative cells were calculated (Fig.8).
- The samples were also analyzed under a **microscope** by an expert pathologist and divided in four groups, linking the positive cells with the Schwannian-like cells in the tumor (Fig.9).
- We compared the results obtained by quantitative digital analysis and the pathologist scoring using **SPSS**.

Interpretation of immunohistochemistry staining by the pathologist:

- **Scale of intensity**
- 1. **negative (-)** (cases without Schwann-like cell)
- 2. **weak (+)** (between 1 and 100 cells)
- 3. **moderate (++)** (between 100 and 300 cells)
- 4. **strong (+++)** (more than 300 cells)

• **Pattern of distribution:** nuclear in Schwann-like cells.

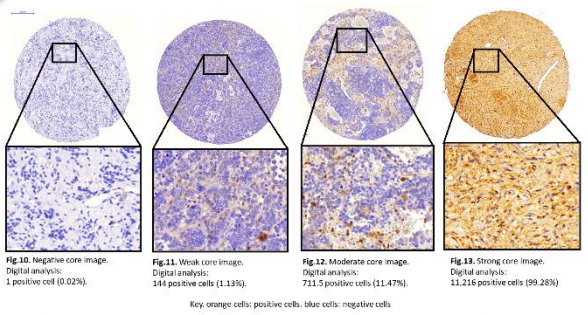
Results

Correlation between pathologist scoring and digital analysis (Table 1).

In order to discover if the digital analysis could be more sensitive than the pathologist inspection, for each group that the pathologist defined, the mean of positive cells and the percentage of positive expression for the data given by the digital analysis were calculated.

Table 1. Results from the comparison between the pathologist scoring and quantitative digital analysis.

Pathologist score	Digital analysis		
	Number of samples	Mean of positive cells	Percentage of positive expression
Negative	161	23	0.57%
Positive +	184	134	2.14%
Positive ++	70	327	6.31%
Positive +++	67	2,881	80.61%



Conclusions

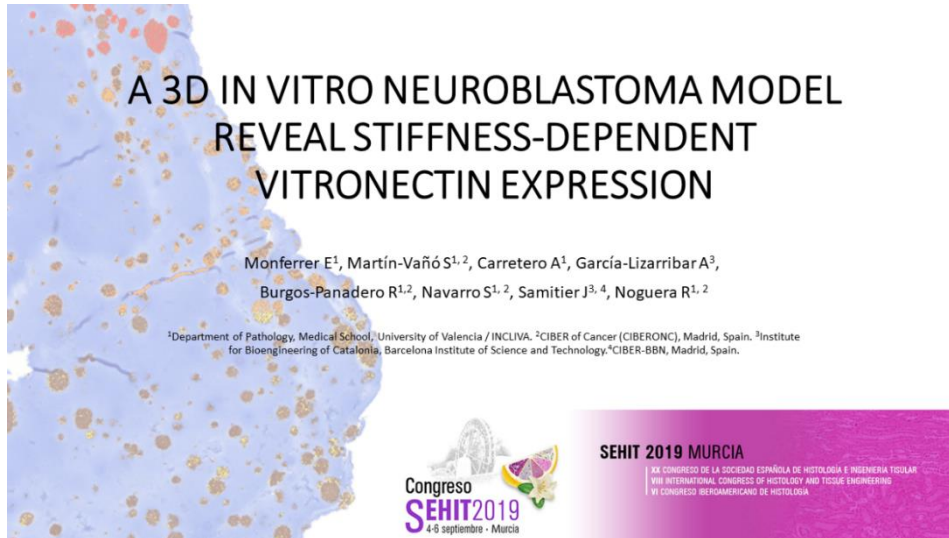
- Quantitative digital analysis is **highly sensitive** and **relatively specific** when compared to pathologist evaluation in detecting S100A6 protein expression.
- It represents a **potential reliable tool** for future therapeutics quantitative immunohistochemistry analysis with refinement and precision.

References

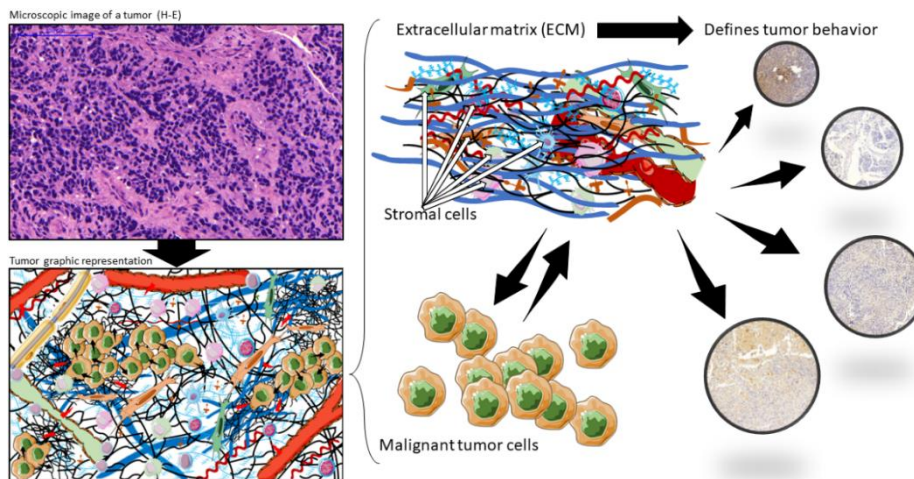
1. Acosta, S., Mayol, G., Rodriguez, E., Lavarino, C., De Preter, K., Kumps, C., ... & Mora, J. (2011). Identification of tumoral glial precursor cells in neuroblastoma. *Cancer letters*, 312(1), 73-81.
2. Florea, A. M., Varghese, E., McCallum, J. E., Mahgoub, S., Helmy, I., Varghese, S., ... & Büsnelberg, D. (2017). Calcium-regulatory proteins as modulators of chemotherapy in human neuroblastoma. *Oncotarget*, 8(14), 22876.
3. Maris, J. M., & Matthay, K. K. (1999). Molecular biology of neuroblastoma. *Journal of clinical oncology*, 17(7), 2264-2264.



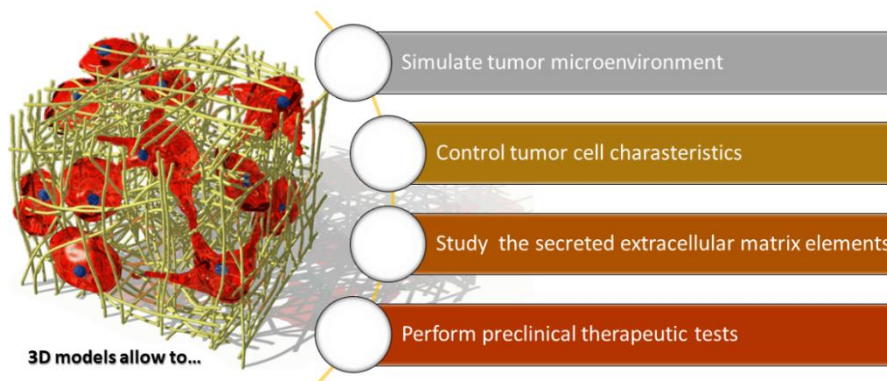
- III. A 3D in vitro neuroblastoma model reveals stiffness-dependent vitronectin expression. **Monferrer E**, Martín-Vañó S, Carretero A, García-Lizarribar A, Burgos-Panadero R, Navarro S, Samitier J, Noguera R. *SEHIT2019*. Murcia (Spain), September 2019.



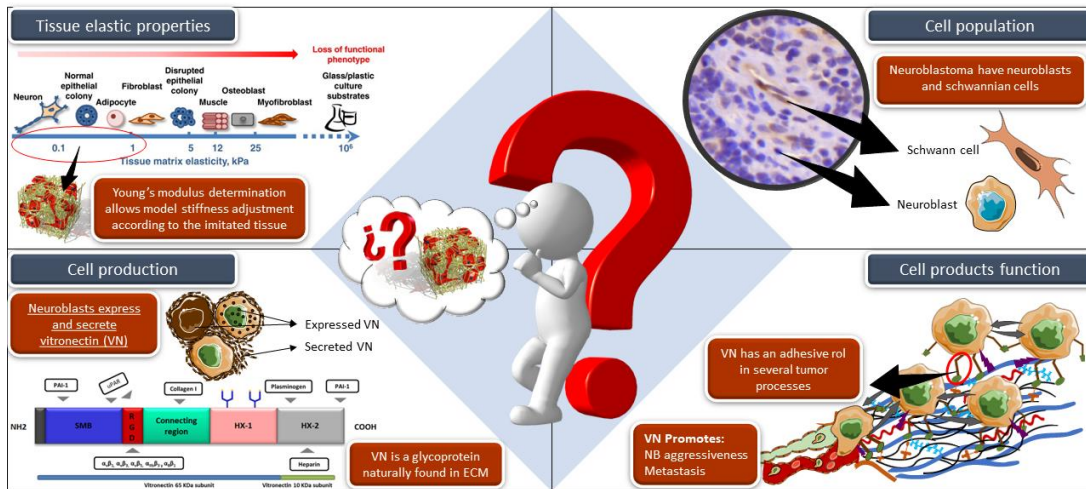
Introduction



Introduction



Introduction



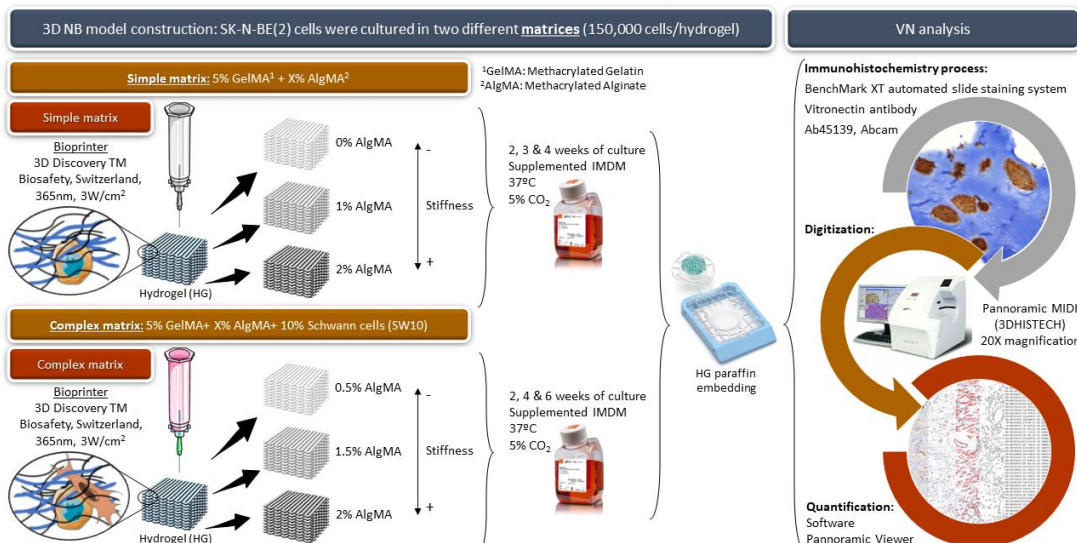
Objectives



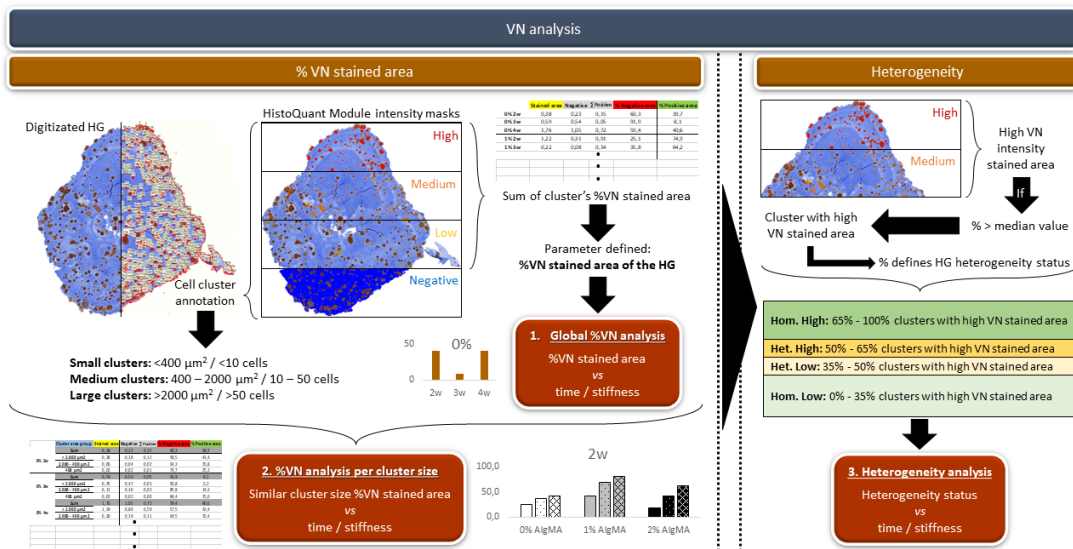
To determine the effect of ECM characteristics on the neuroblast VN expression and secretion using 3D bioprinted cell culture models

To define the physical cues that promote NB aggressiveness in relation with VN and its expression pattern

Methodology

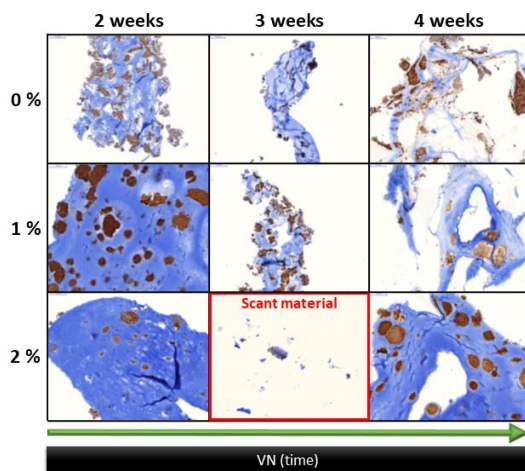
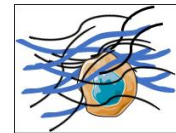


Methodology

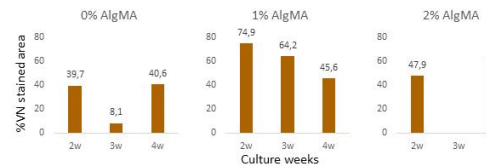


Results

1. Global %VN analysis



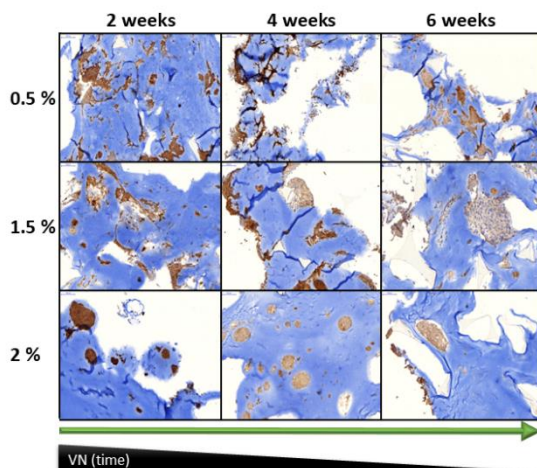
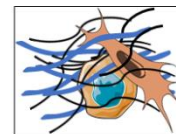
Relationship between VN expression and time
Simple matrix



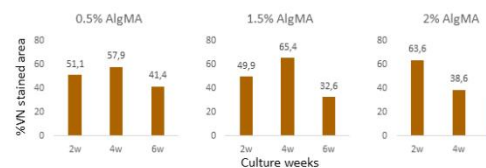
Time does not have a specific effect on VN expression

Results

1. Global %VN analysis



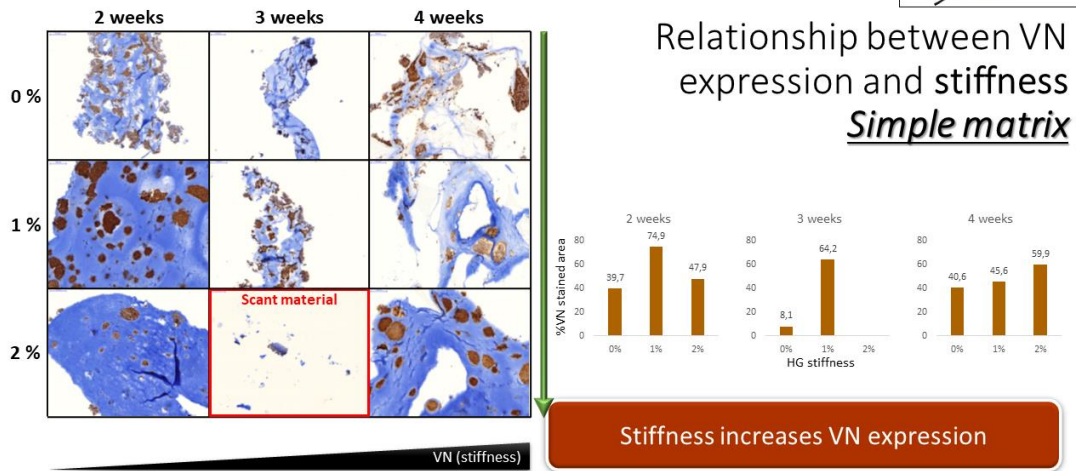
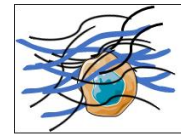
Relationship between VN expression and time
Complex matrix



VN expression decreases with time

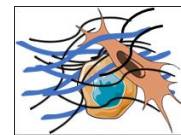
Results

1. Global %VN analysis



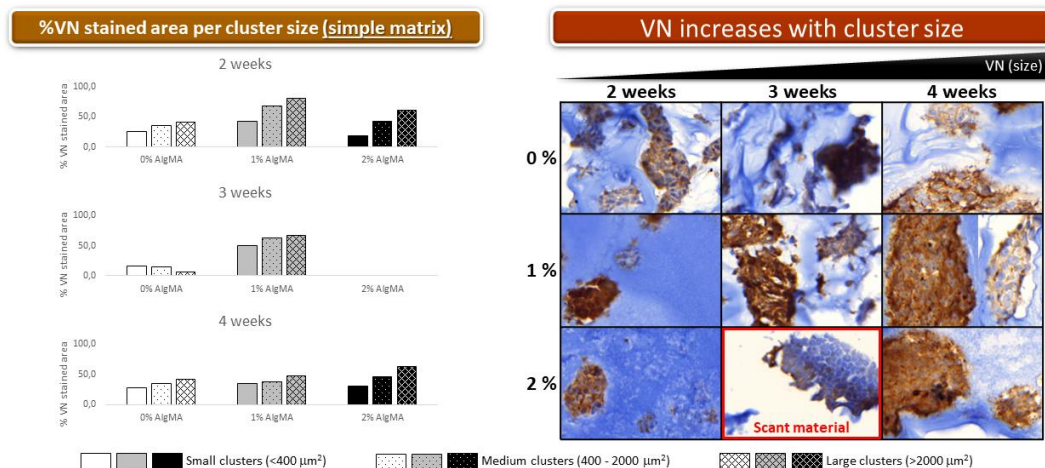
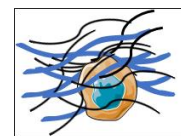
Results

1. Global %VN analysis



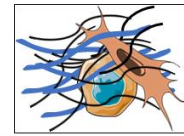
Results

2. %VN analysis per cluster size

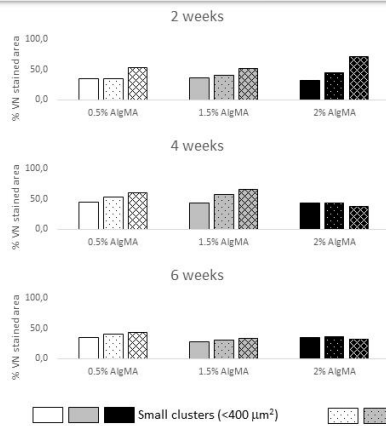


Results

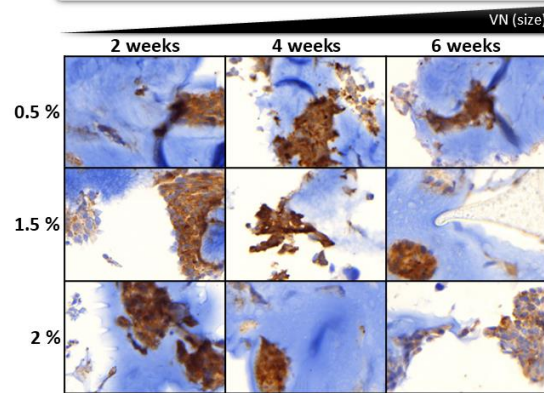
2. %VN analysis per cluster size



%VN stained area per cluster size (complex matrix)

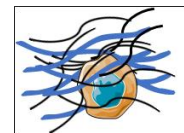


VN increases with cluster size

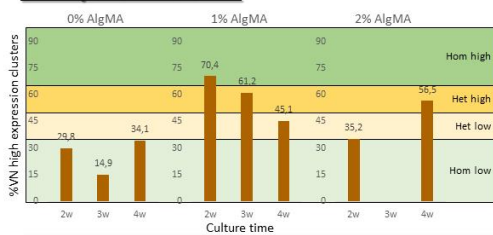


Results

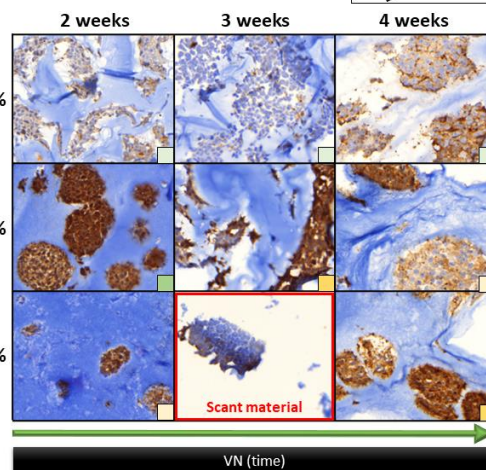
3. Heterogeneity vs time / stiffnes



Relationship between VN heterogeneity and time
Simple matrix

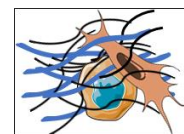


VN expression becomes heterogenic and varies over time

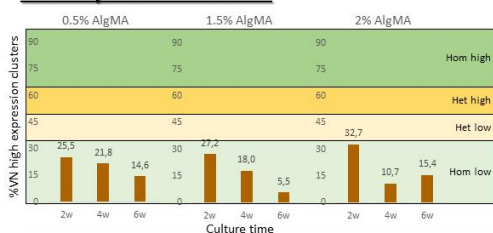


Results

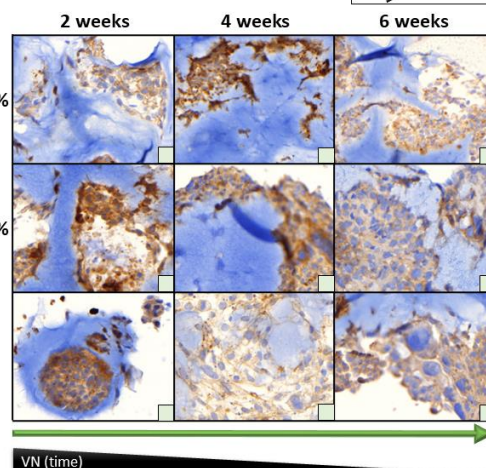
3. Heterogeneity vs time / stiffnes



Relationship between VN heterogeneity and time
Complex matrix

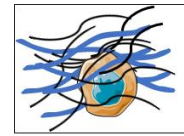


VN expression remains homogenic and decreases with time

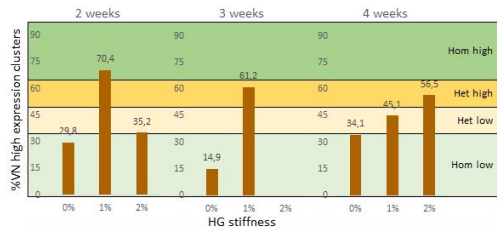


Results

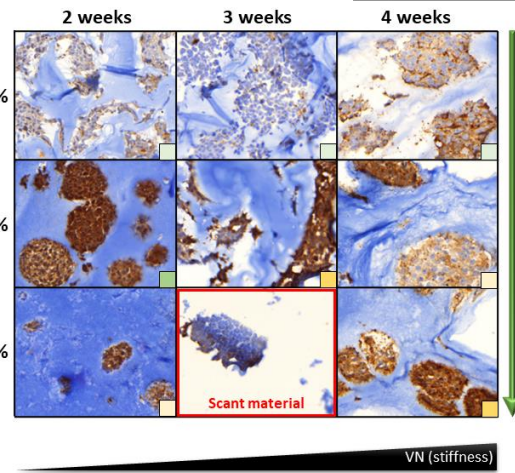
3. Heterogeneity vs time / stiffness



Relationship between VN heterogeneity and stiffness
Simple matrix

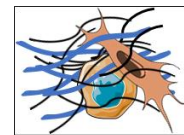


VN expression becomes heterogenic and increases with stiffness

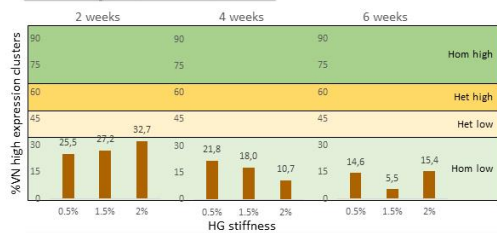


Results

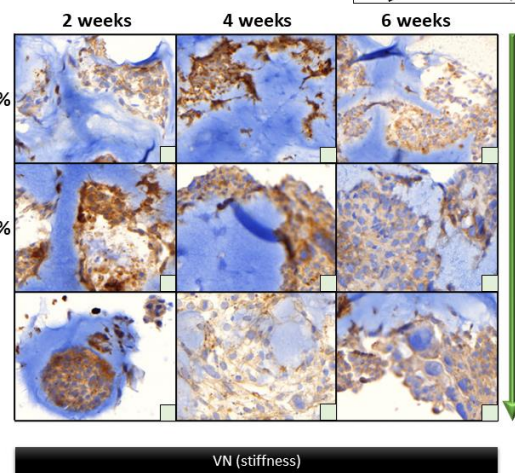
3. Heterogeneity vs time / stiffness



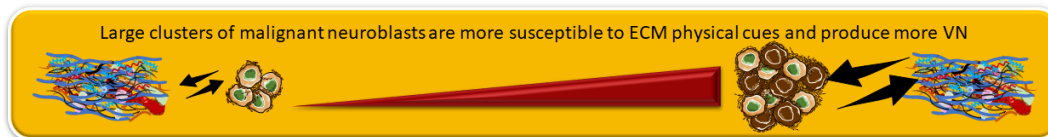
Relationship between VN heterogeneity and stiffness
Complex matrix



VN expression remains homogenic, with little variations due to stiffness



Conclusions



Microenvironment differences affect VN expression

Simple matrix: only have neuroblasts

Complex matrix: have neuroblasts + schwann

High VN general expression

Low VN general expression

VN expression increases with stiffness

VN expression decreases with time

VN tends to heterogeneous states with time and stiffness

VN remains homogenic over the time and stiffness

- IV. Vitronectin and its receptors: human neuroblastoma 2D in vitro characterization. Burgos-Panadero R, Monferrer E, Noguera I, Navarro S, Noguera R. *SEHIT2019*. Murcia (Spain), September 2019.

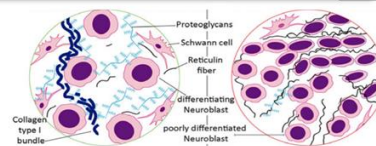
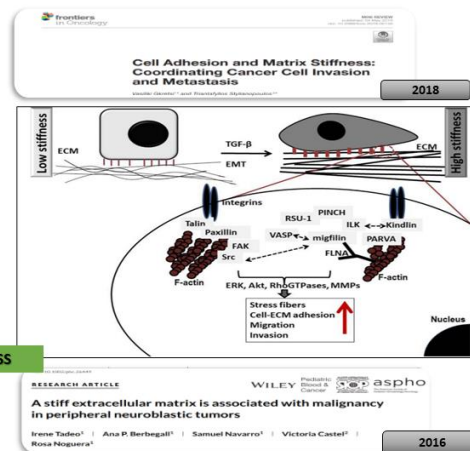
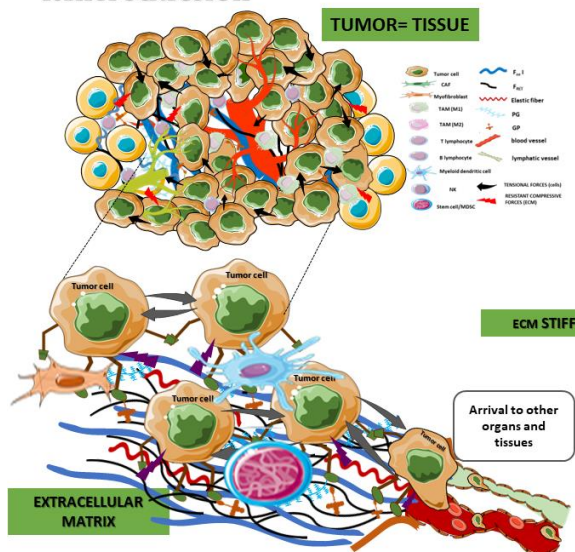
VITRONECTIN AND ITS RECEPTORS: HUMAN NEUROBLASTOMA 2D IN VITRO CHARACTERIZATION

Burgos-Panadero R^{1,2}; Monferrer E¹; Noguera Salvá I³; Navarro S^{1,2}; **Noguera R^{1,2}**.

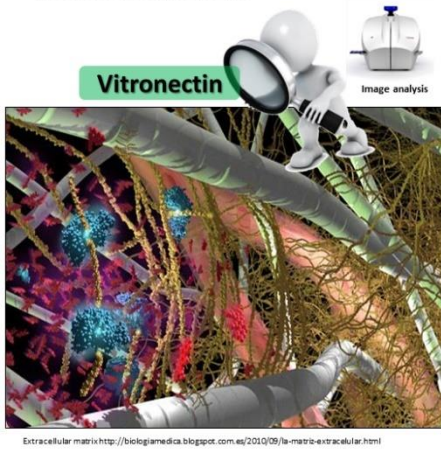
¹Department of Pathology, Medical School, University of Valencia/ INCLIVA. Valencia, Spain. ²CIBER of Cancer (CIBERONC), Madrid, Spain. ³Central Support Service for Experimental Research (SCSIE), University of Valencia, Spain.



1. Introduction



1.Introduction



Extracellular matrix <http://biologiamedica.blogspot.com.es/2010/09/la-matriz-extracelular.html>

Morphometric

Features	Age 25 months	Stage IV	Met4-6B	Met5	Gen profile	Vis High	Ris group	Gen
IP	Yes	Yes	Yes	Yes	Yes	Yes	Yes	Yes
Nude	Yes	Yes	Yes	Yes	Yes	Yes	Yes	Yes
Met4	Yes	Yes	Yes	Yes	Yes	Yes	Yes	Yes
Met5	Yes	Yes	Yes	Yes	Yes	Yes	Yes	Yes
Gen profile	Yes	Yes	Yes	Yes	Yes	Yes	Yes	Yes
Vis High	Yes	Yes	Yes	Yes	Yes	Yes	Yes	Yes
Ris group	Yes	Yes	Yes	Yes	Yes	Yes	Yes	Yes
Gen	Yes	Yes	Yes	Yes	Yes	Yes	Yes	Yes

Topological

BMC Cancer

RESEARCH ARTICLE

Vitronectin as a molecular player of the tumor microenvironment in neuroblastoma

2019

JHC

The topology of vitronectin: A complementary feature for neuroblastoma risk classification based on computer-aided detection

2019

Features	B	SE	Top 10 (p<0.01)	Z value	P (adj)
Risk stratification group					
Intermediate	-1.50	0.01	0.01 (0.01-0.11)	-4.36	1.12E-04
High	0.45	0.26	1.92 (1.15-3.20)	2.49	0.013
Low	2.66	0.61	14.36 (6.36-47.50)	4.36	1.26E-05
Stage					
Stage I	-4.95E-03	0.01	0.99 (0.87-1.02)	-0.51	0.61E-01
Stage II	-1.61E-01	0.01	0.99 (0.91-1.02)	-0.50	0.62E-01
Tumor genetic instability criteria					
Regular logistic regression					
Intermediate	-21.64	2.91E-01	5.05E-11 (0-Inf)	-0.01	0.99E
High	1.50	0.58	4.46 (1.64-13.80)	2.60	0.009
Low	19.89	2.91E-01	4.17E-08 (0-Inf)	0.01	0.99E
APC (SNP)	21.58	1.24E-01	4.95E-09 (0-Inf)	0.01	0.99E
Protein	-1.83E-01	1.12E-01	1.00 (0.99-1.00)	-1.21	0.02E

1.Introduction

Structure of Vitronectin adapted from (Schwarz et al., 1999).

uPAR function in the complex uPA/uPAR-VN (Smith and Marshall, 2010).

Oncotarget, 2016 Mar 22;7(12):15016-32. doi: 10.18632/oncotarget.7588.

Cilengitide in newly diagnosed glioblastoma: biomarker expression and outcome.

Weller M¹, Nabors LP², Gorlia T³, Leake L⁴, Rushing E⁵, Bady P^{6,7}, Hickling CJ⁸, Perry J⁹, Hong YK¹⁰, Both P¹¹, Wick W^{11,12}, Goodman SL⁴, Hegel ME⁷, Priced M⁸, Moch M¹³, Straub J⁴, Stupp S¹⁴

2016

Cancer Res, 2013 Apr 1;73(7):2070-81. doi: 10.1158/0008-5472.CCR-12-3020. Epub 2013 Feb 11.

Targeting uPAR with antagonistic recombinant human antibodies in aggressive breast cancer.

LeBeau AM¹, Duvicet S, Murphy ST, Peckol E, Hann B, Gray JW, Van Brocklin HE, Czihak CS

2013

Biomedicine & Pharmacotherapy

Volume 107, September 2018, Pages 59-74

Plasminogen activator inhibitor-1 in cancer research

2018

2.Hypothesis and objectives

Looking for therapeutic targets

Aggressive tumor tissue

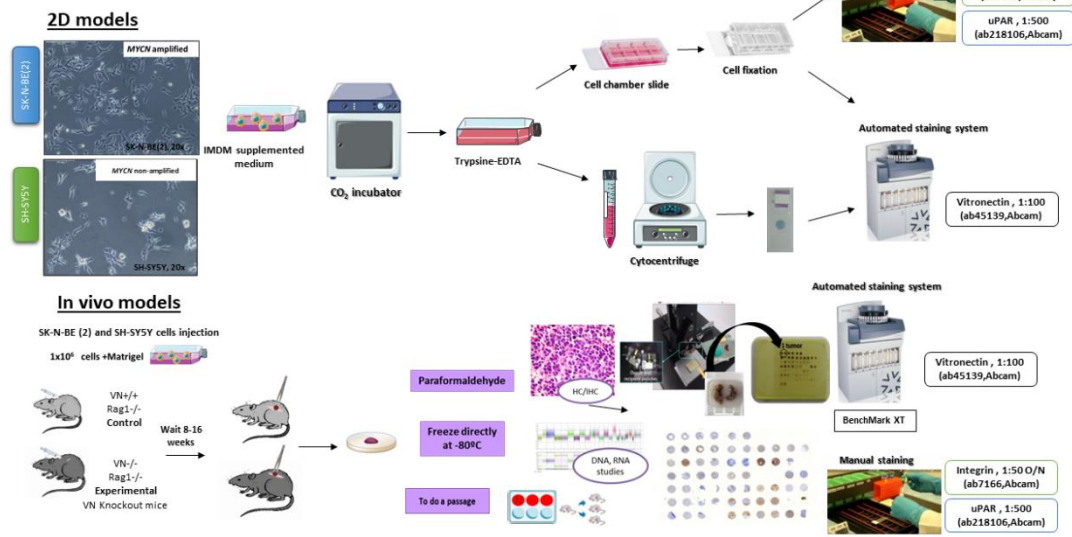
Residual tissue

MALIGNANT NEUROBLASTIC CELLS

- To characterize the vitronectin expression in vitro 2D and in vivo.
- To characterize the vitronectin ligands (uPAR and $\alpha_5\beta_3$) in vitro 2D and in vivo.

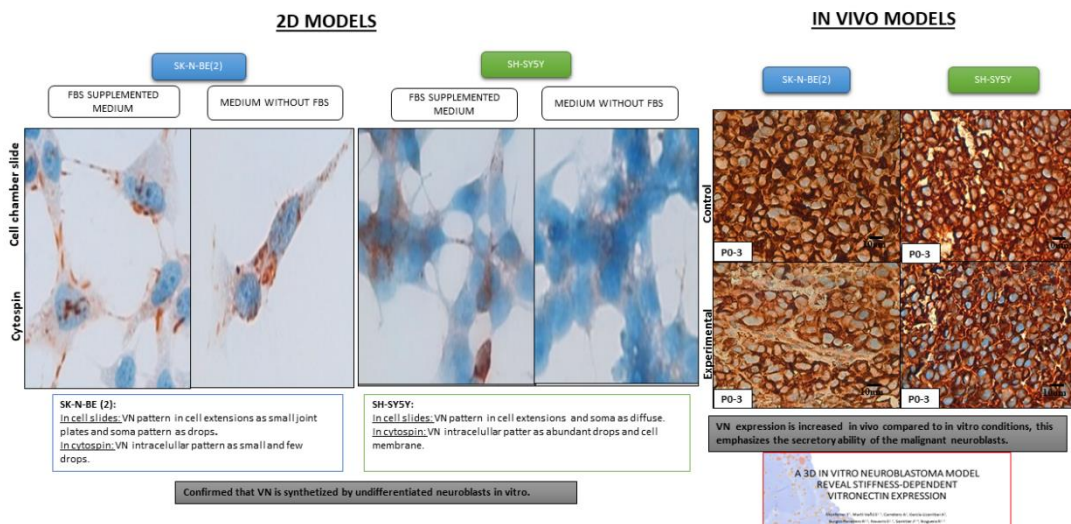
{ 207 }

3. Material and Methods



4. Results

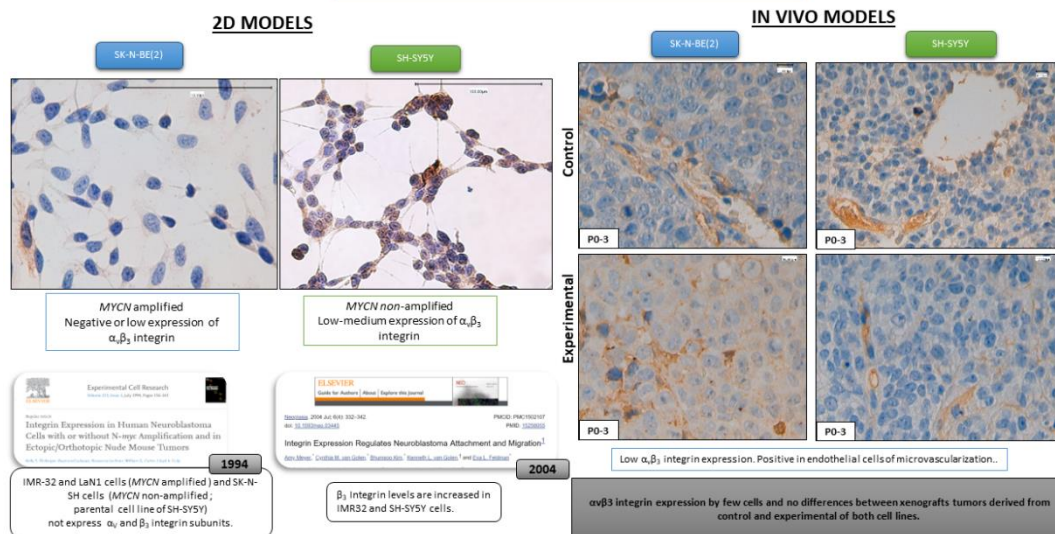
Characterization of vitronectin



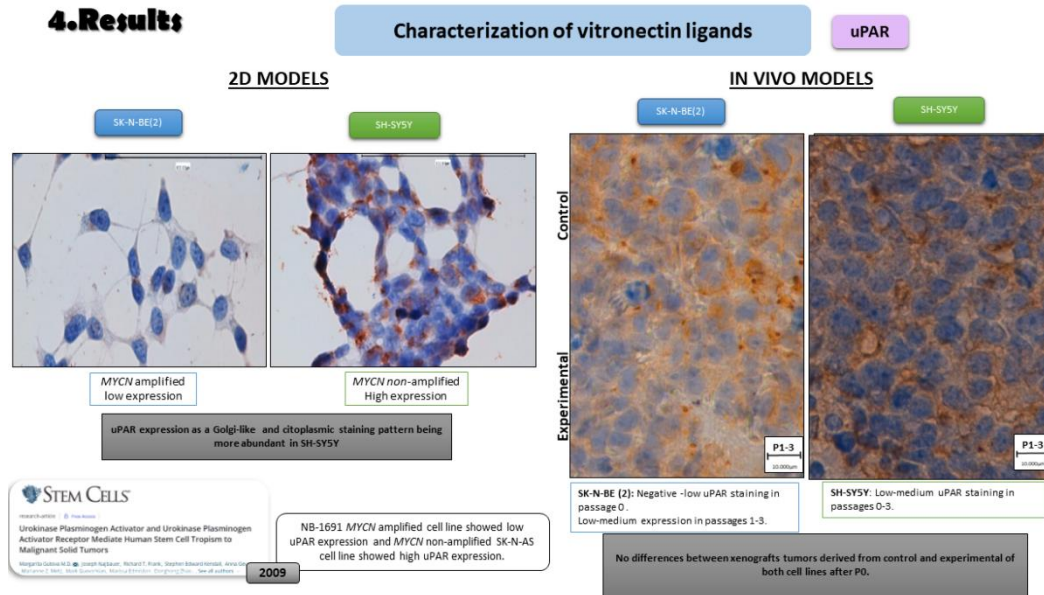
4. Results

Characterization of vitronectin ligands

$\alpha_v\beta_3$ integrin



4. Results




5. Conclusions




- The modulation of **vitronectin** secretion seems to be a strategy for malignant neuroblasts to respond to local microenvironmental changes. **Host VN/-/ microenvironment does not influence the neuroblastic VN synthesis in vivo.**
- The low *in vitro* and *in vivo* **$\alpha_v\beta_3$ integrin** staining pattern staining drives us to study the expression of $\alpha_v\beta_5$ integrin (ongoing studies). **$\alpha_v\beta_3$ integrin is discarded as a main ligand for malignant neuroblasts-VN-ECM adhesion.**
- The *in vitro* **uPAR** expression by **MYCN** non-amplified malignant neuroblasts and the *in vivo* uPAR expression by cells with both genetic features, suggest that it could be a good therapeutic target. **Diachronic in vivo uPAR expression need to carry out an in-depth study.**
- Further *in vitro* and *in vivo* studies to prove the potential use of VN and its receptors as future therapeutic targets are needed. **We highlighted the importance of VN and its ligands in histology and histopathology.**

V. Building silk-fibroin 3D hydrogels with enzymatically cross-linked vitronectin to study neuroblastoma aggressiveness. Vieco-Martí I, Monferrer E, López-Carrasco A, Granados-Aparici S, Navarro S, Noguera R. *SEHIT2022*. Granada (Spain), September 2022.






ITTA-P10



BUILDING SILK-FIBROIN 3D HYDROGELS WITH ENZYMATICALLY CROSS-LINKED VITRONECTIN TO STUDY NEUROBLASTOMA AGGRESSIVENESS

Vieco-Martí I.^{1,2}, Monferrer E.^{1,2}, López-Carrasco A.^{1,2}, Granados-Aparici S.¹, Navarro S.^{1,2}, Noguera R.^{1,2}

¹ Department of Pathology, Medical School, INCLIVA Biomedical Health Research Institute, University of Valencia, Valencia, Spain; ² Low Prevalence Tumors, Centro de Investigación Biomédica en Red de Cáncer (CIBERONC), Instituto de Salud Carlos III, Madrid, Spain.

1. VITRONECTIN IN HIGH-RISK NEUROBLASTOMA AND SILK FIBROIN SCAFFOLDS



Vitronectin (VN) is a glycoprotein involved in biological processes such as cell growth, angiogenesis and metastasis in different tumors. The presence of VN may confer mechanical properties which increase high-risk neuroblastoma (HR-NB) aggressiveness [1]. Silk-fibroin (SF) is an easy tunable biomaterial which enable the building of hydrogels with enzymatically-linked molecules. The aim of this study is to build a SF and gelatin-tyramine (GTA) 3D hydrogels (HG) with different amounts of VN to study its role in the aggressiveness of the HR-NB.

2. MATERIALS & METHODS

2.1. Experimental conditions

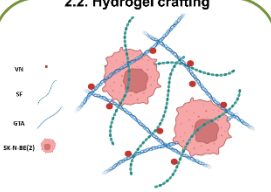
Model 1. 25_75

- Total solute: 4% w/v
- Model 1.1. 25%GTA_75%SF
- Model 1.2. 25%GTA_75%SF + VN (0.6mg/ml)
- SK-N-BE(2) cells (2 million/ml)
- Culture days: 03,07,14,21

Model 2. 50_50

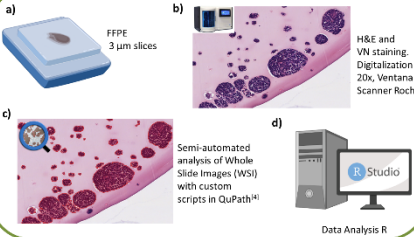
- Total solute: 4% w/v
- Model 2.1. 50%GTA_50%SF
- Model 2.2. 50%GTA_50%SF + VN (0.4mg/ml)
- SK-N-BE(2) cells (2 million/ml)
- Culture days: 03,07,14,21

2.2. Hydrogel crafting



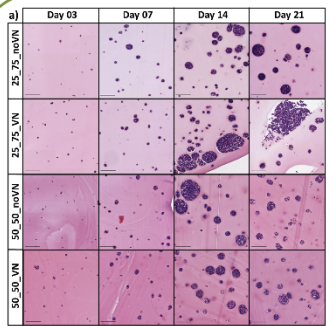
Mix the components in IMDM cell culture media. Cross-link(37) by adding Horseradish Peroxidase (20U/ml) and H₂O₂ (0,01%). 65um drops in 24 well cell culture plates Keep 45 minutes at 37°C

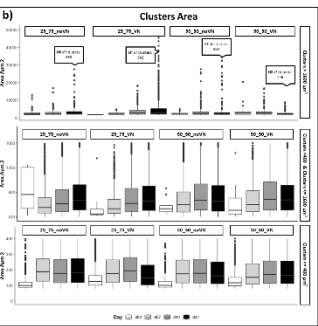
2.3. Tissue processing & Analysis

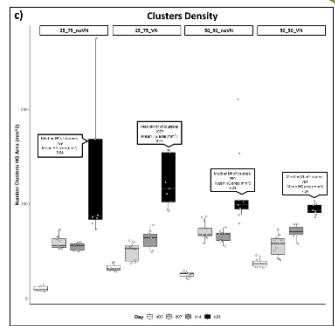


3. RESULTS

3.1. SK-N-BE(2) cells behavior in different models

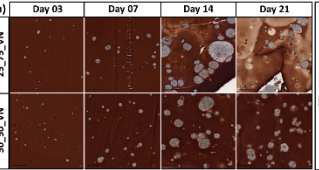
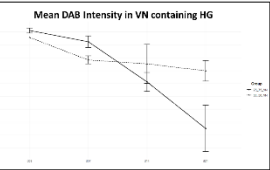






Total HG: 16 (one per condition). Images analyzed: 135 WSI. Total clusters detected: 94,012. Figure a) Representative H&E staining of the HGs. Isolated cells and clusters of malignant neuroblasts are shown. Scale bar: 100µm. Figure b) Boxplot of the clusters area. Data split in three cluster size ranges: < 400 µm² (< 5 cells); between 400-1600 µm² (5-20 cells); >1600 µm² (>20 cells). Interestingly, the model 25_75_VN contains the biggest clusters at day 21. Figure c) Boxplot of the clusters density, each point represents one image. In all conditions, the maximum density is reached at day 21. The presence of VN in 25_75 models trends to increase the density of clusters.

3.2. VN is effectively cross-linked to the HG

Images analyzed: 23 WSI. Total clusters detected: 13,014. Figure a) Immunostaining against VN in VN-containing HG. Intensity decreases with time due to VN detachment or degradation by cells. Scale bar: 100µm Figure b) Line plot Mean Diaminobenzidine (DAB) intensity (arbitrary units) with time.

3.3. SK-N-BE(2) cells secrete VN in noVN HG

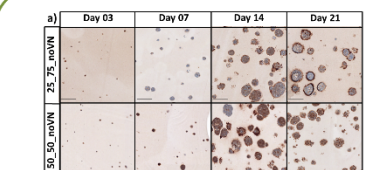


Figure a) Immunostaining against VN in noVN-containing HG. SK-N-BE(2) cells secrete the VN in a coronary conformation predominantly in 25_75 HG at day 21. Scale bar: 100µm

4. CONCLUSIONS

We successfully built SF based 3D HG with enzymatically cross-linked VN. We observe different behaviors of HR-NB cells in different conditions. Those 3D models are suitable to perform further studies to reveal the role of the VN in the aggressiveness of HR-NB.
 Funding: Spanish University Ministry (FPU20/05344); ISCIII (P120/01107); CIBERONC (CB16/12/00484)

5. REFERENCES & RESOURCES

[1] Burgos-Panadero, R. et al. BMC Cancer 19, (2019)
 [2] Sakai, S. et al. Biomaterials 30, 3371–3377 (2009)
 [3] Hasturk, O. et al. Biomaterials 232, 119720 (2020)
 [4] Bankhead, P. et al. Sci. Rep. 7, (2017)
 Pictures: Worm @finalname7.psd ; M&M with BioRender.com